The Pulsar Radio Emission and Polarization

A thesis
submitted for the degree of

Doctor of Philosophy

in

The Department of Physics,
Pondicherry University,
Puducherry - 605 014, India

by

Tridib Roy
Indian Institute of Astrophysics,
Bangalore - 560 034, India

20 June 2020

The Pulsar Radio Emission and Polarization

Tridib Roy
Indian Institute of Astrophysics

Indian Institute of Astrophysics
Bangalore - 560 034, India

Title of the thesis	:	**The Pulsar Radio Emission and Polarization**
Name of the author	:	**Tridib Roy**
Address	:	Indian Institute of Astrophysics II Block, Koramangala Bangalore - 560 034, India
Email	:	tridib@iiap.res.in
Name of the supervisor	:	**Prof. R.T. Gangadhara**
Address	:	Indian Institute of Astrophysics II Block, Koramangala Bangalore - 560 034, India
Email	:	ganga@iiap.res.in

Declaration of Authorship

I hereby declare that the matter contained in this thesis is the result of the investigations carried out by me at the Indian Institute of Astrophysics, Bangalore, under the supervision of Prof. R.T.Gangadhara. This work has not been submitted for the award of any other degree, diploma, associateship, fellowship, etc. of any other university or institute.

Signed: Tridib Roy

Date: 20 June 2020

Certificate

This is to certify that the thesis entitled **'The Pulsar Radio Emission and Polarization'** submitted to the Pondicherry University by Mr. Tridib Roy for the award of the degree of Doctor of Philosophy, is based on the results of the investigations carried out by him under my supervision and guidance, at the Indian Institute of Astrophysics. This thesis has not been submitted for the award of any other degree, diploma, associateship, fellowship, etc. of any other university or institute.

Signed: 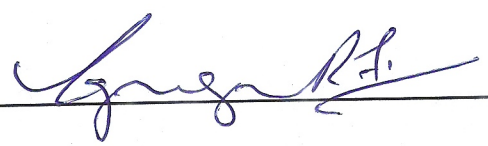

Date: **20 June 2020**

Acknowledgements

Abinitio, I would like to express my intimation, sincere help, gratefulness, humble tribute, and regards to my supervisor Prof. R.T. Gangadhara for his indispensable support, overwhelming guidance, encouragement, and constant engagement immensely throughout my research problem. His perspectives, specialization in the subject of radio pulsars helped me immensely during my Ph.D. tenure. I am delighted to work under his guidance.

I also want to devote my sincere thanks to my doctoral committee members Prof. B. Muthukumar (Pondicherry University) and Prof. M. Sampoorna (Indian Institute of Astrophysics) and all the staffs of the Indian Institute of Astrophysics and Pondicherry University for their timely, consistent significant help related to synopsis and thesis submission.

My special thanks to the Bhaskara guest house's local hospitality for providing me a beautiful accommodation and delicious food. Of course, my sincere gratitude goes to every living and non-living creatures of nature, with whom I and directly and indirectly involved as I believe them to be connected with human psychology, and therefore, it could give us power in terms of self-motivation serendipitous via a spontaneous rhythmic pattern of nature as well as some other sorts of positive feedback.

I am thankful to the IIA computer center for providing a cluster account in Fornax to run necessary theoretical simulations and the IIA library for providing books to me. Finally, the IIA as a whole for providing a vibrant academic/research ambiance to do necessities for my research work during my tenure.

I also thank all my seniors, fellow students, and batchmates at the IIA and my college life friend Monoseej Banerjee for their unstoppable support.

I also thank my family members and my childhood teachers for their encouragement in pursuing me for higher studies. I am also grateful to my uncle Dr. Pradipta Basu (Professor of chemistry, Hooghly Mohsin College, West Bengal), for being the source of my inspiration and encouragement.

Last and most important, I would like to acknowledge my pleasure and unconditional love to my parents for making me what I am today. No literature will be sufficient enough to portray their dedication in my whole journey, till date. I would definitely like to overwhelming gratitude and humble regards to them from the deep of my heart for everything.

Finally, I would like to mention one of the unforgettable tragedies: My elder sister, who committed suicide in 2013 September due to some anonymous reason or more pronouncedly because of the poor financial condition of my parents. So I would like to pay my humble tribute and dedicate my thesis to the departed soul (Sudeshna Roy, elder sister).

Data usage

My thesis problem mainly focuses on theoretical aspects of radio pulsar's emission mechanism, so I have barely used any data according to my knowledge. But in the 3rd Chapter, I have used data from ATNF (Australian Telescope National Facility) catalogue to calculate brightness temperature and compared my theoretical model predictions.

Abstract

The thesis is mainly focused on the modeling of pulsar radio emission and polarization. The radio emission mechanism of pulsar is not fully understood, because of the lack of understanding about the kinematical processes involved in pulsar magnetosphere, radio emission geometry and magnetic field topology obviously. Observation strongly suggest that pulsar radio emission is a coherent process, as very high energetic emission with corresponding brightness temperature $\approx 10^{25}$ K is taken place from a source with size around 10 km.

From an astrophysical point of view, pulsars are often characterized as quantum degenerate stars i.e., neutron star, which is highly magnetized ($B = 10^8 - 10^{13}$ G), highly compact rotating object. There has been attributed specific locations or magnetospheric gaps, for example polar gap, outer gap etc. in literatures, which are demarcated as the locations exclusively for originating radio emission and X-ray emission respectively. Polar cap boundary is defined as the footprint of last open magnetic field lines. On the other hand outer gap is located in a region close to neutron star's surface and in between open and closed magnetic field lines. As pulsar is spinning rapidly with huge magnetic field, it induces large electric field across polar cap region, which is around 10^{12} volt per cm. This huge electric field exceeds the vacuum breakdown condition and as a result the region above polar cap is filled with charged particles. Due to huge background magnetic field, the momentum of particles, perpendicular to magnetic field is dissipated away very quickly and thereafter they continue to accelerate along the open magnetic field line. As a result of charged particle acceleration due to movement along curved magnetic field line, curvature radiation photons (gamma-rays) are generated. These curvature photons subsequently decay into electron and positron pairs via cascade process which produce a cloud of secondary charged particles with Lorentz factor 100-1000. This secondary charged particles are believed to be responsible for pulsar radio emission.

There have been suggested three processes to explain pulsar radio emission mechanism, (i) Antenna mechanism, (ii) Relativistic plasma instabilities and (iii) Maser emission mechanism, whose elaborate descriptions are provided with sufficient details in chapter 1 and chapter 2. Masers are in fact closely related to plasma instabilities. Abinitio a generic introduction to radio pulsar is given in chapter 1 with different polarization related properties. Nevertheless the main aim of this thesis is to make a model by considering collective plasma process and suitably chosen geometry to estimate radio pulsar brightness temperature theoretically, which is shown in 3^{rd} chapter. We develop a mechanism for pulsar radio emission which takes into account of the detailed viewing geometry of pulsars and dipolar magnetic field configuration. By using a suitably chosen geometry and plasma parameters we derive analytical expressions for the Stokes parameters of the radiation field in the neutron star centered frame. We have simulated the pulse profiles based on our analytical formulation. It seems we can explain the enhanced radiation and most of the diverse polarization properties of radio pulsars. We have estimated the brightness temperature, which seems to agree with the observations. The polarization angle predicted by the model is in good agreement with the rotating vector model. The brightness temperature shows a reasonably good agreement between theoretically computed values and observation.

In 4^{th} chapter, I have discussed about the power spectra modeling of radio pulsars by introducing plasma processes such as Stimulated Raman scattering (SRS) and Stimulated Compton Scattering (SCS). Usually flux of pulsars in radio regime falls inversely with frequency, with mean value of index lying between -3 to -1. There has been proposed different types of power spectra like simple power law, two segmented broken power law, log-parabolic etc. It is evident that, two different distinct plasma processes are responsible for generating two segmented broken power law. So in chapter 4 I have used SRS and SCS as potential tools to reproduce power spectra of a few pulsars theoretically. It seems like about 80% of pulsars exhibit single power law and rest of the 20% show two segmented broken power law and other types. In chapter 4, I have basically shown how non-linear plasma processes such as SRS and SCS can

be applied to pulsars and reproduce their power spectra in radio regimes theoretically. In chapter 5, I have investigated the role of SRS on the polarization state of pulsar radio emission. It is shown that rapid temporal variability of intensity and switching of polarization state from elliptical to circular, linear and vice-versa can be incorporated by implementing SRS, under different plasma conditions. Apart from that, it is shown that the effect of SRS is more pronounced in the typical pulsar magnetosphere than other effects such as Faraday rotation. In chapter 6, all the chapters are summarized together and merits of the theories in connection to observations are justified with future implication.

My future plans are to: (1) Make observations of pulsars and their power-law spectra, (2) Estimate the aberration-retardation (A/R) effects on pulsar spectra, (3) Study the orthogonal polarization mode (OPM) phenomena. In addition to pulsars, my other future plans are to study Fast Radio Bursts (FRB).

Publications:

1. **Radio emission in pulsars due to relativistic plasma**

Tridib Roy, R.T. Gangadhara, 2019, Astrophysical Journal (ApJ), Volume 156, article id. 148, pp. 24

DOI: 10.3847/1538-4357/ab1fe5

2. **Semi analytical modeling of radio pulsar power spectra using non-linear plasma process**

Tridib Roy, (under preparation/ongoing project).

3. **Influences on polarization state of radio pulsars due to stimulated Raman scattering instability**

Tridib Roy, (under preparation/ongoing project).

Conferences attended :

National:

1. National Conference on Recent Trends in the Study of Compact Objects - Theory and Observation (RETCO -III), June $5^{th} - 7^{th}$, 2017, IIST, Valiamala, Thiruvananthapuram, India.
Nature of participation: Contributed talk
Title: Pulsar Radio Emission and Polarization
Authors: Tridib Roy and R. T. Gangadhara

2. 36^{th} Astronomical Society of India meeting, February 5^{th} – 9^{th}, 2018, Osmania University, Hyderabad, India.
Nature of participation: Poster presentation
Title: Radio emission of pulsar and polarization
Authors: Tridib Roy and R. T. Gangadhara

International:

1. Conference on Physics of Neutron Stars, July 10^{th} – 14^{th}, 2017, Ioffe institute, Saint Petersburg, Russia.
Nature of participation: Poster presentation
Title: Radio emission mechanism in pulsar magnetosphere
Authors: Tridib Roy and R. T. Gangadhara

2. Exploring the universe near earth space science to extra-galactic astronomy, November 14^{th} – 17^{th}, 2018, S N Bose national center for basic science, Kolkata, India.
Nature of participation: Poster presentation
Title: Some glimpses of the plasma process involved in pulsar radio emission mechanism
Author: Tridib Roy

3. 30^{th} Texas Symposium on Relativistic Astrophysics, December 15^{th}– 20^{th}, 2019, University of Portsmouth, United Kingdom.
Title: Semi analytical modeling of Radio pulsar's Power Spectra by implementing nonlinear plasma process
Author: Tridib Roy
Nature of participation: Oral presentation

Contents

List of Figures

List of Tables

Chapter 1

General introduction to radio pulsars

Pulsar discovery is no doubt one of the most interesting astrophysical discoveries. It helps one to get a wealth of information about the interstellar medium, testing the formula of general theory of relativity, nuclear physics, probing gravitational wave physics and so on. On 6^{th} August 1967 the Mullard radio astronomy observatory, consisting with 2048 dipole arrays with operating frequency 81.5 MHz, encoded one series of signal with regular spacing near 19^h19^m right ascension and 21 degree declination in northern direction. Jocelyn Bell was a student at Mullard radio astronomy observatory, who noticed the periodic signals for the first time. Initially it was realized that the signal could be originating from terrestrial interference or might be from extra terrestrial civilization. After confronting with several speculations, it was recognized that, signal to be purely from celestial origin and eventually it was named as pulsar. Like as other astrophysical source in the sky, pulsar nomenclature is also followed from the convention of rough location in the sky, and the first discovered pulsar is known as PSR 1919+21, where right ascension and declination are 19^h19^m and 21 degree plus respectively. Neverthless,

this discovery helped to earn a Nobel Prize and it went to the observatory director, Antony Hewish.

First it was hypothesized that surface oscillation could be the reason for generating pulse profile in a high sequential or periodic manner. Periods of fundamental modes of oscillation of white dwarfs are in the range of 2-10 s, and those of neutron stars in the range of 1-10 ms (Meltzer & Thorne 1966). But it was quite difficult to explain the short periodicity of central object sitting in crab and vela nebula (periodicity 33 ms and 89 ms respectively) by incorporating white dwarf oscillation. So surface oscillation was rulled out and next rotating white dwarf was taken into consideration. The shortest period P or the highest angular velocity Ω at which a star of mass M and radius R can rotate is obtained by balancing centrifugal force and gravitational force on a test particle:

$$\Omega^2 R = GM/R^2. \tag{1.1}$$

In terms of the average density ρ of the star, breakup angular velocity can be obtained from the above equation as

$$\Omega = K(G\rho)^{1/2}, \tag{1.2}$$

where K is some proportionality constant, G is well known universal gravitational constant. So white-dwarf with density $\rho = 10^7 - 10^8$ g cm^{-3} corresponds to breakup rotation periods $P = 2\pi/\Omega \approx 1$ – 10 s.

Baade and Zwicky in 1932, had long ago suggested that some extreme or highly compact object might be found in supernova remnants and they coined the object as neutron star. Later Oppenheimer & Volkoff (1939) had calculated the average density of neutron star which is typically around $\rho \approx 10^{14}$ g cm^{-3}. So neutron star corresponds to break up rotation period of 1 ms. Thus rotation periods $P \geq 1$ ms, all are possible candidate for neutron star. Below figure 1.1 is

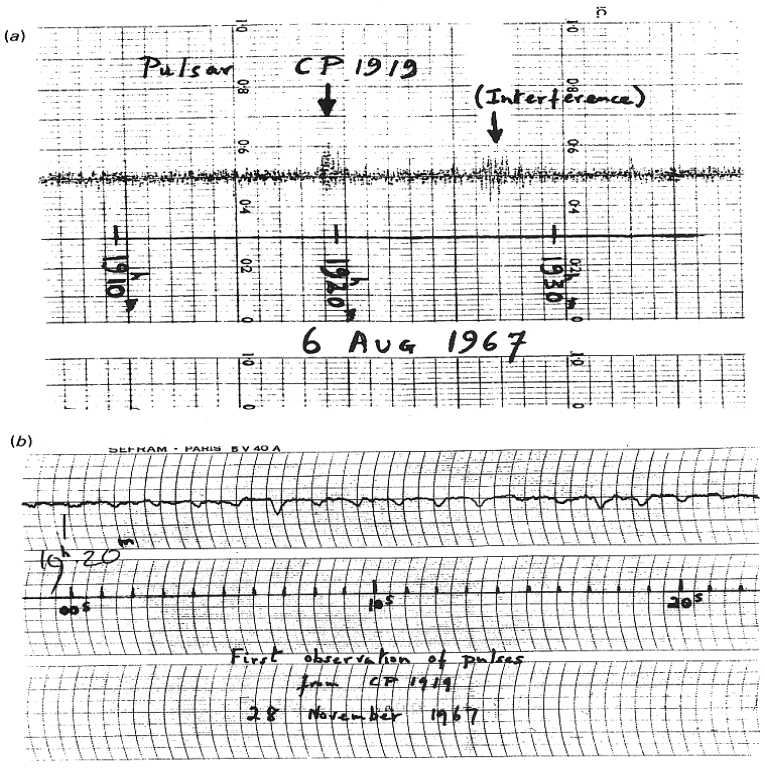

FIGURE 1.1: This figure shows the first radio signal detected from source CP 1919+21 in Cambridge, which was recorded by using fast chart recorder. Later this radio source was recognized as a pulsar. Picture credit Hewish et al. (1968).

adopted from Hewish et al. (1968), showing the first detected pulsar CP 1919+21 which shows scruffy nature of the signal, using fast chart recorder.

1.1 Galactic distribution of pulsars

In the advent of modern radio telescope facilities across the world, search strategy of new pulsars has become much more accessible to people. Therefore a lot of new radio pulsars have been discovered in the last two decades. So far there are more than 2500 radio pulsars, and most of them have been discovered by Parkes muti-beam telescope and Arecibo. In the below figure 1.2, pulsar's distribution is shown across the Galactic plane. Distribution of pulsars is done using Hammer-Aitoff i.e., equal projection area. More than 1000 pulsars have been discovered in the last 15

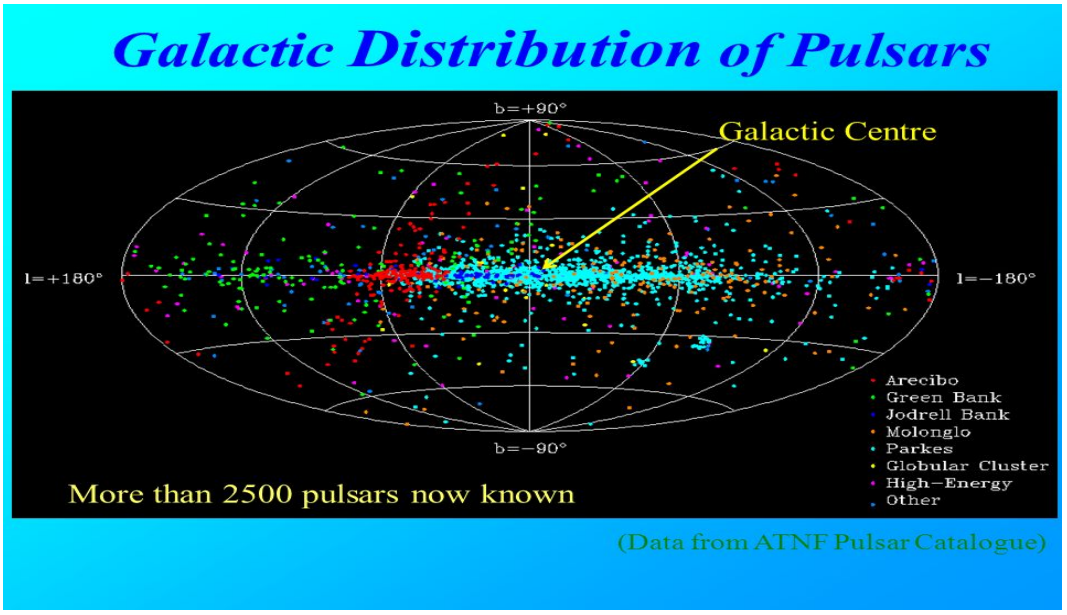

FIGURE 1.2: Galactic distribution of pulsars (available in ATNF catalogue.)

years, since Manchester et al. (2005) made a catalogue consisting of roughly 1500 pulsars. Figure 1.2 shows different category of pulsars like anomalous X-ray pulsars (AXP), soft γ-ray repeaters (SGR), isolated neutron star or radio pulsars. AXP and SGR are high energy emitting pulsars, whose emission mechanism is mainly described by synchrotron radiation and possibly by inverse-Compton radiation.

Different colours in figure 1.2 does identify the pulsars, which were discovered by different observatories such as Arecibo, Parkes telescope, Molongo, Jodrell bank and Green bank observatory etc. But most of the discovered pulsars around 80% emits in radio-band. Apart from some bright pulsars in large Magellanic clouds (LMC), small Magellanic clouds (SMC) and globular clusters (GC), most of the pulsars are emitting in radio band and most of them are seen to have been populated in the disk of our Galaxy (Crawford & Kazanas 2001). It is speculated that, only tiny fraction of total existing pulsars around 10^6 in our galaxy have been discovered so far due to several observational challenges. Pulsars distributions are very similar like massive O and B stars, which are densely populated in the galactic plane of our Galaxy. The standard picture of the birth of neutron star from core collapse supernova support this standard scenario. But birth rate

of neutron stars and frequency of supernova explosion is not fully matching according to observational data, which indicate that birth of neutron star associated with supernova explosion is not fully established (Kaspi & Helfand 2002). Gunn & Ostriker (1970) first tried to understand the birth connection of neutron star associated with core collapse supernova, from the height distribution of pulsars with respect to the galactic plane. But it is evident that pulsar takes birth from violent supernova explosion. Due to asymmetry in cavity inside massive progenitor stars, neutron star gets kicked away during supernova explosion with high space velocity and eventually it could escape from galactic potential (Lyne & Lorimer 1994).

1.2 The life cycle of pulsars

The P-$\dot{P}$ diagram is useful for tracking the life cycle of pulsars, playing similar role like Hertzsprung-Russell (H-R) diagram for ordinary stars. This diagram is useful to analyze the population of normal pulsars (stellar rotation period ~ 1 s), life span, spin-down luminosity due to magnetic-dipole radiation, magnetic field, population of millisecond pulsars (stellar rotation period of the order of a few ms) and so on. So one can extract tremendous amount of information from P-$\dot{P}$ diagram. Each pulsar has a characteristic age $\tau = P/(2\dot{P})$, minimum magnetic field strength $B = ((3c^3I)/(8\pi^2R^6))^{1/2}(P\dot{P})^{1/2}$, and spin-down luminosity $\dot{E}$ can be uniquely expressed in terms of the observable parameters P and $\dot{P}$ (see Ruderman & Sutherland (1975); Arons & Scharlemann (1979); Shapiro & Teukolsky (1983)). So it is quite easy to measure the observable fundamental parameters of pulsars such as magnetic field, characteristics age, spin down luminosity by identifying their location on the P-$\dot{P}$ diagram.

In figure 1.3 some series of parallel lines are shown, where each parallel line indicate constant value of magnetic field and characteristics age. Young pulsars

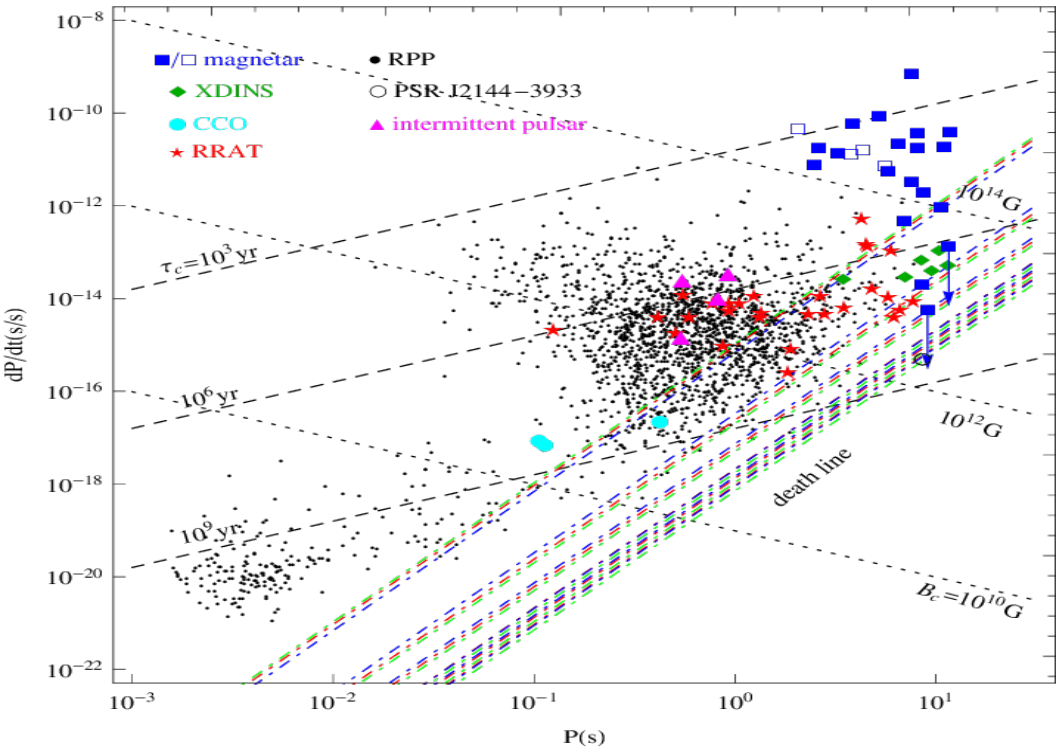

FIGURE 1.3: The evolution trajectory of pulsars in $P-\dot{P}$ plane. Picture credit: Zhou et al. (2017).

do reside in the upper middle of the diagram are often associated with supernovae remnants (SNRs) and emit high-energy radiation. They slow down as they evolve over millions of years until their rate of rotation is too slow to initiate pair-multiplicity process, so as to produce minimum detectable amount of flux in radio band. After elapsing million years, normal radio pulsars cross the death line and disappear from the view. The millisecond pulsars in the lower left are mostly in binary systems and were "recycled" via accretion from their companion stars. Millisecond pulsars have comparatively lesser magnetic field 10^8 G and they are confined in the left bottom side of P-$\dot{P}$ diagram (see figure 1.3).

The plot of spin period P vs magnetic field B in log scale is shown in figure 1.4, which is regarded as a very important diagram to demonstrate the evolution of spin as well as magnetic field of pulsars. B-P diagram includes both rotation powered and accretion powered pulsars and it is having the same potentiality as

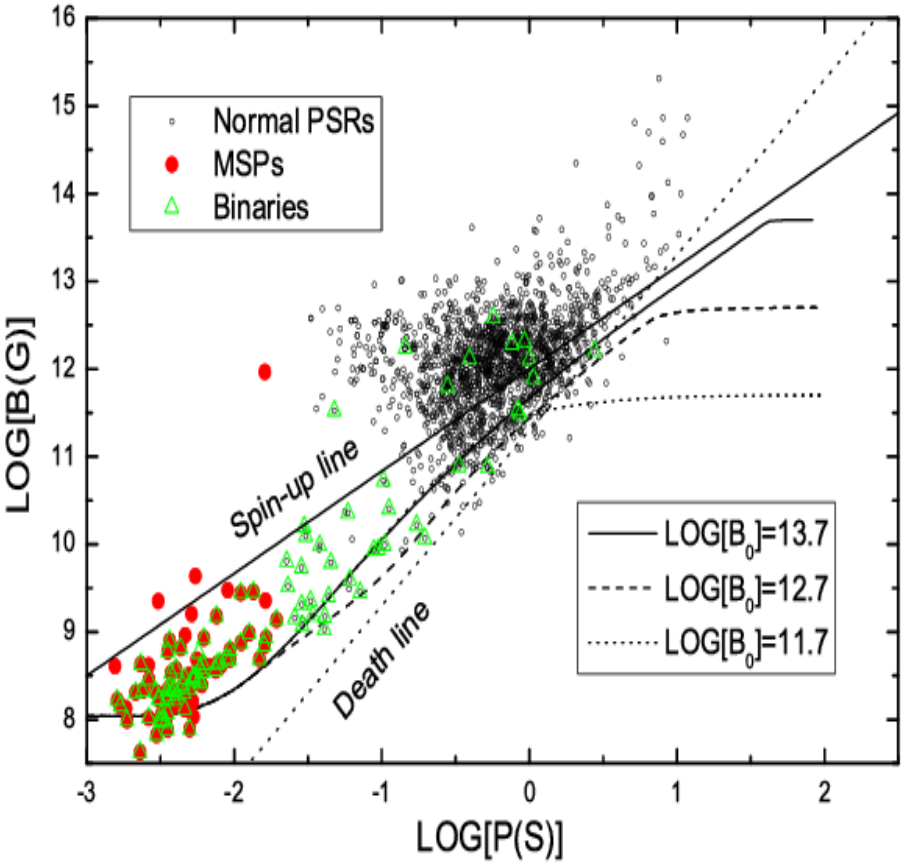

FIGURE 1.4: Magnetic field vs spin period in log scale for different initial value of magnetic field. Picture credit: Credit: Xu & Wang (2010).

H-R diagram, to explain the spin and magnetic field evolution of neutron star at various stages of their life. For rotation powered pulsars, magnetic field B is usually estimated from the observed period P and period derivative $\dot{P}$. For accretion powered pulsars, one used to measure magnetic field from cyclotron features. So only those pulsars, whose magnetic field have been observed from cyclotron features, can be put in the period-magnetic field diagram. The period and magnetic field of majority of the rotation powered pulsars fall in the range 50 ms $\leq$ P $\leq$ 1 s and 10^{11} G$\leq$ B$\leq$ 10^{13} G respectively, which undergo spin-down and slowly approaches towards the death line. Once a pulsar cross

the death line, it can be revived only through recycling process. Via Recycling process pulsars get resurrection and get convert themselves from normal pulsars to millisecond pulsars. Recycles happens, if there is an adjacent binary companion. So recycling process essentially make changes of the associated magnetic field and spins up pulsars significantly. For high mass X-ray binary (HMXBs) interaction, the typical time scale for recycling is 10^4 – 10^5 years, and it shortens the period of pulsars to 10 – 100 ms and reduces the magnetic field to $\sim 10^{10}$ – 10^{11} G. In LMXBs (Low mass X–ray binary), where recycling operates over longer time scale 10^8 – 10^9 years, shortens the spin period to 1 – 10 ms and reduces the magnetic field to 10^8 G approximately. So recycles essentially makes pulsars to migrating on a diagonal track, downward on the B-P diagram and finally ending up in the left bottom side of the recycle pulsars. But the pulsars recycled through HMXB ending up in a position, relatively upper and right parts in the bottom region of B-P diagram, compare to that by LMXB. Now if the binary-companion gets eliminated, accretion process stops and it's start dominating in radio region.

1.3 Polarization property of radio pulsars

Pulsars are one of the highest polarized objects in the radio counterpart of sky and exhibiting diverse polarization properties. Polarization property of radio pulsars can be categorized mainly into two part: (i) Individual pulse profiles (ii) Integrated or average pulse profiles. A basic fact about rotation powered pulsar is that, individual pulses from a given pulsars show rapid variation over tiny time scale. The degree of polarization of individual pulses reach to a very high value and sometimes it becomes 100%. Integrated or average pulse profile is usually constructed by summing and averaging thousand of individual pulses, which is very stable in nature and can be regarded as the unique signature of a pulsar.

1.3.1 Individual pulse profile

If one carefully analyze individual pulses, they reveal different pulse structure related properties on a range of timescale such as pulse nulling, drifting, mode changing, micro-structure, giant pulse etc. One can extract wealth of information about the location of emitting source in pulsar magnetosphere and involved emission process by analyzing high resolution data. For analyzing micro-structure one needs high time resolution data. Pulse profile structure with a resolution of the order of few microsecond is called micro-structure, for example see Bartel & Sieber (1978) and Craft et al. (1968). So far our understanding about micro-structure is not satisfactory due to lack of high resolution data. Some observation shows that micro-structure is broad-band in nature and some do show quasi-periodicity (Rickett 1975; Cordes 1976; Boriakoff et al. 1981). More recently there has been discussion of this kind of issue in the FRB context by Cordes & Wasserman (2016).

On the other hand giant pulse is a rapid phenomenon which releases very highly energetic emission in terms of fast radio burst. It is evident that, micro-structure and nano-structure are the most fundamental entities associated with the spatial scale of pulsar radio emission and to generate such small scale structure, they are attributed to the background stochastic process (Eilek & Hankins 2016). Crab pulsar was first recognized through its giant pulse emission and from long time it was regarded to be the only known pulsar to emit giant pulses (Staelin & Reifenstein 1968). Giant pulses reveal structure in nano-second time scale and it corresponds to huge emission with intensity up to 1000 times approximately that of an individual pulse (Cordes et al. 2004). With the enhancement of sensitivity of more radio telescopes, more number of giant pulses were detected in the past two decades and it indeed helped astronomers to understand wide range of physics, relevant to the emission mechanism of pulsars. Giant micro-pulses were seen in comparatively young aged, Vela pulsar (Cairns et al. 2001), and it was speculated that there might exist some correlation between giant pulses and the high energy

emission among pulsars.

It is observed that, some pulsars switch off emission suddenly for several pulse periods. This phenomenon is called nulling, which was first observed by Backer (1970). The probable reason for nulling could be an insufficient supply of plasma, which may be a sign of the ending of pulsar's active life (Ritchings 1976; Biggs 1992). Below figure 1.5 depicts absence of emission or nulling from PSR B1133+16 in addition to sub-pulse drifting. However the duration of the nulls has been seen to vary from pulsars to pulsars, with possible null fractions ranging between zero to unity. Some observers suggest that pulsars are visible in terms of short time-scale faint emission in between nulls. There are some exception for nulling also, for example J0437-4715, don't show any observational proof for nulling (Vivekanand et al. 1998).

Next I will discuss another interesting phenomenon of pulsar called "drifting sub-pulses". It is seen that well ordered temporal modulated structure of sub-pulses pattern to drift across the pulse window at a fixed rate for a particular pulsars. In most of the literature, drifting sub-pulses is commonly described by two parameters: first one is P_a, which characterize the spacing between subsequent sub-pulses and second one is $P = P_b$, which is the period of repetition of a specific pattern associated with a train of sub-pulses across pulse window. These two quantities are usually measured in terms of the spin period of pulsars. A theoretical explanation of sub-pulse drifting phenomenon was first given by Ruderman & Sutherland (1975), which is due to rotation of carousel like sub-beams structure within a hollow emission cone.

In addition to sub-pulse drifting and nulling pulsar sometimes shows a mode-changing. Mode-change is usually recognized as a transition between two different modes, in which emission characteristics are somewhat different. There are two

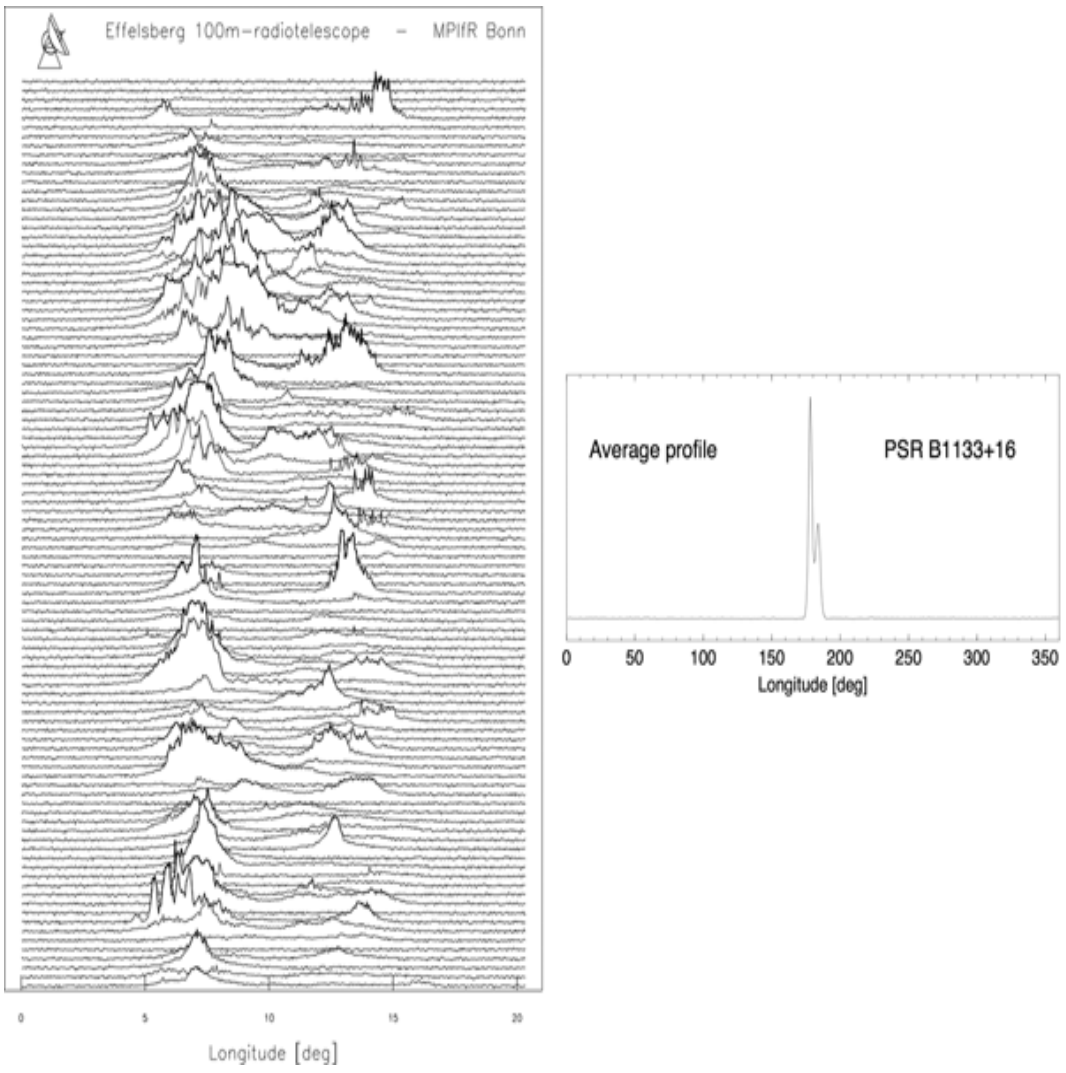

FIGURE 1.5: Left panel shows individual pulses from PSRB 1133+16 and right panel shows corresponding average pulse profile. Picture credit:Seiradakis & Wielebinski (2004).

types of modes identified in pulsar astronomy, which are normal mode and abnormal mode. Most of the times pulsars emit in normal mode and abruptly switches to abnormal mode. By analysing individual pulses from pulsars, one can identify such different modes.

Some special case is orthogonal polarization mode, where the polarization angle curve exhibits 90^o jumps with respect to normal mode. For example one can see Manchester et al. (1978), Weisberg et al. (1981) etc. But still there are some ambiguities regarding mode-changing, like what background process is responsible

to trigger such phenomenon and how do they change mode from one to another in different epochs.

1.3.2 Property of integrated pulse profiles

Integrated pulse profile is produced by averaging thousand of individual pulses, which is unique property of any given pulsar. After aligning the signals associated with lower and higher frequency part of individual pulses, they are coherently added together and this process is called folding. As pulsar radio emission mechanism is broad-band in nature, so lower frequency part travel with lower speed and higher frequency part travel with higher speed in the ISM. As a result, there is a phase difference between lower part and higher part of the frequency bandwidth, when the signal reaches the receiver. Apart from that there is Faraday rotation effect, which influences the pulsar signal due to interstellar magnetic field. So in all standard observation, one usually divide the signal into higher and lower frequency channels first. Then all the correction due to Faraday rotation, scintillation due to earth atmospheric propagation is done before doing dedispersion and folding the signals. After doing all the procedure one can produce average pulse profiles. The basic aim to produce an integrated pulse profile is to generate stable Stokes parameters (Intensity, linear & circular polarization and polarization angle), which is shown in figure 1.7.

Average pulse profiles exhibit a great diversity in shapes between one pulsar to another (see figure 1.7). This can be attributed partly due to the line of sight cutting geometry across the radiation beam, and partly due to inhomogeneities within an individual emission beam of pulsar. Rankin (1983) first introduced nested hollow cone structure model in order to explain different pulse profile morphology. Rankin model assumed that emission beam of pulsar is not a solid cone

but rather it's a concentric set of hollow cones and a core component at the center. Another model which was proposed by Manchester et al. (1978) assumed that emission beam is patchy or random and the emission sources are arbitrarily distributed across the area of emission beam and depending upon the number of components presents along line of sight it will appear in the pulse profile structure. But most of the observation support Rankin (1983) model to be the successful candidate. However profile classification scheme of Rankin based on the number of emission components, is regarded as a useful beginning point to study the emission characteristics of pulsars. One can see the details classification scheme as introduced by Rankin (1983), such as triple (T), five–component (M), conal triple (cT), conal quadruple (cQ), core single (S t), conal double (D), conal single (S d) etc. They have reached to the conclusion that there are two separate kinds of emission components in pulsar profiles: central core emission and surrounding hollow conal emission, which results from two distinct type of emission mechanisms. Manchester et al. (1978) also confirmed the difference in properties between core and conal emissions, but finally they inferred that the observations are best explained by a progressive change in emission characteristics from the core zone to the outer edge of the emission beam rather than two distinct emission process.

Apart from the study of main pulse property, two more interesting things are inter-pulse emission and profile evolution with frequency. There are secondary pulses or inter pulses, which are separated by 180^o with respect to main pulse. Simplest explanation for this kind of phenomenon is that the main pulse and inter-pulse are generated from two opposite magnetic poles of neutron star. Both pulses and inter-pulse can be visualized if spin axis and magnetic axis are aligned orthogonally. For example figure 1.6 shows three inter-pulse emission from pulsars J0737-3039A, B1702-19, B1937+21. Another last property I discuss here is the profile evolution of main pulse associated with frequency. Pulsars shows well pronounced evolution in pulse shape as a function of observing frequency. For example figure 1.8 shows profile evolution with respect to frequency, and it reveals

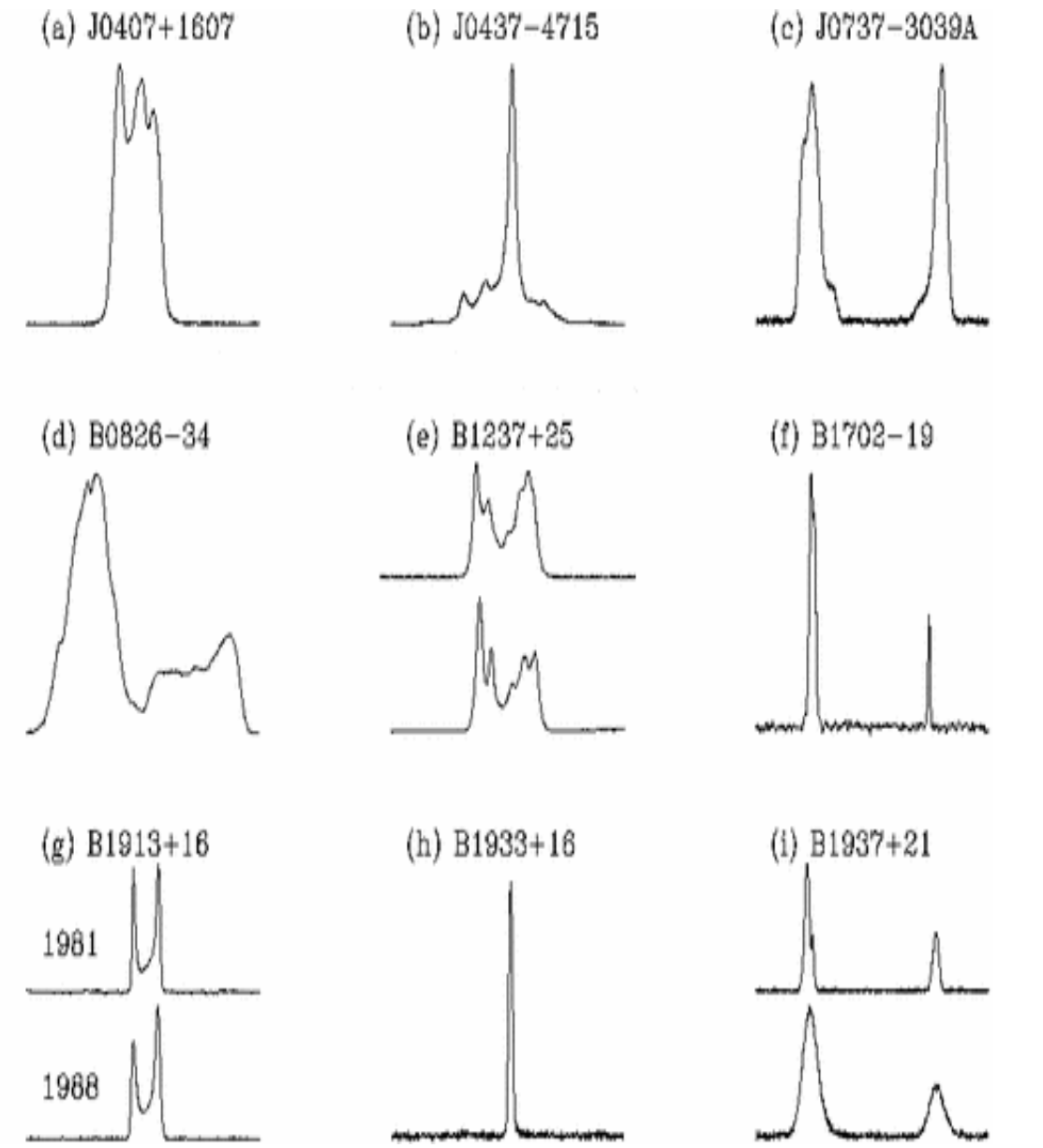

FIGURE 1.6: Picture is showing various shapes associated with intensity of average pulse profiles. Picture courtesy: http://www.jb.man.ac.uk/ pulsar/

that higher frequency profiles are noisy and shrinking in component separation. Most normal period pulsar shows a gradual decreasing of pulse width and separation of profile components when observed at higher frequency. But this effect is less pronounced in milli-second pulsars and they show a very little evolution of pulse width and component separation with frequency (Kramer et al. 1999).

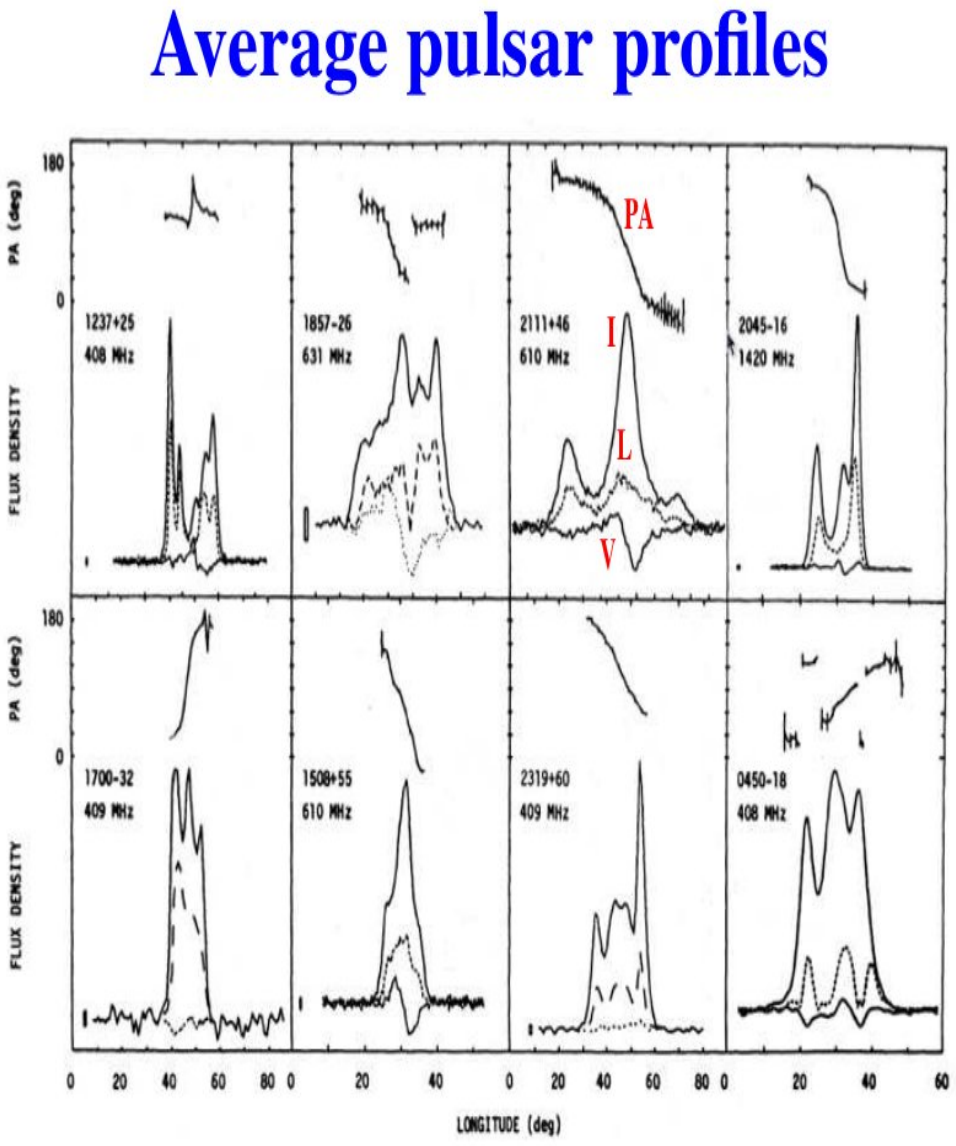

FIGURE 1.7: Picture is showing various shapes associated with intensity of average pulse profiles. Picture courtesy: http://www.jb.man.ac.uk/ pulsar/

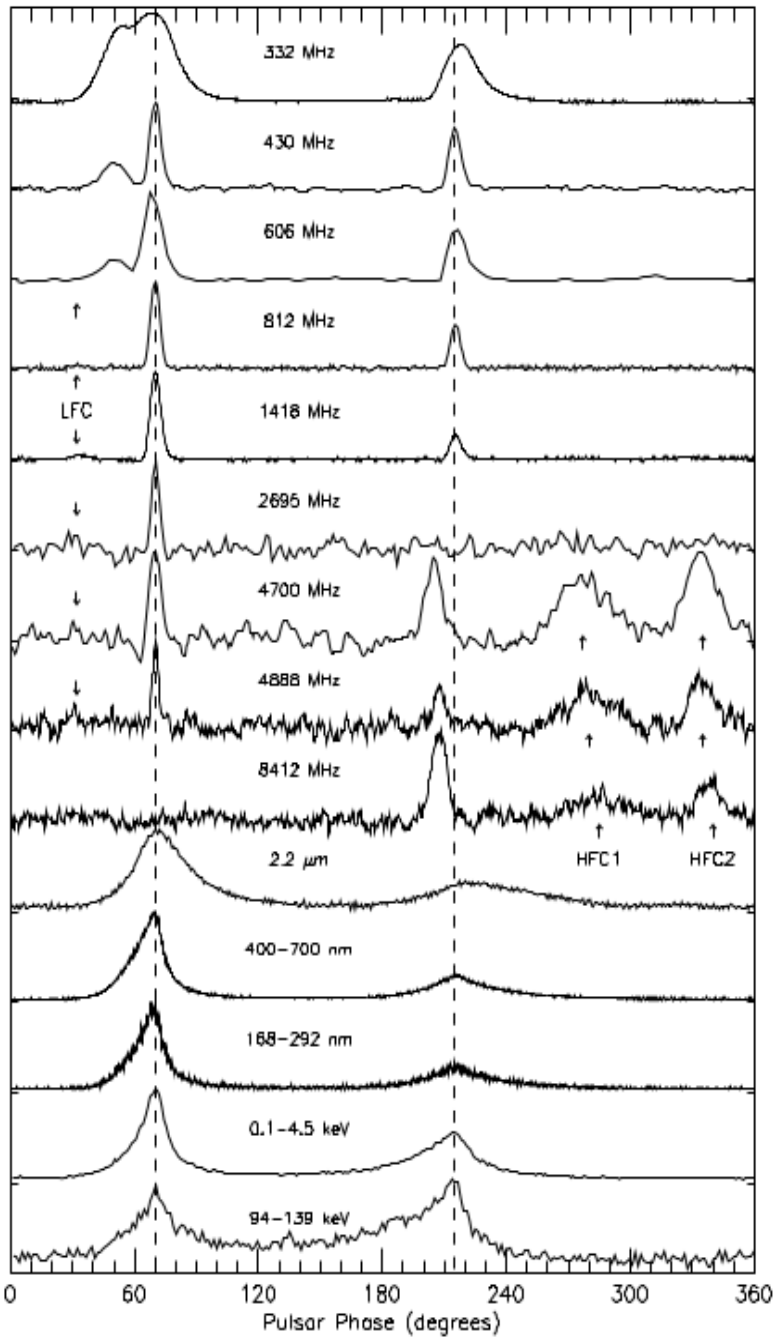

FIGURE 1.8: The integrated profiles of the Crab pulsar and their evolution from low frequency radio waves to soft gamma-rays. Picture Courtesy: Hankins & Eilek (2007).

1.3.3 The rotating vector model

In 1969, Radhakrishnan and Cooke suggested a pioneering geometrical model related to radio emission beam geometry of pulsar, which proved to be a very important model to interpret observed position angle (PA) swing curve. One can fit the observed data with Radhakrishnan & Cooke (1969) model to extract information about the magnetic axis inclination angle as well as line of sight impact angle with respect to the spin axis. Normally we make the following assumptions to derive the polarization angle expression in terms of pulse longitude. (i) Magnetic field of pulsar is dipolar in nature and it is undisturbed by any perturbation. (ii) Curvature radiation emitted by charged particles acceleration is along open magnetic field lines and it is polarized along the curvature vector of magnetic field lines. The position angle ψ of polarization is measured with respect to the projected direction of the rotation axis of pulsar on the plane of sky. ψ will vary with pulse longitude ϕ' according to the following relation (Komesaroff 1970):

$$\tan\psi = \frac{\sin\alpha\sin\phi'}{\sin\zeta\cos\alpha - \cos\zeta\sin\alpha\cos\phi'}. \tag{1.3}$$

Here α is the angle between rotation axis and magnetic axis, ζ the angle between spin axis and line of sight and ϕ' the pulse longitude. If we do differentiation of the above equation (1.3), then it can be found that slope of the PA curve attains a maximum at meridian plane i.e., $\phi' = 0$. Meridian plane is the plane, at which rotation axis, magnetic axis and line of sight lie at $\phi' = 0^o$. So maximum slope of position angle is given by the following expression:

$$\left(\frac{d\psi}{d\phi}\right)_{max} = \frac{\sin\alpha}{\sin(\zeta-\alpha)}. \tag{1.4}$$

The polarization angle as shown equation (1.3) exhibit "S" shaped swing with respect to pulse longitude unless there is no perturbation. Kumar & Gangadhara (2012b) have shown that if there is any longitudinal current across polar cap, the

polarization angle will not swing very smoothly, rather there will be some kinky nature due to distortion of magnetic field line from exact dipole.

1.4 Spectra of pulsars

The flux density of a radio source and its frequency evolution (spectrum) is the basic information that relates to the emission mechanism. However, one of the problems with flux densities is that pulsar radio emission vary on various time scales: (a) due to inherent variations, (b) due to scintillation, (c) due to scattering etc. For low frequency radio waves of the Milky Way the spectrum of the radio emission could be explained only by the non-thermal (synchrotron) emission process.

From the very beginning of pulsar observations it was clear that the spectra of pulsars were very different from all other known radio sources. Instead of values of $\epsilon \approx 0.8$ (flux $S \propto f^{\epsilon}$), as in cosmic radio sources, the observed spectral index of pulsars was $\epsilon \approx 1.5$ on average (Maron et al. 2000). Here f is the observed frequency and ϵ is the power spectra index. For some objects the spectral index at the higher frequencies was much higher than this average value. At lower radio frequencies a spectral turn-over was observed at some cases. It was known in the earliest papers that pulsars were very weak at higher frequencies posing in fact a great instrumental challenge to study these objects at cm wavelengths. The measurement of average spectrum was slowly extended to 2.7 GHz and suggested a spectral break with an index of $\epsilon \approx 3.0$ above 1.4 GHz. The data collection for determining flux densities of a larger sample of pulsars took many years to complete the work. While numerous observatories (Arecibo, Jodrell Bank, Green Bank, Parkes) made observations at frequency 1.4 GHz and below only the Goldstone facility detected pulsars at 13 cm. Observations of the low frequency extension

of pulsar spectra were carried out in the Soviet Union at frequency as low as 10 MHz and three pulsars were detected at high frequency relatively 8.1 GHz (Malofeev et al. 1994). The suggested existence of a spectral break at high radio frequencies was later confirmed and a major step forward in the measurement of pulsar flux densities at high radio frequencies was measured by 100-m Effelsberg radio telescope. Immediately, six pulsars were detected at 2.8 cm wavelength. This telescope continued to set records of the highest frequencies at which pulsars could be studied by reporting detection at 22.7 GHz and finally in the mm-wavelengths. A detection of the pulsar PSR B0355+54 at 3 mm wavelength has also been achieved with the Pico Veleta telescope. The early measurements of flux density of the strongest pulsars had to give way to studies of larger samples, if possible with a wide frequency flux density coverage. An early compendium of pulsar spectra was given for 27 pulsars (Malofeev et al. 1994; Maron et al. 2000). Further multi-frequency spectra have been presented.

Low radio frequency observations confirmed the cut-off in pulsar spectra for a number of objects. Subsequently, the flux density of a larger sample of pulsars was measured at several frequencies and spectra of pulsars were derived. From some of the published literature such as Maron et al. (2000) concluded that the average spectral index of radio pulsar is $\epsilon = 1.8$ and most of the pulsars do follow simple power law. Some 10% pulsars from populations requires broken power law to fit the entire spectrum both in the high frequency and low frequency regime. A small number of pulsars have been recognized with almost flat spectrum ($\epsilon \geq 1.0$). In addition pulsar spectra seem to follow the power law down to low frequencies (a few of 10 MHz) with a few exceptions, where a turn-down is observed. Early studies of millisecond pulsars suggested that these objects have spectra steeper than slow pulsars. Recently high frequency observations of millisecond pulsars were also made in spite of their low flux densities (Seiradakis & Wielebinski 2004). The spectra of 20 objects were studied at lower radio frequencies in a survey of 280 pulsars in the northern hemisphere. Several southern millisecond pulsars were also

studied in a narrow frequency range. A major study of millisecond pulsars showed that once a volume-limited sample or sampling done randomly at radio window for a fixed field of view is considered, many of the characteristics of slow and fast pulsars (spectrum, pulse shapes, number of sub-pulse components, polarization) remain the same but definitely there is a finite difference in the luminosity. An investigation of the low frequency turn-over of millisecond pulsars revealed that the morphology of millisecond pulsars is very similar to that of normal pulsars but with lower luminosity (Seiradakis & Wielebinski 2004).

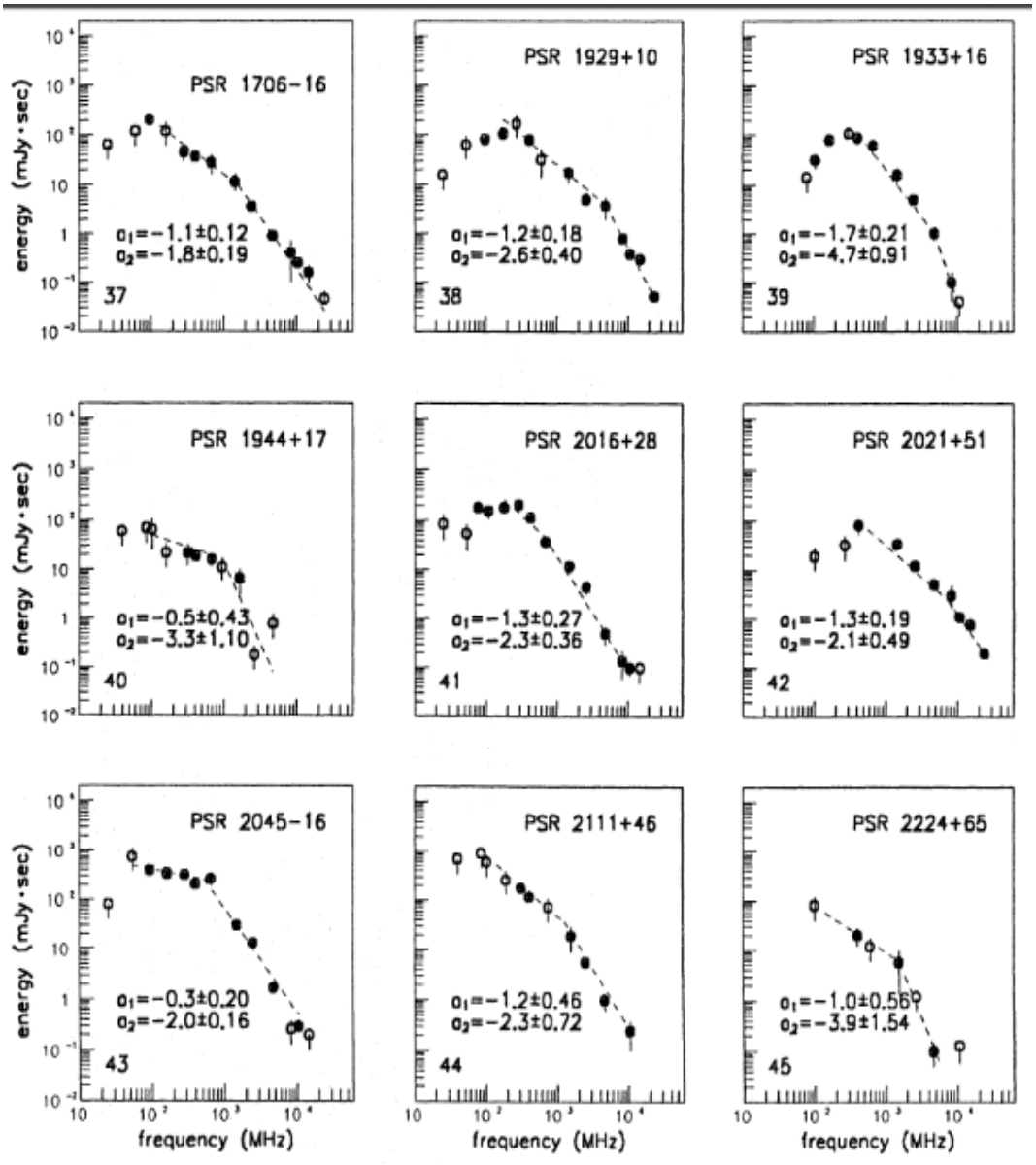

FIGURE 1.9: Power spectra of a few pulsars, mostly showing broken power laws. Picture coutesy: Malofeev et al. (1994).

1.5 Brightness temperature of pulsar

When pulsar luminosity or flux is interpreted it corresponds to huge brightness temperature around 10^{25} K, in the radio band. It is believed that pulsars radio emission mechanism is a coherent process and it's brightness temperature is the highest among all radio sources. Evaluation of pulsar radio luminosity L is quite a difficult task for numerous reasons such as (i) pulsar radio emission do not come from the uniformly illuminating sphere, (ii) geometrical shape of pulsar radio emitting region is unknown and (iii) flux density spectrum is different for different pulsars and also, reliable estimation of flux get's effected by scintillation. Here I have tried to show the derivation, leading to the expression of brightness temperature in a few steps. If $S(f)$ represents the expression of flux density as a function of frequency f, then the luminosity L of a pulsar located within distance d from earth is given by the following equation:

$$L = \Omega d^2 \int S(f)_{max} df. \tag{1.5}$$

Here Ω represent the solid angle as illuminated by pulsar beam or it is called a beaming fraction. $S(f)_{max}$ represent the maximum value of flux. If ρ_{rb} represent the angular radius of the emitting cone then beaming fraction Ω can be calculated as follows:

$$\Omega = \int_0^{\rho_{rb}} 2\pi \sin\rho' d\rho' = 4\pi \sin^2(\rho_{rb}/2). \tag{1.6}$$

Now we define mean flux density S_{mean} as the integrated flux, by averaging over full stellar rotation of pulsar. So mean flux can be written roughly as $S_{mean} = (W_{eq} S_{peak})/P$. Here W_{eq} represent the equivalent pulse width and P the pulse period. We assume that mean flux density follows the following power law with index ϵ as follows:

$$S_{mean}(f) = S_{mean}(f_0)(f/f_0)^{\epsilon}, \tag{1.7}$$

where $S_{mean}(f_0)$ is the mean flux density measured at frequency f_0. Now by inserting all these factors into equation (1.5), we get

$$L = \frac{2\pi d^2(1-\cos\rho_{rb})}{\delta} S_{mean}(f_0)\frac{f_0^{-\epsilon}}{1+\epsilon}(f_2^{1+\epsilon} - f_1^{1+\epsilon}), \tag{1.8}$$

where, $\delta = W_{eq}/P$ is the pulse duty cycle, and f_1, f_2 are the frequencies corresponding to the flux maximum and the maximum extent of frequency up to which flux density of pulsar is detectable. Now the observed flux density S_f observed at a given frequency for a pulsar at distance d and angular width of the radio beam ρ_{rb} is connected to the thermodynamic brightness temperature T_b by Rayleigh-Jeans formula as follows:

$$S_f = \frac{2\pi\rho_{rb}^2 f^2}{d^2} k_B T_b, \tag{1.9}$$

Here k_B is the well known Boltzman constant. If one receives a pulse of peak flux density S_{peak} with duration Δt from such a source, then corresponding brightness temperature can be computed as follows:

$$T_b = \frac{S_{peak}}{2\pi k_B}\Big(\frac{f\Delta t}{d}\Big)^2. \tag{1.10}$$

In chapter 3, I have made a model of pulsar radio emission due to relativistic plasma, where I have calculated brightness temperature both from theoretical model as well as from observation. In chapter 3, I have shown that there is reasonably good agreement of calculated brightness temperature between theory and observation.

1.6 Fundamental idea of pulsar magnetosphere

Goldreich & Julian (1969) started off with the vacuum assumption to demonstrate that it was inconsistent with the resulting strong forces on charges in the crust; so the surroundings of the neutron star could not be a vacuum. As Lorentz forces on

the charged particles in the interior of neutron star is huge compared to the gravitational force, the neutron star can be approximated as a highly magnetized and conducting sphere. Goldreich & Julian (1969) first computed the induced external electric field 10^{12} V cm^{-1} and have shown that such an enormously high electric field can surpass the high gravitational pull of compact object and eventually lead to the extraction of charged particles from the surface. However this work is a follow-up work of Deutsch (1955), who obtained the solution of magnetic field and electric field in polar co-ordinate due to the rotation of neutron star in vacuum. However Godreich-Julian first established neutron star in a frame filled up with plasma-filled magnetosphere. Below I have tried to show some steps, leading to the expression of potential drop across polar cap. If one assume neutron star to be a conducting sphere, the charge distribution due to the induced electric field will be balanced and it will create a charge separated magnetosphere. So for force-free configuration we can write

$$\vec{E} + \frac{(\vec{\Omega} \times \vec{r}) \times \vec{B}}{c} = 0, \tag{1.11}$$

where $\vec{B}$ is the magnetic field, $\vec{E}$ the induced electric-field, c the speed of light and $\vec{\Omega}$ the spin frequency of neutron star. The solution of external quadrupole field due to uniformly spinning magnetized sphere, surrounded by vacuum was given by Deutsch (1955) in polar co-ordinates (r,θ):

$$\phi(r, \theta) = \frac{B_s \Omega R^5}{6cr^3}(3\cos^2\theta - 1), \tag{1.12}$$

where B_s is the surface magnetic field, R the radius of canonical neutron star, and θ the polar co-ordinate measured along the magnetic field lines. So the component of electric field, parallel to magnetic field at stellar surface is given by

$$E_{in\parallel} = \frac{\vec{E} \cdot \vec{B}}{B}|_{r=R} = -\frac{\Omega B_s R}{c}\cos^3\theta. \tag{1.13}$$

The parallel electric field can easily exceed gravity by 10 order of magnitude and particles from neutron star surface can be easily extracted unless they are heavily bound. So the charge density can be computed from the Poisson equation as follows:

$$\rho_e(r,\theta) = \frac{\nabla \vec{E}}{4\pi} = -\frac{\vec{\Omega}.\vec{B}}{2\pi c} = -\frac{B_s \Omega R^3}{4\pi c r^3}(3\cos^2\theta - 1). \tag{1.14}$$

By equating equation (1.14) to zero, one can easily infer that the distribution of charged particles change sign at $\cos\theta = \sqrt{1/3}$. So once the charge distribution is arranged outside the star, the electric field $E_{\parallel}$ gets canceled, and thereafter force-free condition is maintained. Then, the equilibrium number density of charged particles at $r \ll r_{\rm LC}$ becomes

$$n_{GJ} = (\rho_e/e) = \frac{\vec{\Omega}.\vec{B}_s}{2\pi c e} \approx 10^{10}\ {\rm cm}^{-3}\ (P/{\rm s})^{-1/2}(\dot{P}/10^{-15})^{1/2}. \tag{1.15}$$

A typical neutron star surface magnetic field can be expressed roughly in terms of observable parameters as $B_s \approx 10^{12}(P/s)^{1/2}(\dot{P}/10^{-15})^{1/2}$. Anyway the number density as quoted in equation (1.15) is referred to as the Goldreich-Julian charge density.

Now because of $\vec{E}\times\vec{B}$ force, charged particles in the region outside magnetosphere will co-rotate. But this co-rotation can be maintained up to a certain distance from the center of neutron star, beyond which co-rotation speed will exceed the speed of light c. So the distance upto which co-rotation is maintained makes a imaginary surface and in literature it is called as light cylinder surface with radius $R_{Lc} = P\,c/(2\pi) \approx 10^4{\rm km}(P/{\rm s})$. Now we will compute the voltage drop across polar cap region for typical pulsar. Polar cap basically is a region on neutron star surface centered around magnetic pole, whose boundary is defined by the locus of last open magnetic field lines. For a given dipolar magnetic field line $\sin^2(\theta)/r$ is a constant quantity. For the last open field line we can write:

$$\sin^2\theta/r = 1/R_{LC} = \sin^2\theta_p/R, \tag{1.16}$$

where θ_p corresponds to the polar co-ordinate for last open field line. So the radius of polar cap can be written roughly as

$$R_p \approx R \sin\theta_p = \sqrt{(2\pi R^3)/(Pc)} \approx 145(P)^{-1/2} m, \tag{1.17}$$

for neutron star with radius $R = 10$ km. So by using equations (1.12) and (1.16) one can obtain the voltage drop across polar cap:

$$\Delta\phi = (B_s \Omega^2 R^3)/(2c^2) \approx 10^{13}(P/s)^{-3/2}(\dot{P}/10^{-15})^{1/2} \text{V cm}^{-1}. \tag{1.18}$$

It is believed that the higher order magnetic pole i.e. does exist apart from di-polar configuration near to neutron star surface and it is regarded as the root cause for supplying enough plasmas and thereafter produce observed radio emission (Jones 1980; Gil & Mitra 2001).

There have been mentioned two major gaps in the literature of pulsar astronomy (Cheng et al. 1976), such as polar gap and outer gap. Gap is a zone in the magnetosphere, which is depleted of plasma. In the gaps, Goldreich Julian concept of co-rotating magnetosphere breaks down and therefore a residual electric field $E_\parallel$ must exist. Pulsar radio emission is generally expected to take place over an altitude range of about $0.05 r_{\rm LC}$ – $0.2 r_{\rm LC}$ above the polar gap region. Due to huge residual electric field with a voltage drop 10^{13} V across polar cap (see equation (1.18)), charged particles are pulled out from Neutron star (NS) surface and gets accelerated along curved magnetic field lines relativistically with Lorentz factor $\gamma \approx 10^6$ (Sturrock 1971; Ruderman & Sutherland 1975). These charged particles emit gamma–ray photons via curvature radiation (Ruderman & Sutherland 1975; Arons 1983).

In the presence of a strong magnetic field, the γ-ray photons can decay into secondary electron-positron pair creation. This pair creation is possible only when photon energy exceeds twice the rest mass energy of electron $E_\gamma \geq 2m_e c^2$ (Erber

(1966)). Secondary electron-positron pair can further produce gamma-ray photons and hence the pair particles creation by cascade process continues. Therefore the number density of electron-positron pairs keep on multiplying and enhancing the initial plasma density by a several factor. But the pair creation process cannot continue for indefinite time scale, this process inhibits when the residual electric field in the polar gap becomes equal to the electric field summed over all secondary or tertiary particles. When such balance is established, the gap gets shielded and the column of secondary-pair particles leaves the gap and we get radio emission. Lack of pair-cascade process will prevent pulsars from emitting strong radio pulse. From equation (1.18) it is evident that, millisecond pulsars have strong accelerating potential than normal period pulsars.

As a pulsar ages, it slows down. So there exist some critical value of spin period for typical pulsar, beyond which accelerating potential is not sufficient to initiate cascade process and thereafter stops radio emission. Pair cascade process can be interrupted, if the magnetic field strength exceeds the critical magnetic field (Daugherty & Harding 1983) $B_{crit} = (2\pi m_e^2 c^3)/(eh) = 10^{13}$ G. In case of very strong magnetic field, curvature photon will decay into positronium, which is a bound electron-positron state or alternatively it cannot decay into two other gamma photons. Such logic was implemented to explain the absence of radio emission from magnetar (Melrose 1996; Baring & Harding 1998). However, we know some magnetars do show radio emission, e.g., Kramer et al. (2007) have presented the polarization observations of the radio emitting magnetar AXPJ1810−197. Further, Torne et al. (2017) have reported the magnetar SGR J1745−2900 with detections up to 291 GHz (1.03 mm), together with evidence of linear polarization in its millimetre emission.

Other gaps like outer-gaps also predicted by Holloway (1973), which is responsible for X-ray emission. This gap is located near light cylinder and in between open and closed magnetic field lines. X-ray emission is either taking place from

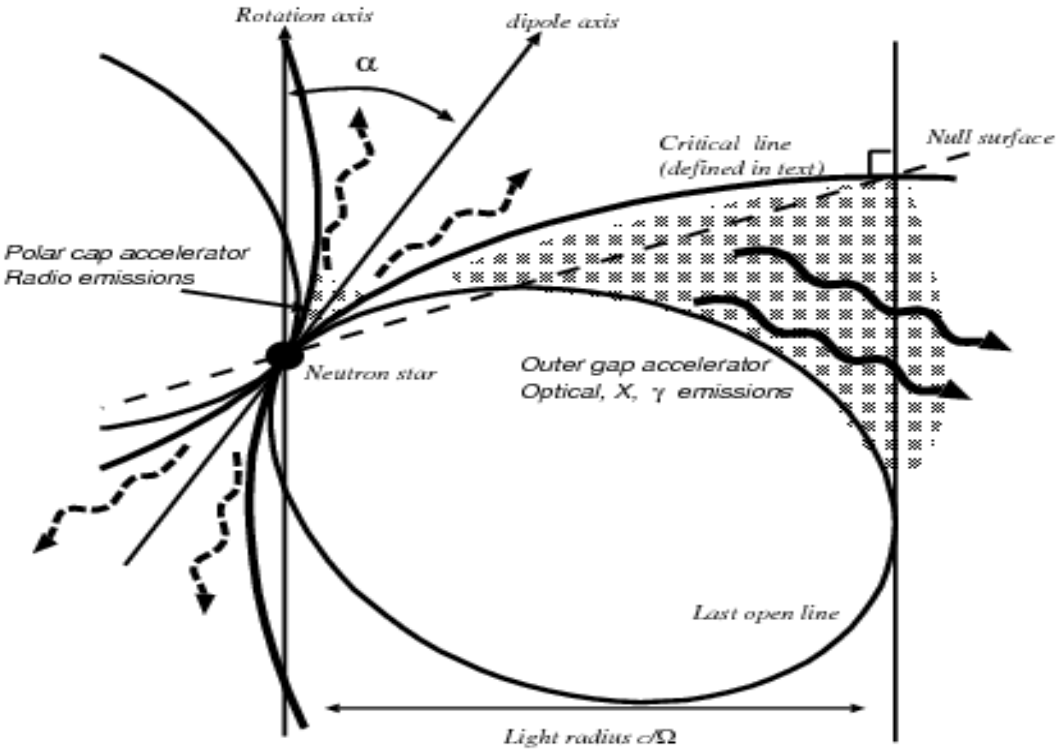

FIGURE 1.10: The particle acceleration in different gaps: cascade process, radio, X-ray emission. Usually Radio emission is expected to take place from polar cap region and X-ray emission from outer gap.

outer-gap region either by synchrotron emission mechanism or by inverse Compton scattering. For more details reader can see the details of outer gap model, which was developed by Cheng et al. (1986) and Romani (1996a).

1.7 Radio emission mechanism of pulsars

There has been proposed three types of mechanism to explain the pulsar radio emission mechanism: (i) Antenna Mechanism (ii) Relativistic plasma emission and (iii) Maser emission. The antenna mechanism is similar to emission by bunches, where particles inside bunch is assumed to be correlated in space. Antenna mechanism was proposed by Benford & Buschauer (1977), where N number of particles with charge q are confined in a volume of dimension smaller than half of the emitted

wavelength. Here Plasma is behaving like a phased array in an extended antenna, correlated in space. So all the particles will be radiating in phase and naturally the radiated power will be N^2 times the power radiated by a single particle. Different models associated with bunched curvature emission was progressively developed by Sturrock (1971), Ruderman & Sutherland (1975) and Buschauer & Benford (1976). Although bunched curvature emission was the only reliable candidate to explain pulsar radio emission, it was criticized by Melrose (1981, 1992), as there was no well established mechanism to create bunches and maintain their stability over long time scales.

The Second mechanism involves relativistic plasma emission. All the plasma emission mechanisms invoke a certain type of instability and it is a multi-stage mechanism with the first stage being generation of Langmuir waves through two stream instability, and the subsequent stages involve partial conversion of the Langmuir turbulence into escaping radiation at the plasma frequency. Different types of plasma emission mechanism have been proposed to explain the pulsar radio emission by Arons & Barnard (1986); Melrose (1992) and Asseo (1993), etc.

The third mechanism is the maser emission mechanism, which can be interpreted as negative absorption. There has been suggested several maser mechanisms in the literature of pulsar astronomy such as free electron maser, linear accelerated emission (Melrose 1989; Rowe 1995) or emission operated by curvature drift instability and cyclotron instability (Kazbegi et al. 1991a). But most of the maser emission mechanisms failed to achieve the high brightness temperature of pulsars in the radio regime, and also their polarization signatures.

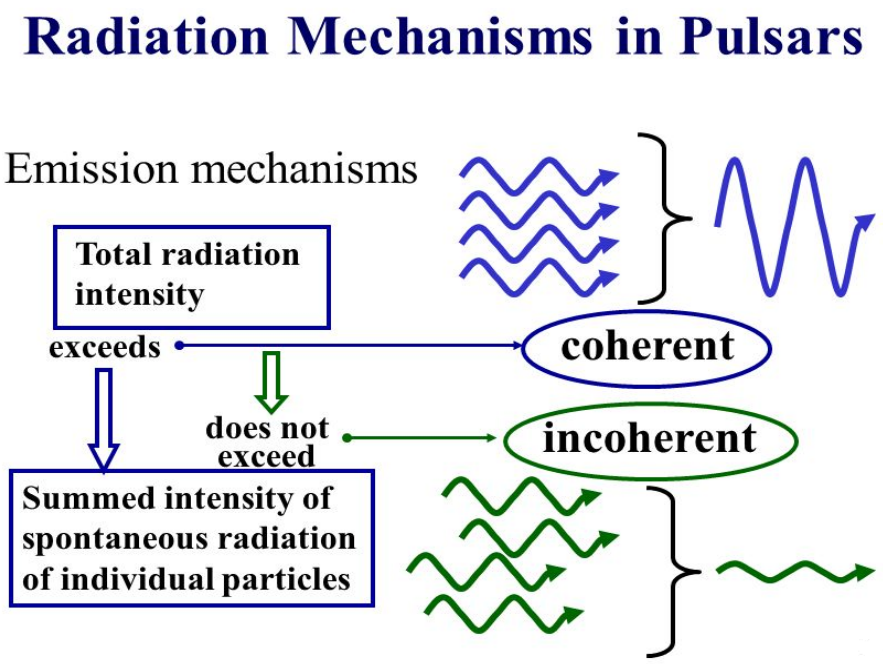

FIGURE 1.11: The difference between incoherent and coherent emission. In coherent emission waves are correlated in phase, whereas there is no such correlation among the waves in an incoherent emission.

1.8 Magnetic field of pulsars

In this section I have tried to throw some enlightening discussion regarding evolution and decay of pulsar magnetic field. The magnetic field is probably one of the most important parameters altering the evolution and the observational behavior of radio pulsars. Although it is believed that magnetic field configuration of pulsar magnetosphere is predominantly dipolar in nature, specifically adjacent to radio emission regime, but near to the surface of neutron star it is expected to have some multi-polar components. Existence of multi-polar components intuitively helps to make sufficient flow of plasma into magnetosphere. Magnetic field strength determines the loss rate of rotational energy and thereafter the spin down luminosity and spin evolution. Measuring the spin period and rate of change of spin period precisely helps one to discriminate between kinematical age and characteristics age

and thereafter use it as a potential probe of magnetic field decay in an isolated neutron star. An impressive study carrying the signature of magnetic field decay was done earlier by Ostriker & Gunn (1969), Gunn & Ostriker (1970), Lyne et al. (1985), Lyne (1982),Stollman (1987), Menou et al. (1999), Bhattacharya (1992), Harrison & Lyne (1993), Lorimer et al. (1997), Mukherjee & Kembhavi (1997), Han (1997), Igoshev & Popov (2015), Xue et al. (2017) etc. In a statistical study of pulsar properties, Gunn & Ostriker (1970) concluded that pulsar magnetic field decays on a timescale of 10^6 yr. A similar inference regarding the temporal behavior of the magnetic field can be reached by comparing pulsar's kinematic age with spin down age. The kinematic age is defined as $\tau_k = z/v_z$, where z is their current distance from the galactic plane, and v_z is their velocity transverse to it. τ_k denote the actual age of pulsars, since the formation of them in the galactic plane and thereafter they are ejected with a high velocity.

Another indicator of pulsar's age is spin-down age, which is defined roughly as $P/(2\dot{P})$. Here P is the spin period of pulsar and $\dot{P}$ is the rate of change of spin period of pulsar. All standard literature usually assumes that due to magnetic dipole radiation, torque due to back reaction is implemented on pulsar and during the life cycle of pulsar, magnetic field remains constant. As a consequence spin period of pulsars increases with time. But it is noticed that as pulsars get aged, the spin down age lengthened relative to τ_k , which is an indirect signature of magnetic field decay (Helfand & Tademaru 1977; Lyne et al. 1982, 1985). Through a diagram using recent data, of the kinematic age against the spin down age, showing huge scatter hence establishing the trend. Hence it is imperative that the hypothesis of retaining constant magnetic field through out the life time of radio pulsars is definitely inconsistent.

It is believed that some quantum forms of fluxoid namely neutron fluxoid and proton fluxoid are generated by vortex and pinning forces in the core of neutron star, which are comprised predominantly of neutron-proton superconducting Fermi

liquid (Ostriker & Gunn 1969; Konar 2017). Due to neutron star rotation these fluxoid structures drag each other and slowly magnetic flux structure comes out from the core region to the crust. On the theoretical side, it has been suggested that the magnetic field decay from the crust on a timescale of a few million years through ohmic dissipation of electrical currents in the neutron star. Another mechanism to explain the decay of magnetic field has been suggested such as non-linear Hall effect (Romani 1996b). But calculation based on ohmic decay shows that magnetic field does not decay on the Hubble time scale, if there is any penetration of the magnetic field lines into the interior of the star (Sang & Chanmugam 1990, 1987). However if one addresses the realistic thermal evolution condition and conductivity, an isolated neutron star can retain it's large magnetic field strength up to a time scale of 10^{10} year (Romani 1996b).

For accretion powered pulsars mechanism of magnetic field decay is based on different mass accretion rate. If there is enough accretion, sufficient materials will be under laid over the crust, so current carrying layers will be pushed to interior of neutron star. So in this scenario magnetic field is buried into the interior of neutron star's crust. So magnetic field decay again depends upon the confinement depth, material composition and conductivity of the crust.

Again some potential mechanism such as diamagnetic screening has been proposed to explain the magnetic field decay of pulsars such as accreting materials from binary companion (Bhattacharya 1992; Bhattacharya & van den Heuvel 1991). Depending upon the magnetic behavior of the accreted material susceptibility it can differs and for diamagnetic case it can significantly dilute the magnetic field strength. Based on some statistical approach by Narayan & Ostriker (1990) have found that magnetic field decays on a time scale of 1 Myr. However Hartman et al. (1997) have obtained a slightly different result from the simulation of birth and evolution of radio pulsars throughout the Galaxy and simply exponential decay model in the calculation. Several authors have tried to probe the pulsar

statistics with a non-exponential decay model of the magnetic field (Narayan & Ostriker 1990), but it failed to show it's success over the exponential model. Although lot of research has been dedicated towards the magnetic field evolution and decay of neutron star all of them have relative success and demerit as well. But in this thesis it is beyond my scope to discuss all the theories and observational predictions.

1.8.1 Aims of the thesis at a glance

1. Develop a coherent curvature radiation model for pulsar radio emission, which has the potential to explain the high brightness temperature in the radio band. By incorporating a suitably chosen emission beam geometry try to simulate pulse profiles.

2. Estimate the brightness temperature of radio pulsars for allowed value of bunch dimensions. Compute brightness temperature of 10 pulsars from a given data as provided in ATNF catalogue and compare with theoretical model.

3. Simulate polarization profiles of pulsar radio emission due to coherent curvature radiation by incorporating dipolar magnetic field line configuration with uniform plasma distribution and non-uniform distribution as well.

4. Develop a theoretical model to explain the power spectra of radio pulsars by incorporating different plasma process, such as Stimulated Raman Scattering and Stimulated Compton Scattering. I have tried to explain power spectra of two pulsars PSR 2111+46 and PSR 0329+54, which have a clear core-cone structure and broken power law spectra, by tuning different plasma parameters associated with our theoretical model.

5. Investigate the influence of stimulated Raman scattering on the polarization state of pulsar radio emission, and compare with the other prominent

perturbation effect, such as Faraday rotation. Due to Faraday rotation the plane of polarization of electromagnetic radiation rotates while propagating through the interstellar medium, which is magnetized.

Chapter 2

Probing pulsar radio emission and polarization from curvature radiation

2.1 Introduction

In this chapter, I have elaborated the various diverse polarization properties of pulsar radio emission based on the curvature radiation model. The curvature radiation basically occurs from the charged particles, confined in different planes associated with magnetic field lines. But the case we have presented in this chapter, is assumed to have no phase relationship among the constituents plasma particles, contributing towards radio emission in pulsar. The rotating magnetic field induces a strong electric field that accelerates charged particles from the surface of the neutron star into a magnetosphere consisting of a predominantly dipolar magnetic field and co-rotating relativistic pair plasma. Most of the models relate to pulsar

radio emission introduce pre-requisite conditions such as (i) radiation emitted tangentially to the field lines on which plasma is moving and (ii) the polarization electric field vector of the emitted radiation is confined to the plane of magnetic field lines at the emission spot. In the general framework of models in which the curvature radiation as emitted by charged bunches are constrained to follow field lines. The polarization property of pulsar such as linear polarization is intrinsic to the emission mechanism and it is purely a property of curvature radiation and viewing geometry.

Several pulsar researchers have shown that the properties such as the polarization angle (PA) swing can be explained within the framework of curvature radiation. The radio emission from particle bunches is highly polarized, and the radiation received by a distant observer will be less polarized due to the incoherent superposition of emissions from different magnetic field lines (Gil & Rudnicki 1985). Gil (1986) has argued for the connection between pulsar emission beams and polarization modes and suggested that out of two orthogonal- polarization modes, one corresponds to the core emission and the other to the conal emissions. They are highly linearly polarized and the observed depolarization is due to the superposition of modes at any instant (Gil 1987). By considering a charged a particle moving along the curved trajectory (circular) confined to the xz-plane, Gil & Snakowski (1990a) have deduced the polarization state of the emitted radiation and produced the creation of an anti-symmetric circular polarization in curvature radiation. By introducing a phase, as a propagation effect, the difference between the components of radiation electric field in the directions parallel and perpendicular to the plane of particle trajectory, Gil & Snakowski (1990b) have developed a model to explain the depolarization and polarization angle deviations in sub-pulses and micro-pulses. Gil et al. (1993) have modeled the single-pulse polarization characteristics of pulsar radiation and demonstrated that the deviations of the single-pulse position angle from the average are caused by both propagation and geometrical effects. Mitra et al. (2009), by analyzing the strong single pulses

with highly polarized sub-pulses from a set of pulsars have given very positive and strong arguments in favor of the coherent curvature radiation mechanism as a possible mechanism of the pulsar radio emission.

There are two types of claims for the origin of circular polarization: intrinsic to the emission mechanism (Michel 1987; Gil & Snakowski 1990a,b; Radhakrishnan & Rankin 1990; Gangadhara 2010) or generated by the propagation effect. Cheng & Ruderman (1979) and Radhakrishnan & Rankin (1990) have suggested that the propagation origin of anti-symmetric circular polarization is very unlikely but the symmetric circular polarization appears to be possible. On the other hand, Kazbegi et al. (1991b,a) have argued that the cyclotron instability, rather than the propagation effect, is responsible for the origin of circular polarization in pulsars. Melrose & Luo (2004) have discussed possible circular polarization induced by intrinsically relativistic effects associated with pulsar plasma. Fussell et al. (2003) have reviewed the properties of intrinsic circular polarization based on cyclotron absorption. The correlation between the anti-symmetric circular polarization and the polarization angle swing is a geometric property in principle (Radhakrishnan & Rankin 1990). By carefully modeling the polarization state of the radiation in terms of Stokes parameters, it is possible to construct the geometry of the emission region (Gangadhara 2004). So far very few literature shows full modeling of Stokes polarization due to pulsar radio emission, only the polarization angle has been widely recognized (Radhakrishnan & Cooke 1969; Komesaroff 1970) and followed by that it is attempted to be fit with the average radio profile data (Lyne & Manchester 1988).

In this chapter, for the sake of completeness, I have shown a pre-existing three-dimensional (3D) model of curvature radiation by relativistic sources accelerated along the dipolar magnetic field lines. In incoherent curvature radiation model relativistic plasma (a bunch, i.e., a point-like huge charge) moving along the dipolar magnetic field lines, emits curvature radiation. While deriving the

radiation field, actual dipolar magnetic field lines are considered here (not the circles) in a slowly rotating (non-rotating) magnetosphere such that the rotation effects can be neglected. It is shown that, this model reproduces the polarization angle swing of Radhakrishnan & Cooke (1969), and predicts that the correlation of anti-symmetric circular polarization and polarization angle swing is solely a geometric property of the emission process. The electric fields of the radiation are derived in Section 2.2 and thereafter the Stokes parameters of the radiation field are constructed in Section 2.3. Simulated profiles based on the theoretical model for different configurations of dipolar magnetic field line are presented in Section 2.3.1.

2.2 Formulation of emission beam geometry of pulsars

In spherical polar coordinates (r, θ, ϕ) centered on the magnetic axis, the unperturbed dipole field is given as

$$\vec{B} = \left\{ \frac{2\mu\cos\theta}{r^3}, \frac{\mu\sin\theta}{r^3}, 0 \right\}, \tag{2.1}$$

where μ is the magnetic moment, r the radial co-ordinate, θ the polar coordinate and ϕ the magnetic azimuth. If we neglect any perturbation, like field aligned current across polar cap, then induced azimuthal component of magnetic field can be taken to be zero. Now common differential equation of magnetic field lines is given by:

$$\frac{dr}{B_r} = \frac{rd\theta}{B_\theta} = \frac{r\sin\theta d\phi}{B_\phi}, \tag{2.2}$$

where B_r, B_θ and B_ϕ are the radial, polar and azimuthal component of magnetic field respectively. Now equating the radial and polar components and integrating

we get,

$$\int \frac{dr}{r} = \int \frac{B_r}{B_\theta} d\theta, \tag{2.3}$$

which gives

$$\log r = 2\log(\sin\theta) + \text{constant}.$$

Assuming that at $\theta = \pi/2$, $r = r_e$. So the above equation reduces to the well known di-polar field line equation

$$r = r_e \sin^2\theta. \tag{2.4}$$

Here r_e is di-polar field line constant which is defined as the distance between origin and the point at which magnetic field line intersect at magnetic equatorial plane i.e., $\theta = \pi/2$. We consider magnetic dipole situated at the origin with magnetic dipole moment $\hat{m}$ inclined with the rotation axis $\hat{\Omega}$ by an angle α. In a Cartesian coordinate system with the z-axis parallel to $\hat{\Omega}$ (see figure 2.1), the position vector of an arbitrary point Q on a field line is given by Gangadhara (2004):

$$\vec{r} = r_e \sin^2\theta \left\{\sin\theta\cos\phi, \sin\theta\sin\phi, \cos\theta\right\}. \tag{2.5}$$

Now the above expression of $\vec{r}$ the position vector is framed with respect to magnetic axis, which is tilted and rotated with respect to rotation axis by an angle α and ϕ' respectively. So in order to get an expression of position vector in rotation axis centered frame, we need to multiply the position vector by transformation matrix Λ. Here Λ is a product of two matrices as: rotation matrix ($M_{\rm rot}$) and inclination matrix ($M_{\rm inc}$). So, we have $\Lambda = M_{\rm rot} \cdot M_{\rm inc}$, where

$$M_{\rm inc} = \begin{bmatrix} \cos\alpha & 0 & \sin\alpha \\ 0 & 1 & 0 \\ -\sin\alpha & 0 & \cos\alpha \end{bmatrix}, \quad M_{\rm rot} = \begin{bmatrix} \cos\phi' & -\sin\phi' & 0 \\ \sin\phi' & \cos\phi' & 0 \\ 0 & 0 & 1 \end{bmatrix}$$

and $\phi' = \Omega t$ is the rotation phase.

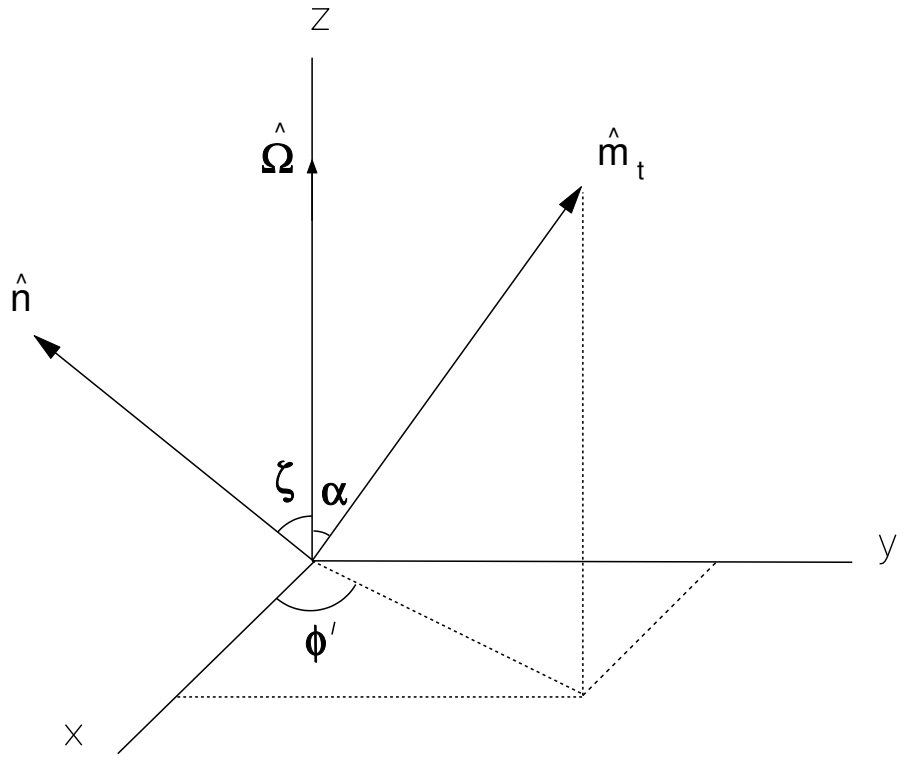

FIGURE 2.1: The basic geometry of pulsar, where the origin is assumed to coincide with the center of neutron star. Magnetic axis $\hat{m}$ is inclined with respect to rotation axis $\hat{\Omega}$ by an angle α and rotated by an angle $\phi' = \Omega t$ with respect to x axis.

The matrix M_{inc} produces clockwise rotation of the dipole around the y-axis, M_{rot} produces counter clock-wise rotation around z-axis. So the expression of Λ becomes

$$\Lambda = \begin{bmatrix} \cos\alpha\cos\phi' & -\sin\phi' & \cos\phi'\sin\alpha \\ \sin\phi'\cos\alpha & \cos\phi' & \sin\phi'\sin\alpha \\ -\sin\alpha & 0 & \cos\alpha \end{bmatrix} \tag{2.6}$$

So the expression of position vector in rotation axis centered frame becomes

$$\vec{r}_{ct} = \Lambda.\vec{r} = r_e \sin^2\theta\{\cos\theta\cos\phi\sin\alpha + \sin\theta(\cos\alpha\cos\phi\cos\phi' - \sin\phi\sin\phi'),$$

$$\cos\phi'\sin\theta\sin\phi + \sin\phi'(\cos\theta\sin\alpha + \cos\alpha\cos\phi\sin\theta), \cos\alpha\cos\theta - \cos\phi\sin\alpha\sin\theta\},$$

So, the tangent vector to a field line can be found by evaluating $\vec{b}_t = \partial\vec{r}_{ct}/\partial\theta$ and the curvature vector by evaluating $\vec{k}_t = d\hat{b}_t/ds$. Here $\hat{b}_t = \vec{b}_t/|\vec{b}_t|$ is a unit tangent vector, ds is arc length of the field line. The magnitude of the tangent vector is:

$$|\vec{b}_t| = r_e(\sqrt{5 + 3\cos(2\theta)}\sin\theta)/\sqrt{2}. \tag{2.7}$$

Once the curvature vector is derived, then the reciprocal of it's magnitude will give the expression of radius of curvature:

$$\rho = 1/|\vec{k}_t| = \frac{r_e \sin\theta(5 + 3\cos(2\theta))^{3/2}}{3\sqrt{2}(3 + \cos(2\theta))}. \tag{2.8}$$

Since $\hat{m}$ is chosen to be parallel to $\hat{z}$, the transformed magnetic dipole moment is given by

$$\hat{m}_t = \Lambda.\hat{z} = \{\sin\alpha\cos\phi', \sin\alpha\sin\phi', \cos\alpha\}\,. \tag{2.9}$$

Hence, the magnetic field of a dipole (Jackson 1975) that is inclined and rotated can be easily derived from the given expression of $\hat{m}$ as follows:

$$\vec{B}_t = B_0(r_{NS}/r)^3(3(\hat{r}.\hat{m}_t)\hat{r} - \hat{m}_t), \tag{2.10}$$

where B_0 is the surface magnetic field and r_{NS} = 10 km is the radius of the neutron star. The dominant magnetic field in the emission region is often shown to be consistent with being dipolar and used to study the shapes of pulsar radio beams (Narayan & Vivekanand 1983; Lyne & Manchester 1988; Kramer et al. 1994; Kramer et al. 1997). The typical timescale of pulse phase bin is small compared to the rotation period, therefore rotion effect can be ignored. So the rotating magnetic dipole can be approximated as a static dipole to understand the radio emission

geometry of pulsar, and hence the polarization profiles. Gangadhara (2004) has derived the accurate geometry of pulsar radio emission and subsequently, Gangadhara (2010) developed the full polarization model due to pulsar radio emission. Below I have elucidated the details of the emission geometry-related parameters, polar cap shape, polarization profiles, etc.

2.2.1 Magnetic colatitude and azimuth of emission spot

Consider the sight line $\hat{n} = \{\sin\zeta, 0, \cos\zeta\}$ that lies in the x-z plane and makes an angle ζ with respect to $\hat{\Omega}$, where $\zeta = (\alpha + \sigma)$ and σ is the angle of closest approach of the sight line with respect to the magnetic axis. The half-opening angle Γ of the pulsar emission beam is given by

$$\hat{n}.\hat{m}_t = \cos\Gamma = \cos\alpha\cos\zeta + \sin\alpha\sin\zeta\cos\phi'. \tag{2.11}$$

Since γ is already used for Lorentz factor, we use Γ for the half-opening angle of the emission beam. If τ is the angle between $\hat{b}_t$ and $\hat{m}_t$ then we have,

$$\cos\tau = \hat{b}_t.\hat{m}_t = \frac{1}{\sqrt{2}}\frac{1+3\cos 2\theta}{\sqrt{5+3\cos 2\theta}}. \tag{2.12}$$

In a relativistic plasma flow, radiation is beamed and directed along the magnetic-field line tangent. Thus, at any moment, the radiation is received from a spot in the magnetosphere where the tangent vector $\hat{b}_t$ points in the direction of $\hat{n}$. Thus at the emission spot $\tau \approx \Gamma$, and one can derive an expression of magnetic colatitude in terms of Γ as follows:

$$\cos(2\theta) = \frac{1}{3}(\cos\Gamma\sqrt{8+\cos^2\Gamma} - \sin^2\Gamma), \qquad -\pi \leq \Gamma \leq \pi. \tag{2.13}$$

However for $\Gamma \ll 1$, the above expression reduces to the well known approximate form $\theta \approx (2/3)\Gamma$. In order to get the expression of magnetic azimuth one has to

invoke $\hat{n}.\hat{b}_t = 1$ and $\hat{n} \times \hat{b}_t = 0$. So we get the expression of magnetic azimuth as

$$\sin\phi = -\sin\zeta \sin\phi' \csc\Gamma, \tag{2.14}$$

and

$$\cos\phi = (\cos\alpha \sin\zeta \cos\phi' - \cos\zeta \sin\alpha) \csc\Gamma. \tag{2.15}$$

So we have from the above two equations

$$\phi = \arctan\Big(\frac{\sin\zeta \sin\phi'}{\cos\zeta \sin\alpha - \sin\zeta \cos\alpha \cos\phi'}\Big). \tag{2.16}$$

2.2.2 Polar cap boundary from geometrical point of view

The polar cap boundary is demarcated by foot-print of the last open field lines for which $\vec{k}_t.\hat{z} = 0$ at the light cylinder. Therefore, the magnetic colatitude $\theta_{lof} = \theta$ at which $\vec{k}_t.\hat{z} = 0$ vanishes is given by

$$\cos(2\theta_{lof}) = \frac{-3a_1^2 - a_2\sqrt{8a_1^2 + a_2^2}}{9a_1^2 + a_2^2}, \quad -\pi/2 < \phi \leq \pi/2, \tag{2.17}$$

where $\mathrm{a}_1 = \sin\alpha\cos\phi$ and $\mathrm{a}_2 = 3\cos\alpha$. Next, for the range of $\pi/2 < \phi \leq 3\pi/2$, the colatitude is given by $\pi - \theta_{lof}$. Now we introduce the angle η between r_{ct} and $\hat{z}$, which is given by the following expression:

$$\cos\eta = \hat{z}.\hat{r}_{ct} = \cos\alpha\cos\theta - \sin\alpha\sin\theta\cos\phi. \tag{2.18}$$

If $\eta_{lof} = \eta$ at the light cylinder for the last open field line, then we have $|r_{ct}| \sin\eta_{lof} = r_{LC}$, and the last open field line constant is given by,

$$r_{e,lof} = r_{LC} \csc^2\theta_{lof} \csc\eta_{lof}. \tag{2.19}$$

Hence, the radial position of the foot of the last open field line from the magnetic axis is given by

$$s_p = r_{NS}\theta_p, \tag{2.20}$$

where $\theta_p = \arcsin((r_{NS}/r_{e,lof})^{1/2})$ is the colatitude of the foot of the last open field line. In order to make a parametric plot of the polar cap boundary, we consider a Cartesian coordinate system (x_B, y_B, z_B) such that the axis z_B is parallel to $\hat{m}_t$ and x_B lies in the meridional plane. The coordinates of the foot of the last open field line is given by

$$(x_B, y_B) = (s_p \cos\phi, s_p \sin\phi). \tag{2.21}$$

Using $\alpha = 30°$, spin period $P = 1$ s, $r_{NS} = 10$ km, the locus of polar cap is plotted in figure 2.2. It is elliptical, with the dimension 138 m in the x direction and 145 m along the y direction. In figure 2.3, we have shown most simple shape of polar cap region for $\alpha = 0°$, which is perfectly symmetric and circular in nature. The range of polar cap as shown in figure 2.3 lies -145 m$\leq x \leq 145$ m and -145 m$\leq y \leq 145$ m.

Also, we have plotted the polar cap boundary for $\alpha = 80°$ in figure 2.4, and it shows a asymmetric and elliptical shape with -100 m$\leq x \leq 100$ m and -145 m$\leq y \leq 145$ m. Since equation (2.17) becomes approximate at large α, the polar cap boundary at $\alpha = 80°$ is plotted by determining the last closed field line with the condition that the field line be tangent to the light cylinder at $\vec{d} = \vec{r}_{\rm ct} - (\vec{r}_{\rm ct} \cdot \hat{Z})\hat{Z}$, and $|\vec{d}| = r_{LC}$, where the unit vector $\hat{Z}$ is parallel to the spin axis.

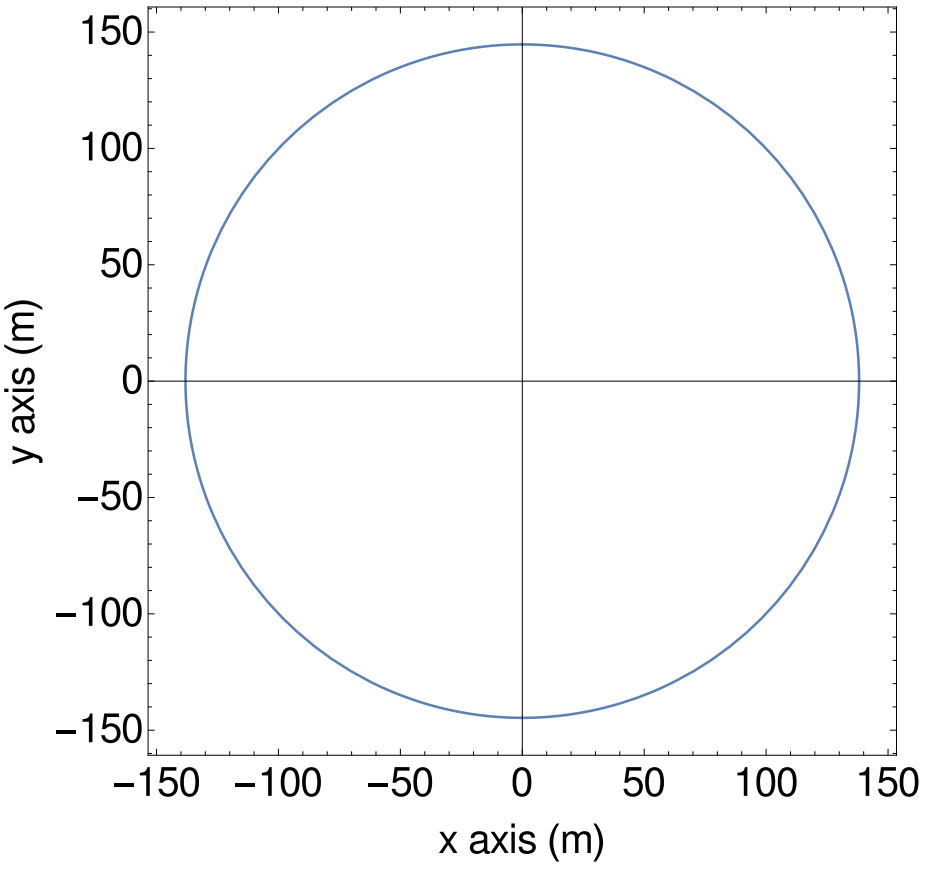

FIGURE 2.2: Figure shows the boundary of polar cap, which is generated by using $\alpha = 30^{\circ}$ and $P = 1$ s. The range of polar cap along the x direction lies in -138 m$\leq x \leq 138$ m and range along y direction lies in -145 m$\leq y \leq 145$ m. The shape of polar cap is symmetric and elliptical in nature.

2.3 Electric field of curvature radiation

Consider a magnetosphere having dipole magnetic field with axis $\hat{m}$ inclined by an angle α with respect to the rotation axis $\hat{\Omega}$ (see figure 2.5). We assume that the magnetosphere is stationary or slowly rotating such that the rotation effects are negligible. The relativistic pair plasma, generated by the induced electric field followed by pair creation, is constrained to move along the curved dipolar magnetic field lines.

The high brightness temperature of the pulsar indicates coherency in the pulsar radiation, which in turn forces one to postulate the existence of charged bunches.

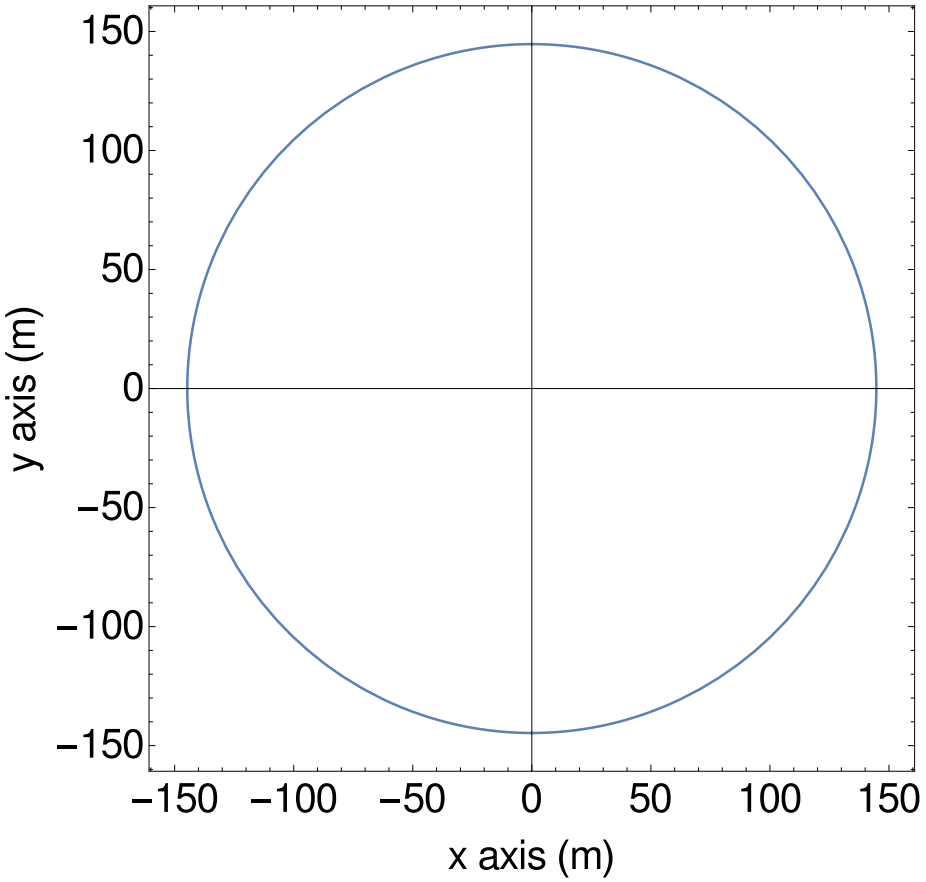

FIGURE 2.3: The above figure shows the boundary of polar cap, which is generated by using $\alpha = 0^{\circ}$ and $P = 1$ s. The range of polar cap along the x direction lies in -145 m$\leq x \leq 145$ m and range along y direction lies in -145 m$\leq y \leq 145$ m. The shape of polar cap is symmetric and circle in nature.

The formation of bunches in the form of solitons has been proposed (Cheng & Ruderman 1979; Pataraia & Melikidze 1980) but it was strongly criticized by Melrose (1992) for violating fundamental principle. However, Gil et al. (2004) have generalized the soliton model by including the formation and propagation of coherent radiation in the pulsar magnetosphere. Their results strongly support coherent curvature radiation by the spark-associated solitons as a plausible mechanism of pulsar radio emission. Following these views, we assume that the plasma in the form of bunches move along the open field lines in the pulsar magnetosphere. The velocity of the bunch moving across the curved field line can be expressed as:

$$\vec{v} = \frac{d\vec{r}}{dt} = \frac{\partial \vec{r}}{\partial \theta}\frac{\partial \theta}{\partial t} = |\vec{b}|\hat{b}\frac{\partial \theta}{\partial t}. \tag{2.22}$$

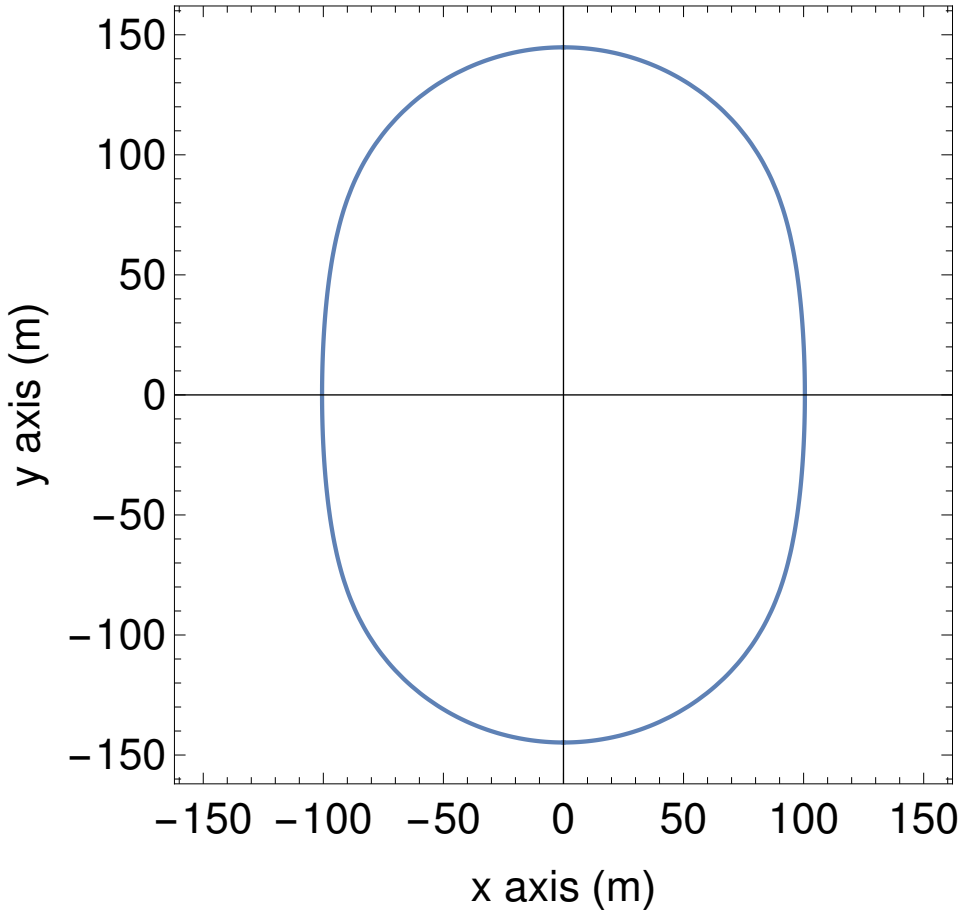

FIGURE 2.4: The above figure shows the boundary of polar cap, which is generated by using $\alpha = 80°$ and $P = 1$ s. The range of polar cap along the x-direction lies in -100 m$\leq x \leq 100$ m and range along y-direction lies in -145 m$\leq y \leq 145$ m. The shape of polar cap is symmetric and nearly elliptical in nature.

Due to curvature in the field lines, the plasma bunch, a point like huge charge, collectively radiates relativistically beamed radiation in the direction of velocity $\vec{v}$. In a slowly rotating or non-rotating case (Gangadhara 2010) aberration-retardation effects are ignored, hence $\vec{v}$ becomes parallel to the field line tangent $\hat{b}$. To receive the beamed emission, the observer line of sight $\hat{n}$ must align with $\vec{v}$ within the beaming angle $\frac{1}{\gamma}$, where γ is the Lorentz factor of the bunch. In other words, a distant observer at P (see figure 2.5) receives beamed emission only when $\hat{n}.\hat{v} = \cos\tau \approx 1$, i.e., $\tau \leq \pm 1/\gamma$, here $\hat{v} = \vec{v}/|\vec{v}|$. Let s be the infinitesimal arc-length of the magnetic field line. Then, $ds = |\vec{b}|d\theta$, where

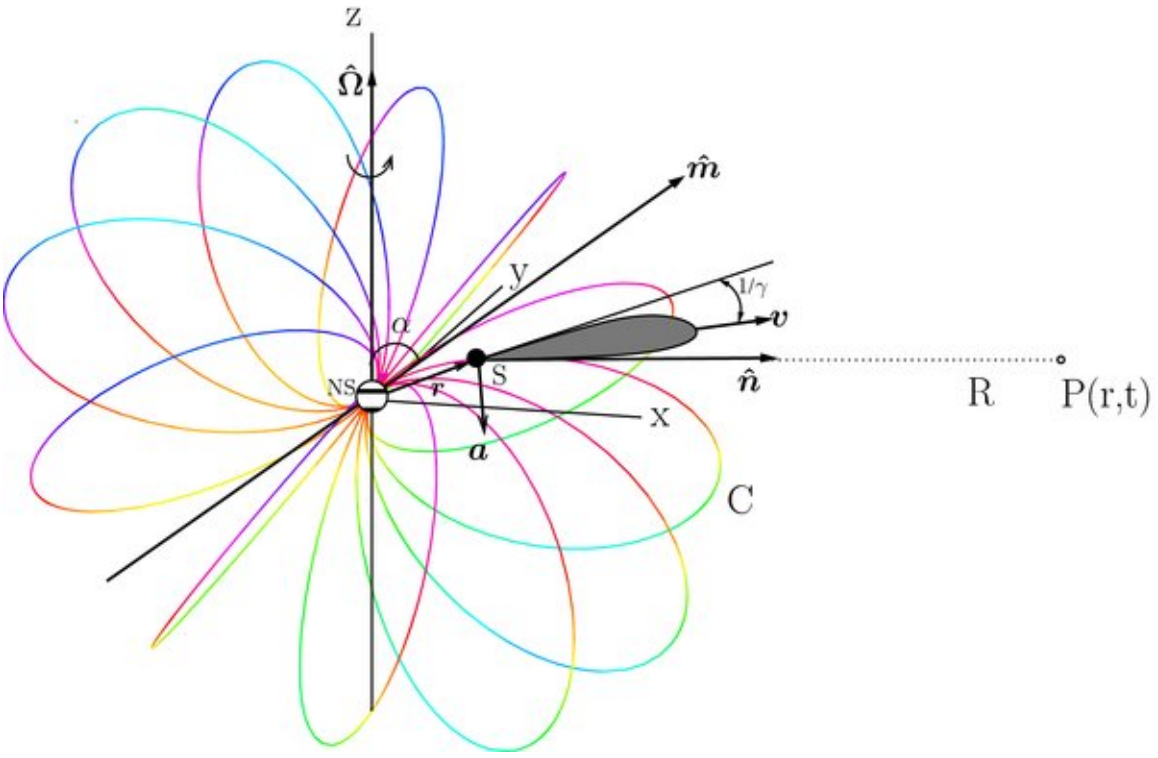

FIGURE 2.5: Above picture shows di-polar magnetic field lines surroundings neutron star. Dipolar field lines are plotted with a step of magnetic azimuth $\phi = 30^o$. Rotation axis $\hat{\Omega}$ is parallel with $\hat{z}$ axis and magnetic axis $\hat{m}$ is inclined with respect to rotation axis by an angle α. Radiation is highly beamed along the velocity vector of plasma blob and line of sight vector is aligned with respect to velocity vector by an angle $1/\gamma$. Here γ is the Lorentz factor associated with plasma blobs. Picture courtesy: (Gangadhara 2010).

$|\vec{b}| = (r_e/\sqrt{2})\sin\theta\sqrt{5+3\cos(2\theta)}$, and the magnitude of velocity $v = ds/dt = \kappa c$, where the parameter κ specifies the speed of bunch as a fraction of the speed of light c. So we have

$$\vec{v} = \kappa c\hat{b}, \tag{2.23}$$

where,

$$\hat{b} = \frac{\vec{b}}{|b|} = \{\cos\tau\cos\phi'\sin\alpha + \sin\tau(\cos\alpha\cos\phi\cos\phi' - \sin\phi\sin\phi'),$$

$\cos\phi'\sin\tau\sin\phi + \sin\phi'(\cos\tau\sin\alpha + \cos\alpha\cos\phi\sin\tau), \cos\alpha\cos\tau - \cos\phi\sin\alpha\sin\tau\}$, .

Here τ is the angle between $\hat{m}$ and $\hat{b}$. In terms of the polar angle θ, the angle τ is given by:

$$\tan\tau = \frac{\sin\tau}{\cos\tau} = \frac{3\sin(2\theta)}{1+3\cos(2\theta)}. \tag{2.24}$$

where $\cos\tau = \hat{b}.\hat{m} = (1+3\cos(2\theta))/(\sqrt{10+6\cos(2\theta)})$ and $\sin\tau = (\hat{m}\times\hat{b}).\hat{e}_\phi = (3\sin(2\theta))/(\sqrt{10+6\cos(2\theta)})$, and

$$\hat{e}_\phi = \{-\cos\alpha\sin\phi\cos\phi' - \cos\phi\sin\phi', \cos\phi\cos\phi' - \cos\alpha\sin\phi\sin\phi', \sin\alpha\sin\phi\}$$

is the binormal vector to the field line. Now equation (2.24) can be solved for θ, so we have,

$$\cos(2\theta) = \frac{1}{3}(\cos\tau\sqrt{8+\cos^2\tau} - \sin^2\tau). \tag{2.25}$$

Note equation (2.25) is more generalized and superior compared to equation (2.13), as $\tau = (\Gamma+\eta)$, which includes the more precise information of the angle between magnetic axis and line of sight vector at emission spot. Due to relativistic beaming line of sight and velocity vector can be inclined by a maximum angle $1/\gamma$, beyond which radiation would not be received. Here γ is the Lorentz factor of the radiating entity. Next, the acceleration of bunch moving along field line is given by,

$$\vec{a} = \frac{\partial\vec{v}}{\partial t} = \frac{(\kappa c)^2}{|\vec{b}|}\frac{\partial\hat{b}}{\partial\theta} = (\kappa c)^2\vec{k}, \tag{2.26}$$

where $|\vec{k}| = (1/|\vec{b}|)\frac{\partial\hat{b}}{\partial\theta}$ is the curvature of the field line. Then the radius of curvature of the field line is given by

$$\rho = \frac{1}{|\vec{k}|} = \left(1 - \frac{4}{9+3\cos(2\theta)}\right)|\vec{b}|. \tag{2.27}$$

Therefore, using $\vec{k} = \hat{k}/\rho$, we can write

$$\vec{a} = \frac{(\kappa c)^2}{\rho}\hat{k}. \tag{2.28}$$

Here

$$\hat{k} = \{(\cos\alpha\cos\phi\cos\phi' - \sin\phi\sin\phi')\cos\tau - \cos\phi'\sin\alpha\sin\tau,$$

$$(\cos\phi'\sin\phi + \cos\alpha\cos\phi\sin\phi')\cos\tau - \sin\alpha\sin\phi'\sin\tau, -\cos\phi\sin\alpha\cos\tau - \cos\alpha\sin\tau\}$$

is the unit curvature vector. The relativistic bunch, i.e., point-like huge charge, q collectively emits curvature photons as it accelerates along the curved field line. Then the electric field of the radiation at the observation point is given by Jackson (1975):

$$\vec{E}(\vec{r},t) = \frac{q}{c}\Big[\frac{\hat{n}\times[(\hat{n}-\vec{\beta})\times\dot{\vec{\beta}}]}{R\xi^3}\Big]_{ret}, \tag{2.29}$$

where $\xi = (1-\vec{\beta}.\hat{n})$ is the beaming factor, R the distance from the radiating region to the observer, $\vec{\beta} = \vec{v}/c$ the velocity, and $\dot{\vec{\beta}} = \vec{a}/c$ the acceleration of the bunch. Where ret means, integration evaluated at the retarded time. The radiation emitted by a relativistic bunch has a broad spectrum, and it can be estimated by taking the Fourier transformation of the electric field of radiation:

$$\vec{E}(\vec{r},\omega) = \frac{1}{\sqrt{2\pi}}\int_{-\infty}^{\infty}\vec{E}(\vec{r},t)\exp[i\omega t]dt. \tag{2.30}$$

In order to compute the electric field at the retarded time, we need to change the variable from t to t', where $t' + R(t')/c = t$. Therefore we obtain,

$$\vec{E}(\vec{r},\omega) = \frac{1}{\sqrt{2\pi}}\frac{q}{c}\int_{-\infty}^{\infty}\frac{\hat{n}\times[(\hat{n}-\vec{\beta})\times\dot{\vec{\beta}}]}{R\xi^3}\exp[i\omega(t'+R(t')/c)]dt'. \tag{2.31}$$

Here we have used $dt = \xi dt'$, when the observation point is far away from line of sight it can be approximated as constant in time. Further more, the distance $R(t')$ can be approximated as $R(t') \approx R_0 - \hat{n}.\vec{r}(t')$, where R_0 is the distance between the origin and the observation point P (see figure 2.5), and $\vec{r}(t')$ is the position vector of the bunch relative to origin. Since bunches move with speed κc along the dipolar field lines, over the incremental time dt the distance (arc length) covered

is $ds = \kappa c dt = |\vec{b}| d\theta$. Therefore, we have

$$t = \frac{1}{\kappa c} \int |\vec{b}| d\theta = \frac{r_e}{\sqrt{2}\kappa c} \int \sin\theta \sqrt{5 + 3\cos(2\theta)} d\theta. \tag{2.32}$$

If we choose at the beginning of the acceleration of particle along magnetic field lines i.e., $t = 0$ at $\theta = 0$, then by evaluating the above integration we obtain

$$t = \frac{r_e}{12\kappa c}[12 + \sqrt{3}\log(14 + 8\sqrt{3}) - 3\sqrt{10 + 6\cos(2\theta)}\cos\theta - 2\sqrt{3}\log(\sqrt{6}\cos(\theta) + \sqrt{5 + 3\cos(2\theta)}]. \tag{2.33}$$

Now converting the time domain integration into θ domain, the frequency dependent expression of electric field becomes

$$\vec{E}(\vec{r}, \omega) = \frac{q \exp[i\omega R_0/c]}{\sqrt{2\pi}\kappa R_0 c^2} \int_{-\infty}^{\infty} |\vec{b}| \frac{\hat{n} \times [(\hat{n} - \vec{\beta}) \times \dot{\vec{\beta}}]}{\xi^2} \exp[i\omega(t - \hat{n}.\vec{r}/c)] d\theta. \tag{2.34}$$

where the expression for t is given in equation (2.33). Point to note that the prime on the time variable t has been omitted for brevity. The integration limits have been extended to $\pm\infty$ for mathematical convenience, as the integrand vanishes for $|\theta - \theta_0| \geq 1/\gamma$. At any rotation phase ϕ', there exists a magnetic colatitude θ_0 and a magnetic azimuth ϕ_0 at which the field line tangent $\hat{b}$ gets exactly aligned with $\hat{n}$, i.e., $\hat{b}.\hat{n} = 1$ and $\tau = \Gamma$, where Γ is the half opening angle of the pulsar emission beam centered on $\hat{m}$. The polarization state of the emitted radiation can be determined using $\vec{E}(\omega)$ with the known $\vec{r}(t)$, $\vec{\beta}$, and $\dot{\vec{\beta}}$. By assuming $\kappa \approx 1$, we have plotted t as a function of θ for different r_e (see figure 2.6). It shows time t increases much faster at larger r_e than at lower r_e. This is due to the fact that for a given range of θ, the arc-length of the field line becomes larger at higher r_e. Now the polarization state of the emitted radiation can be estimated using the expression of $\vec{E}(\omega)$ (see equation (2.34)) with the known $\vec{r}(t)$, $\vec{\beta}$, and $\dot{\vec{\beta}}$. Now let

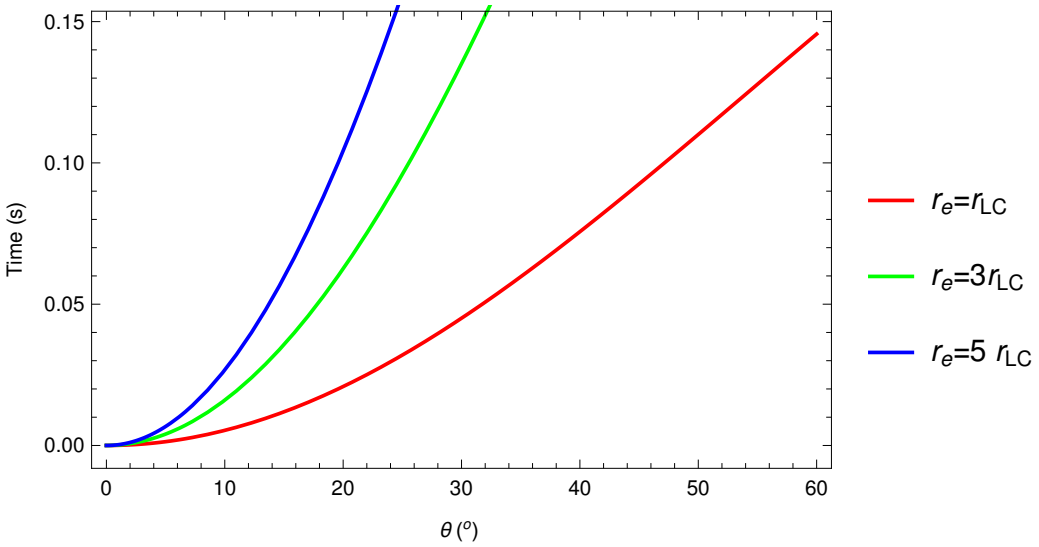

FIGURE 2.6: Time vs colatitude is plotted for different values of field line constant. Chosen value of κ is 0.9 .

we introduce a vector,

$$\vec{A} = \frac{1}{\kappa c}|\vec{b}|\frac{\hat{n}\times[(\hat{n}-\vec{\beta})\times\dot{\vec{\beta}}]}{\xi^2}. \tag{2.35}$$

By substituting the value of $\dot{\vec{\beta}} = \vec{a}/c$, from equation (2.28), equation (2.35) reduces to the following equation:

$$\vec{A} = \{A_x, A_y, A_z\} = \frac{\hat{n}\times[(\hat{n}-\vec{\beta})\times\vec{N}]}{\xi^2}.$$

Here $\vec{N} = \partial\vec{\beta}/\partial\theta$. Now substituting $\vec{\beta} = \vec{v}/c$ and making power series expansion of $\vec{A}$ in powers of θ about θ_0 we obtain,

$$A_x = A_{x0} + A_{x1}(\theta-\theta_0) + A_{x2}(\theta-\theta_0)^2 + A_{x3}(\theta-\theta_0)^3 + O[(\theta-\theta_0)^4], \tag{2.36}$$

$$A_y = A_{y0} + A_{y1}(\theta-\theta_0) + A_{y2}(\theta-\theta_0)^2 + A_{y3}(\theta-\theta_0)^3 + O[(\theta-\theta_0)^4], \tag{2.37}$$

$$A_z = A_{z0} + A_{z1}(\theta-\theta_0) + A_{z2}(\theta-\theta_0)^2 + A_{z3}(\theta-\theta_0)^3 + O[(\theta-\theta_0)^4]. \tag{2.38}$$

where A_{xi} , A_{yi} and A_{zi} with i = 0, 1, 2, 3 are the series expansion coefficients, and their expressions are given in Appendix A of Gangadhara (2010). Using the

analytical expressions of the power series expansion coefficients is a bit difficult task, therefore we have computed numerically to simulate pulse profiles. Now the scalar product between $\hat{n}$ and $\vec{r}$ is given by the following expression:

$$\hat{n}.\vec{r} = r_e \sin^2\theta[\cos\alpha(\cos\theta\cos\zeta + \cos\phi\cos\phi'\sin\theta\sin\zeta) -$$

$$\cos\zeta\cos\phi\sin\alpha\sin\theta + \sin\zeta(\cos\theta\cos\phi'\sin\alpha - \sin\theta\sin\phi'\sin\phi)] \ .$$

Now substituting the value of t from equation (2.33) and $\hat{n}.r$ into the exponential argument of equation (2.34) we get,

$$\omega(t - \hat{n}.\vec{r}/c) = c_0 + c_1(\theta - \theta_0) + c_2(\theta - \theta_0)^2 + c_3(\theta - \theta_0)^3 + O[(\theta - \theta_0)]^4. \quad (2.39)$$

where c_0, c_1, c_2, c_3 are the series expansion coefficients of the exponential argument. The series expansion coefficients are evaluated numerically to estimate the electric field components and thereafter the Stokes parameters. Once the expression of series expansion coefficients of $\vec{A}$ and the exponential arguments are computed, then electric field components reduce to the following:

$$\vec{E}(\omega) = \{E_x(\omega), E_y(\omega), E_z(\omega)\} \, .$$

Here

$$E_x(\omega) = E_0 \int_{-\infty}^{\infty} (A_{x0} + A_{x1}\mu + A_{x2}\mu^2 + A_{x3}\mu^3) \exp[i(c_1\mu + c_2\mu^2 + c_3\mu^3)]d\mu \quad (2.40)$$

$$E_y(\omega) = E_0 \int_{-\infty}^{\infty} (A_{y0} + A_{y1}\mu + A_{y2}\mu^2 + A_{y3}\mu^3) \exp[i(c_1\mu + c_2\mu^2 + c_3\mu^3)]d\mu \quad (2.41)$$

$$E_z(\omega) = E_0 \int_{-\infty}^{\infty} (A_{z0} + A_{z1}\mu + A_{z2}\mu^2 + A_{z3}\mu^3) \exp[i(c_1\mu + c_2\mu^2 + c_3\mu^3)]d\mu, \quad (2.42)$$

where $\mu = \theta - \theta_0$ and $E_0 = \frac{q}{\sqrt{2\pi}R_0 c} \exp[i\omega(c_0 + R_0/c)]$. Now by substituting the integral solution into the x, y and z components of the electric field we get,

$$E_x(\omega) = E_0(A_{x0}S_0 + A_{x1}S_1 + A_{x2}S_2 + A_{x3}S_3), \quad (2.43)$$

$$E_y(\omega) = E_0(A_{y0}S_0 + A_{y1}S_1 + A_{y2}S_2 + A_{y3}S_3), \tag{2.44}$$

$$E_z(\omega) = E_0(A_{z0}S_0 + A_{z1}S_1 + A_{z2}S_2 + A_{z3}S_3). \tag{2.45}$$

Now to find the polarization angle of radiation field $\vec{E}(\omega)$, we need to specify two reference directions perpendicular to the sight line vector $\hat{n}$. One could be the projected spin axis on the plane of the sky: $\hat{\epsilon}_{\|} = \{-\cos\zeta, 0, \sin\zeta\}$, and then the other direction is specified by $\hat{\epsilon}_{\perp} = \hat{\epsilon}_{\|} \times \hat{n} = \hat{y}$, where $\hat{y}$ is a unit vector parallel to the y-axis. Then the components of $\vec{E}(\omega)$ in the directions $\hat{\epsilon}_{\|}$ and $\hat{\epsilon}_{\perp}$ are given by

$$E_{\|} = \hat{\epsilon}_{\|}.\vec{E}, \tag{2.46}$$

and

$$E_{\perp} = \hat{\epsilon}_{\perp}.\vec{E}. \tag{2.47}$$

Below we have tried to elucidate the integral solution briefly. Let's consider the following integral equations:

$$S_0 = \int_{-\infty}^{\infty} \exp[i(c_1\mu + c_2\mu^2 + c_3\mu^3)]d\mu. \tag{2.48}$$

By changing the variable of integration $t = (x/l) + m$, where $l = c_3^{1/3}$ and $m = -c_2/(3c_3)$, the above integrals reduces to the following form:

$$\int_{-\infty}^{\infty} \exp[i(c_1\mu + c_2\mu^2 + c_3\mu^3)]d\mu = U\int_{-\infty}^{\infty} \exp[i(zx + x^3)]dx. \tag{2.49}$$

Here $z = (1/c_3^{1/3})(c_1 - c_2^2/(3c_3))$ and $U = (1/c_3^{1/3})\exp[i(c_2/(3c_3))(2c_2^2/(9c_3) - c_1)]$. Now the solution of the above integration has some standard value, which is given in Abramowitz and Stegun (1964):

$$j_0 = \int_{-\infty}^{\infty} \exp[i(zx + x^3)]dx = (\frac{2\pi}{3^{1/3}})Ai(z/3^{1/3}).$$

Here $Ai(z)$ is an Airy function of z with no branch cut discontinuities. Another standard integral solution which is as follows:

$$j_1 = \int_{-\infty}^{\infty} x \exp[i(zx + x^3)]dx = -\frac{2\pi i}{3^{2/3}} Ai'(z/3^{1/3}),$$

where Ai′ is the derivative of Airy function $Ai(z)$. Therefore we have,

$$S_0 = U j_0. \tag{2.50}$$

Now differentiating equation (2.49) both side with respect to c_1 and doing algebric manipulation we get,

$$S_1 = \int_{-\infty}^{\infty} \mu \exp[i(c_1\mu + c_2\mu^2 + c_3\mu^3)]d\mu = (U/c_3^{1/3})[j_1 - j_0 c_2/(3c_3^{2/3})]. \tag{2.51}$$

Next by differentiating equation (2.49) with respect to c_2 we get

$$S_2 = \int_{-\infty}^{\infty} \mu^2 \exp[i(c_1\mu + c_2\mu^2 + c_3\mu^3)]d\mu = (U/(3c_3))[((2c_2^2)/(3c_3) - c_1)j_0 - (2c_2)/(c_3^{1/3})j_1] \tag{2.52}$$

Next by differentiating equation (2.49) with respect to c_3 we get,

$$S_3 = \int_{-\infty}^{\infty} \mu^3 \exp[i(c_1\mu + c_2\mu^2 + c_3\mu^3)]d\mu = \frac{U}{9c_3^{7/3}}\Big[\frac{9c_1c_2c_3 - 4c_2^3 + i9c_3^2}{3c_3^{2/3}} j_0 + (4c_2^2 - 3c_1c_3)j_1\Big]. \tag{2.53}$$

At any rotation phase ϕ', the observer receives the radiation from all those field lines whose tangents lie within the angle $1/\gamma$ with respect to the sight line $\hat{n}$. Let η be the angle between the $\hat{b}$ and $\hat{n}$ then $\cos\eta = \hat{b}.\hat{n}$, and the maximum value of η is $1/\gamma$. Therefore, at $\phi = \phi_0$ we solve $\cos(1/\gamma) = \hat{b}.\hat{n}$ for τ, and find the allowed range $(\Gamma - 1/\gamma) \leq \tau \leq (\Gamma + 1/\gamma)$ of τ or $-1/\gamma \leq \eta \leq 1/\gamma$ of η, which in turn allows one to find the range of θ with the help of equation (2.25).

If we substitute $\Gamma \pm 1/\gamma$ in place of τ in Equation (2.25) then we get the

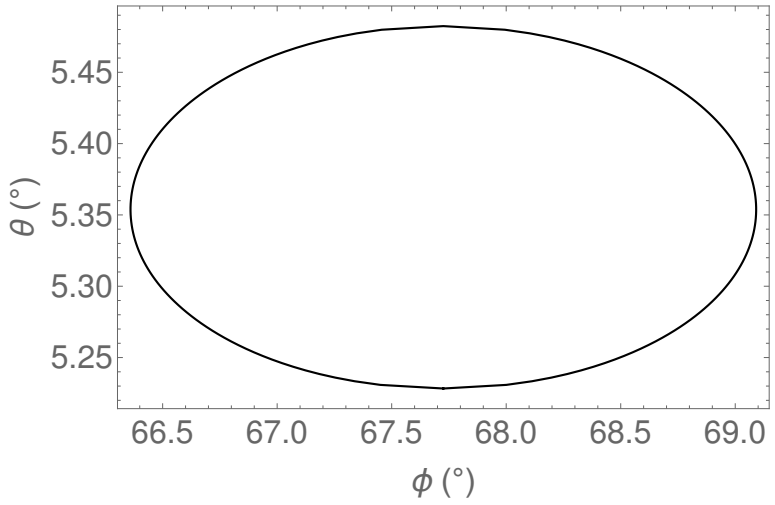

FIGURE 2.7: Emission region is mapped on to the $\theta\phi$–plane corresponding to rotation phase $\phi' = -30°$. Others geometrical parameters are $\alpha = 30°$, $\beta = 5°$, $\gamma = 300$.

corresponding range of θ. Then, for any given r_e, we can estimate the range of emission altitude $r = r_e \sin^2\theta$ over which observer receives the radiation.

Next, for any given η within its range, we find ϕ by solving $\cos\eta = \hat{b}.\hat{n}$. It gives $(\phi_0 - \delta\phi) \leq \phi \leq (\phi_0 + \delta\phi)$, and the expression of $\delta\phi$ was derived in Gangadhara (2010)

$$\cos(\delta\phi) = \frac{\sin\Gamma[\cos(1/\gamma)\csc(\Gamma+\eta) - \cos\Gamma\cot(\Gamma+\eta)]}{(\cos\zeta\sin\alpha - \cos\alpha\cos\phi'\sin\zeta)^2 + \sin^2\zeta\sin^2\phi'}. \tag{2.54}$$

Hence by knowing the ranges of θ and ϕ at any given ϕ', we can estimate the net contributions of the electric field from all those field lines, whose tangents lie within the angle $1/\gamma$ with respect to $\hat{n}$. In figure 2.7 and figure 2.8, we have plotted those regions at two phases: $\phi' = -30^o$, and 30^o and by using other fixed parameters $\alpha = 10^o$, $\beta = 5^o$, and $\gamma = 400$. Note that at the center of each region, $\hat{b}$ exactly aligns with the sight line, i.e., $\hat{b}.\hat{n} = 1$.

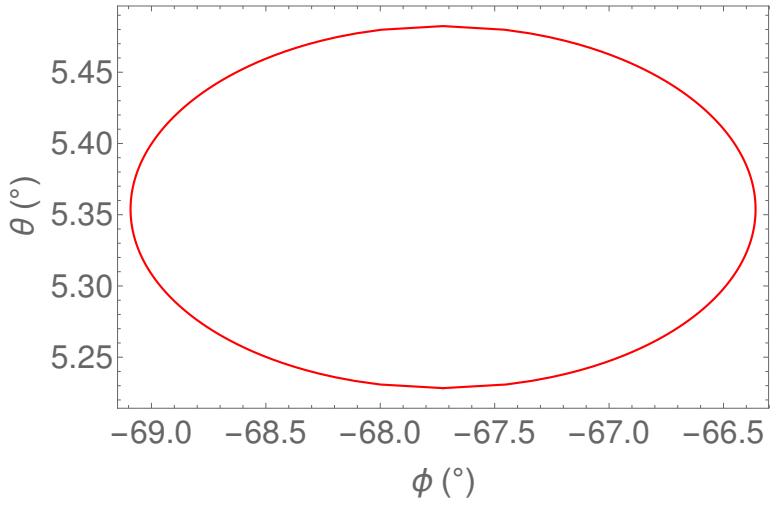

FIGURE 2.8: Emission region is mapped on to the $\theta\phi$–plane corresponding to rotation phase $\phi' = 30°$. Other geometrical parameters are $\alpha = 30°$, $\beta = 5°$, $\gamma = 300$.

The net emission, which the observer receives along $\hat{n}$ will have contributions from the neighboring field lines, whose tangents are within the angle $1/\gamma$ with respect to $\hat{n}$. Hence the radiation received at any given phase is the net contribution from a small tube of field lines having an angular width of about $2/\gamma$. Thus, the radiation in the direction of the line of sight should be integrated over a solid angle $d\Omega = \sin\theta d\theta d\phi$. We choose limits on the angles ϕ and θ such that the integration over them will cover the solid angular region (beaming region) of radial width $1/\gamma$ around $\hat{n}$. Since θ and ϕ are orthogonal co-ordinates, choosing them as the variables of integration is justified.

For example, we assume that the width of the bunch η_0 is much smaller than the wavelength λ of the radio waves, so that the radiation emitted by a bunch is coherent, and the bunches, within the beaming region, are closely spaced, so that the net emission becomes smooth and continuous. Consider a bunch having $\gamma \approx 400$ emitting radio waves at frequency $\nu = 600$ MHz or $\lambda = c/\nu = 50$ cm at an altitude of about 400 km. Then the angular width of the beaming region corresponding to $\sim 2/\gamma$ is $\sim 0.3°$, which corresponds to a width of ~ 2 km at an altitude of 400 km. For coherence to be effective the bunch width $w_0 \leqslant \lambda$.

Therefore, choosing $w_0 \leqslant 50$ cm for $\lambda = 50$ cm is well justified. Since these values of w_0 are much smaller than the width of the beaming region (~ 2 km), the Stokes parameters can be integrated as continuous functions of θ and ϕ. So Stokes parameters integrated over solid angle can be written as follows:

$$I_s = \int_{\phi_0-\delta\phi}^{\phi_0+\delta\phi} \int_{\theta_0-\delta\theta}^{\theta_0+\delta\theta} I \sin\theta d\theta d\phi \tag{2.55}$$

$$Q_s = \int_{\phi_0-\delta\phi}^{\phi_0+\delta\phi} \int_{\theta_0-\delta\theta}^{\theta_0+\delta\theta} Q \sin\theta d\theta d\phi \tag{2.56}$$

$$U_s = \int_{\phi_0-\delta\phi}^{\phi_0+\delta\phi} \int_{\theta_0-\delta\theta}^{\theta_0+\delta\theta} U \sin\theta d\theta d\phi \tag{2.57}$$

$$V_s = \int_{\phi_0-\delta\phi}^{\phi_0+\delta\phi} \int_{\theta_0-\delta\theta}^{\theta_0+\delta\theta} V \sin\theta d\theta d\phi. \tag{2.58}$$

Then the linear polarization is given by

$$L_s = \sqrt{Q_s^2 + U_s^2}, \tag{2.59}$$

and the polarization angle is given by

$$\psi_s = (1/2)\tan^{-1}(U_s/Q_s). \tag{2.60}$$

2.3.1 Modulation function and it's implication on radio emission profiles of pulsar

Most of the literature suggest that pulsar radio emission is coming from mostly open magnetic field lines, whose foot points define the polar cap. The shape of pulsar profiles indicates that the entire polar cap does not radiate; but rather some selected portion of open magnetic field line regions radiate. The morphological classification scheme of the pulsar radio emission cone is comprising of a

central core emission encompassing coaxial conal emissions, which has overwhelming support from observations (Rankin 1990, 1993a). Hence, the radiating region over the polar cap region can be thought of as a hollow cone nested structure i.e., a combination of a few coaxial conal regions of emission (cones) with a central column of emission (core) (Kijak & Gil 1997; Gangadhara & Gupta 2001; Gupta & Gangadhara 2003; Dyks & Harding 2004). It is well known that the components of a pulsar profile can be decomposed into individual Gaussians by fitting one with each of the sub-pulse components. We know pulsar emission is relativitically beamed, and hence the cross sections of pulsar emission beams and sub-pulse beams may be approximately assumed to be Gaussians. For example, the components in the pulse profile of PSR 2351+61 was fitted with appropriate Gaussians by Kramer et al. (1997). When the line of sight crosses the emission region, it encounters a pattern in intensity due to Gaussian modulation in the azimuthal direction. Because of the Gaussian modulation in the azimuthal direction or perturbations due to inhomogeneous plasma distribution, the intensity becomes non-uniform in the polar directions too. But here we have considered only perturbation along azimuthal direction for less complication. So, we define a modulation function for a pulse component as:

$$f(\phi) = f_0 \exp\left[-\left(\frac{\phi - \phi_p}{\sigma_\phi}\right)^2\right], \tag{2.61}$$

where ϕ_p is the peak location of the Gaussian function and f_0 is the amplitude. If w_ϕ is the full width at half-maximum (FWHM), then $\sigma_\phi = w_\phi/(2\sqrt{\ln 2})$. So including the modulation function, the expression of full Stokes parameters reduces to

$$I_s = \int_{\phi_0-\delta\phi}^{\phi_0+\delta\phi} \int_{\theta_0-\delta\theta}^{\theta_0+\delta\theta} fI \sin\theta d\theta d\phi \tag{2.62}$$

$$Q_s = \int_{\phi_0-\delta\phi}^{\phi_0+\delta\phi} \int_{\theta_0-\delta\theta}^{\theta_0+\delta\theta} fQ \sin\theta d\theta d\phi \tag{2.63}$$

$$U_s = \int_{\phi_0-\delta\phi}^{\phi_0+\delta\phi} \int_{\theta_0-\delta\theta}^{\theta_0+\delta\theta} fU \sin\theta d\theta d\phi \tag{2.64}$$

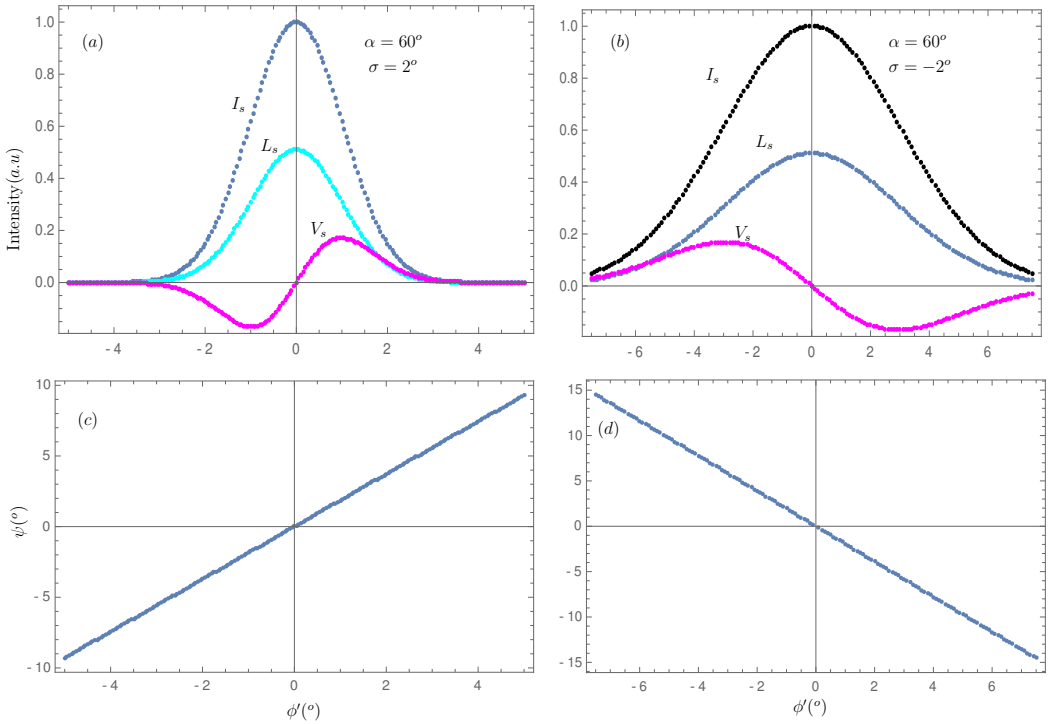

FIGURE 2.9: Simulated pulse profiles. Chosen $P = 1$ s and $\gamma = 400$. For panels (a) and (c) $\sigma_\phi = 1$, $\phi_p = 0^o$, and $f_0 = 1$, respectively, are used for the Gaussian. Similarly, for panels (b) and (d) $\sigma_\phi = 1$, $\phi_p = 180^o$, and $f_0 = 1$ are used, respectively.

$$V_s = \int_{\phi_0-\delta\phi}^{\phi_0+\delta\phi} \int_{\theta_0-\delta\theta}^{\theta_0+\delta\theta} fV \sin\theta d\theta d\phi. \tag{2.65}$$

Using a Gaussian with peak located at the meridional plane ($\phi' = 0^o$), we have simulated the pulse profiles in the two cases of impact parameter (σ) and various inclination angles (α). We observe that the profile in the case of negative σ is broader than that in the positive case. This difference is due to the projection of the emission region onto the equatorial plane of the pulsar. In the case of positive σ, the nature of polarization angle χ_s swing follows counter clockwise (ccw) direction and the sign change of V_s is -/+ (anti clock-wise to clock wise) with respect to ϕ', while in the case of negative σ the χ_s swing is clock wise (cw) and the sign change of V_s is +/- (clock-wise to anti clock-wise). Hence, we find that the polarization angle swing is correlated with the circular polarization sign reversal. This correlation is invariant with respect the stellar spin directions.

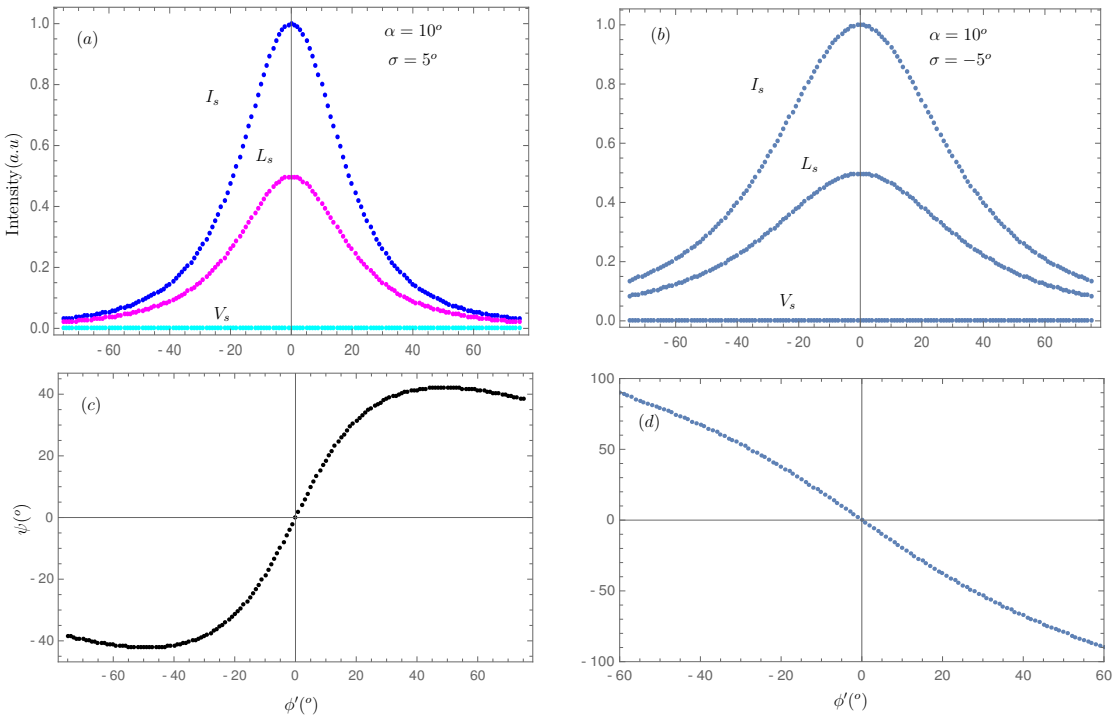

FIGURE 2.10: Simulated pulse profiles: in panels (a) and (b) intensity (I_s), linear polarization (L_s), and circular polarization (V_s), and in lower panels (c) and (d) the corresponding polarization angle (ψ_s) curves are plotted. Chosen $P = 1$ s and $\gamma = 400$. Note that profiles are normalized with the peak intensity.

To investigate the polarization of sub-pulses in such profiles, we have reproduced single component, three component and five-component profiles by considering single Gaussian, three Gaussians and five Gaussians (see figure 2.9, figure 2.11, figure 2.12). The central component is presumed to be a core, and the other components are symmetrically located on either side of the core forming the cones. Note in figure 2.10, circular polarization got vanished as it corresponds to the case of uniform plasma distribution. Note all the profiles from figures 2.9-2.12 are simulated theoretically. Dotted points arises here (figures 2.9-2.12) as numerical simulations were done with finite step size in rotation phase. We find across each component that circular polarization changes the sign and is correlated with the polarization angle swing. It is also observed that the circular polarization of the outermost components is weaker compared to that of inner ones, which is more obvious in the case of large inclination angles. This is due to the fact that the sight line crosses the field lines in the almost edge-on position in the case of outermost

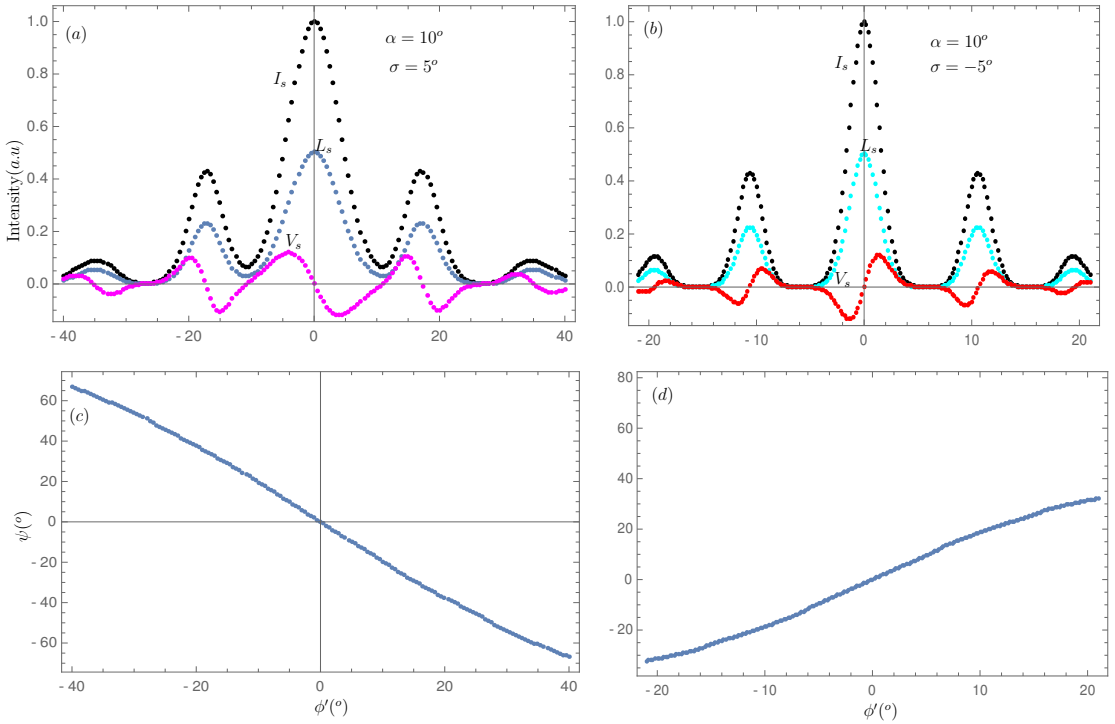

FIGURE 2.11: Simulated pulse profiles. Chosen $P = 1$ s and $\gamma = 400$. For panels (a) and (c) $\sigma_\phi = 0.14, 0.10, 0.07,$, $\phi_p = 0^o, \pm 30^o, \pm 50^o$ and $f_0 = 1, 0.75, 0.5$ respectively, are used for the Gaussians. Similarly, for panels (b) and (d) $\sigma_\phi = 0.14, 0.06, 0.03$, $\phi_p = 180^o, 180^o \pm 16^o, 180^o \pm 26^o$, and $f_0 = 1, 0.75, 0.5$ respectively, are used from the central component to the outermost one.

components.

2.4 Discussion

We believe, the pulsar radio emission contain both the incoherent and coherent contributions. Though the emission from a single bunch is highly polarized, the radiation received by a distant observer will be less polarized, as the radiation from many bunches is incoherently superposed (Gil & Rudnicki 1985). Also, the degree of polarization is found to rely on the time resolution chosen in the observation (Gangadhara et al. 1999). Circular polarization is generally strongest in the central regions of a profile but relatively weaker at outermost profiles. The anti-symmetric

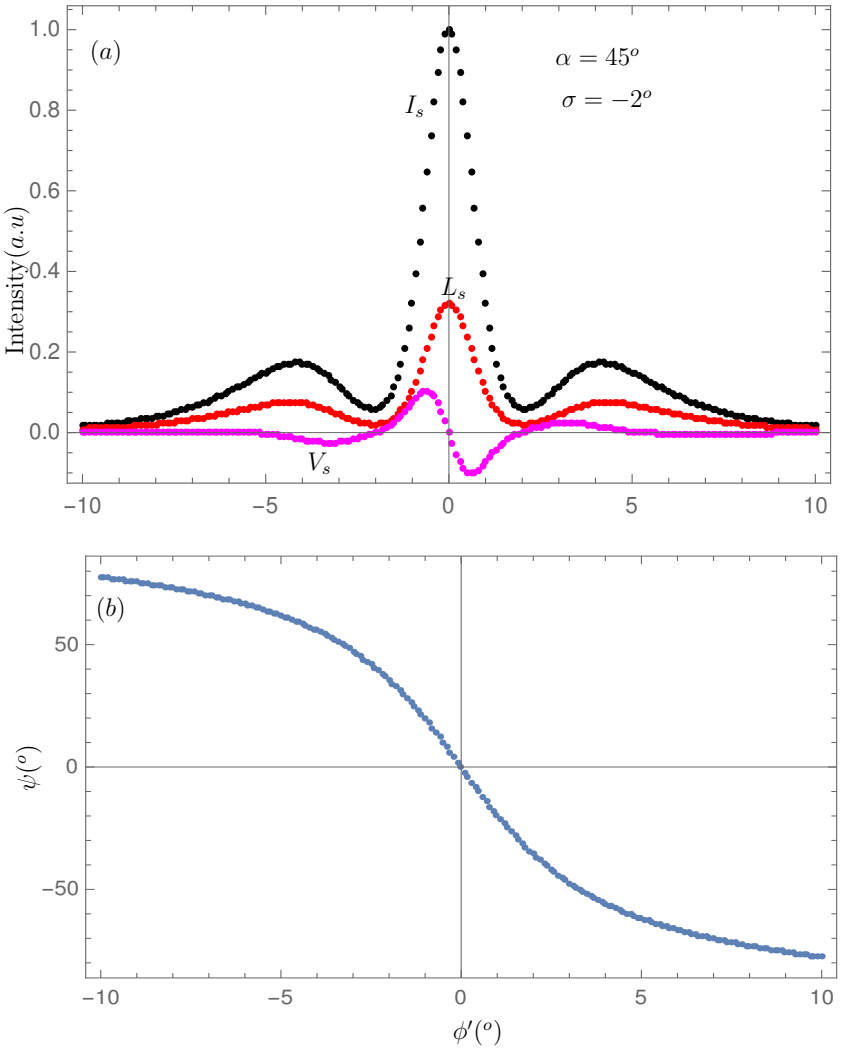

FIGURE 2.12: For panels (a) and (b) $\sigma_\phi = 0.45, 0.32$, $\phi_p = 180^o, 180^o \pm 60^o$, and $f_0 = 1, 0.9$, respectively, are used from the central component to the outer one.

type of circular polarization for both conal and core components have been found to be highly correlated with the polarization angle swing (You & Han 2006).

In most cases, the sense reversal of circular polarization is nearly independent of frequency, suggesting that the circular polarization does not arise from propagation or plasma effects (Michel 1987; Radhakrishnan & Rankin 1990). Radhakrishnan & Rankin (1990) have argued that the circular polarization is an intrinsically anti-symmetric type and correlated with the polarization angle swing. The anti-symmetric circular polarization of curvature radiation becomes significant if there

are gradients in the emissivity over angular scales comparable with the emission cone of a single charge. The results predicted by incoherent curvature radiation model (see figures 2.9-2.12) strongly suggest that the correlation of anti-symmetric circular polarization with the polarization angle swing be geometric property of emission mechanism.

Since this model deals with the steady flow of the relativistic plasma along the dipolar field lines, it is relevant only for average profiles and reflects the well fascinating results which are more geometric dependent. The rotation and plasma effects are not included in this model (Gangadhara 2010). Therefore we can not expect the roles of rotation and plasma effects on the model predicted intensity and polarization of single pulses. However, in the followup works one can see their roles (Kumar & Gangadhara 2012a,b, 2013). By considering the antenna mechanism, Buschauer & Benford (1976) have derived a formalism for relativistic curvature radiation. However, the treatment given does not include the detailed geometry of dipolar field lines and the estimation of polarization, particularly circular. Since radiation from many bunches is superposed on any given pulse longitude, the circular polarization of different signs and magnitudes is added. The result of such an addition could be the reason for the diversities in the observed circular polarization.

2.5 Conclusion

By taking into account a detailed geometry of dipolar magnetic field lines, we have derived the polarization state of the incoherent curvature radiation due to relativistic plasma in the pulsar magnetosphere and drawn the following conclusions:

1. Though the radio emission from a single bunch is highly polarized, the net

emission from several bunches within the beaming region becomes less polarized due to an incoherent superposition of radiation fields.

2. The incoherent curvature radiation has basically an anti-symmetric type of circular polarization.

3. Based on the Stokes parameters of the curvature radiation, we have deduced the polarization angle swing and it is found to be consistent with the rotating vector model.

4. Based on the incoherent curvature radiation, the anti-symmetric type of circular polarization and its correlation with the polarization angle swing is revealed. Observationally such correlations have been found for many pulsars.

5. The addition of circular polarization with different signs and magnitudes at any given rotation phase could be responsible for the wide diversity in circular polarization across the pulse.

Chapter 3

Radio emission in pulsars due to relativistic plasma

3.1 Introduction

Pulsars are highly magnetized ($B \approx 10^8 - 10^{13}$ G), highly gravitating and highly compact (interior density is comparable to nuclear density or even higher) rotating neutron stars. They are expected to take birth in supernovae remnants, e.g., Crab and Vela pulsars. Most of them emit electromagnetic radiation in the form of periodic radio signals with periodicity exactly equal to the rotation period of pulsar. Pulsar radiation is coherent, highly polarized and variable in single pulses. There are at least two valid logics to trust this: (i) The brightness temperature in radio band of pulsar ranges from 10^{25} to 10^{42} K, and (ii) the signal shows erratic nature on a time scale far faster than the pulse width (Ginzburg & Zhelezniakov 1975). Later on the more convincing model of polar gaps, sparks and microwave radiation came out for explaining the observed radio luminosity and the various properties

of integrated pulse profile shapes, polarization etc (Sturrock 1971; Ruderman & Sutherland 1975).

Coherent synchrotron radiation has been proposed as one of the possible high energy emission mechanisms in pulsar. The lifetime of synchro-electron/positron is shown to be $t_{\rm sph} \approx E_{\rm sph}/\dot{E}_{\rm sph} = (\gamma_{\rm p} m_{\rm e} c^2)/P$, where $\gamma_{\rm p} \approx 10^6$ is Lorentz factor of primary plasma, $m_{\rm e}$ and q are electron mass and charge, c the light velocity, and $P = (2/3)^2 r_0^2 c \beta^2 \gamma_{\rm p}^2 B^2$ the power radiated by the primary plasma. The classical electron radius $r_0 = q^2/(m_e c^2) \sim 10^{-13}$ cm, and β is the velocity factor of primary plasma particles (Rybicki & Lightman 1985). In the huge ambient magnetic field, the synchrotron-photons (γ-ray) decay into electrons and positrons, and the further pair cascade leads to secondary pair plasma. For $B \approx 10^{12}$ G and the Lorentz factor of primary plasma $\gamma_{\rm P}$ which ranges from 10^3 to 10^6 we get the life time of synchrotron photon $\sim 10^{-22}$ s which is too short. Hence the plasma particles dissipate away their perpendicular component of momentum very quickly, and thus they hardly continue gyrating around the magnetic field lines. Therefore the motion of plasma particles almost becomes one dimensional and curved, which may be approximated with bead-on-wire motion.

Most of the emission models claim that the source of radio emission is due to the secondary pair plasma and place the origin in the inner magnetosphere. Based on observations, several authors (e.g., Cordes 1979) believe that coherent curvature radiation is a promising radio emission mechanism. However the emission by bunches has been criticized by Melrose et al. (1981) for it's failure to explain the bunch formation mechanism and stability. However, the coherent curvature radiation does not require that coherence due to bunching. Benford & Buschauer (1977) have shown that the two-stream instability is the most favorable plasma process, which dominates over all other plasma mechanisms in pulsar. They have also said that the other type of instabilities like beam-plasma instability, does not grow rapidly enough to produce appreciable bunching so as to reach the observed

radio luminosity of pulsar. According to Benford & Buschauer (1977) the plasma is perturbed by plane waves and simple electrostatic streaming instability drive the electron-positron plasma into a phased array of antennae. They have also conjectured that the high frequency steepening of luminosity curve as a function of frequency arising from linear growth near the pulsar while the low frequency turnover appears when relativistic plasma energy density exceeds the dipolar field energy density, rather than from self-absorption.

Pulsars are known to be highly polarized among all the known radio sources (Gould & Lyne 1998) and individual pulses sometimes show 100 percent polarization. Using a well-calibrated polarimeter one can observe pulsars and construct a full set of Stokes parameters. The percentage of polarization can significantly vary depending upon the sampling time as well as the observing frequency (e.g., Gangadhara et al. 1999). The high frequency ($\gtrsim$ 5 GHz) profiles usually show a diminish in the degree of linear polarization (Manchester 1971; Xilouris & Kramer 1996). Generally the polarization angle (PA) exhibits a smooth swing with respect to the rotation phase, like "S" shaped curve. This behavior was first interpreted by Radhakrishnan & Cooke (1969) in their rotating vector model (RVM). We normally fit the observed PA data with the RVM model to obtain the magnetic axis inclination angle α and line-of-sight impact parameter σ. However, the method does not give unique values in most cases. Hence constraining the geometry with the RVM leads to large uncertainties sometimes. Thus it does not really help to get confident estimates about the angles involved.

The circular polarization in pulsar radio profiles is an important property of the radio emission mechanism. Basically we observe two types of circular polarization namely anti-symmetric type and symmetric type. The anti-symmetric type circular polarization is found to be correlated with the PA angle swing (Radhakrishnan & Rankin 1990; Han et al. 1998; Gangadhara 2010). Another intriguing

phenomenon in pulsar polarization is orthogonal mode switching. From the observational study of single pulses it was shown that several sources exhibit rapid jumps ($\sim 90^{\circ}$) in their position angle swing (Manchester et al. 1975; Backer & Rankin 1980). Such discontinuities in PA are believed to arise due to the presence of two orthogonal polarization modes. The jump from one "S" curve to another happens when one polarization mode dominates over the other Gangadhara (1997). Circular polarization also shows a similar type of jumps between left-handed and right-handed or vice versa senses (Cordes et al. 1978).

For pulsars with well-ordered position angle swing and periods between 0.06 and 3.7 seconds it is possible to estimate the radio emission height, and found to be not more than 2000 km in the frequency range of 0.43 to 1.4 GHz (e.g., Blaskiewicz et al. 1991; Gangadhara & Gupta 2001; Gupta & Gangadhara 2003). They have also shown that the higher frequency radio emission comes from lower altitude compared to that at a lower frequency. By developing a relativistic-phase shift method for estimating pulsar radio emission altitude, Gangadhara (2005) has confirmed the above results, and also shown that emission at any given frequency do not come from the same altitude across the pulse window.

In literature several mechanisms have been suggested for pulsar radio emission, which can be broadly classified into three groups: (i) plasma antenna mechanisms (Benford & Buschauer 1977), (ii) maser amplification (Luo & Melrose 1992; Melrose 1978; Kazbegi et al. 1991b) and (iii) relativistic plasma instabilities (Asseo et al. 1990; Asseo & Porzio 2006). Maser emission mechanism has been proposed as an alternative source of pulsar radiation, which is interpreted as negative absorption. Suppose a low amplitude electromagnetic wave (EM) is launched very near to polar cap and start propagating along our line of sight. Now if several discrete set of columns, filling with negative absorption coefficient materials, are arranged along the propagation direction of EM wave, then EM waves get amplified due to the transferred of energy from particle free energy, i.e., from counter-streaming

beams; so it is not substantially different from the two-stream instability. Again different types of maser mechanism have been suggested: among them the two prominent ones are (i) free electron maser (Melrose 1989; Rowe 1995), and (ii) emission driven by curvature drift instability (e.g., Luo & Melrose 1992).

The rotationally induced electric field $\vec{E}$ does have some non-zero component along the open magnetic field line, i.e., $\vec{E} \cdot \vec{B} \neq 0$. Therefore the induced electric field accelerates charged particles and produces curvature photons. Radio emission of a pulsar is generated from secondary plasma whose detailed description is given by Gurevich et al. (1993). The basic curvature radiation model was developed by Sturrock (1971) and Ruderman & Sutherland (1975), and including the relativistic effects by Blaskiewicz et al. (1991).

Later Gangadhara (2010) developed the incoherent curvature radiation model by including the detailed viewing geometry and the modulation effect, and simulated pulse profiles by integrating over the emission region. Further the perturbation effects like aberration-retardation and polar-cap current effects were successfully introduced in this theoretical model to explain the observed asymmetry in the phase location of trailing and leading side components relative to the core (Kumar & Gangadhara 2012a,b, 2013; Wang et al. 2012). In their single-particle model the full set of Stokes polarization profiles were simulated for a given set of geometrical parameters: α (inclination of magnetic axis with the rotation axis), σ (line of sight impact parameter) and $r_{\rm e}$ (dipolar field line constant of magnetic field). But the incoherent curvature radiation is not worthy enough to explain the high brightness temperature of pulsars $10^{20} - 10^{25}$ K (Cordes 1979). A model for the coherent radio emission by relativistic plasma bunch accelerated along a curved trajectory is developed by Sturrock (1971) and Buschauer & Benford (1976). However they have not taken into account the viewing geometry in a dipolar magnetic field line topology and lack with the polarization details: linear and circular polarizations. Hence there is a strong need to develop the coherent curvature radiation model

which can produce polarization and explain the observations.

In this chapter we develop a model for pulsar radio emission due to collective plasma emission, and estimate the polarization and brightness temperature. The contents of this chapter was published by Roy & Gangadhara (2019). We consider the actual dipolar magnetic field lines in a slowly rotating (non-rotating) magnetosphere such that the rotation effects can be ignored. In section 3.2 we have discussed the basic idea of the proposed model, and given the relevant details of viewing geometry with details mathematical description for the simulation of pulse profiles. Transformation of electric field to neutron star origin's frame is given in section 3.3. Neutron star origin's frame is a stationary laboratory frame i.,e, the observer frame-xyz (see Figure 3.1) such that it's origin is at the center of neutron star. Neutron star spins about it's rotation axis $\hat{\Omega}$ which is parallel to the z-axis. In section 3.4 the computation of emission region is shown, and in section 3.5 we have depicted the simulated pulse profiles. In section 3.10 estimated the typical brightness temperature of pulsars. Finally we have ended up with a discussion in section 3.11 and a conclusion in section 3.12.

3.2 Collective plasma radio emission

Observations suggest that the radio emission of pulsars is coherent and highly polarized. The typical brightness temperature of pulsars range from 10^{25} to 10^{32} K in normal radio emission. However, Hankins & Eilek (2007) by making high time resolution (0.4 ns) observations, have captured giant nanoshots from Crab pulsar, and their brightness temperature can reach as high as 10^{42} K. Radio emission of pulsar is believed to originate from polar cap region, whose boundary is demarcated by the foot-print of last open field lines. The ultra-strong magnetic field of

pulsar induces large electric field of the order 10^{11} to 10^{12} V cm^{-1} due to rotation. This large electric field pulls out charged particles from neutron star surface gearing up primary particles motion along open curved magnetic field lines, it results in an acceleration and produce curvature radiation. The curvature radiation (γ-ray) photons produce secondary pair plasma by pair cascade process. The typical Lorentz factor γ of the secondary plasma is expected to be around 10–1000 (Ruderman & Sutherland 1975; Gil 1983; Lyubarskii & Petrova 2000; Gedalin et al. 2002; Gangadhara 2004). Physicists believe that the generation of pulsar radio emission is mainly originated from the secondary pair plasma or soliton-like charge clumps with smaller transverse dimension, whose power spectrum corresponds to very high brightness temperature in the radio-band. Some literature suggest that modulation instability can be one of the promising mechanism for bunch formation in pulsar magnetosphere, but still now it is a paradox, as there is no entirely understandable theory, which can explain both bunch formation mechanism as well as stability. However, bunches need not to be stable for longer time, they only need to last for time $\delta t \sim 1/\nu$ for 10 MHz $\leq \nu \leq$ 10 GHz in normal pulsars and 100 GHz or more for magnetars.

The collective radio emission due to relativistic plasma constrained to move in dipolar magnetic fields has been suggested to explain the high brightness temperature of pulsars and their polarization properties. When the mean free path of radiating particles is much less than the emitted radiation wavelength, the emissions can be treated as collective emission (Rybicki & Lightman 1979). In chapter 2, we discussed curvature emission from single particles and spherical bunches with size less than the wavelength of the emitted radio waves. In that simple picture we get an enhanced radiation, which is $\sim N^2$ times the intensity of single particle curvature emissions, where N is the number of co-operating particles in a plasma bunch.

3.2.1 Radio emission from a cylindrical bunch

Consider a cylindrical bunch as shown in figure 3.1, constrained to move along the dipolar field line. Plasma bunches and waves are expected to build up due to an instability process (e.g., two stream instability). We basically assume that the growth and decay of longitudinal plasma waves can happen within the bunch medium. Due to the building up of waves by wave-wave interactions, the plane waves will attain a steady non-linear state and finally they partially get converted into large amplitude transverse EM waves and low amplitude longitudinal waves. The derivation of electric field of radio waves emitted collectively by bunched plasma is given in section 3.7. The list of symbols appearing in this chapter are listed in Appendix A.

We make the the following assumptions:

1. Mean free path of constituent particles of plasma bunch is much less than the emitted radio wavelength λ_0.

2. Plasma in the bunch (see figure 3.1) can support growth and decay of the longitudinal waves. We assume that the transverse dimensions of bunch ξ_0 and η_0 are much less than λ_0. The plasma waves are confined within the bunch even after traversing distance by one unit or integer multiple number of wavelength of longitudinal waves, and find themselves in phase. In another words they behave like a phased array antenna, correlated in phase and emit EM waves coherently (Benford & Buschauer 1977). But no restriction on the S_0 (bunch length) in principle, i.e., it could be either smaller or larger than the emitted wavelength. Plasma bunch with bigger length intuitively helps to accommodate integer multiple number of plasma waves and hence build up waves to large amplitude by wave-wave interaction. The visibility

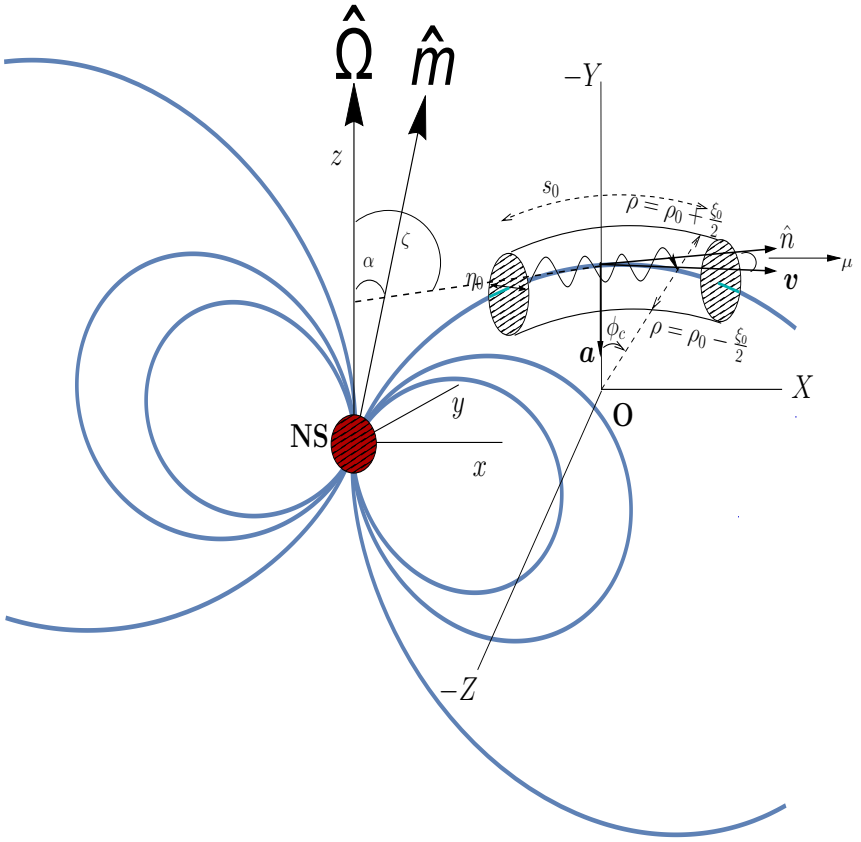

FIGURE 3.1: Geometry for collective plasma radio emission from a cylindrical bunch in pulsar magnetosphere. The Cartesian coordinate system-xyz is the observer frame whose origin is at the center of NS. $\hat{m}$ is the magnetic axis which is inclined by an angle α with respect to spin axis $\hat{\Omega}$. The line of sight of observer is $\hat{n}$. The bunch dimensions (s_0, ρ_0, η_0) are the length, radius and height, respectively. ξ_0 is the radial width of bunch, and ϕ_c is the angle subtended by the position vector of an arbitrary point in the bunch with respect to Y-axis. $\vec{v}$ and $\vec{a}$ are the center of momentum (CM) velocity and acceleration of the bunch. The Cartesian coordinate system-XYZ is chosen in such way that X-axis is parallel to the line of sight $\hat{n}$, $-Y$-axis is parallel to the curvature vector $\hat{k}_{\rm t}$ and $-Z$-axis parallel to the bi-normal $\hat{b}_{\rm nt}$.

of the angular span of bunch gets restricted by relativistic beaming effect, we can see up to angular span of $2/\gamma$ only.

3. The cylindrical beam plasma is charge neutral and non-relativistic in the beam frame, but it is highly relativistic in the laboratory frame.

4. Changes in the radius of curvature of the field lines are negligible during the time of beamed radiation received by the observer.

5. Plasma motion is described by current density and charge density perturbations, which hold the form of sinusoidal functions of space and time. Actually this assumption has significance in the following limit: whole bunch is behaving like a fluid and flowing with some average velocity. The sinusoidal oscillation of plasma makes the particles to radiate collectively in phase.

6. We represent the plasma motion as plane waves. Realistically it has implication in two limits: (a) linear growth rate of the wave is very low and (b) due to wave-wave or wave-particle interaction linear growth of phase attain a steady non-linear state. Finally the non-linear wave dissipates and partially gets converted into electromagnetic waves.

7. We assume that plasma bunches possess cylindrical symmetry for simplicity of calculation.

3.3 Transformation of electric field to laboratory frame

By assuming pulsar or neutron star magnetic field is dipolar, as evident from observations, Gangadhara (2004) has derived the expression of tangent and curvature vectors of magnetic field lines at the emission point in his tangent model by adopting the following conditions:
(i) Curvature radiation is emitted along magnetic field line tangent, (ii) For receiving radiation observer's line of sight has to be aligned along the field line tangent. In real case of pulsars, magnetic axis is tilted by an angle α with respect to rotation axis and rotated by angle ϕ'. The expression of tangent vector and curvature vector are derived in magnetic axis frame by using spherical-polar co-ordinates and Cartesian geometry. Then by operating tilt and rotation matrices successively on the aforementioned vector quantities, they are transformed to rotation axis frame

(lab frame). The details of radio emission geometry of pulsar are given in Gangadhara (2004, 2010). But for the sake of completeness, we only give the expression of curvature vector and bi-normal vectors in rotation axis centered frames. Respective symbols used to represent unit tangent vector, unit curvature vector and unit bi-normal vector in rotation axis centered frame are $\hat{b}_{\rm t}$, $\hat{Y} = \hat{k}_{\rm t}$, $\hat{\epsilon} = \hat{b}_{\rm nt} = \hat{b}_{\rm t} \times \hat{k}_{\rm t}$ respectively. The expression of unit curvature vector and unit bi-normal vector appearing in Equations (3.38) and (3.39) are mentioned below,

$$\hat{Y} = \{k_{t1},\, k_{t2},\, k_{t3}\}, \quad \hat{\epsilon} = \{b_{\rm nt1},\, b_{\rm nt2},\, b_{\rm nt3}\}, \tag{3.1}$$

where

$$k_{\rm t1} = \frac{\cos\alpha\cos\phi\cos\phi'(1+3\cos(2\theta)) - 6\cos\theta\sin\alpha\sin\theta\cos\phi' - (1+3\cos(2\theta))\sin\phi\sin\phi'}{\sqrt{10+6\cos(2\theta)}},$$

$$k_{\rm t2} = \frac{\sin\phi\cos\phi'(1+3\cos(2\theta)) + \sin\phi'(\cos\alpha\cos\phi(1+3\cos(2\theta)) - 6\cos\theta\sin\theta\sin\alpha)}{\sqrt{10+6\cos(2\theta)}},$$

$$k_{\rm t3} = -\frac{((1+3\cos(2\theta))\sin\alpha\cos\phi + 6\cos\alpha\cos\theta\sin\theta)}{\sqrt{10+6\cos(2\theta)}},$$

$$b_{\rm nt1} = -\cos\alpha\sin\phi\cos\phi' - \cos\phi\sin\phi',$$

$$b_{\rm nt2} = \cos\phi\cos\phi' - \cos\alpha\sin\phi\sin\phi',$$

$$b_{\rm nt3} = \sin\alpha\sin\phi.$$

Here ϕ' is the rotation phase or pulse longitude, α is the magnetic axis inclination, θ the magnetic colatitude, and ϕ the magnetic azimuth.

The radius of curvature of dipolar magnetic field lines is given by

$$\rho_0 = (1/12) r_e \sin\theta \sqrt{(10+6\cos(2\theta))^3/(3+\cos(2\theta))^2}.$$

The expressions of θ and ϕ are taken from Gangadhara (2004) to simulate the pulse profiles. Using the bi-normal and curvature vectors in the xyz-frame, the

electric field in the neutron star origin's frame can be expressed as

$$\vec{E}_{\rm NS} = \{E_{\rm cf\parallel}k_{\rm t1} + E_{\rm cf\perp}b_{\rm nt1},\quad E_{\rm cf\parallel}k_{\rm t2} + E_{\rm cf\perp}b_{\rm nt2},\quad E_{cf\parallel}k_{\rm t3} + E_{\rm cf\perp}b_{\rm nt3}\}. \tag{3.2}$$

Then we have to find the components of $\vec{E}_{\rm NS}$ in the plane of the sky. The projected spin axis on the plane of sky is $\hat{\epsilon}_{\parallel} = \hat{\Omega}_{\rm p} = \{-\cos\zeta, 0, \sin\zeta\}$ and $\hat{\epsilon}_{\perp} = \hat{\epsilon}_{\parallel} \times \hat{n}$ is perpendicular to $\hat{\epsilon}_{\parallel}$ in the plane of sky. Therefore we have

$$E_{\parallel} = \hat{\epsilon}_{\parallel} \cdot \vec{E}_{\rm NS} \tag{3.3}$$

$$E_{\perp} = \hat{\epsilon}_{\perp} \cdot \vec{E}_{\rm NS}. \tag{3.4}$$

The Stokes parameters are constructed below by using Equations (3.3) and (3.4):

$$\begin{aligned} I &= E_{\parallel}E^*_{\parallel} + E_{\perp}E^*_{\perp}, \quad Q = E_{\parallel}E^*_{\parallel} - E_{\perp}E^*_{\perp} \\ U &= 2{\rm Re}[E^*_{\parallel}E_{\perp}], \quad V = 2{\rm Im}[E^*_{\parallel}E_{\perp}]. \end{aligned} \tag{3.5}$$

The linear polarization and polarization angle (PA) are defined as $L = \sqrt{Q^2 + U^2}$ and $\psi = (1/2)\tan^{-1}(U/Q)$, respectively.

3.4 The emission region computation

The relativistically beamed emissions due to collective emission from plasma bunches adds up to form pulsar main beam of radiation, which sweeps past the observer in each cycle of rotation. The half beam opening angle of the emission from individual particles is $\theta_b \sim 1/\gamma$. In Figure 3.2 for $\alpha = 10^\circ$ and $\sigma = 5^\circ$ we have presented the emission region within $1/\gamma$ at rotation phase $\phi' = 0^\circ$ of the magnetic axis. Using Equations (8) and (28) from Gangadhara (2010), we have estimated the emission region: Figure 3.2a for emission in magnetic axis centered frame and Figure 3.2b for the corresponding region in rotation axis centered frame, and hence estimated

the resultant or net contributed intensity by integrating over the emission region. By choosing a grid of size of 100×100 on $2/\gamma$ region, we have estimated the emission region presented in panels (a) and (b) of Figure 3.2.

We observe that due to geometric effects the emission regions in rotation axis centered frame are smaller in (Θ, Φ) plane compared to the corresponding regions in (θ, ϕ) plane of magnetic axis centered frame. In Figure 3.4 we have shown the distribution of center of emission region points throughout the entire pulse longitude for both magnetic axis and rotation axis centered frames. From Figure 3.4 we can see that distribution pattern of emission region's center points, in rotation axis frame got reversed with respect to the magnetic axis frame, due to geometrical mapping. Owing to compatibility of notation according to Equation (1) as given by Gangadhara (2005), we have replaced Θ by θ' while plotting emission regions boundary in Figure 3.2b. For the sake of completeness we have given the formulation for the transformation of emission region from magnetic axis centered frame to rotation axis centered frame in section 3.6. We observe that when α is small the emission regions in both the frames looks nearly same whereas when α is large the emission region in rotation axis centered frame (lab.) becomes smaller than that in magnetic axis centered frame, and it is evident from Equations 3.10 and 3.11. It is an effect of geometric mapping on the emission region in the (θ, ϕ)-plane of magnetic axis centered frame to the corresponding region in the (Θ, Φ)-plane of rotation axis centered frame. The rotation axis is always perpendicular to equatorial plane of pulsar whereas the magnetic axis is inclined.

The radius of curvature of field lines at the emission point are plotted in Figure 3.5 for different α: panel (a) is for positive σ, and panel (b) for negative σ. Though the difference between the panels (a) and (b) is minimal at $\sigma = \pm 2^\circ$ but increases at $|\sigma| \geq 5^\circ$. According to Ruderman & Sutherland (1975)'s polar cap model, the electric field due to curvature radiation is inversely proportional

to radius of curvature of magnetic field lines. Hence the profiles for negative σ becomes broad compared to those for positive σ. In addition to geometric effects, (i) coherence variations, (ii) radiation reaction and (iii) intermittency of the polar cap currents and their particle compositions are also expected to play major roles in the pulsar radio emission.

3.5 Simulation of pulse profiles

We have simulated pulse profiles with the help of Equations (3.3) and (3.4) and the formulae for pulsar radio emission geometry given by Gangadhara (2004) and Gangadhara (2010). For simulation the chosen bunch length is $S_0 \approx 30\% r_{\rm LC}$ and transverse dimensions $\xi_0 = \eta_0 = 12$ cm, and $\mu = 0^\circ$. The current density is 10^{14} esu cm^{-2} s^{-1}, plasma density in co-moving frame $n' = 1.24 \times 10^{10}$cm^{-3}, and the corresponding density in lab frame is $n_{e0} = \gamma n' = 6.94 \times 10^{12}$cm^{-3} for Lorentz factor $\gamma = 560$, and evolves with altitude as $n_e(r) = n_{e0}(r_{\rm NS}/r)^3$. The light cylinder radius $r_{\rm LC}$ =4.7$\times 10^9$ cm for pulsar with period 1 s, which is at distance $R = 1$ kpc. The plasma wave frequency $\omega_0 = 6.2 \times 10^9$ rad s^{-1} and wave number $k_0 = 2\pi/\lambda_0$, and $\lambda_0 = 30$ cm. In the comoving frame the plasma wave frequency is $\omega_0' = 4\pi \times 10^4$ rad s^{-1}, and it's phase velocity $\omega_0'/k_0' = 3.43 \times 10^4$cm s^{-1}.

We have simulated pulse profiles for different geometrical parameters α, σ and field line constant $r_{\rm e}$, and shown in Figures 3.6 to 3.9. For smaller α pulse profiles are usually broad compared those at larger α because the radius of curvature encountered by the line of sight is smaller at smaller α as evident from figure 3.5a. The radio emission intensity is roughly inversely proportional to square of ρ (Ruderman & Sutherland 1975). Another main noticeable features of pulse profiles is that they show broadening for negative σ compared to positive σ for the same α and $r_{\rm e}$ combinations. This is evident from Figure 3.5b, as the curves become

more flat compared to panel 3.5a, for same α and $r_{\rm e}$ combinations. Since the parameters I and L are inversely proportional to square of radius of curvature, the Stokes profiles corresponding to negative σ does not fall quickly. For negative σ, line of sight gets aligned with tangent vector at smaller polar angle θ, which corresponds smaller height, hence smaller radius of curvature. Again for smaller α with same set of σ and $r_{\rm e}$ (see Figure 3.5a), slope of radius of curvature profiles are less, hence smaller α generates sporadically broadened pulse profiles as I and L are inversely proportional to square of radius of curvature. When the field lines are viewed edge on the circular polarization goes to zero.

By treating μ, the angle between plane of field line and line of sight, as a free parameter and choosing bunch length $S_0 = 20\%$ of $r_{\rm LC}$, and the transverse dimensions are $\xi_0 = \eta_0 = 3$ cm, phase $\phi' = 0^\circ$ and rest of the parameters same as mentioned above, we have generated pulse profiles, and plotted in Figures 3.10 and 3.11. We observe the sign change of circular polarization when line of sight cuts the plane of magnetic field lines, is determined by the sign of σ, i.e, whether line of sight impact angle is negative or positive.

By considering multiple bunches at different rotation phases simulated multi-component pulses profiles and plotted in Figures 3.12 - 3.15. Using $\alpha = 10^\circ$, $\sigma = 5^\circ$, $\mu = -0.007^\circ$, $r_e = 20 r_{LC}$, bunch length $S_0 = 30\% r_{\rm LC}$ and transverse dimensions $\xi_0 = \eta_0 = 3$ cm, a triple component profile is simulated and presented in Figure 3.12. The bunch emitting core component is chosen at $\phi' = 0^\circ$, and the conal outriders at $\phi' = \pm 75^\circ$ and field line constant is $r_e = 18\ r_{\rm LC}$. The bunch length chosen for sub-pulse component is 0.3 times the bunch length corresponding to core component. Chosen transverse dimensions for sub-pulse is same as main pulse component. Rest of the other parameters chosen are same as in Figure 3.6. These profiles are similar to single pulses in pulsar observations when the line of sight encounters field lines at any arbitrary values of μ. Similarly in Figure 3.13 a triple components profile is presented for $\alpha = 10^\circ$, $\sigma = -5^\circ$ and $\mu = 0.007^\circ$.

Similarly simulated five component profiles and plotted in Figures 3.14 and 3.15.

The pulse profiles in Figures 3.16 - 3.19 are simulated by integrating over emission region as well as over μ within $\pm 1/\gamma$ region to include the net emission coming from all those field lines from the polar cap which contribute to beaming effect. Figures 3.16 and 3.17 show one component pulse profiles whereas Figures 3.18 - 3.19 show three component pulse profiles. For producing three component profiles we have used three individual coherent sources separated in phase by $\pm 12^{\circ}$ with respect to meridional plane. It is also interesting phenomenon to see that our simulated pulse profiles shows a low degree of symmetric type circular polarization, which is induced intrinsically by the modulation effect of the bunch. In coherent case it might be the expected scenario because, cylindrical shaped bunch is encompassed by series of parallel magnetic field lines to maintain the coherence condition. As the field lines are parallel and spaced compactly, the electric fields align in the direction of curvature vector and add up in phase. In other words magnetic field lines adjacent to the center of momentum of bunch are behaving like a single entity for coherent case although they are collective in nature. So observer will find maximum circular polarization near to center of bunch and slowly it will decrease along the side of bunch boundary, as field lines start deviating from strict parallelism.

However in the weak coherence regime each individual field line will behave like a single entity and circular polarization profiles resemble as Figures 3.10 and 3.11. In the region where magnetic field lines are not parallel to each other emission will be in the weak coherence limit. So it is expected that circular polarization profile to be same as incoherent curvature radiation case. In the coherent radiation limit observer will not able to separate two subsequent planes of magnetic field lines individually but for incoherent case observer can distinguish it. We know in the case of incoherent curvature radiation, circular polarization do show anti-symmetric nature mostly (Gangadhara 2010) and some cases it switches to

single sense depends upon the perturbation effects such as aberration-retardation (Kumar & Gangadhara 2013).

3.6 Formulation of the emission region in rotation axis frame

Here we have shown the transformation of magnetic colatitude (θ) and magnetic azimuth (ϕ) from magnetic axis frame to rotation axis frame. It is well known that magnetic dipole field lines are governed by the field line equation:

$$r = r_{\rm e} \sin^2 \theta, \tag{3.6}$$

where $\rm r_e$ is di-polar field line constant and θ is polar angle and r the distance from the origin. The parameter $r_{\rm e}$ is the field line constant, which is a distance from origin to the point of field line intersection with the magnetic equatorial plane, which is at $\theta = \pi/2$. Since the values of r_e exceeds the light cylinder radius, it may be redifined as $r_{\rm e} = r_{\rm NS}/\sin^2(\theta_{\rm NS})$, where r_{NS} is the neutron radius and $\theta_{\rm NS}$ is the polar angle at the surface of neutron star (NS). The position vector of an arbitrary point on the magnetic field line in magnetic axis frame is

$$\vec{r} = r\{\sin\theta\cos\phi,\ \sin\theta\sin\phi,\ \cos\theta\}. \tag{3.7}$$

Now for the magnetic axis is rotated and inclined with respect to rotation axis by angles ϕ' and α, respectively, we construct a matrix Λ, which is product of rotation matrix ($\rm M_{rot}$) and inclination matrix ($\rm M_{inc}$). The details of rotation and inclination matrix again can be found in Gangadhara (2004). In order to get an expression of position vector in rotation axis frame, we have to multiply

Equation (3.7) with $\Lambda = M_{\rm rot} \cdot M_{\rm inc}$. So we get

$$\vec{r}_{\rm b} = \Lambda \cdot \vec{r} = r\{r_{\rm bx},\, r_{\rm by},\, r_{\rm bz}\}, \tag{3.8}$$

where

$$r_{\rm bx} = \cos\theta \sin\alpha \cos\phi' + \sin\theta(\cos\alpha \cos\phi \cos\phi' - \sin\phi \sin\phi'),$$

$$r_{\rm by} = \sin\theta \sin\phi \cos\phi' + \sin\phi'(\cos\theta \sin\alpha + \cos\alpha \cos\phi \sin\theta),$$

$$r_{\rm bz} = (\cos\alpha \cos\theta - \cos\phi \sin\alpha \sin\theta).$$

In analogy we can define the position vector in the rotation axis frame as

$$\vec{r}_{\rm rot} = r\{\sin\Theta\cos\Phi,\, \sin\Theta\sin\Phi,\, \cos\Theta\}, \tag{3.9}$$

where $(\Theta,\, \Phi)$ are the co-latitude and azimuth in rotation axis frame. Now Equations (3.8) and (3.9) both represent the same quantity, i.e., $\vec{r}_{\rm b} = \vec{r}_{\rm rot}$. So by equating the vector components of Equations (3.8) and (3.9), and doing some algebraic manipulations, we get

$$\cos\Theta = \cos\theta' = \cos\alpha\cos\theta - \cos\phi\sin\alpha\sin\theta, \tag{3.10}$$

and

$$\tan\Phi = \frac{\cos\phi'\sin\theta\sin\phi + \cos\theta\sin\alpha\sin\phi' + \cos\alpha\cos\phi\sin\theta\sin\phi'}{\cos\theta\cos\phi'\sin\alpha + \cos\alpha\cos\phi\cos\phi'\sin\theta - \sin\theta\sin\phi\sin\phi'}. \tag{3.11}$$

These two Equations (3.10) and (3.11) are used for simulating emission regions in the rotation axis centered frame. The derivation of radio emission height from geometrical point of view is given in Appendix B.

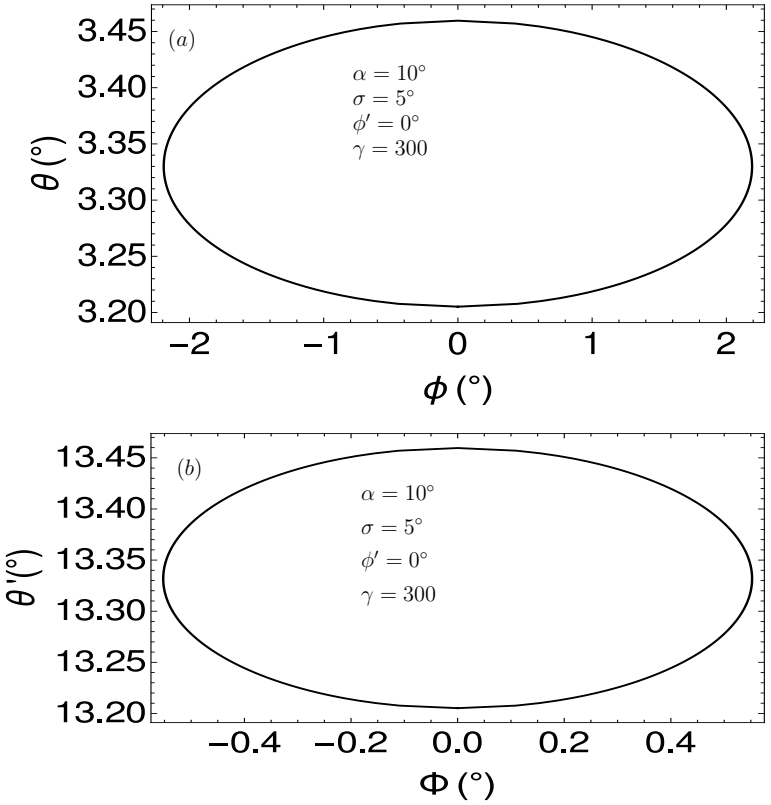

FIGURE 3.2: Emission regions having angular radius $\sim 1/\gamma$ centered on line of sight, which is at $\phi' = 0°$: panel (a) for magnetic axis centered frame and panel (b) for rotation axis centered frame (lab).

3.7 Derivation of Electric field of radio waves emitted by plasma

Consider a relativistic plasma bunch accelerated along dipolar magnetic field lines of neutron star emitting radio waves due to a collective plasma process. To model the radio emission we consider three Cartesian coordinate systems: xyz, XYZ and $x'y'z'$. The co-ordinate system-xyz is the stationary laboratory frame of the observer whose origin is assumed to be at the center of neutron star (NS). The z-axis is aligned along the rotation axis ($\hat{\Omega}$) and the magnetic axis ($\hat{m}$) is inclined with respect to $\hat{\Omega}$ by an angle α. The line of sight $\hat{n} = \{\sin\zeta, 0, \cos\zeta\}$ lies in the xz-plane, where $\zeta = \alpha + \sigma$ is the angle between ($\hat{\Omega}$) and $\hat{n}$, and σ is the impact angle of $\hat{n}$ with respect to $\hat{m}$, as shown in Figure 3.1.

The frame-XYZ is chosen in such a way that the X-axis is parallel $\hat{b}_{\rm t}$, and the XY-plane define the plane of magnetic field line at any given rotation phase ϕ'. The origin of the frame-XYZ is at the local center of curvature of the magnetic field line, whose tangent $\hat{b}_{\rm t}$ aligns with the $\hat{n}$. Note that the analytical formulae for magnetic colatitude θ and magnetic azimuth ϕ (see Gangadhara 2004, Eqs. 9 and 11) uniquely identities the specific tangent $\hat{b}_{\rm t}$ which is parallel to $\hat{n}$ at any given rotation phase of pulsar. The Y-axis is chosen to be parallel to the corresponding curvature vector $\hat{k}_{\rm t}$. Then Z-axis will be parallel to the bi-normal $\hat{b}_{\rm nt} = \hat{b}_{\rm t} \times \hat{k}_{\rm t}$. Hence as the neutron star spins the frame-XYZ reorients in such way that the XY-plane lies parallel to the plane of field line, whose tangent aligns with $\hat{n}$. In the systems-xyz and XYZ the plasma bunch motion is relativistic with center of momentum velocity $\vec{v}$.

Next, the system-$x'y'z'$ is a co-moving frame (rest frame) of the bunch in which the plasma motion is non-relativistic, and it's coordinate axes are chosen in such a way that $x' \parallel X$, $y' \parallel Y$, and $z' \parallel Z$ at time $t = 0$. The frame-$x'y'z'$ is co-moving with velocity $\vec{v}$ along curved magnetic field line as time progresses. As line of sight is a constant vector, we keep it fixed in both the frame-xyz and XYZ. But in order to receive radiation, we make XYZ frame to rotate in such a way that, tangent vector corresponds to each rotation phase subtends an maximum angle $\pm 1/\gamma$ with respect to line of sight. Here γ is the Lorentz factor corresponds to the bulk velocity of collective plasma. To make it more generalized we invoke a very small angle μ (ranges from $-1/\gamma$ to $1/\gamma$), which denotes the angle between line of sight and plane of magnetic field line. So according to our geometry line of sight in XYZ-frame confines in X-Z plane. So we denote the expression of line of sight vector in XYZ-frame as $\hat{n}_{cf} = \{\cos\mu, 0, \sin\mu\}$. Note that $\mu = 0^{\circ}$ is the special case, called edge on position, where specific tangent vector exactly gets aligned with line of sight vector, therefore circular polarization vanishes. So while computing electric field in XYZ-frame, we substituted $\hat{n} = \hat{n}_{cf}$ in order to obtain generalized expression of circular polarization for any orientation. After

transforming the electric field back to xyz-frame one is always free to use the conventional expression of line of sight vector as mentioned in the first paragraph of this particular section. Note that the Equation 3.12 below is applied in XYZ-frame first.

Consider the electric field of radiation due to an accelerated charge given by Jackson (1975):

$$\vec{E}(\vec{r},\, t) = \frac{q}{c}\left[\frac{\hat{n}\times[(\hat{n}-\vec{\beta})\times\dot{\vec{\beta}}]}{R_0\xi^3}\right]_{\rm ret}, \tag{3.12}$$

where q is the charge of particle and c the velocity of light. The velocity and acceleration of relativistic charge are $\vec{\beta}$ and $\dot{\vec{\beta}}$ as fractions of light speed, $\xi = 1-\vec{\hat{n}}\cdot\vec{\beta}$ is the beaming factor, and R_0 is the distance between the center of XYZ frame and observation point. We find the Fourier transform of $\vec{E}(\vec{r},t)$ at the retarded time t' using the relation $t = t' + (R_0 - \hat{n}\cdot\vec{r}_{\rm b})/c$. Then we have the following expression for radiation field due to a collective system of N particles (bunch):

$$\vec{E}_{\rm cf}(\omega) = -i\omega\frac{e^{i\omega R/c}}{\sqrt{2\pi}R_0 c}\sum_{j=1}^{N} q_j\int_{-\infty}^{\infty}(\vec{\hat{n}}\times(\vec{\hat{n}}\times\vec{\beta}))\exp\left\{i\omega\left(t-\frac{\vec{\hat{n}}\cdot\vec{r_b}}{c}\right)\right\}dt. \tag{3.13}$$

If the mean free path of radiating entities in the bunch is much less than the wavelength of the emitted radiation, then the discrete sum can be replaced by continuous integration. For mathematical convenience of defining the bunch dimensions we adopt cylindrical coordinates $(\rho_{\rm cf}, \phi_{\rm c}, \eta_{\rm c})$, where $\rho_{\rm cf}$ is the radial co-ordinate of an arbitrary point of the bunch in cylindrical co-ordinate, $\phi_{\rm c}$ angle subtended between position vector of an arbitrary point in the bunch and negative Y-axes (see Figure 3.1), η the vertical height of the cylindrical bunch. The cylindrical symmetry axis is the Z-axis, which is parallel to the bi-normal $\hat{b}_{\rm nt}$ and perpendicular to the plane of magnetic field line, i.e., the XY–plane. In terms of cylindrical co-ordinates the position vector $\vec{r}_{\rm c}$ of an arbitrary point inside the

bunch with respect to the origin O, and the local direction of motion $\hat{e}_{\phi \rm c}$ are given by

$$\vec{r}_{\rm c} = \{\rho_{\rm cf}\sin(\phi_{\rm c}),\, -\rho_{\rm cf}\cos(\phi_{\rm c}),\, \eta\}, \tag{3.14}$$

$$\hat{e}_{\phi \rm c} = \{\cos(\phi_{\rm c}),\, \sin(\phi_{\rm c}),\, 0\}, \tag{3.15}$$

By making the substitutions: (i) $\sum_{i=1}^{N} q_i = \int\int\int \sigma_{\rm cf}\rho_{\rm cf} d\rho_{\rm cf} d\phi_{\rm c} d\eta$ and (ii) $\sigma_{\rm cf}\vec{\beta} = (J/c)\,\hat{e}_{\phi c}$, where $\sigma_{\rm cf}$ is the charge density, J is the current density and $\hat{e}_{\phi \rm c}$ is the local direction of motion of plasma particles, into Equation (3.13) we get

$$\vec{E}_{\rm cf}(\omega) = -i\omega \frac{e^{i\omega R/c}}{\sqrt{2\pi} R_0 c^2} \int\int\int \rho_{\rm cf} d\rho_{\rm cf} d\phi_{\rm c} d\eta \int_{-\infty}^{\infty} (\hat{n}\times(\hat{n}\times\vec{J})) \exp\left\{ i\omega \left(t - \frac{\hat{n}\cdot\vec{r_{\rm b}}}{c} \right) \right\} dt, \tag{3.16}$$

where $\vec{J}$ is the current density in the coordinate system-XYZ. We assume that the current density and the charge density in co-moving frame–$(x'y'z')$, possess the following sinusoidal forms:

$$J' = J'_0 \sin(k'_0 x' - \omega'_0 t'), \quad \sigma' = \sigma'_0 \sin(k'_0 x' - \omega'_0 t'). \tag{3.17}$$

The phase of the longitudinal wave $k'_0 x' - \omega'_0 t'$ is a Lorentz invariant quantity. Therefore using Lorentz transformation and continuity equation $\nabla' \cdot \vec{J'} + (d\sigma'/dt') = 0$, we get the expression of current density in the frame XYZ:

$$\vec{J} = \gamma\sigma'_0 \left(v_{\rm cm} + \frac{\omega'_0}{k'_0} \right) \sin(k_0 X - \omega_0 t)\hat{e}_{\phi c} = J_0 \sin(k_0\rho_0\phi_c - \omega_0 t)\hat{e}_{\phi c}, \tag{3.18}$$

where γ is the Lorentz factor corresponding to the center of momentum velocity ($v_{\rm cm}$) of the plasma bunch with respect to the rest frame of observer (laboratory frame). The angular frequency and wave-number of longitudinal waves (ω_0, k_0) in laboratory frame are connected to (ω'_0, k'_0) in co-moving frame by Doppler effect (Buschauer & Benford 1976). $J_0 = \gamma\sigma'_0\,(v_{\rm cm} + \omega'_0/k'_0)$ is the magnitude of current density, ω'_0/k'_0 the phase velocity of longitudinal waves in the co-moving frame of plasma, and ρ_0 the radius of curvature of magnetic field line tied to the plasma

bunch. Here $\sigma'_0 = n'q$ is the charge density in co-moving frame and n' is the charge number density. By substituting current density from Equation (3.18) into Equation (3.16) we get,

$$\vec{E}_{cf}(\omega) = -i\omega J_0 \frac{e^{i\omega R/c}}{\sqrt{2\pi}R_0 c^2} \int\int\int \rho_{\rm cf} d\rho_{\rm cf} d\phi_{\rm c} d\eta \int_{-\infty}^{\infty} (\hat{n}\times(\hat{n}\times\hat{e}_{\phi \rm c}))\sin(k_0\rho_0\phi_{\rm c} - \omega_0 t)\times$$

$$\exp\left\{ i\omega\left(t - \frac{\hat{n}\cdot\vec{r_{\rm b}}}{c}\right)\right\} dt. \tag{3.19}$$

It can be shown that the vector quantity $\hat{n}\times(\hat{n}\times\hat{e}_{\phi \rm c}) = \hat{\epsilon}\sin\mu\cos\phi_c - \hat{Y}\sin\phi_c$, where $\hat{\epsilon} = \hat{n}\times\hat{Y}$ is the bi-normal vector, which lies perpendicular to the plane of magnetic field line and curvature vector $\hat{Y}$ lies in the plane of magnetic field line. μ is the angle between the plane of magnetic field line and the line of sight. Due to relativistic effect we get radiation in a narrow cone with beaming angle $\sim 1/\gamma$ around tangent vector, i.e., along $\hat{X}$. We resolve the electric field in the frame–XYZ into the components in the plane of magnetic field line and perpendicular to it:

$$E_{\rm cf\parallel}(r,\omega) = \frac{i\omega J_0 e^{i\omega R_0/c}}{\sqrt{2\pi}R_0 c^2} \int_{-\eta_0/2}^{\eta_0/2} \exp\left[-\frac{i\omega\eta\sin\mu}{c}\right] d\eta \int_{\rho_0-\xi_0/2}^{\rho_0+\xi_0/2} \rho_{\rm cf} d\rho_{\rm cf} \int_{-\infty}^{\infty} e^{i\omega t} dt \times$$

$$\int_{\phi_0-\alpha_m/2}^{\phi_0+\alpha_{\rm m}/2} \sin\phi_{\rm c}\sin(k_0\rho_0\phi_{\rm c} - \omega_0 t) \times \exp\left[-i\frac{\omega}{c}\rho_{\rm cf}\cos\mu\sin\phi_{\rm c}\right] d\phi_{\rm c}, \tag{3.20}$$

$$E_{\rm cf\perp}(r,\omega) = \frac{-i\omega J_0 e^{i\omega R_0/c}}{\sqrt{2\pi}R_0 c^2} \int_{\eta=-\eta_0/2}^{\eta_0/2} \exp\left[-\frac{i\omega\eta\sin\mu}{c}\right] d\eta \int_{\rho_{\rm cf}=\rho_0-\xi_0/2}^{\rho_0+\xi_0/2} \rho_{\rm cf} d\rho_{\rm cf} \int_{-\infty}^{\infty} e^{i\omega t} dt \times$$

$$\int_{\phi_{\rm c}=\phi_0-\alpha_m/2}^{\phi_0-\alpha_{\rm m}/2} \mu\cos\phi_c\sin(k_0\rho_0\phi_{\rm c} - \omega_0 t) \times \exp\left[-i\frac{\omega}{c}\rho_{\rm cf}\cos\mu\sin\phi_{\rm c}\right] d\phi_{\rm c}, \tag{3.21}$$

where ξ_0 is the radial width of the bunch, ϕ_0 is the angular co-ordinate of center of momentum of bunch, $\alpha_{\rm m} = S_0/\rho_0$ is the angular span of the bunch, S_0 the length of the bunch, η_0 the vertical dimension or height of the bunch. The integration with respect to η is straight forward, and evaluated to be $\sin((\omega\eta_0\mu)/(2c))/((\omega\mu)/(2c))$. At the center of momentum we can assume $J = 0$ which readily translated to

$\phi_0 = (v_{\rm cm}t)/\rho_0$ and $v_{\rm cm} \approx c$. So $\phi_{\rm c}$ is a time dependent quantity, which can be expressed as

$$\phi_{\rm c} = \frac{ct}{\rho_0} + \alpha_{\rm m}. \tag{3.22}$$

The length of the bunch in the frame–XYZ can be written as $S = \rho_0\phi_{\rm c}$ and hence $dS = \rho_0 d\phi_{\rm c}$. We make the following approximations for evaluating the time integral and ϕ_c integral: (i) $\cos\mu \approx 1 - (\mu^2/2)$, (ii) $\sin\phi_{\rm c} \approx \phi_{\rm c} - \phi_c^3/6$, (iii) $\rho_{\rm cf} \approx \rho_0(1 + (\xi_0/\rho_0))$. We introduce a function $F_{\rm n}$ for representing the electric field in more simplistic and compact way:

$$F_n = e^{i\omega t}\sin(k_0\rho_0\phi_c - \omega_0 t)\exp\left[-i\frac{\omega}{c}\rho_0\left(1+\frac{\xi_0}{\rho_0}\right)\left(1-\frac{\mu^2}{2}\right)\sin\phi_c\right]. \tag{3.23}$$

After doing some algebraic manipulation we get

$$\int\int F_{\rm n} d\phi_{\rm c} dt = (2i)^{-1}\Big(\Delta_1 T_- - \Delta_2 T_+\Big), \tag{3.24}$$

where

$$\Delta_1 = \frac{1}{\rho_0}\int_{-S_0/2}^{S_0/2}\exp[iS\Big(k_0 - kM\Big)]dS, \tag{3.25}$$

$$\Delta_2 = \frac{1}{\rho_0}\int_{-S_0/2}^{S_0/2}\exp[-iS\Big(k_0 + kM\Big)]dS. \tag{3.26}$$

Here $M = (1-\mu^2/2)(1+\xi_0/\rho_0)(1-\alpha_m^2/6)$ and $T_\pm$ (time integrations) are mentioned below,

$$T_- = \int_{-\infty}^{\infty}\exp[i(C_1 t + C_2 t^2 + C_3 t^3)]dt, \tag{3.27}$$

$$T_+ = \int_{-\infty}^{\infty}\exp[i(C_{1a} t + C_2 t^2 + C_3 t^3)]dt. \tag{3.28}$$

The Coefficients are

$$C_1 \approx \omega\left(\frac{1}{2\gamma^2} - \frac{\omega_0'}{\gamma\omega} + \frac{\alpha_m^2}{2} + \frac{\mu^2}{2} - \frac{\xi_0}{\rho_0}\right),$$

$$C_{1a} \approx \omega\left(\frac{1}{2\gamma^2} + \frac{\omega_0'}{\gamma\omega} + \frac{\alpha_m^2}{2} + \frac{\mu^2}{2} - \frac{\xi_0}{\rho_0}\right),$$

$$C_2 = -k\rho_0 A_2 \left(1 - \frac{\mu^2}{2}\right)\left(1 + \frac{\xi_0}{\rho_0}\right) \approx \frac{\omega c \alpha_m}{2\rho_0},$$

$$C_3 = -k\rho_0 \left(1 - \frac{\mu^2}{2}\right)\left(1 + \frac{\xi_0}{\rho_0}\right) A_3 \approx \frac{\omega c^2}{6\rho_0^2}.$$

We avoid the bi-product term arising from the product of ξ_0 with μ^2 and α_m^2, while estimating C_1, C_{1a}, C_2, C_3, as they are small entities. The maximum length of coherently emitting column is $S_0 \leq (\rho_0/\gamma_0)$, and radial width is $\Delta\rho = \xi_0 \leq \rho_0/\gamma_0^2$ (Buschauer & Benford 1976). Moreover the transverse dimensions ξ_0 and η_0 both should be less than the emitted wavelength for satisfying coherent condition. But length of the bunch can pervade upto 10 to 35 % of light cylinder radius in normal radio pulsars.

Due to the factor $k_0 + kM$ in Δ_2 the resonance condition is not satisfied, and hence we drop Δ_2. So we deal with $\Delta_1 T_-$ term:

$$\Delta_1 = \int_{-S_0/2}^{S_0/2} \exp[iS(k_0 - kM)]dS = 2\frac{\sin[(k_0 - kM)S_0/2]}{(k_0 - kM)}.$$

This term is called selection factor, we can see that resonance condition is satisfied in the limit of $k_0 \rightarrow k\ M$. Here k and ω are the wave number and frequency of emitted electromagnetic waves. Perfect coherence occurs, when M attains maximum value. This occurs at $\mu = 0°$, i.e., in the plane of magnetic field lines for any combination of geometrical parameters allowed by observations. This happens because at $\mu = 0^\circ$, both ξ_0 and α_m become zero.

The solution to integral along radial direction is straightforward and it is given by

$$\int_{\rho_0 - \xi_0/2}^{\rho_0 + \xi_0/2} \rho_{\rm cf} d\rho_{\rm cf} = \rho_0 \xi_0.$$

This integral solution is important only in the aspect of boosting up the peak magnitude of intensity. Apart from that another significant role played by transverse dimensions is that smaller the transverse dimensions (ξ_0, η_0), compared to radio

wavelength, more pronounced will be the proportion of circular polarization.

The solution to time integrals in Equations (3.20) and (3.21) carries all the information regarding pulse profile structure and polarization. The time integrals appearing in the parallel and perpendicular components of electric field are

$$T_{\parallel} = \int_{-\infty}^{\infty} (A_0+A_1t+A_2t^2+A_3t^3)\exp[i(C_1t+C_2t^2+C_3t^3)]dt = A_0L_0+A_1L_1+A_2L_2+A_3L_3, \tag{3.29}$$

$$T_{\perp} = \int_{-\infty}^{\infty} (B_0+B_1t+B_2t^2+B_3t^3)\exp[i(C_1t+C_2t^2+C_3t^3)]dt = B_0L_0+B_1L_1+B_2L_2, \tag{3.30}$$

where A_i and B_i, (i=0 1, 2, 3), are the series expansion coefficients. Here $A_0 = \alpha_m(1-\alpha_m^2/6)$, $A_1 = (c/\rho_0)(1-\alpha_m^2/2)$, $A_2 = -(c^2\alpha_m)/(2\rho_0^2)$, $A_3 = -c^3/(6\rho_0^3)$, $B_0 = (1-\alpha_m^2/2)$, $B_1 = -(\alpha_m c)/\rho_0$, $B_2 = -c^2/(2\rho_0^2)$ and $B_3 = 0$. The integrals L_0, L_1, L_2 and L_3 are:

$$L_0 = \int_{-\infty}^{\infty} \exp[i(C_1t + C_2t^2 + C_3t^3)]dt, \tag{3.31}$$

$$L_1 = \int_{-\infty}^{\infty} t\exp[i(C_1t + C_2t^2 + C_3t^3)]dt. \tag{3.32}$$

$$L_2 = \int_{-\infty}^{\infty} t^2\exp[i(C_1t + C_2t^2 + C_3t^3)]dt \tag{3.33}$$

$$L_3 = \int_{-\infty}^{\infty} t^3\exp[i(C_1t + C_2t^2 + C_3t^3)]dt \tag{3.34}$$

The limits of the time integral are deliberately pushed to $\pm\infty$ as the emissions received over a short interval of time during which $\hat{n}$ and the velocity vector ($\hat{v}$) are within $1/\gamma$ angle. Outside this interval, the time integrand oscillates very rapidly and contribute negligibly small amount to the radiation.

Let $t = (x/l) + m$ then $dt = dx/l$, where $l = C_3^{1/3}$ and $m = -C_2/(3C_3)$. Then solution to the integrals in Equations (3.31) – (3.34) are given by

$$\begin{aligned} L_0 &= Uj_0,\ L_1 = \frac{U}{C_3^{1/3}}\left(j_1 - \frac{C_2}{3C_3^{2/3}}j_0\right),\ L_2 = U\left(\frac{j_0}{3C_3}\left(\frac{2C_2^2}{3C_3} - C_1\right) - 2j_1\frac{C_2}{3C_3^{4/3}}\right), \\ L_3 &= \frac{U}{9C_3^{7/3}}\left(j_1(4C_2^2 - 3C_1C_3) + j_0\frac{9C_1C_2C_3 - 4C_2^3 + 9ic_3^2}{3C_3^{2/3}}\right) \end{aligned} \tag{3.35}$$

where

$$U = \frac{1}{C_3^{1/3}}\exp\left[i\frac{C_2}{3C_3}\left(\frac{2C_2^2}{9C_3} - C_1\right)\right],$$

$$\begin{aligned} j_0 &= \frac{2}{3}z^{1/2}K_{1/3}\left(\frac{2}{3^{3/2}}z^{3/2}\right), \quad j_1 = \frac{2iz}{3^{3/2}}K_{2/3}\left(\frac{2}{3^{3/2}}z^{3/2}\right) \quad \text{and} \\ z &= \frac{1}{C_3^{1/3}}\left(C_1 - \frac{C_2^2}{3C_3}\right). \end{aligned} \tag{3.36}$$

The functions $K_{1/3}$ and $K_{2/3}$ are the modified Bessel functions of order 1/3 and 2/3, respectively.

If we plug in the values of C_1, C_2, C_3 into the expression of z and simplify, we get

$$z = \left(\frac{6\omega^2\rho_0^2}{c^2}\right)^{1/3}\left(\frac{1}{2\gamma_0^2} - \frac{\omega_0'}{\gamma\omega} + \frac{\mu^2}{2} - \frac{\xi_0}{\rho_0}\right). \tag{3.37}$$

Finally the components of radiation electric field in the frame–XYZ are given by

$$\begin{aligned} \vec{E}_{\mathrm{cf}\parallel}(r,\omega) = A_{\mathrm{m}}E_0\frac{\sin\left[(k_0 - kM)S_0/2\right]}{(k_0 - kM)S_0/2}\frac{\sin(k\eta_0\mu/2)}{k\eta_0\mu/2}\times, \\ (A_0L_0 + A_1L_1 + A_2L_2 + A_3L_3)\hat{Y}, \end{aligned} \tag{3.38}$$

$$\begin{aligned} \vec{E}_{\mathrm{cf}\perp}(r,\omega) = -A_{\mathrm{m}}E_0\ \mu\frac{\sin\left[(k_0 - kM)S_0/2\right]}{(k_0 - kM)S_0/2}\frac{\sin(k\eta_0\mu/2)}{k\eta_0\mu/2}\times, \\ (B_0L_0 + B_1L_1 + B_2L_2)\hat{\epsilon}, \end{aligned} \tag{3.39}$$

where

$$A_{\rm m} = \frac{\omega\gamma n' \left(v_{\rm cm} + \omega_0'/k_0'\right) S_0 \xi_0 \eta_0}{c} \quad \text{and} \quad E_0 = \frac{q}{2\sqrt{2\pi} R_0 c} \exp(i\omega R_0/c).$$

3.8 Behavior of angle μ angle with respect to rotation phase

In this section, we briefly elaborate the behaviour of angle μ. Since we have given the details of radio emission geometry such as expression of magnetic co-latitude and magnetic azimuth at emission spot in the previous chapter, we only discuss the behaviour of angle μ. But for sake of completeness reader can always see the details of radio emission geometry of pulsar in Gangadhara (2004).

Let μ be the angle between line of sight and plane of magnetic field lines at the time of receiving the emission. In equation 3.1, we have given the expression of bi-normal vector. So

$$\mu = \arcsin\left(\hat{n}.\hat{\epsilon}\right) = \arcsin\Big(-\sin\zeta(\cos\alpha\sin\phi\cos\phi' + \cos\phi\sin\phi') + \cos\zeta\sin\alpha\sin\phi\Big). \tag{3.40}$$

Now, if we substitute the expression of ϕ from Equation (2.16) into Equation (3.40) and after that apply $\phi' = \phi' + \delta\phi p$ to get the span of pulse phase around the peak point of main pulse and sub-pulses. Sub-pulses span in μ space corresponds some spread around the peak point in the domain of rotation phase.

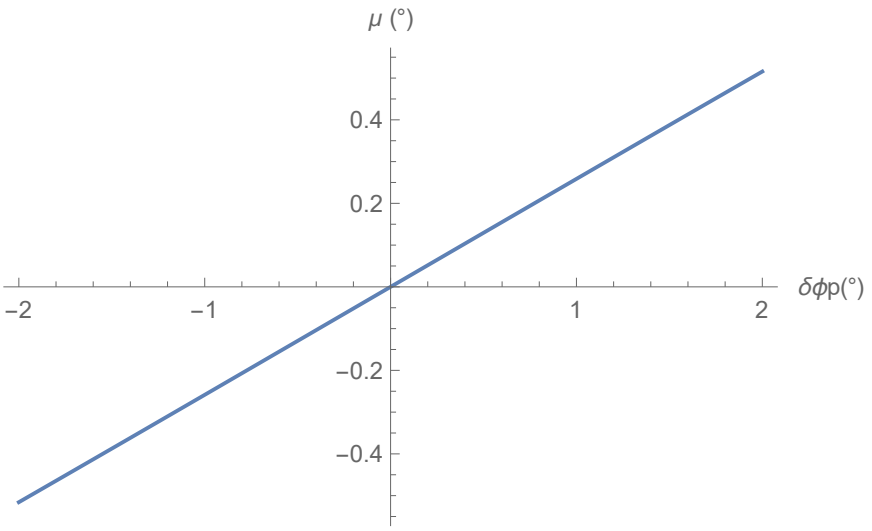

FIGURE 3.3: μ is plotted with respect to pulse phase, typically representing the variation of μ with respect to pulse width. The parameters chosen to generate the plot are $\alpha = 10°$, $\sigma = 5°$ and $\phi' = 0°$.

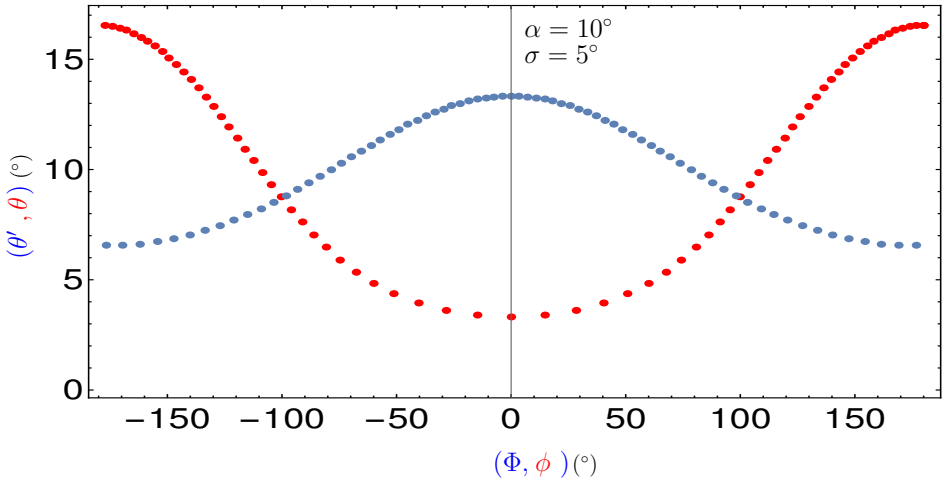

FIGURE 3.4: Beaming regions specifying the range of colatitude and azimuth: in rotation axis frame (blue) and magnetic axis frame (red). They are plotted for the full range of phase -180° $\leq \phi' \leq$ 180° with a step of 5°. Lorentz factor chosen here is $\gamma = 300$.

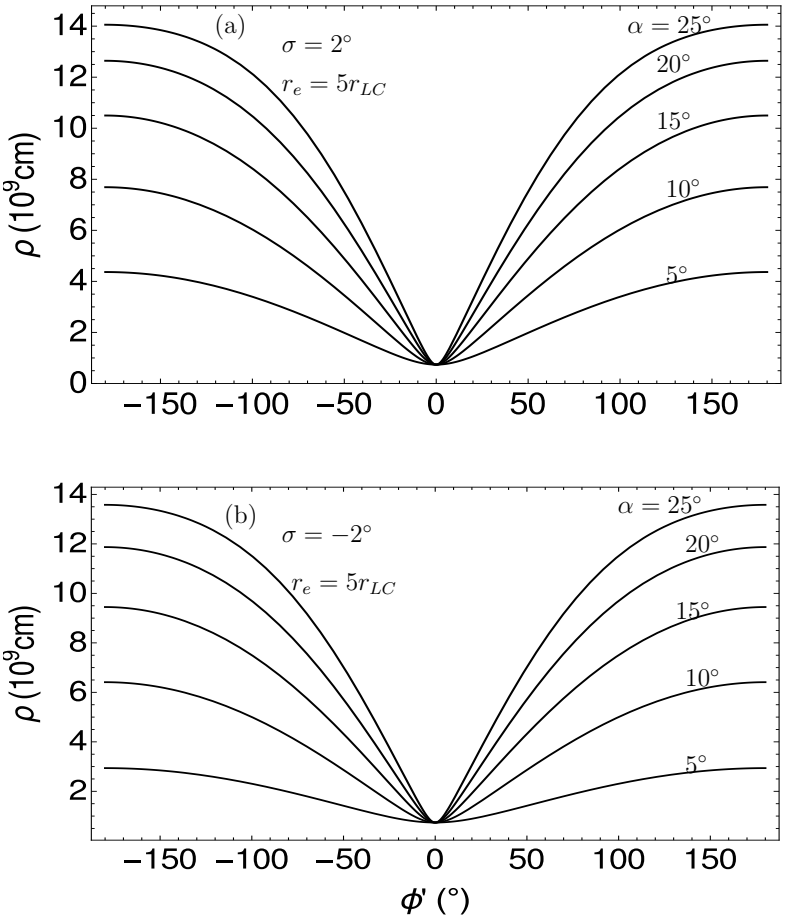

FIGURE 3.5: Plot of radius of curvature of magnetic field line vs rotation phase, based on geometry of di-polar magnetic field line at the emission point: panel (a) for $\sigma = 2°$ and (b) for $\sigma = -2°$.

3.9 Calculation of sub-pulse width of pulsar for collective plasma system

We calculate width of sub-pulses from the expression of radius of curvature associated with bunch (see Equation (2.8). If we project the transverse width of the source in meridional plane, we can estimate the width of main pulse as well as sub-pulses also. From Equation (2.8) we see that ρ is a function of r_e and θ. So we can write

$$\rho = f(r_e, \theta). \tag{3.41}$$

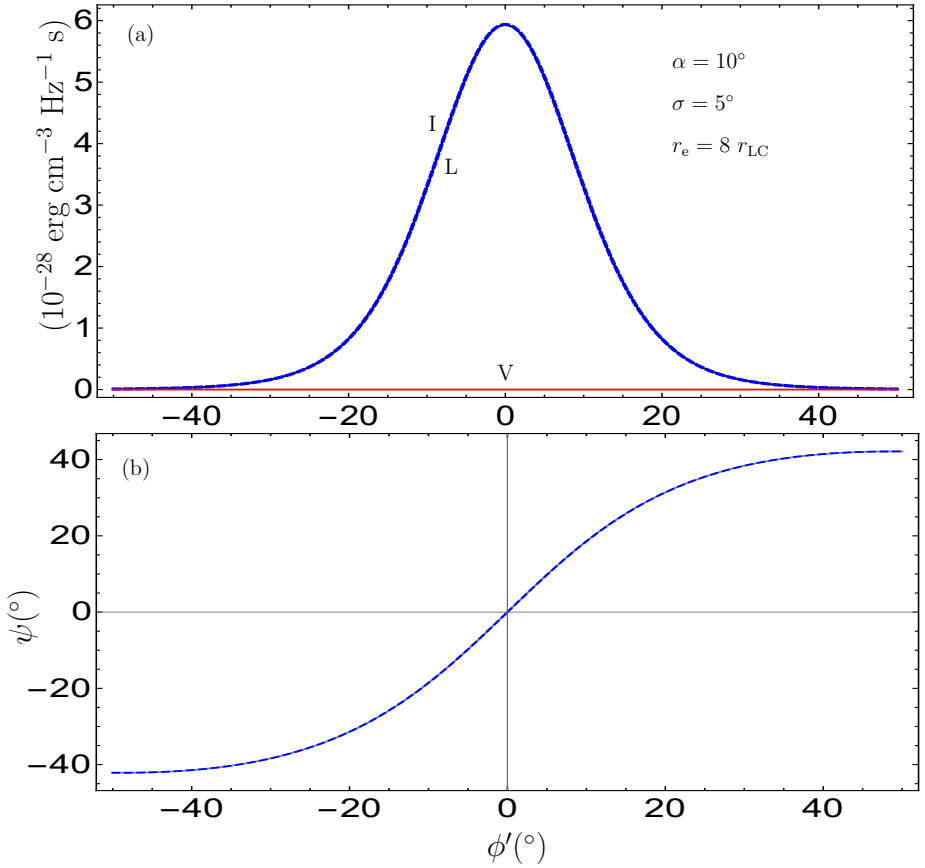

FIGURE 3.6: The model pulse profile for pulsar with period 1 s: in panel (a) intensity I (black continuous line), linear polarization L (blue dashed line) and circular polarization V (red line) are plotted with rotation phase ϕ'. In panel (b) polarization curve, which is superposed with RVM curve (Radhakrishnan & Cooke 1969). The chosen bunch length is $S_0 \approx 30\% r_{\rm LC}$ and transverse dimensions $\xi_0 = \eta_0 = 12$ cm, and $\mu = 0°$. The current density is 10^{14} esu cm^{-2} s^{-1}, plasma density in co-moving frame $n' = 1.24 \times 10^{10}$cm^{-3}, and the corresponding density in lab frame is $n_{e0} = \gamma n' = 6.94 \times 10^{12}$cm^{-3} for Lorentz factor $\gamma = 560$. The light cylinder radius r_{LC} =4.7×10^9 cm for pulsar with period 1 s, which is at distance $R = 1$ kpc.

Differentiating the above equation we get

$$\xi_0 = d\rho = \frac{\partial f}{\partial r_e}\delta r_e + \frac{\partial f}{\partial \theta}\delta\theta, \tag{3.42}$$

where ξ_0 (radial width of bunch) is nothing but the variation of radius of curvature. So from Equation (2.8) we have

$$\frac{\partial f}{\partial r_e} = \frac{\sin\theta(5 + 3\cos 2\theta)^{3/2}}{3\sqrt{2}(3 + \cos 2\theta)},$$

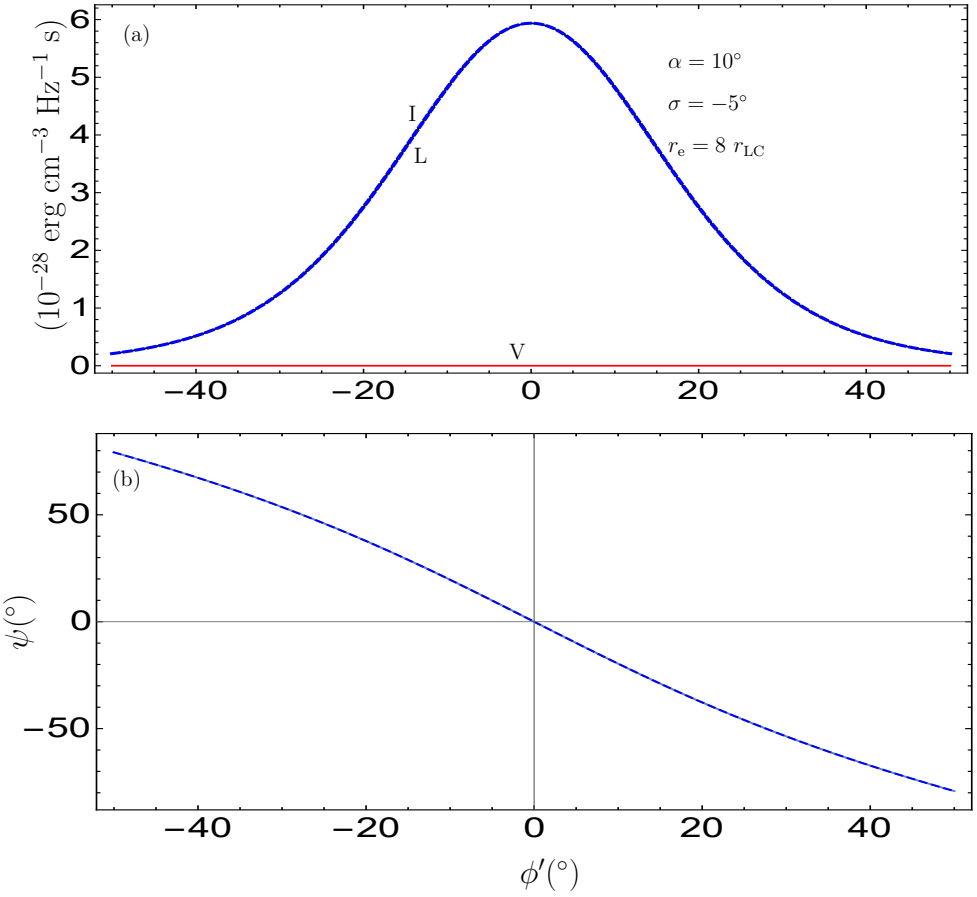

FIGURE 3.7: Plotted in panel (a) I, L, V vs rotation phase ϕ', and polarization angle (superposed with the RVM curve) in panel (b). Geometrical parameters are mentioned in panel (a) and rest of the parameters are same as figure 3.6.

and

$$\frac{\partial f}{\partial \theta} = \frac{r_e(5+3\cos 2\theta)^{1/2}(30\cos\theta + 31\cos 3\theta + 3\cos 5\theta)}{6\sqrt{2}(3+\cos 2\theta)^2}.$$

Again for a particular pulsar, colatitude at emission spot is a function of rotation phase only (see Equation (2.13) in chapter 2). So by differentiating Equation (2.13) with respect to rotation phase we get,

$$\delta\theta = \frac{\sin\alpha\sin\zeta\sin\phi'(\cos\Gamma + (8+\cos^2\Gamma)^{1/2})^2}{6(8+\cos^2\Gamma)^{1/2}(1-\frac{1}{9}(-1+\cos\Gamma(8+\cos^2\Gamma)^{1/2}+\cos^2\Gamma)^2)^{1/2}}\delta\phi' \quad (3.43)$$

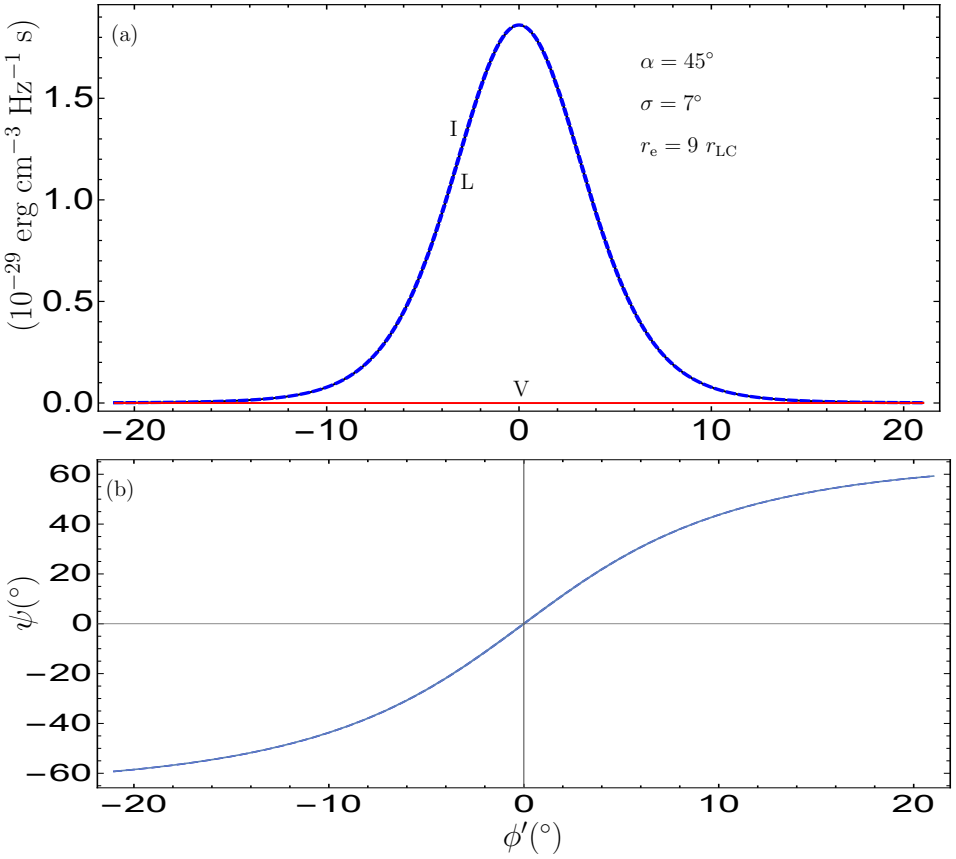

FIGURE 3.8: Plotted in panel (a) I, L, V vs rotation phase ϕ', and polarization angle (superposed with the RVM curve) in panel (b). Geometrical parameters are mentioned in panel (a) and rest of the parameters are same as figure 3.6.

So once we know half beam opening angle (Γ), α, σ, peak location of sub-pulse, radial width, span of di-polar field line constant as well as di-polar field line constant of bunch at the particular phase location of sub-pulse, we can easily get the width of sub-pulse with the help of Equation (3.43).

3.10 Brightness temperature of radio pulsars

Brightness temperature or radiance temperature is the temperature of a black body in thermal equilibrium with it's surroundings would have to have been representing the observed intensity of a gray body object at a frequency ν. This concept is

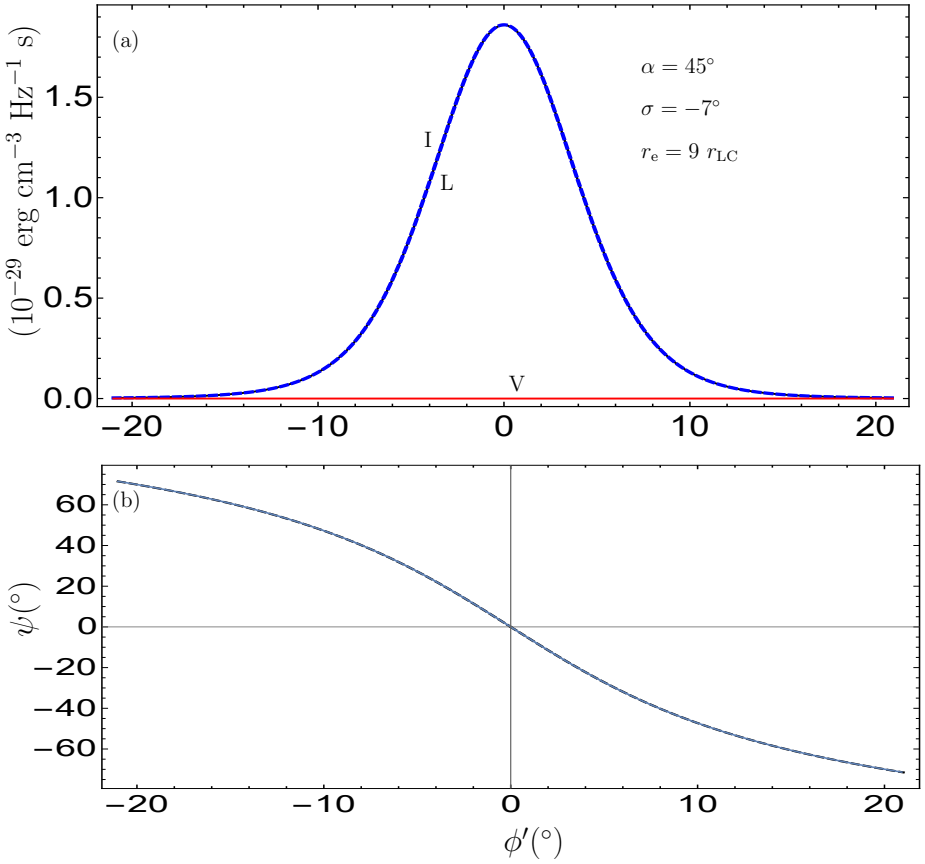

FIGURE 3.9: Plotted in panel (a) I, L, V vs rotation phase ϕ', and polarization angle (superposed with the RVM curve) in panel (b). Geometrical parameters are mentioned in panel (a) and rest of the parameters are same as figure 3.6.

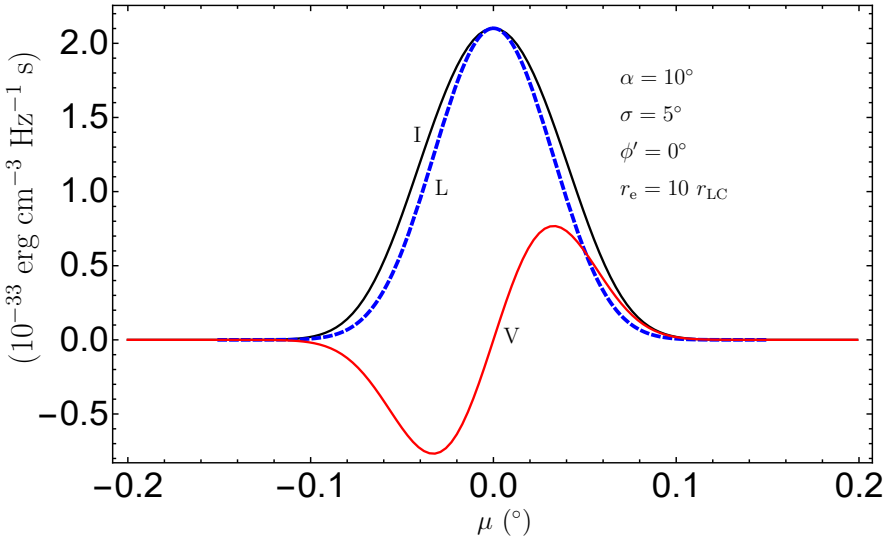

FIGURE 3.10: This is the plot of I, L, V vs angle μ in degree. Bunch length chosen here is $S_0 = 20\%$ of r_{LC} (light cylinder radius is 4.77×10^9 cm for pulsar with rotation period 1 s) and transverse dimensions are $\xi_0 = \eta_0 = 3$ cm. Others parameters are same as mentioned in figure 3.6

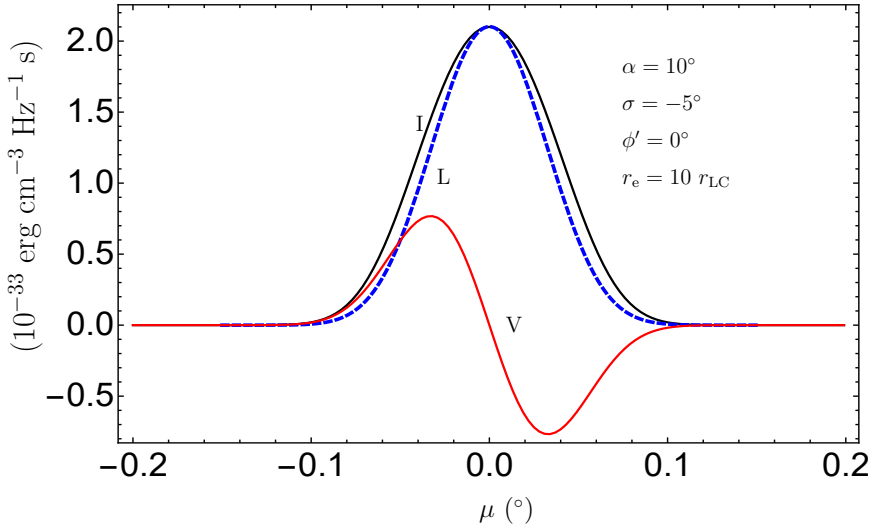

FIGURE 3.11: This plot is also similar as figure 3.10 except for $\sigma = -5^0$.

used in radio astronomy and sometimes in planetary science too. The brightness temperature is not a temperature as ordinarily understood. It characterizes radiation, and depending upon the mechanism of radiation it can differ significantly from the physical temperature of a radiating body. Non-thermal radiation can have high brightness temperature, for example observed pulsar luminosity corresponds high brightness temperature which ranges from 10^{25} K to 10^{32} K roughly. The brightness temperature can be derived from Planck's law in the limit of long wavelength regime.

The Stokes parameters I, Q, U and V as defined above in equations (3.5), are due to Rybicki & Lightman (see 1979, Eq. 2.40a-d), a clear, straightforward, and fundamental definitions for physicist's from the point of view-radiation processes and their applications to astrophysical phenomena and space science. In a theoretical modeling, a theorist first estimates radiation electric field $\vec{E}(\omega)$ due an accelerated charge or bunch , and then construct the Stokes parameters. Then all the Stokes parameters will have the units "erg cm^{-3} Hz^{-1} s", as per the dimensional analysis, for example, $I = |\vec{E}(\omega)|^2$. Rybicki and Lightman (1979, see Eq.2.54) have also called Stokes parameter I as intensity.

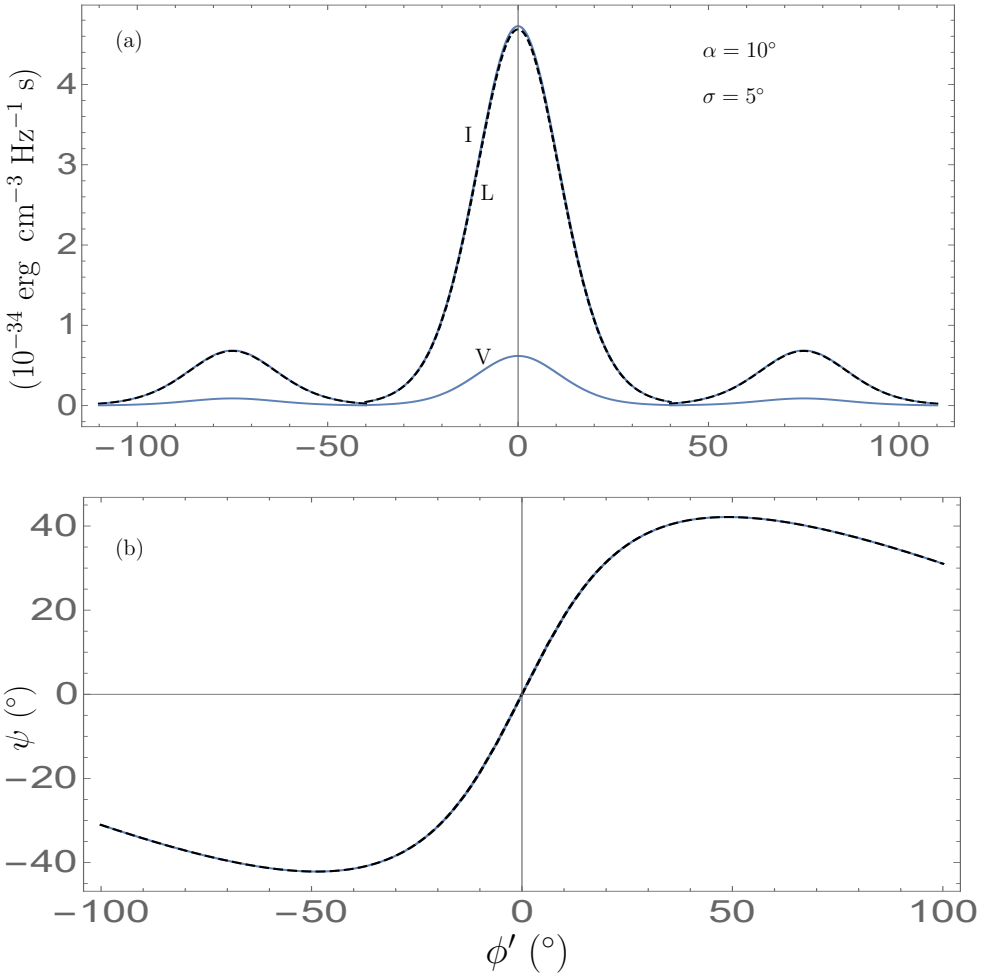

FIGURE 3.12: A triple component profile: panel (a) plotted I, L, V vs rotation phase ϕ' in degree and in panel and panel (b) polarization angle superposed with RC curve vs rotation phase. Using $\mu = -0.007°$, $r_e = 20r_{LC}$, bunch length $S_0 = 30\% r_{\rm LC}$ and transverse dimensions $\xi_0 = \eta_0 = 3$ cm. The bunch emitting core component is chosen at $\phi' = 0°$, and the conal outriders at $\phi' = \pm 75°$ and field line constant is $r_e = 18\ \ r_{\rm LC}$. The bunch length chosen for sub-pulse component is 0.3 times the bunch length corresponding to core component. Chosen transverse dimensions for sub-pulse is same as main pulse component. Rest of the other parameters are same as in figure 3.6.

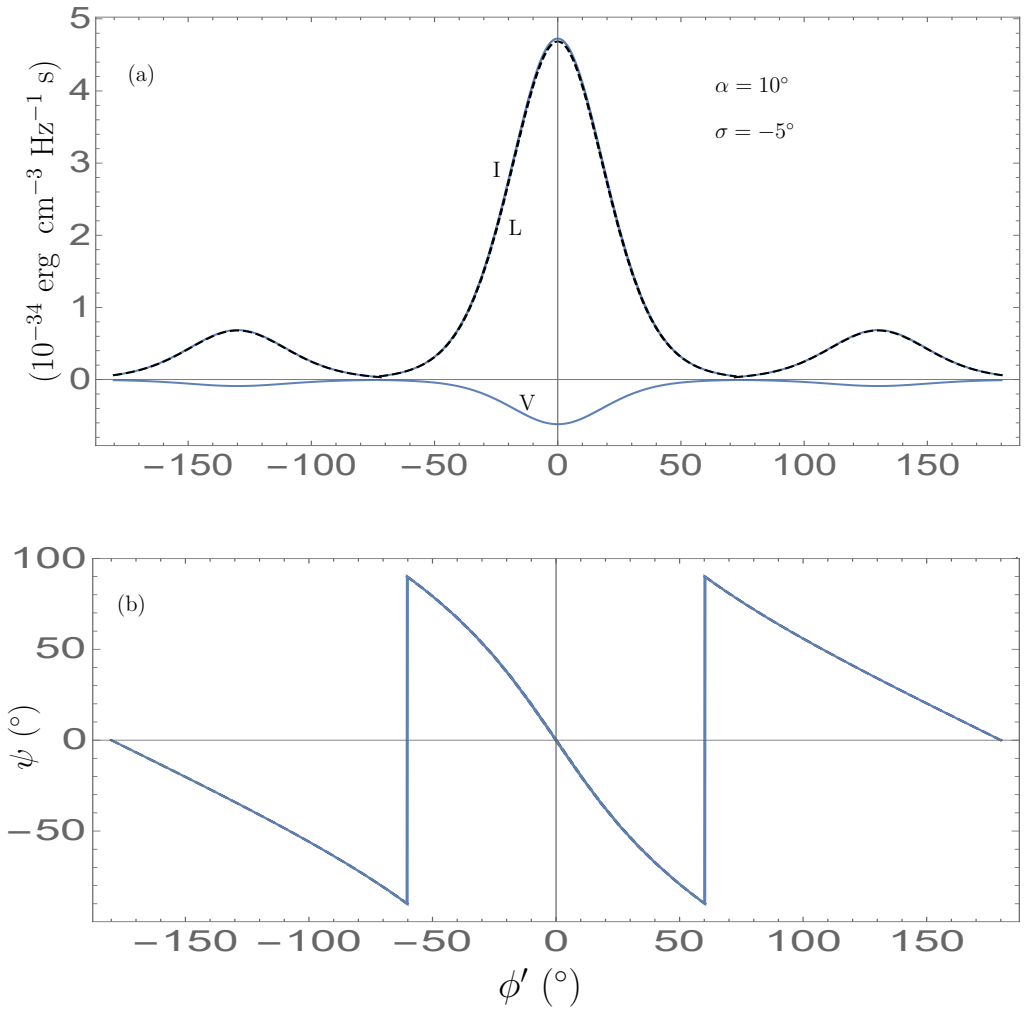

FIGURE 3.13: A triple component profile: panel (a) plotted I, L, V vs rotation phase ϕ' in degree and in panel (b) polarization angle superposed with RC curve. Here everything is same as figure 3.12 except $\sigma = -5°$. As σ is negative here, μ is measured in anti-clockwise direction.

The Stokes parameter I is non-negative and is *proportional* to the total energy flux or intensity of the wave. In practice, it is customary to choose a single proportionality factor in all of the definitions of (2.40-a-d) so that I is precisely the flux or intensity. Hence to convert Stokes parameter I into flux, Rybicki and Lightman (1979, see Eq.2.34), have further suggested to choose a proportionality c/T, where c is the speed of light and T is the average time scale over which electric field shows a significant variation, which is determined by analyzing the spectrum. In other words one can infer the correct value of T by analyzing a portion of signal so that a suitable frequency resolution $\Delta\omega \approx 1/T$ can be obtained. Therefore, we

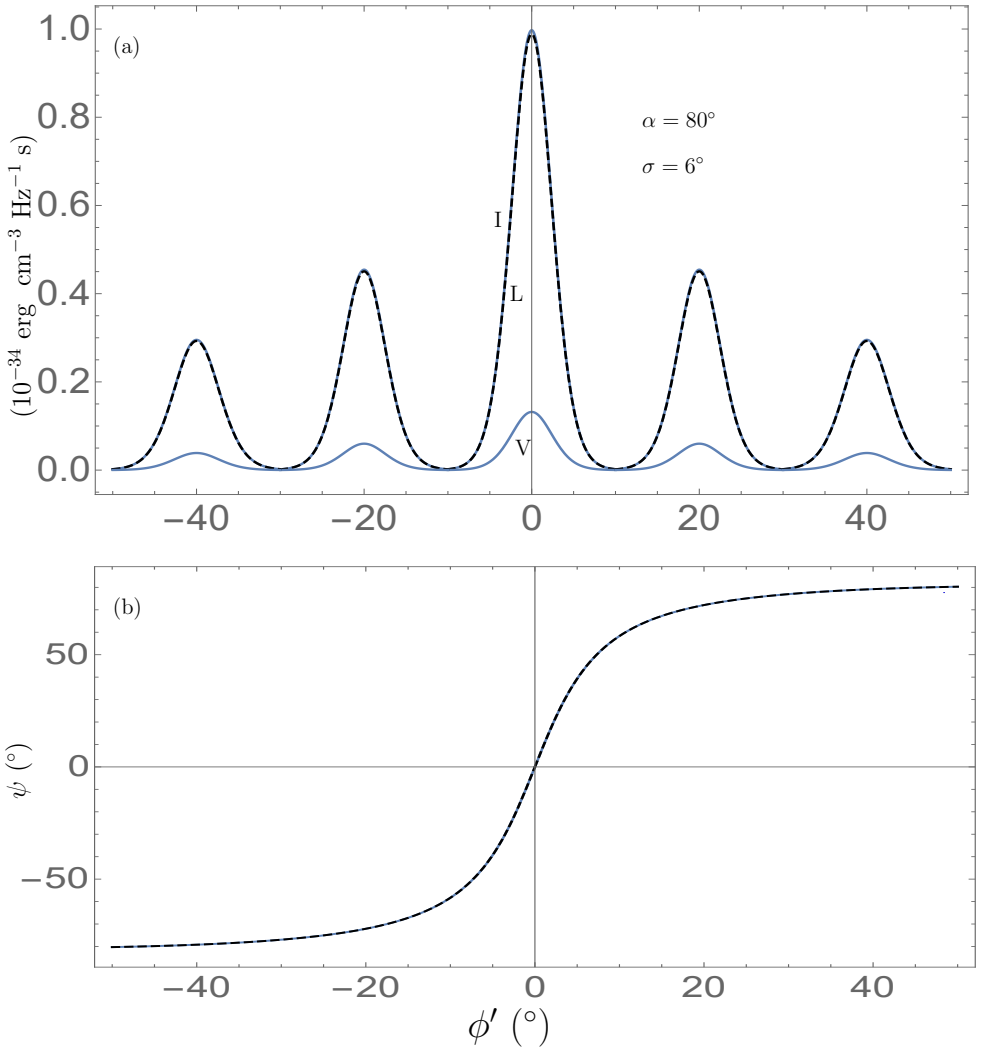

FIGURE 3.14: A five component profile: panel (a) plotted I, L, V vs rotation phase and panel (b) polarization angle superposed with RC curve plotted with rotation phase. For core component we chose phase location $\phi' = 0°$, $r_e = 22r_{\rm LC}$, bunch length $S_0 = 30\%$ $r_{\rm LC}$ and transverse dimensions $\xi_0 = \eta_0 = 3$ cm. For sub-pulses (conal components) we chose the phase locations $\phi' = \pm 20°$, $\pm 40°$ and $r_e = 20r_{\rm LC}$, $18r_{\rm LC}$, for first and second conal components, respectively. Bunch length chosen for sub-pulse components are 0.5 and 0.3 times the size corresponding to the core component. Transverse dimensions of sub-pulse are kept same as main pulse component. Rest of other parameters are kept fixed across all pulse components which are same as mentioned in figure 3.6. Here σ is positive hence measurement direction of μ is clockwise.

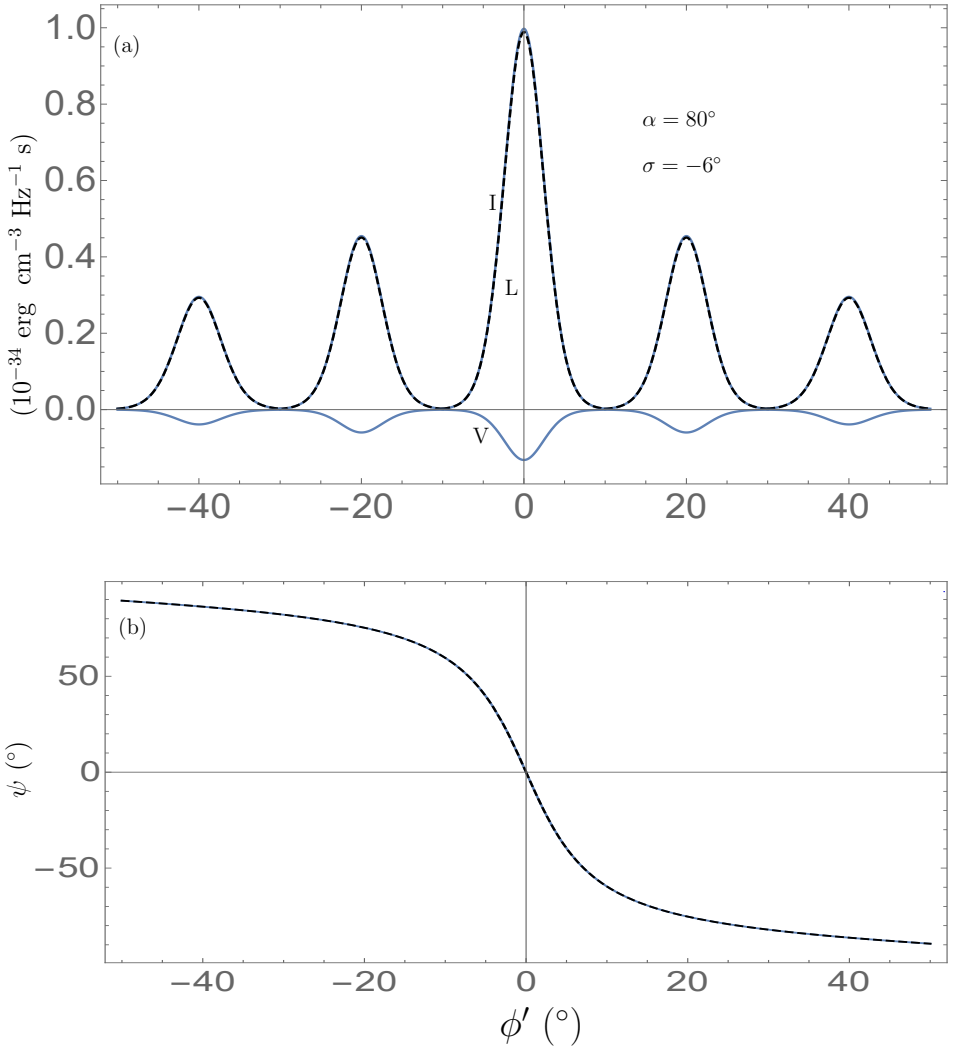

FIGURE 3.15: In panel (a) plotted I, L, V vs rotation phase and in panel (b) polarization angle superposed with RC curve plotted with rotation phase. Here everything is same as figure 3.14 except $\sigma = -6^0$. As σ is negative, hence measurement direction of μ is anti-clockwise.

have

$$\frac{dW}{dAd\omega dt} = S_\nu = \frac{c}{T}I, \tag{3.44}$$

where s_ν is the flux density and has the units: erg cm^{-2} Hz^{-1} s^{-1}. We estimate the brightness temperature using the formula given by Cordes (1979), in the Rayleigh-Jeans limit of black body spectrum:

$$T_\mathrm{b} = \frac{1}{2k_\mathrm{B}} \frac{\lambda^2 S_\nu}{(c\Delta t/R)^2}, \tag{3.45}$$

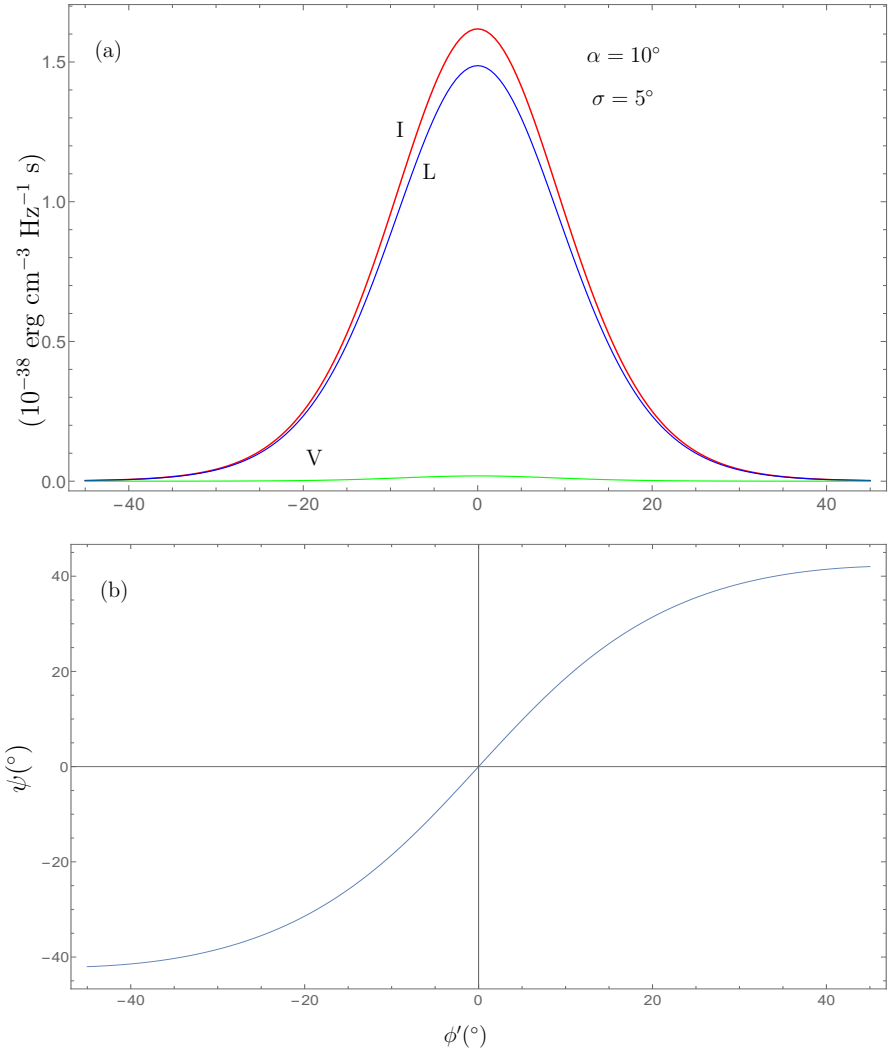

FIGURE 3.16: A single component profile:panel (a) plot of I, L, V vs rotation phase and panel (b) polarization angle ψ vs rotation phase. For simulating profiles we integrated over emission region over μ from $-1/\gamma$ to $1/\gamma$, where Lorentz factor $\gamma = 560$. Parameters chosen here are $r_e = 20r_{LC}$. The bunch related parameters are $S_0 = 30\%r_{LC}$, $\xi_0 = \eta_0 = 3$ cm and the emitted radiation frequency chosen here is $\nu_{em} = 1$ GHz.

where λ is the wavelength of emitted radio signal, Δt is same as T, and R is the distance between observer and pulsar. Literature (e.g., Cordes 1979) suggests the value of Δt is of the order of a few ms for sub pulses and 10 μs to 1 ms for micro pulses. For main pulses we have taken the average duty cycle of pulse $\Delta t \approx T$, which ranges from 0.1 s to 0.5 s in the case of normal pulsars. By making high time resolution (0.4 ns) observations, Hankins & Eilek (2007) have captured giant nanoshots in the individual pulses from Crab pulsar, and their brightness

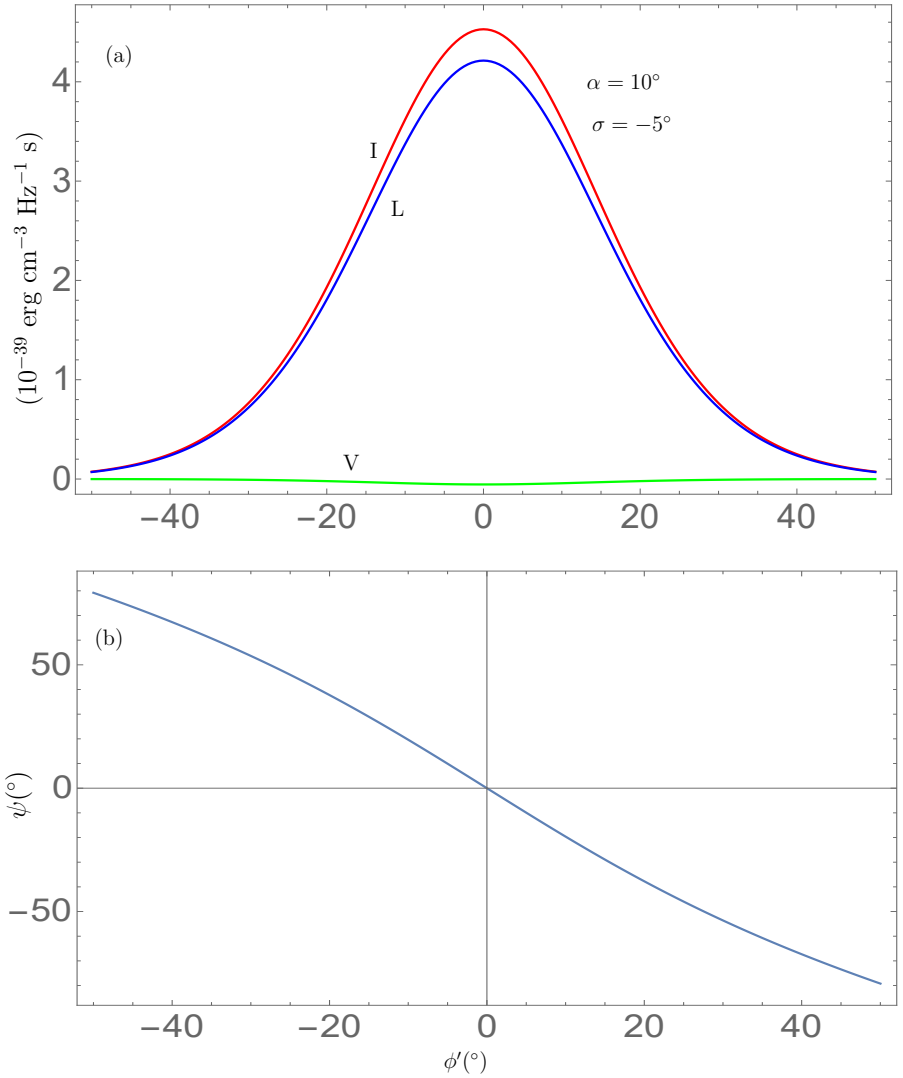

FIGURE 3.17: Here everything is same as figure 3.16 except $\sigma = -5°$.

temperature estimated to be $\sim 10^{42}$ K.

In Table 3.1, we have estimated the brightness temperature of a few pulsars (10) based on the data from ATNF catalogue. In column 1 given the pulsar name, column 2 pulsar period (in the order of increasing period), column 3 gives distance between pulsar and observer, column 4 and 5 gives the flux density at 900 MHz and 1.4 GHz respectively, column 6 gives on pulse width at 10% intensity level, and the columns 7 and 8 gives the estimate of brightness temperature.

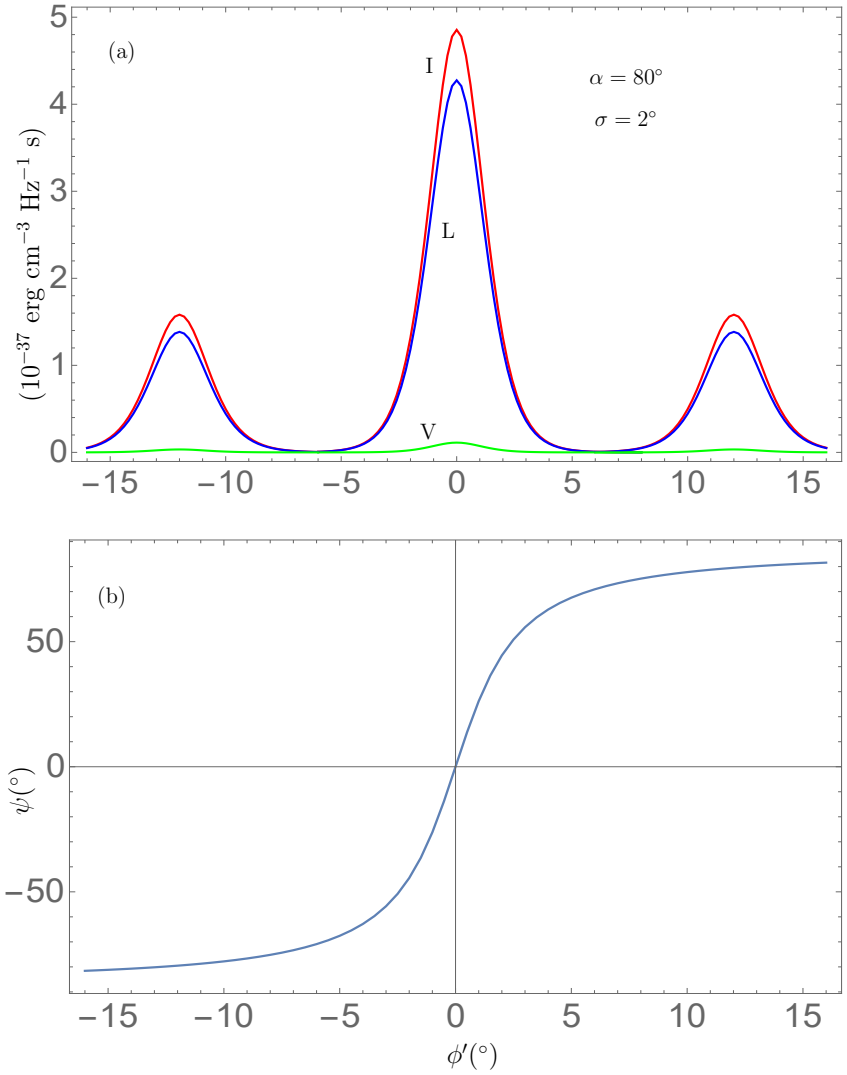

FIGURE 3.18: A tripe component profile: panel (a) plot of I, L, V vs rotation phase and panel (b) polarization angle vs rotation phase. Here the parameters chosen for the core component are same as figure 3.16 except di-polar field line constant $r_e = 25\ r_{LC}$. For sub pulse components we have chosen the peak locations at $\phi' = \pm 12°$, di-polar field line constant $r_e = 22\ r_{LC}$ and length of source $S_0 = 15\% r_{LC}$.

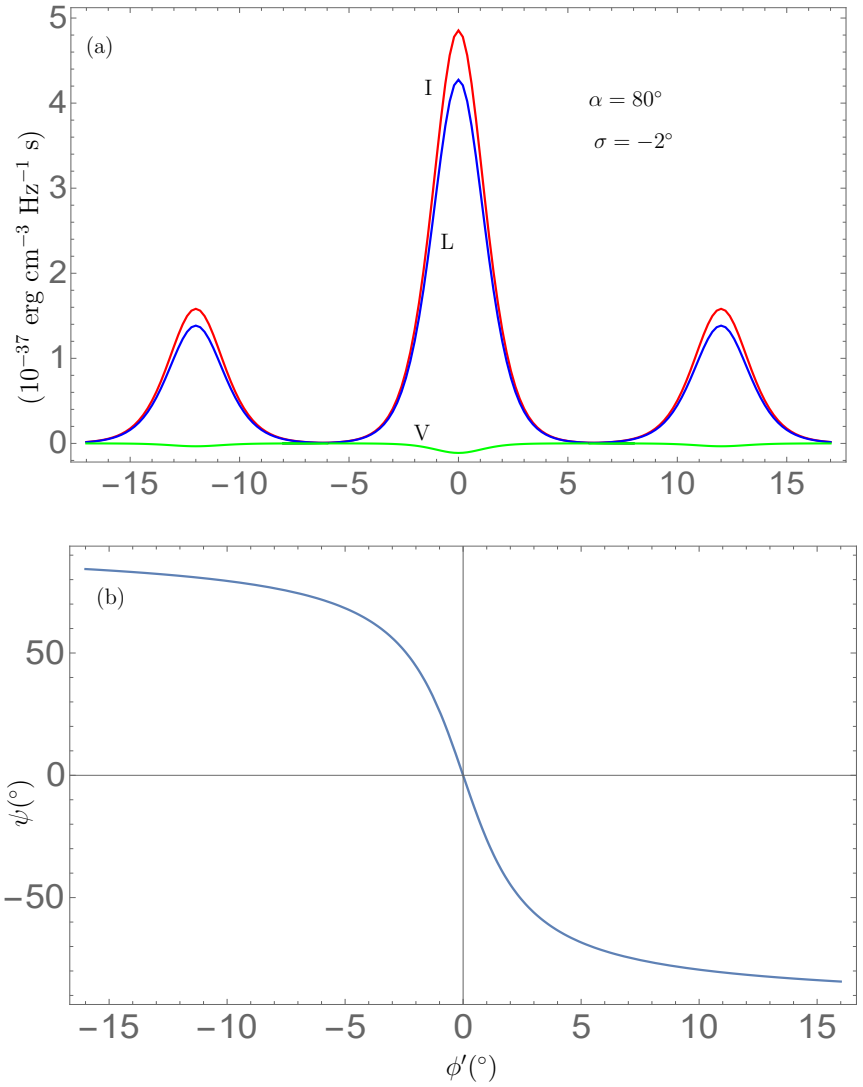

FIGURE 3.19: Here everything is same as figure 3.18 except $\sigma = -2°$.

In Table 3.2, we have estimated brightness temperature for multi-component profiles purely from theoretical origin. If we compare the Tables 3.1 and 3.2, we can infer that theoretical estimates of brightness temperature are roughly comparable with the observational data. However some differences do exit which could be due to parameters differences. For example peak frequency of radio emission chosen in our model is 1 GHz, whereas observational flux data are at 900 MHz and 1.4 GHz. Apart from that the pulsar period is also slightly different, which can effect the light cylinder radius, and hence the di-polar field line constant as well. Another important factor of discrepancy between observation and theory is the

Pulsar Name	Period (s)	distance (kpc)	$S_{900\ \mathrm{MHz}}$ (mJy)	$S_{1.4\ \mathrm{GHz}}$ (mJy)	W_{10} (ms)	$T_b\ ^{\Delta t=W_{10}}_{1.4\ \mathrm{GHz}}$ (K)	$T_b\ ^{\Delta t=W_{10}}_{900\ \mathrm{MHz}}$ (K)
B2111+46	1.014	4.00	44	19	152.8	1.47×10^{17}	8.22×10^{17}
B2044+15	1.138	3.34	-	1.7	50.1	1.32×10^{18}	-
B1133+16	1.187	0.35	37	20	41.8	2.46×10^{17}	1.10×10^{18}
B0138+59	1.223	2.30	13	4.5	104.2	3.84×10^{17}	2.69×10^{18}
B0818-13	1.238	1.90	14	6	35.6	3.00×10^{18}	1.69×10^{19}
B0628-28	1.244	0.32	57	31.9	119.7	4.00×10^{16}	1.73×10^{17}
B0834+06	1.275	0.19	5	5	33.9	2.75×10^{16}	6.66×10^{16}
B0809+74	1.292	0.43	-	10	89.5	4.05×10^{16}	-
B1237+25	1.381	0.84	26	23.2	60.6	7.82×10^{17}	2.12×10^{18}
B2154+40	1.525	2.90	-	17	114.2	1.92×10^{18}	-

TABLE 3.1: Computed brightness temperature of pulsars based on the data from ATNF catalog

difference between on pulse width, which can significantly vary depending upon geometrical parameters likes as α, σ and r_e and bunch dimensions. So without knowing the details of pulse period, distance, magnetic axis inclination angle, line of sight impact angle, r_e and possibly plasma parameters also, fine tune adjustment between theory and observation seems to be a difficult task.

In Table 3.3 we have estimated brightness temperature for fully linearly polarized profiles from theoretical point of view. We see that brightness temperature in Table 3.3 are bit higher compared to those reported in Table 3.2. This is because of the di-polar field line constant r_e chosen for profiles in Table 3.2 are bit larger compared to Table 3.3.

For our calculations we have assumed distance to the pulsar as $R_0 = 1$ kpc, radio wavelength $\lambda = 30$ cm. The peak value of I in Figure 3.6 is around 5.91×10^{-28} erg cm^{-3} Hz^{-1} s. If we plug in all these values in Equation (3.45), then we

Figure number and Pulse component	$\delta\phi'$ (°)	$\delta t = (P/360)\delta\phi'$ (s)	I_{max} (10^{-34} erg cm^{-3} Hz^{-1} s)	$S_\nu = (c/\delta t)I_{max}$ (Jy)	T_b (K)
Figure 3.12, Core	80	0.220	4.68	6.31	4.45×10^{19}
Figure 3.12, conal component	50	0.140	0.69	1.49	2.68×10^{19}
Figure 3.14, Core	20	0.056	0.99	5.34	6.01×10^{20}
Figure 3.14, 1st conal component	10	0.028	0.45	4.86	2.19×10^{21}
Figure 3.14, 2nd conal component	8	0.022	0.29	3.91	2.75×10^{21}
Figure 3.16, Core	80	0.220	1.68×10^{-4}	2.16×10^{-4}	1.50×10^{15}
Figure 3.18, Core	10	0.028	4.85×10^{-3}	5.238×10^{-2}	2.34×10^{19}
Figure 3.18, conal component	5	0.014	1.58×10^{-3}	3.41×10^{-2}	6.10×10^{19}

TABLE 3.2: Theoretical estimation of brightness temperature for multi-component profiles by using Equation (3.44). Chosen pulse period $P = 1$ s, distance $R = 1$ kpc and emitted frequency $\nu = 1$ GHz respectively for simulating pulse profiles. 2nd column represents pulse width in rotation phase, 3rd column gives pulse width in time, 4th column represent maximum value of profile I, 5th column represents flux density in Jansky (Jy), 6th column represents brightness temperature in Kelvin (K).

Figure number	$\delta\phi'$ (°)	$\delta t = (P/360)\delta\phi'$ (s)	I_{max} (10^{-24} erg cm^{-3} Hz^{-1} s)	$S_\nu = (c/\delta t)I_{max}$ (Jy)	T_b (K)
Figure 3.6	80	0.22	5.91×10^{-4}	7.97×10^{6}	5.61×10^{25}
Figure 3.8	30	0.08	1.86×10^{-5}	6.69×10^{5}	3.35×10^{25}

TABLE 3.3: Theoretical estimation of brightness temperature for fully linearly-polarized profiles. Chosen pulse period $P = 1$ s, distance $R = 1$ kpc and emitted frequency $\nu = 1$ GHz for simulating the pulse profiles. We have used the maximum value of parameter I, appearing in Figure 3.6 and Figure 3.8 to compute the flux density and hence the brightness temperature. 2nd column represents pulse width in rotation phase, 3rd column gives pulse width in time, 4th column represent maximum value of profile I, 5th column represents flux density in Jansky (Jy), 6th column represents brightness temperature in Kelvin (K).

get $T_{\rm b} \sim 5.61 \times 10^{25}$ K. Similarly, the Figure 3.8 give the peak value $1.86{\times}10^{-29}$ erg cm^{-3} Hz^{-1} s, which corresponds to the $T_{\rm b}$ around $3.35{\times}10^{25}$ K, respectively. We observe that our brightness temperature calculation based on I from Figures 3.12, 3.14, 3.16, and 3.18 are quite close to the values as reported in Table 3.1.

Point to note here is that we have not fitted to the actual data of any pulsar, we only have estimated the brightness temperature of pulsars and reported in Table 3.1. The pulsars, as shown in Table 3.1, are selected based on the spin period ~ 1 s. As there is no readily available data of brightness temperature of pulsars, we have just estimated and reported in 3.1. The model predicted values of T_b are reported in Tables 3.2 and 3.3.

We have estimated the brightness temperature of sub-pulses (conal components), as reported in Table 3.2, which shows in some cases the brightness temperature of conal components are comparatively more than the core component, as their phase ranges narrower then that of core. We have simulated the multi-component profiles at the chosen emission frequency, i.e., $\nu = 1$ GHz, and comparing $T_{\rm b}$ values between core and the conal components. Note that we are not comparing here the pulses at different frequencies. Though we have not simulated micro-pulses but we can guess that they can show even higher $T_{\rm b}$ as their phase ranges are of the order of microsecond, and $T_{\rm b}$ is inversely proportional to the square of Δt. So the micro-pulses and nanoshots are expected to show even higher $T_{\rm b}$ compared to the sub-pulses.

3.11 Discussion

Our model includes the actual dipolar field lines and viewing geometry which use the accurate coordinates of emission region and also estimate the polarization of

the emitted radiation. The model of Buschauer & Benford (1976) considers an arbitrary trajectory of source and not deduced polarization of emitted radiation, but it is an important property of pulsar radio emission. We have simulated the pulse profiles (see Figures 3.6 – 3.19), and estimated the brightness temperature, which is found to be comparable to the observed values $\sim 10^{25}$ K.

By assuming dipolar magnetic field, we have developed our model and the PA swing predicted agrees with the RVM model (Radhakrishnan & Cooke 1969; Komesaroff 1970). The linear polarization is comparable with the total intensity, and the circular polarization is nearly zero as we have estimated the radiation electric field in the plane of magnetic field lines ($\hat{n} \cdot \hat{v} = 1$) for most of the cases. In actual observations we find some portion of unpolarized emission which could be due to the superposition of radiation field emitted from the sources which are in out of phase. The simulated pulse profiles (shown in Figures 3.6 – 3.9) show the profile broadening and narrowing features due to geometric effects.

From our analysis (specially for simulating profiles from Figures 3.6 – 3.9) we have chosen the longitudinal dimension of the collective system $\leq 30\%$ r_{LC} and transverse dimensions $\xi_0 = \eta_0 = 12$ cm. Transverse dimensions are carefully chosen below the half of emitted radio wavelength ($\lambda_0 = 30$ cm) to satisfy the conditions of coherency. It is evident from our theoretical analysis that the pulsar with smaller $\alpha \sim 2^\circ$ are capable of producing highly energetic electromagnetic radio emission, so as to reach very high brightness temperature of the order of 10^{30} K. But for $\alpha = 10^\circ$ and 45° the brightness temperature reaches to the order of 10^{26} and 10^{25} K respectively for the same dimensions of the collective system. This analysis clearly indicate that pulsars with larger α are not efficient enough to produce highly energetic radio emission compared to lower α.

We have found that if we set the length of collective system at least to 30% r_{LC}, then it is sufficient enough to reach the observed brightness temperature

for all possible α, ranging from 1° to 80°. However, this may not be a unique solution by any means; measured intensities depend on the degree of coherence as well. Also, an emission depth of 30% of the light cylinder radius has aberration-retardation implications on the arrival times, which might introduce more distortions in the structure of pulse profiles. Secondly we have simulated sub-pulse component profiles (see Figures 3.13 – 3.15) by choosing different bunch length ($S_0 \sim 20\%\ r_{LC}$ and transverse dimensions $\xi_0 = \eta_0 \sim 3$ cm). We have produced the multi component profiles by using the collective emission property of source and pulsar emission beam geometry. Although many literature have suggested that source modulation is responsible for sub-pulse generation in pulsar magnetosphere, they did not implement this concept to simulate multi-component pulse profile so far, rather used Gaussian function in both polar and azimuth direction around magnetic axis as a source of perturbation.

Our estimates of brightness temperature from multi-component profiles ranges from 10^{19} K to 10^{21} K, which is quite close to the values existing in literature. But for fully linearly polarized profiles, we are able to reach brightness temperature of the order of 10^{26} K. Although lot of work has been done on pulsar coherent radio emission mechanism but hardly there is an estimation of brightness temperature purely from theoretical perspective. Many have rather tried to generate multi-segment broken power law of pulsar radio spectra and radio luminosity by assuming either different possible scenario of magnetic field trajectory family associated with curvature radiation or different plasma dispersion relation associated with non-linear plasma process. Though the chosen parameters ($P = 1$ s, $\nu = 1$ GHz, and $R = 1$ kpc) for our theoretical estimates are slightly different from those reported in Table 3.1 we can see that theoretical and observational estimates of brightness temperature are roughly matching. We explored polarization properties of radio pulsar without introducing any perturbation effect (like aberration-retardation, polar cap current etc) from our formulation and the polarization angle swing agrees well with the famous rotating vector model, as both

the models assume dipolar magnetic field.

3.12 Conclusion

We decipher some of the salient features of our models below:

1. The polarization angle (PA) swing predicted by our model is well consistent with the rotating vector model (RVM).

2. For small inclination angle α the pulse profiles are usually broader than those for higher values of α. Similarly the sight line impact angle σ makes the profile to become broad when it is negative and narrow when it is positive.

3. In collective radio emission due to plasma process the broadening and narrowing effects are much more sensitive to inclination angle compared to them in incoherent model.

4. Our model predicts the brightness temperature of pulsars $\sim 10^{25}$ K comparable to the values deduced from observation.

5. Our model also predicts symmetric type of circular polarization profiles, which we believes to be induced intrinsically by the property of bunch. But it vanishes, when it is computed exactly at the plane of magnetic field lines.

6. Our model also predicts that, circular polarization corresponding to core component is always more than conal components, which is agreeing with existing literatures.

Chapter 4

Power spectra modeling of a radio pulsar by using non-linear plasma processes

4.1 Introduction

There is no doubt that pulsar discovery is among the most remarkable discoveries in astronomy. They provide a diverse window for observation spanning from radio to gamma-rays. Neutron stars are ubiquitous objects which manifest themselves across a wide range of multi-frequency signals of electromagnetic radiation from radio to gamma-rays, cosmic rays, neutrinos, and gravitational waves. Their extreme density, gravity, and magnetic fields make them unique astrophysical laboratories for the exploration of nuclear physics, general relativity, and electromagnetism at extreme conditions that are hardly possible to achieve in normal conditions. The neutron stars are is famous for producing powerful radio beam, which corresponds

to very high brightness temperature. To understand the underlying physical origin of radio pulsar properties, one must analyze an extensive data set in the radio bands. Population studies and studying time series analysis of pulsar's radio signal can map the electron density distribution along the propagation path associated with the interstellar medium. Nevertheless, in this chapter, I mainly focus on power spectra modeling associated with radio pulsars only. Although the classification of power spectra of radio pulsars is well understood, it is not clear why different pulsars show a different spectra type? One of the major underlying reasons for the issue, as mentioned above, can be attributed to the few archival data availability associated with flux in the radio band, which covers high-frequency regimes beyond 3.5 GHz. But recently, there is some progress associated with flux measurement in the high-frequency radio counterpart; for example, one can see Jankowski et al. (2018), which used a 3.1 GHz wide-band receiver. Hence there is a strong need to make a theoretical model by ascribing specific kinematic theories of plasma in the pulsar magnetosphere to probe power spectra associated with radio emission.

Two proper flux density measurements are the peak flux density, i.e., the maximum intensity of a pulse profile, and the mean flux density, i.e., the integrated intensity of the pulse profile average over the pulse period. In a general point of view, pulsars are weak radio sources whose flux density usually lies in the range of a few μJy to few times Jy approximately.

Usually, the mean flux densities of pulsars have a strong inverse dependence with observing frequency, and it is characterized by some power-law (Sieber 1973). Suppose $S_{\rm mean}$ is the mean observed flux density, and f is the observing frequency. In that case, their dependence is approximated by $S_{\rm mean} = S_0(f/f_0)^{\epsilon}$, where ϵ is the power-law index, S_0 the peak value of flux and f_0 the corresponding frequency to flux maximum. From the literature, it is clear that most of the power spectra exhibited by pulsars can be fitted by a single power law, and a very few fractions of

the pulsar's population show complex behavior, which requires a two-component broken power-law (Maron et al. 2000; Jankowski et al. 2018). The two-component broken power law is probably responsible for two distinct scattering processes, such as SRS and SCS, although in the secondary plasma stream. The model shows that if the electron beam plasma has a smaller spread in the Lorentz factor, then the spectrum's break frequency (where the slope of the power spectrum gets changed) is shifted to a higher observed frequency. So in the study, I have shown that the spread of the Lorentz factor ($\delta\gamma$) decides the break frequency. For a particular value of smaller $\delta\gamma$ can make the break frequency preferentially so high that the SCS process doesn't occur in the radio frequency regime. In this case, a full radio spectrum can be reproduced by a single power law. However, one can give a more straightforward interpretation of break frequencies, at least in some cases: core and conal components have different spectra, with cores stronger at lower frequencies. When the total flux density (integrated across the pulse) is used to form the spectrum, we may expect to see a break frequency. In this regard, one can see the interpretations and expectations given, for example, by Rankin (1983, 1990, 1993a) and Lyne & Manchester (1988).

Another intriguing phenomenon of pulsar power spectra is low frequency turn over, which can be seen to happen below 100 MHz and can be described by free-free absorption by electrons (Malofeev et al. 1996). Apart from that, a spectral increase or turn-up has been observed in a few pulsars at millimeter wavelength. Some earlier literature, e.g, Morris et al. (1997), suggests that the successful highest frequency over which pulsar observation was done is at 87 GHz. But now, in the advent of modern telescope facilities, Jankowski et al. (2018) have produced a larger data set of pulsar's power spectrum: around 441 pulsars by using Parkes multi-beam radio telescope, with a strong emphasis of their survey lies in both higher frequency as well as in the lower frequency of the radio continuum. For exploring the lower frequency spectral behavior, several low-frequency surveys such as Long Wavelength Array (LWA), Low-Frequency Array (LOFAR), and

Murchinson Widefield Array (MWA) (Stovall et al. 2015; Bell et al. 2016; Bilous et al. 2016). Maron et al. (2000) has been done and shown that the spectral index associated with a single power law of radio pulsars lies in the range of $0 \leq \epsilon \leq -4$ with a mean value of index -1.8. Moreover, an independent study by Kramer et al. (1998) and Toscano et al. (1998) shows that the spectral index of millisecond pulsar doesn't differ too much from normal pulsars. Since the discovery of pulsars, several hundred publications containing pulsar flux or energy data have been displayed in the literature, but only a few of them have reported the integrated power spectra. Although more than 50 years have gone after pulsar discovery, only a few papers show full power spectra of pulsars in the radio band. The first pulsar spectrum of PSR B1919+21, covering the frequency range from 85 MHz to 2.7 GHz was published by Robinson et al. (1968). Rankin et al. (1970) made another attempt to produce a power spectrum of PSRB 0531+21, over a wide frequency range. Sieber (1973) and Malofeev (1993) made extensive presentations and analysis of 27 and 45 pulsars, respectively, over a wide range of frequency, compiled from their own observations as well as from literature. Sieber (1973) has pointed out that one must be careful to compute energy values at different frequencies, as the intrinsic intensity can be time-dependent. Seiradakis et al. (1995) published a collection of high energy data on pulsar profiles and flux densities for 183 pulsars at 1.4 GHz, 46 pulsars at 4.85 GHz, and 24 at very high frequency 10.5 GHz. The pulsars flux density catalog at a frequency ranging from 400 MHz to 1.6 GHz was published by Lorimer et al. (1995).

Pulsar does show significant variations in their power spectra daily, but the average range, in general, corresponds closely to that compiled from the literature (Brueck 1978). The fact that intrinsic intensity of pulsar is highly time-dependent was adequately taken care of by Malofeev & Malov (1980) and had published pulse energy of 39 pulsars at low frequency. Subsequently, Izvekova et al. (1981) produced average spectra by compiling a pulse energy data set. Slee et al. (1986) have produced spectra of several pulsars located in the southern hemisphere from

a low-frequency energy survey. Later on, Foster et al. (1991) have presented spectra of four-millisecond pulsars. Later on, Kramer et al. (1999) and Kramer (1998) showed the results of flux density measurements and emission properties with detailed analysis of their spectral behavior of 23-millisecond pulsars at frequencies 1.4 GHz and 1.7 GHz. Kijak et al. (1998) first showed a large sample of flux densities of weak pulsars at 4.85 GHz. van Ommen et al. (1997) presented polarimetric data together with flux density measurements for a large number of southern pulsars at frequencies of 800 MHz and 950 MHz. Maron et al. (2000) have shown from their analysis of 281 pulsars sample, taken from EPN database (Lorimer et al. 1995; Kramer et al. 1998; Kramer et al. 1999), that majority of the pulsars can be modeled by a single power-law with an average index of approximately -1.8 and 10% requires a two-segmented broken type of power law. Rankin (1993b) and Gil (1993) have developed methods allowing unique identification of inner and outer cones of pulsar beams. Using this method Malofeev (1993) has shown that 70% of inner cone dominated pulsars falls in the first group of pulsars, i.e., single power law, and 56% outer cone dominated pulsars falls in the category of two segmented power law.

There are many publications on different aspects of pulsar emission theory (Sturrock 1971; Ruderman & Sutherland 1975; Cheng et al. 1986) etc., but very few have investigated the shape of the spectrum (Buschauer & Benford 1976; Benford & Buschauer 1977; Melrose 1978; Michel 1978; Buschauer & Benford 1980). Yang & Zhang (2018) have investigated the power spectrum theoretically by using the formulation of general theory of coherent curvature radiation (Buschauer & Benford 1976), different topology associated with three-dimensional bunch embedded on dipolar magnetic field lines, a different scenario of trajectories of particles and energy distribution function of electrons. Observation relevant to power spectra was done by Jankowski et al. (2018) with a comparatively bigger sample of 441 radio pulsars. Their rigorous study and analysis help us to understand the different morphological classification of pulsar power spectra. They have classified

power spectra into three broad categories: (i) simple power-law, (ii) two-segmented broken power law, and (iii) log parabolic spectrum. According to their study, the majority, around 79% can be modeled by a simple power-law, and the rest of the morphological structure falls in several miscellaneous categories like broken power-law or log parabolic spectrum. In addition to the different categories of spectra, some other mild features associated with power spectra can be observed, such as low-frequency turn over, high-frequency flattening or turning up, GPS pulsars (Gigahertz peaked spectrum), etc (Jankowski et al. 2018). The details of this property are discussed in the discussion section as well as in the summary of the model.

Gangadhara & Krishan (1992) have successfully applied SRS and SCS process on AGN to reproduce the power spectra of 3C273. To explain the power spectra associated with AGN, most of the literature incorporates the shock model and geometry of the inner torus structure. But here, one can reproduce power spectra of AGN in X-ray regime by considering the interaction between outwardly moving electron jets from the central engine and plasma in the accretion disk, without encountering much difficulty. So far, the idea of SRS and SCS processes has not been put forward to reproduce radio pulsars power spectra.

In this Chapter, I have implemented SRS and SCS as potential tools to reproduce the power spectra of the pulsars, e.g., PSRB 0329+54 and PSRB 2111+46, theoretically in radio regime by introducing two sets of guess values of plasma indices, required by the SRS and SCS model, respectively. Since both the pulsars show the clear core-cone structure, we considered these two pulsars to model their spectra and plan to continue a similar study on many more in my following works. I have shown that one can exactly reproduce the power spectra of different radio pulsars if the model's plasma parameter indices values are perfectly tuned. In section 4.2, I have briefly discussed the modeling of power spectra of radio pulsars. In section 4.3, I have elaborated the mathematical formulation associated with the

presented model. Finally, Poynting flux expression in the lab frame is shown with a brief overview to set up a numerical solution to compute the flux. In section 4.4, I have discussed the main results associated with power spectra of radio pulsar of PSRB 0329+54 and PSRB 2111+46, and finally end up with a discussion and a conclusion in sections 4.5 and 4.6, respectively.

4.2 The modeling of radio spectra of pulsars using plasma mechanisms

The non-thermal continuum of pulsars spectra could be due to an outcome of specific plasma mechanisms excited by the backwardly moving curvature radiation by an outflowing relativistic pair plasma. There are basically three types of processes in which an electromagnetic wave can undergo scattering in a plasma:

1. If it occurs by a longitudinal electron plasma mode, it is called Stimulated Raman Scattering (SRS).
2. If it occurs by a weakly damped longitudinal electron plasma mode, it is called Stimulated Compton Scattering (SCS).
3. If the scattering of radiation occurs by a single electron, it is called Compton Scattering, hereafter (CS).

In this section, I focus on the underlying plasma processes involved in the basic interaction scenario of pump wave with the relativistically outflowing plasma (see Figure 4.1), and the generation of power spectra of radio pulsars. In the following section, I have shown radio spectra of some pulsars based on published data by Malofeev (1993) and superposed them with theoretically generated spectra. It

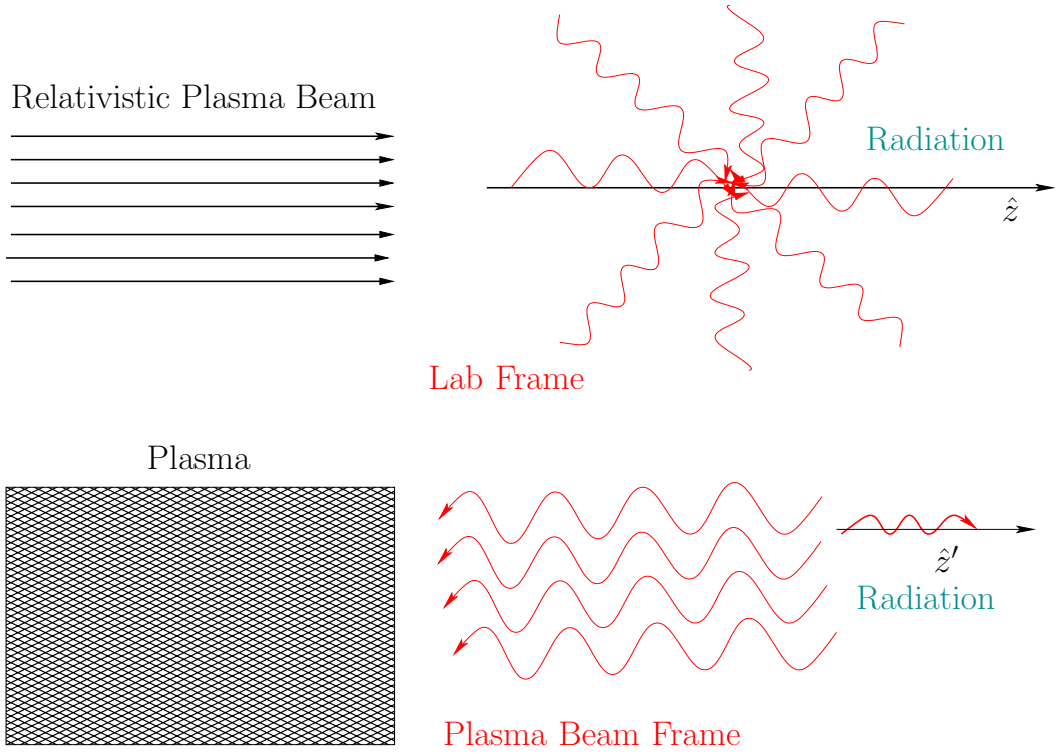

FIGURE 4.1: The above figure illustrates the relativistic beaming effects: (i) beam plasma is moving through the background radiation in the lab frame, and (ii) beamed background radiation interact with the plasma in the beam frame (plasma rest frame).

is shown that for most of the pulsars, intrinsic spectra can be either modeled by a simple power-law or by a two-component segmented broken power law. Two different regimes are expected to exist in the frequency domain for the two-segmented broken power law, hoping that each one is associated with either of the two distinct plasma processes depending upon the plasma conditions.

So, it is possible to generate an empirical formula for each radio pulsar with different plasma indices. The background radiation in the pulsar magnetosphere can act as a pump wave to drive the instability in pair plasma. The phase-matching conditions must be met between the pump and plasma wave for interacting resonantly and exchanging energy. Consequently, input radiation (pump) gets enhanced and backscattered. I assume that pair plasma jets follow the Maxwellian distribution in the plasma rest frame, as the bulk average velocity is zero there.

Now, suppose the phase velocity of background radiation or pump wave falls in the negative slope region of the electrons velocity distribution curve. In that case, electrons will get back energy from the pump wave. However, in the positive slope region, it has precisely the opposite trends, i.e., electrons will transfer energy to the pump waves. Consequently, the Langmuir wave will suffer Landau damping, and the scattered wave amplitude will grow with time. It attains some non-linear unstable stage and finally dissipates energy in terms of radio emission.

4.2.1 Plasma processes involved in radio pulsar

Pulsars are extremely efficient generators of radiation below $\sim$ 10 GHz, which is believed to be the relativistic electron-positron plasma. Benford & Buschauer (1977) have explained three distinct emission regions associated with pulsars radio spectra based on their theory of coherent pulsar radio emission by antenna mechanism. Region 1 corresponds to the radio emission region, where plasma waves grow by a two-stream instability process and emit intense radio pulses. Region 2 is the part of the region of spectra, where it starts showing low-frequency turnover. This region is flat and narrow, where field-plasma pressure is at a balanced point, i.e., energy density due to dipolar magnetic field strictly gets equal to radiation energy density. The third region is the turnover of radio flux in a lower frequency regime. When the energy density of relativistic plasma exceeds the magnetic field energy density, radio flux turnover can be either attributed to the break up of coherence of the associated plasma particles responsible for radiation or self-absorption.

We will briefly discuss the scattering of the incident electromagnetic wave (pump) by the Langmuir plasma wave in two different regimes, namely SRS and SCS. There are expected to have the potentiality to reproduce the complete spectra of radio pulsars. In the case where the velocity of radiating plasma is perpendicular to the acceleration, there can exist two beaming lobes, see Figure (4.11d) in Rybicki

& Lightman (1985). One beaming lobe arising from the emission of curvature radiation in the forward direction of the magnetic field line tangent and another weaker lobe in the backward direction. The backward lobe comes back to the neutron star surface and is expected to serve as a source of incident pump wave in the pulsar ambient medium and interacts with the relativistically moving pair plasma beam. This non-thermal low-frequency electromagnetic wave is considered a pump, which can drive the parametric instabilities. This low-frequency wave may be recognized as backwardly moving curvature photons. For instance, the pump wave considered in the model can be roughly characterized by the backwardly moving EM wave as follows:

$$\vec{E_i} = E_0 \exp[i(\vec{k_i} \cdot \vec{r} + \omega_i t)]\hat{e},$$

where E_0 is the amplitude of EM wave, which is proportional to the square root of the incoming flux of pump wave, $\vec{k_i}$ the wave vector of the incoming pump wave, and ω the angular frequency of pump wave. Angular frequency of pump wave ω_i and wave vector of pump wave $\vec{k_i}$ can be determined from phase-matching condition. The basic scenario consists of a relativistic pair plasma beam that propagates radially outwards from the neutron star and interacts with the pump. It produces radiation at a higher frequency in the radio band. The scattering of the soft photons by pair plasma wave or the collective mode of the relativistic pair plasma beam can be studied more easily in the rest frames of electrons. This process resembles the inverse Compton scattering process and has just the right features to explain power spectra in pulsars.

Now I state the three conditions below under which SRS, SCS, and CS become operative:

1. When $k'\lambda'_D \leqslant 0.4$, then the growth rate of the scattered wave is positive. Therefore the imparted energy to the pump wave will grow with time. This

process is called SRS. Here k' is the wave number corresponding to Langmuir plasma wave, and λ'_D is Debye length.

2. When $k'\lambda'_D \geqslant 0.4$ then the growth rate of the plasma wave will not be positive, rather it will be a weakly damped wave. This process is called SCS.

3. Next, when $k'\lambda'_D \gg 1$, the plasma wave will be highly damped, and the process is called Compton scattering.

4.3 Mathematical formulation of SRS and SCS processes

In the beam frame, the pair will be at rest, and the emitted radiation will be confined to a cone of angular width $\sim 1/\gamma$ because of relativistic beaming, where γ is the relativistic Lorentz factor. Due to the interaction of pump wave with beam plasma, Langmuir plasma wave gets excited due to the onset of SRS instability. Then the flux of backwardly scattered radiation (Stokes mode) is emitted. Since it is much simpler to do the non-relativistic calculation in the beam frame, I compute growth rate and scattered flux in the beam frame then transfer these quantities to the laboratory frame. Consider a linearly polarized electromagnetic wave with electric field (Gangadhara & Krishan 1992):

$$\vec{E_i} = \frac{1}{2}[E_i \exp(i(\vec{k_i}.\vec{r_i} - \omega_i t))\hat{e}_i + cc], \tag{4.1}$$

undergoes scattering from a relativistic beam plasma moving in the z–direction (see Figure 4.1) in the laboratory frame, where cc stands for complex conjugate. In general, $\vec{k_i}$ and ω_i represent the wave-vector and angular frequency of the incident

pump wave. I use primes to denote the quantities in the beam frame and without primes in the laboratory frame.

In addition to the Lorentz transformation of the incident electric field, magnetic field, wave-vector, and angular frequency associated with pump wave (one can see standard textbook like Jackson (1975)), I need to have the transformation of plasma frequency ω_p, the beam thermal speed v_t, and the growth rate Γ. Since the Lorentz contraction increases both density and the effective mass by a factor γ, the plasma frequency $\omega_p = \sqrt{(4\pi nq^2)/m}$ is a Lorentz invariant. Here n is the number density of the pair plasma, and m is the mass of pair plasma particles. The thermal speed v_t in the beam frame can be expressed in terms of the energy spread of the beam in the laboratory frame as follows. The spread of the beam velocity δv_b in the laboratory frame can be expressed in terms of the spread in γ as,

$$\delta v_b \approx c\frac{\delta\gamma}{\gamma^3}. \tag{4.2}$$

Now using the Lorentz transformation of velocity I obtain,

$$\delta v_b = \delta v_z = \frac{\delta v'_z}{\gamma^2(1+(v_b v'_z)/c^2)^2} \approx \frac{\delta v'_z}{\gamma^2} = \frac{v_t}{\gamma^2}, \tag{4.3}$$

as $v'_z = 0$. So, with the help of equation (4.2), I get the thermal speed of plasma particles in the beam frame as

$$v_t = c\frac{\delta\gamma}{\gamma}. \tag{4.4}$$

I now consider the transformation of the growth rate Γ. If a wave with slowly varying amplitude $\mathrm{A}(z', t')$ grows in time and space at a temporal growth rate Γ' in the beam frame, then A' satisfies the following equation:

$$\frac{\partial A'}{\partial t'} + v'_g\frac{\partial A'}{\partial z'} = \Gamma' A', \tag{4.5}$$

where v'_g is the group velocity in the beam frame. The Lorentz transformation of equation (4.5) gives

$$\frac{\partial A'}{\partial t} + \frac{v'_g + v_b}{1 + (v_b v'_g)/c^2}\frac{\partial A'}{\partial z} = \frac{\Gamma'}{\gamma(1 + v_b v'_g/c^2)}A'. \tag{4.6}$$

The amplitude A in the laboratory frame is linearly proportional to A′. So the expression of group velocity as well as the growth rate of wave in the laboratory frame can be expressed as:

$$v_g = \frac{v'_g + v_b}{1 + (v_b v'_g)/c^2}, \tag{4.7}$$

$$\Gamma = \frac{\Gamma'}{\gamma(1 + (v_b v'_g)/c^2)} \approx \frac{\Gamma'}{2\gamma}, \tag{4.8}$$

for $v_b \approx v'_g \approx c$. The derivation of the transformation of wave amplitude is given in Appendix C.

4.3.1 Parametric instability

In the equilibrium, pair plasma particles oscillate with velocity v'_i in the pump field $\vec{E}'_i$. Now I assume that in plasma, propagating density perturbation $\rho'(\vec{k}', \omega')$ associated with plasma wave disturbs this equilibrium. This density perturbation combined with the oscillatory velocity v'_i produce currents at $(\vec{k}'_i \pm \vec{k}',\ \omega'_i \pm \omega')$. These currents will generate mixed electromagnetic-electrostatic side band modes at $(\vec{k}'_i \pm \vec{k}',\ \omega'_i \pm \omega')$. These side-band modes, in turn, interact with the pump wave field, producing a pondermotive bunching force proportional to $\nabla \vec{E}'^{\,2}$, which intern amplifies the original density perturbation. Thus there is a positive feedback system which leads to an instability, called parametric instability. The original density perturbation and the side band modes provided that the rate of transfer of energy to them exceeds their intrinsic damping rates, such as collisional damping.

I consider here a special case of parametric instability in which the high-frequency side-band modes are predominantly electromagnetic. So I am dealing with a case of stimulated scattering, where a pump (electromagnetic waves) excites plasma wave ($\vec{k}',\ \omega'$) and two new electromagnetic waves at shifted frequencies namely: Stokes mode mode ($\vec{k}'_s,\ \omega'_s$) and anti-stokes mode ($\vec{k}'_{as},\ \omega'_{as}$). The instability is excited when the following phase matching conditions are satisfied:

$$\omega'_i = \omega'_s + \omega', \tag{4.9}$$

$$\vec{k}'_i = \vec{k}'_s + \vec{k}', \tag{4.10}$$

$$\omega'_i + \omega' = \omega'_{as}, \tag{4.11}$$

$$\vec{k}'_i + \vec{k}' = \vec{k}'_{as}. \tag{4.12}$$

Each of the excited modes satisfies it's own dispersion relation in the plasma medium. The dispersion relation of the plasma wave in the beam frame is given by Hasegawa & Mima (1978):

$$1 - \frac{\omega_p^2}{k'^{\,2}} \int_{-\infty}^{\infty} \frac{\partial f/\partial \vec{v}}{\vec{v} - (\omega' + i\ o)/\vec{k}'} d\vec{v} = 0, \tag{4.13}$$

where $f(v)$ is assumed to be the Maxwellian velocity distribution function of the pair plasma particles in the beam frame and o is the small imaginary part of frequency associated with the electrostatic perturbation. The numerical solution of equation (4.13) is

$$\omega' \approx \omega_p \qquad \text{for} \quad k'\lambda'_D \ll 0.4; \tag{4.14}$$

$$\omega' \approx k' v_t (1 - io(1)) \qquad \text{for} \quad k'\lambda'_D \geq 0.4, \tag{4.15}$$

where $v_t = [(2/n') \int_{\infty}^{\infty} v^2 f dv]^{1/2}$ and $\lambda'_D = (k_B T/(4\pi n' e^2))^{1/2}$ are the thermal speed and Debye length, respectively. Equation (4.15) indicates that if $k'\lambda'_D \geq 0.4$ then the plasma mode loses its wave nature because of its large Landau damping. The

derivation of pondermotive force is given Appendix D.

4.3.2 Backscattering process

The dispersion relation for ordinary waves in pulsar plasma is given as follows (Petrova & Lyubarskii 2000):

$$(1 - n_{\parallel}^2)\Big(1 - \frac{\omega_p^2}{\omega^2\gamma^3(1 - n_{\parallel}\beta)^2}\Big) - n_{\perp}^2 = 0. \tag{4.16}$$

Here, refractive index parallel and perpendicular to magnetic field line are $n_{\parallel} = ck_{\parallel}/\omega$ and $n_{\perp} = ck_{\perp}/\omega$ respectively, where $k_{\parallel}$ and $k_{\perp}$ are the propagation wave vectors parallel and perpendicular to magnetic field line, ω_p the plasma frequency. Since the pulsar radio beam is emitted tangentially to magnetic field lines, $n_{\perp} \approx 0$. Therefore the equation (4.16) reduces to

$$(1 - n_{\parallel}^2)\Big(1 - \frac{\omega_p^2}{\omega^2\gamma^3(1 - n_{\parallel}\beta)^2}\Big) = 0. \tag{4.17}$$

From equation (4.17), I can see one root is $n_{\parallel} = 1$, which implies that $\omega = ck_{\parallel}$. So this particular mode will travel at light velocity, without much interfering with the plasma. Next the second and third roots give:

$$\omega = ck_{\parallel}\beta \pm \frac{\omega_p}{\gamma^{3/2}}. \tag{4.18}$$

The positive root in equation (4.18) corresponds to the superluminal wave, and the negative root in equation (4.18) corresponds to the subluminal wave. For the case of high Lorentz factor and low density plasma, we have $\omega_p/\gamma^{3/2} \ll ck_{\parallel}\beta$. Therefore the second term in equation (4.18) can be neglected. If the emission takes place at a high altitude in the pulsar magnetosphere, where the plasma density is expected to be low there. Then there will be an almost negligible difference between superluminal and subluminal waves, and they both will travel

at light speed without much interfering with the plasma. For plasma density 7700 cm^{-3} and $\gamma = 1000$, the second term in equation (4.18), $\omega_p/\gamma^{3/2} \approx 150$ rad s^{-1}. So with respect to the first term in equation (4.18), the second term can be neglected. Therefore I can approximately write the dispersion relation of EM wave in plasma frame for simplicity as $\omega'_s \approx ck'_s$ for $\beta = 1$. Here ω'_s and k'_s are the angular frequency and propagation vector of EM wave in plasma frame respectively and k' can be thought of to be analogous with $k_\parallel$.

Now the Stokes mode and anti-Stokes mode are excited by the onset of parametric instability, and satisfy the aforementioned dispersion relation. If the pump wave undergoes back-scattering, i.e., $\vec{k}'_i = -\vec{k}'_s$ and for $(\omega'_i, \omega'_s) \gg \omega_{pe}/\gamma^{3/2}$, so that $\omega'_i = k'_i c$, $\omega'_s = k'_s c$, $|k'_i| \approx |k'_s|$, I get $k' \approx 2k'_s$ (see equation (4.10)). Also in the co-moving frame of plasma, magnetic lines of force as experienced by particles will be frozen. So in the co-moving frame of plasma, the effect of magnetic field on dispersion relation can be used in moderated sense. Hence for a given quality of a beam, if ω'_s is increased by increasing pump frequency ω'_i, then k' which may be smaller than $0.4/\lambda_D$ for some particular plasma constraints, becomes larger than $0.4/\lambda'_D$ at some values of ω'_s. Now, I know that for $k'\lambda'_D \geq 0.4$, the plasma waves suffer strong landau damping. Thus there are two distinct scattering processes: (i) the scattering of an electromagnetic wave of a weakly damped plasma wave known as SRS and (ii) the scattering by a damped plasma wave known as SCS. Hence there exists a critical frequency of the scattered wave above which scattering occurs through the SCS process and below predominantly through the SRS process. If $\omega_i \gg \omega_p$ or $k'\lambda'_D \gg 1$ then the plasma wave vanishes. In this case, the incident photon undergoes Compton scattering from relativistic electrons.

Now in lab frame scattered frequency will transform like the following way:

$$\omega_s = \gamma(\omega'_s + k'_s v_b). \tag{4.19}$$

For $v_b \approx c$ and $\omega'_s = k'_s c$, I get

$$\omega_s \approx 2\gamma\omega'_s. \tag{4.20}$$

We can define a critical frequency $\omega_{cr} = \omega_s$ of the scattered wave, corresponding to $k'\lambda'_D = 0.4$, where $\lambda'_D = (v_t/(\sqrt{2}\omega_p)$ is the Debye length. Using the phase-matching condition for back-scattering, i.e., $k' = 2k'_s$, we get $k' = 0.4\sqrt{2}\omega_p/v_t$ and $k'_s = 0.4\sqrt{2}\omega_p/2v_t$. Therefore we have,

$$\omega'_s \approx ck'_s \approx \frac{0.4c\sqrt{2}\omega_p}{2v_t}. \tag{4.21}$$

Substituting the value of equation (4.21) into equation (4.20) we obtain

$$\omega_{cr} = 0.4\sqrt{2}\gamma\frac{c\omega_p}{v_t}. \tag{4.22}$$

Now using the value of v_t from the expression (4.4) we have

$$\omega_{cr} = 0.4\sqrt{2}\omega_p\frac{\gamma^2}{\delta\gamma}. \tag{4.23}$$

Thus the critical frequency depends on the relative spread $\delta\gamma/\gamma$ of the beam energy observed in the laboratory frame, as well as on the beam plasma density n and γ.

4.3.3 The growth rates of SRS and SCS process

If the excited side-band modes are predominantly electromagnetic, then the plasma dispersion relation to describe parametric instability is given by (Liu & Kaw 1976):

$$1 + \frac{1}{\chi'(k',\omega')} = k'^2\left[\frac{|\vec{k}'_- \times \vec{v}'_i|^2}{k'^2_- D_-} + \frac{|\vec{k}'_+ \times \vec{v}'_i|^2}{k'^2_+ D_+}\right], \tag{4.24}$$

where $\vec{v_i'} = (q\vec{E'}/m'\omega_i')$ is the quiver velocity of the pair plasma particles, $\omega_\pm' = \omega_i' \pm \omega'$, $\vec{k}_\pm' = \vec{k}_i' \pm \vec{k}'$ and

$$D_\pm = c^2 k'^2 \pm 2\vec{k}'.\vec{k}_i' c^2 \mp 2\omega'\omega_i' - \omega'^2. \tag{4.25}$$

For three-wave SRS process, in equation (4.24), ω' and $\vec{k}'$ become the angular frequency and the wave vector of the plasma wave (ω', $\vec{k}'$). The susceptibility function is given by Fried & Conte (1961):

$$\chi'(k', \omega') = \frac{1}{(k'\lambda_D')^2}\left[1 + \frac{\omega'}{k'v_t} Z(\omega'/(k'v_t))\right], \tag{4.26}$$

where

$$Z(\omega'/(k'v)) = \frac{1}{\sqrt{\pi}} \int_{-\infty}^{\infty} \frac{e^{-x^2}}{x - (\omega'/(k'v_t))} dx \tag{4.27}$$

is the plasma dispersion function. The $\chi'(k', \omega')$ has the following asymptotic forms:

$$\begin{aligned} \chi'(k', \omega') &= -\frac{\omega_p^2}{\omega'^2}\left(1 + \frac{3}{2}\frac{k'^2 v_t^2}{\omega'^2}\right) + i\sqrt{\pi}(k'\lambda_D')^2 \exp[-\omega'^2/(k'v_t)^2], \\ &\qquad\qquad \text{for } \omega' \gg k'v_t \\ &= \frac{1}{(k'\lambda_D')^2}\left(1 + i\sqrt{\pi}\frac{\omega'}{k'v_t}\right) \qquad \text{for } \omega' \ll k'v_t. \end{aligned} \tag{4.28}$$

In the case of back-scattering, $\phi_s = \arccos(\hat{k}_i \cdot \hat{k}_s) = 180°$, $\mathrm{D}_- \approx 0$ and $\mathrm{D}_+ \neq 0$. Therefore in the case of back-scattering, the Stokes mode is excited but not the anti-Stokes mode. But in the case of right angle scattering $\phi_s' = 90°$ both $D_- \approx 0$ and $D_+ \approx 0$, and hence both Stokes and anti-Stokes mode can be excited.

When $\omega' > k'v_t$, the plasma mode is well defined and weakly damped. In this case we get $\omega' = \omega_r' + i\Gamma_{SRS}'$ and the asymptotic form of plasma susceptibility

function χ', one can find growth rate (Drake et al. 1974; Liu & Kaw 1976),

$$\Gamma'_{SRS} = -\frac{1}{2}(\Gamma'_l + \Gamma'_c) \pm \frac{1}{2}[(\Gamma'_l - \Gamma'_c)^2 + 4\frac{v'^2_i}{c^2}\sin^2(\psi'_s)\cos^2(\theta')\omega'_i\omega_p]^{1/2}. \quad (4.29)$$

This is the expression for the growth rate of the SRS of an electromagnetic wave in a plasma. Here $\Gamma'_c = (\omega'_p/\omega'_s)^2\nu'_{ep}/2$, denoting the collisional damping rate of the scattered electromagnetic wave $(\omega'_s, \vec{k}'_s)$. In equation (4.29), Γ'_l denotes Landau damping rate of plasma mode, whose expression is the following

$$\Gamma'_l = \frac{\sqrt{\pi}}{2}\frac{\omega_p}{(k'\lambda'_D)^3}\exp[-\frac{1}{(k'\lambda'_D)^2} - 3/2] + \nu'_{ep}. \quad (4.30)$$

Here extra term $\nu'_{ep} = 4\pi n' e^4 \log\Lambda/(m'^2 v_t^3)$ in equation t(4.30) is introduced to denote the electron-positron collisional damping rate of plasma mode, where v_t is the thermal velocity and $\log\Lambda \approx 10$ is the coulomb logarithm. In equation (4.29), θ' is the angle between $\vec{k}'_i$ and $\vec{k}'$, and ψ'_s is the angle between $\vec{E}'_i$ and $\vec{E}'_s$. The growth rate is maximum when the scattered wave has the same polarization as the incident wave i.e., $\psi'_s = 0$.

By setting $\Gamma'_{SRS} = 0$ in equation (4.29), I get

$$\Big(\frac{v'_i}{c}\Big)^2 = \frac{\Gamma'_l\Gamma'_c}{\omega'_i\omega_p\sin^2(\psi'_s)\cos^2(\theta')}. \quad (4.31)$$

Now using the definition of poynting flux $S' = c|\vec{E}'^2_i|/(8\pi)$ and $\vec{v}'_i = q\vec{E}_i/(m'\omega'_i)$, I get

$$S' = \frac{c}{8\pi}\Big(\frac{m'\omega'_i v'_i}{q}\Big)^2. \quad (4.32)$$

Now, using equations (4.31) and (4.32), I get the threshold flux required for the excitation of SRS instability,

$$S_{thr} = \frac{c^3}{8\pi}\Big(\frac{m'}{q}\Big)^2\frac{\omega'_i}{\omega_p}\frac{\Gamma'_l\Gamma'_c}{\sin^2(\psi'_s)\cos^2(\theta')}. \quad (4.33)$$

I now look for plasma mode with frequency $\omega' \approx k' v_t$. In this region, the susceptibility function cannot be expanded. So for the case $k'\lambda'_D \geq 0.4$, the plasma mode is heavily damped in this particular domain. Thus from the imaginary component of equation (4.24), one can write (Gangadhara & Krishan 1992),

$$\Gamma'_{SCS} = -2\frac{v_i'^2}{c^2}\sin^2(\psi'_s)\cos^2(\theta')\omega'_i \mathrm{Im}\Big(\frac{\chi'}{1+\chi'}\Big) - \Gamma'_c. \tag{4.34}$$

Threshold condition can be obtained by setting $\Gamma'_{SCS} = 0$.

4.3.4 Brief overview on finding numerical solution

When $\omega' \approx \omega_p \leq k'\lambda'_D$ or $k'\lambda'_D \approx 0.4$, it is not possible to expand the susceptibility function $\chi'(\omega', k')$ into an asymptotic series. Therefore introducing $\omega' = \omega'_r + i\Gamma'$, I have solved the equation (4.24) for typical pulsar magnetosphere by including all possible damping effects. After separating the real and imaginary part of equation (4.24) I get two coupled equations. To find ω'_r and Γ', I have to solve these two equations with the plasma dispersion function i.e., equation (4.27). I have to find the value of k' such that it satisfies equations (4.9) – (4.13) and $D_- \approx 0$. Currently, I have chosen two radio sources PSRB 0329+54 and PSRB 2111+46, and generated the best fitting values associated with the indices of plasma parameters and flux variation of incident pump wave. So initially I assume that the plasma parameters like density, incident pump wave frequency and flux follow the spatial variations:

$$n = n_0(r/R_0)^{-\alpha_1}, \tag{4.35}$$

$$\nu_i = \nu_0(r/R_0)^{-\alpha_2}, \tag{4.36}$$

$$f_{\nu i} = f_0(r/R_0)^{-\alpha_3}, \tag{4.37}$$

where r is the radial distance from the center of neutron star. I consider the dipolar magnetic configuration, so that, I can choose $\alpha_1 = 3$. Also I have not

considered any spatial variation associated with Lorentz factor, rather it is taken to be constant, as the plasma does loose significant energy in the radio band. But for the case of PSRB 0329+54, I have assumed slow spatial variation associated with Lorentz factor at the lower frequency radio counterpart. In section 4.4 it is shown that, Lorentz factor is constant for force-free configuration. But in reality there might be very slow spatial variation associated with Lorentz factor, depends upon whether the gap above polar cap is completely shielded or not. At a few kilometer above the polar cap region, parallel component of the induced electric field approximately gets canceled by the field of secondary charged particles, generated through pair cascade process. So the general equation of motion becomes almost force-free. Now, I have assumed some suitably chosen plasma density n_0, Lorentz factor γ_0 for a typical pulsar and perform multi-variable fitting for a chosen radio pulsar to get the best fitting indices associated with plasma parameters appearing in the theoretical model. Here $R_0 = 10$ km is the radius of neutron star and initial Lorentz factor of $\gamma_0 \sim 1000$ for radio pulsars. But in the simulation Lorentz factor is chosen 560. The spread of particles energy associated with Lorentz factor of electron beam $\delta\gamma$ can be determined from the expression of critical frequency (see equation (4.23)), once the particle density and Lorentz factor are provided. Other parameters involved here are ϕ'_s, ψ'_s and θ'_e. It is found that growth rate is maximum for back-scattering, i.e., for $\phi'_s = 180^\circ$ and for same polarization state of incident and scattered electric fiel, i.e., for $\psi'_s = 0$. So I used $\phi'_s = 180^\circ$ and $\psi'_s = 0^\circ$ to get numerical solution.

By expressing the spatial variable r in terms of emitted frequency, I have reduced the number of unknown variables and the difficulty of computing the growth rate and achieving the multi-variable fitting (see appendix B). Spatial variation related term r involved via equations (4.35) – (4.37) and does appearing in the final expression of flux density equation (4.52). But in order to compute the power spectra precisely from a theoretical point of view, a power-law with frequency, associated with angular width of emitted radio beam $\Gamma_w = C_1(\nu/\nu_0)^{m/2}$ is assumed.

If you look into the expression of r_{em} (see equation (B.7) with index is chosen (m/2)), it is linked to the expression of poynting flux (See equation (4.51)) via the expression R_b. Here C_1 is the normalization constant, which is chosen to be 1 in the model, and the scaling is done with respect to ν_0. Nevertheless, the main aim is to compute the power spectra of some specific radio pulsars with accurate slopes. Therefore the value of R_b (angular width of radio beam), appearing in the equation (4.51), is computed with the help of equation (B.7) with $\Gamma_w = C_1(\nu/\nu_0)^{m/2}$.

4.3.5 Transformation of poynting flux

The scattered radiation fields $\vec{E}'_s$ and $\vec{B}'_s$ get enhanced as the instability progresses. At critical frequency the Lorentz force $q(\vec{v}'_i \times \vec{B}'_s)$ begins to act on the plasma particles. The associated electric potential traps the beam plasma pair particles which results in an increase in their thermal speed. The trapping potential ϕ'_t, due to the Lorentz force, is obtained as

$$\left|\frac{\partial \phi'_t}{\partial z}\right| = |k'\phi'_t| \approx \frac{1}{c}|v'_i B'_s|, \tag{4.38}$$

so that

$$\phi'_t \approx \frac{|v'_i||B'_s|}{k'c}. \tag{4.39}$$

The effective thermal speed v_t^{eff} due to the trapping potential is

$$v_t^{eff} = (2q\phi'_t/m)^{1/2}. \tag{4.40}$$

The growth rate of the instability reaches a maximum ($\Gamma' = \Gamma'_m$) at the critical frequency when $k' = \omega_p/v_t^{eff}$, because for $v_t^{eff} \geq \omega_p/k'$, Landau damping incepts to play a dominant role and the gain changes from Raman to Compton. Therefore the magnetic field of the scattered radiation, at the critical frequency, is obtained by substituting for $v^{eff} \approx \omega_p/k'$ into equation (4.40) and thereafter using equation

(4.39):

$$B'_{sm} = \frac{m}{2q}\frac{c}{v'_i}\frac{\omega_p^2}{k'}. \tag{4.41}$$

The growth of the scattered radiation magnetic field B'_s is governed by the equation:

$$\frac{dB'_s}{dt'} = \Gamma' B'_s, \tag{4.42}$$

where Γ' is the growth rate in the beam frame. By integrating equation (4.42), I get

$$B'_s(t') = C_m \exp[\Gamma' t'], \tag{4.43}$$

where C_m is the integration constant. The poynting flux vector of the scattered radiation in the beam frame is given by

$$\vec{S}' = \frac{c}{4\pi}(\vec{E}'_s \times \vec{B}'_s). \tag{4.44}$$

At $\Gamma' = \Gamma'_m$ and $B'_s = B'_{sm}$, the flux emitted during the characteristic time is $t' = 1/\Gamma'_m$, the saturation time of the instability. Using equation (4.43) and (4.44), I can write as:

$$\vec{S}' = \frac{c}{4\pi} B'^2_{sm} \exp\left[2\left(\frac{\Gamma'}{\Gamma'_m} - 1\right)\right] \hat{k}'_s. \tag{4.45}$$

To transfer flux to the laboratory frame, first I resolve $\vec{E}'_s$ and $\vec{B}'_s$ into components $\vec{E}'_{s\parallel}$ and $\vec{B}'_{s\parallel}$ (parallel to $\hat{z}'$), and $\vec{E}'_{s\perp}$ and $\vec{B}'_{s\perp}$, perpendicular to $\hat{z}'$. Then the flux in the laboratory frame is given by (Gangadhara & Krishan 1992):

$$\vec{S}_\parallel = \frac{c}{4\pi}\gamma^2 \left[\left(1 + \frac{v_b^2}{c^2}\right)\frac{B'_{s\perp}E'_{s\perp}}{v_b} + \frac{E'^2_{s\perp} + B'^2_{s\perp}}{c}\right]\vec{v}_b \tag{4.46}$$

$$\vec{S}_\perp = -\frac{c}{4\pi}\gamma\left[\left(\frac{E'_{s\perp}}{B'_{s\perp}} + \frac{v_b}{c}\right)B'_{s\parallel}\vec{B}'_{s\perp} + \left(\frac{B'_{s\perp}}{E'_{s\perp}} + \frac{v_b}{c}\right)E'_{s\parallel}\vec{E}'_{s\perp}\right]. \tag{4.47}$$

Taking $\vec{E}'_s$ and $\vec{E}'_i$ to be along $\hat{x}'$ (orthogonal to $\hat{z}'$), the components of $\vec{E}'_s$ and $\vec{B}'_s$ are given by:

$$\vec{B}'_{s\perp} = -B'_s\cos(\phi'_s)\hat{y}', \qquad \vec{E}'_{s\perp} = E'_s\hat{x}'$$

$$\vec{B}'_{s\parallel} = -B'_s\sin(\phi'_s)\hat{z}', \qquad \vec{E}'_{s\parallel} = 0, \tag{4.48}$$

where $\phi'_s = \arccos(\hat{k}'_i \cdot \hat{k}'_s)$ and $\hat{x}'$ is also orthogonal to $\hat{z}'$. Now, the components of the flux vector in the laboratory frame are given by (Gangadhara & Krishan 1992):

$$\vec{S}_{\parallel} = \frac{c}{4\pi}\gamma^2 B'^2_{sm} \exp[2(\frac{\Gamma'}{\Gamma'_m} - 1)][\frac{v_b}{c}(1 + \cos^2\phi'_s) - \cos\phi'_s(1 + \frac{v_b^2}{c^2})]\hat{z}', \tag{4.49}$$

$$\vec{S}_{\perp} = \frac{c}{4\pi}\gamma B'^2_{sm} \exp[2(\frac{\Gamma'}{\Gamma'_m} - 1)][1 - \frac{v_b}{c}\cos\phi'_s]\sin\phi'_s\,\hat{y}'. \tag{4.50}$$

If the pump field strength is increased it produces a spread in the beam velocity due to radiation pressure, consequently it decreases the scattered power even though the growth rate increases. The component $\vec{S}_{\parallel}$ is much stronger than $\vec{S}_{\perp}$ because it is proportional to γ^2, while the latter is proportional to γ. Therefore the scattered radiation flux, at the observer frame, is given by:

$$f_{\nu s} = \frac{1}{2}\left(\frac{R_b}{R_e}\right)^2 \frac{S}{\nu_s}, \tag{4.51}$$

where $S = \sqrt{S_{\parallel}^2 + S_{\perp}^2}$, $\Delta\theta$ the angular radius of the beam, $R_b = r_{em}\tan(\delta\theta)$ the radius of the beam at emission height r_{em} and R_e is the distance to pulsar from earth. Due to the relativistic beaming effect emitted radiation confined to a small angle $\Delta\theta \approx 1/\gamma$. The flux emitted by unit frequency is given by

$$f_{\nu} = f_{\nu s}/\nu_s. \tag{4.52}$$

I have numerically simulated power spectra of a couple of radio pulsars using equation (4.52) and invoking different plasma conditions.

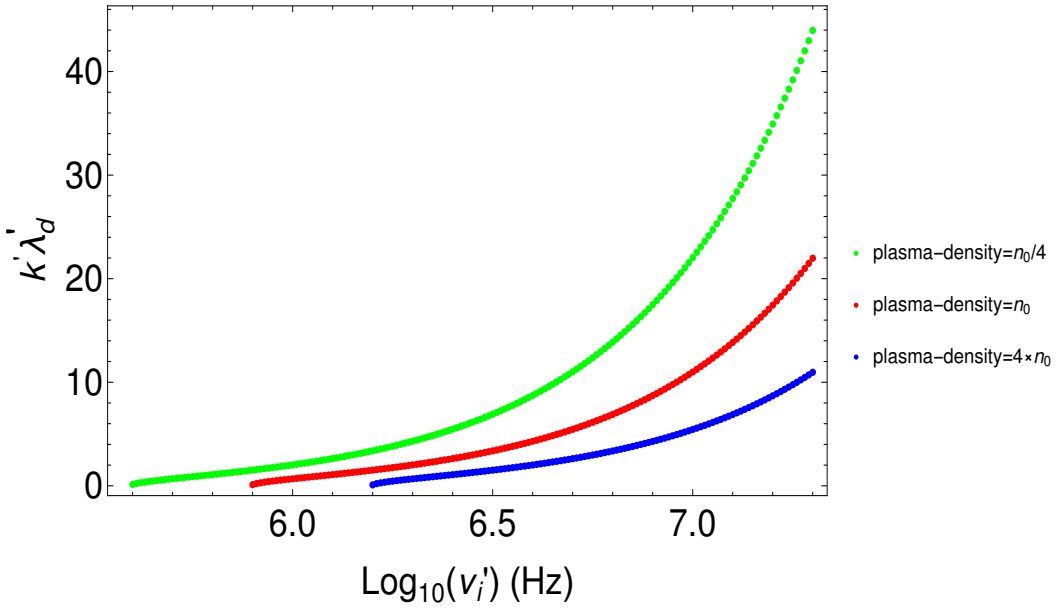

FIGURE 4.2: Plotted the product of Debye length and wave-number of plasma wave with respect to logarithm of input pump frequency in the beam frame. The blue colored curve corresponds to particle density value at 4×7700 cm^{-3}, red colored corresponds to density at 7700 cm^{-3} and green one at 7700/4 cm^{-3}. The other constants chosen were $\gamma_0 = 560$ and plasma temperature $2 \times 10^6 K$. $k'\lambda'_D \leq 0.4$ corresponds to SRS region and $k'\lambda'_D \geq 0.4$ corresponds to SCS region.

4.4 Interpretation of results

I have basically depicted the beam plasma interaction scenario in plasma rest frame as well as in lab frame, respectively (see Figure 4.1). In this Chapter, I have generated power spectra of two well known pulsars, see Figures 4.4 and 4.7. Data is extracted from the table as provided by Malofeev (1993). I have generated power spectra of pulsars theoretically by tuning the indices α_1, α_2, α_3, and m by multi-variable fit, such that it exactly replicate the observed power spectrum of radio pulsar. The pulsars, I have chosen are (i) PSRB 0329+54 and (ii) PSRB 2111+46. I have basically tried to model two-segmented broken power-law by introducing two different scattering processes. For generating the data of flux vs frequency of PSRB 2111+46, I chose: the power-law indices before break frequency as $a_1 = -1.2$, index after spectral break $a_2 = -2.3$, turn over frequency

$\nu_m = 0.1 \times 10^9$ Hz, break frequency $\nu_b = 1.3 \times 10^9$ Hz, maximum flux (all the flux quantities are measured in Jyansky×Second unit, hereafter Jy.s) $F_m = 1$ Jy.s, and flux at break frequency is $F_b = 10^{-2}$ Jy.s. Maximum flux is usually measured at turn-over frequency. Also to generate flux vs frequency data of PSRB 0329+54, I used the following information: $a_1 = -2$, $a_2 = -3.8$, $\nu_m = 0.27$ GHz, $\nu_b = 9.1$ GHz, $F_m = 1$ Jy$\cdot$s, $\mathrm{F}_b = 0.9 \times 10^{-3}$ Jy$\cdot$s (Malofeev 1993). The theoretically predicted spectrum of PSRB 0329+54 is shown in Figure 4.7 (b).

In Figure 4.2, I have plotted the product of plasma wave number and Debye length vs logarithm of pump wave frequency in beam frame. I have shown three curves in Figure 4.2, corresponds to three distinct values of plasma density. It is evident from Figure 4.2 that the value of $k'\lambda'_D$ corresponds to lower density attains 0.4 value, at much lower frequency compared to higher density curve. Therefore it is expected that SCS does happen at higher frequencies in a pulsar with low-density magnetosphere. The growth rate of SCS is negligibly small compared to SRS, due to its strong Landau damping characteristics.

In Figure 4.3, I have shown the growth rates of both SRS and SCS. The growth rate due to SRS is computed analytically by using equation (4.29) but the growth rate of SCS is computed numerically by solving equations (4.24) and (4.26), and (4.34). Hasegawa & Mima (1978) were the first to show that once the plasma system reaches the critical frequency (see equation (4.23)), the imaginary factor associated with the growth rate of scattered wave starts becoming more significant, hence becomes attenuated (see equation (4.13)). As a consequence of large Landau damping plasma system losses energy quickly, and that might be the reason for power spectra becomes steeper after the break. In Figure 4.3 one can see that growth rate does show turn over at lower frequency, which may demarcate the onset of instability. In the lower frequency regime of Figure 4.3, reader can see that the growth rate keeps on decreasing until it reaches some specific value of frequency.

The reason behind decreasing growth is: (i) At lower frequency, the interaction between plasma wave and pump wave doesn't initiate the SRS instability, as threshold flux required is still less to compete with other damping factors of the system. (ii) Secondly, the lower frequency pump wave might favor interacting with plasma wave in the Maxwellian velocity distribution curve's negative slope regime. So rather than plasma imparting energy to the pump wave, it will get back energy from the pump wave. As a consequence, back-scattered waves start losing energy. In between $10^{5.5} - 10^{6.5}$ Hz, interaction of the system is off-resonant, which might be the reason for discontinuity in the frequency domain see Figure 4.3. At a reasonably higher frequency around $10^{6.5}$ Hz, the growth rate due to SRS starts increasing, which might possibly explain if one incorporates the following interaction scenario. In high frequency, the pump wave's phase velocity falls in the positive slope regime of the Maxwellian velocity distribution curve of electrons. Hence back-scattered wave gets back energy from the electrons. Hence growth rate keeps on increasing until it reaches the critical frequency. After reaching critical frequency, the growth rate starts dominating by the SCS process. Figure 4.3 shows that the growth rate due to the SCS process is relatively low compared to the SRS due to large Landau damping, but the growth rate due to SCS increases linearly on a log scale.

The main results are presented in Figure 4.4, which shows broken power law in the radio regime corresponding to the PSRB 2111+46. The continuous black line is generated from the theory, and background dotted points are extracted from the paper of Malofeev (1993). I have attempted to reproduce a two-segmented broken power-law in the model due to two distinct emission processes. For PSRB 2111+46 corresponding to the fitted indices associated with our theory in SRS regime are $\alpha_1 = 3$, $\alpha_2 = 1.5$, $\alpha_3 = 3.78$, $m = -0.72$ and in SCS regime $\alpha_1 = 3$, $\alpha_2 = 1$, $\alpha_3 = 4$, $m = -0.96$. Plasma density (n_0) and Lorentz factor of plasma (γ_0) can be fixed by the expression of critical/break frequency. Then the initial value of pump flux is chosen suitably in such a way that other indices $\alpha_1, \alpha_2, \alpha_3$ as obtained by

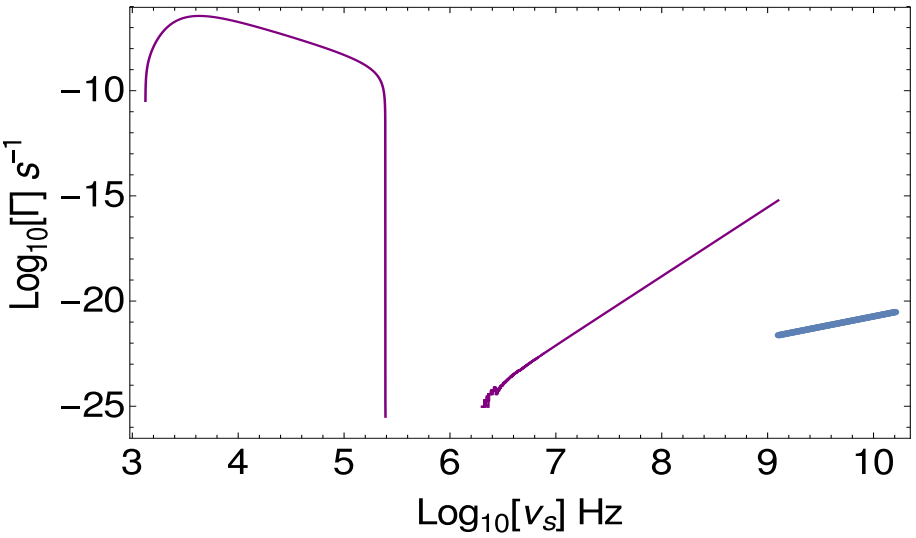

FIGURE 4.3: Logarithm of Growth rate in lab frame is plotted with respect to the logarithm of scattered frequency. Fitted indices used here, corresponds to PSRB 2111+46, which are $\alpha_1 = 3, \alpha_2 = 1.5, \alpha_3 = 3.78$. Purple color represent the growth rate due to SRS in lab frame and blue color is due to SCS. Other parameters used here are $\theta' = 0^o$, $\psi'_s = 1^o$, $\phi'_s = 180^o$, $\gamma_0 = 560$ and lab frame plasma density $n_0 \approx 7700$ cm^{-3}.

non-linear curve fitting does not deviate much from physically accepted values. Here α_1 is the index associated with the spatial variation of plasma density and α_2, α_3 are the index associated with spatial variation of input pump frequency and input pump flux respectively (see equations (4.35)-(4.37)). Here m/2 is the index associated with the frequency variation of the radio beamwidth. Details of the constants chosen for simulating power spectra of PSRB 2111+46 are mentioned in the caption of Figure 4.4. In Figures 4.5(a)-4.5(c), I have shown plots of ω_{cr} (critical frequency) vs $\delta\gamma$, ω_{cr} vs n_0 and ω_{cr} vs γ respectively. Figure 4.5(a) shows that plot between ω_{cr} and $\delta\gamma$ is similar to a rectangular hyperbola, and it shows that, with the increase of Lorentz spread of particle, critical frequency starts going down. It intuitively means that, for the highly monoenergetic beam interaction process, power spectra break at a very high frequency, and for diverging beam interaction, power spectra break at a comparatively lower frequency. Figure 4.5(b) and Figure 4.5(c) both show that critical frequency increases with plasma density and Lorentz factor. So for higher plasma density and highly energetic electron beam interaction, it is expected that spectral break happens at a higher

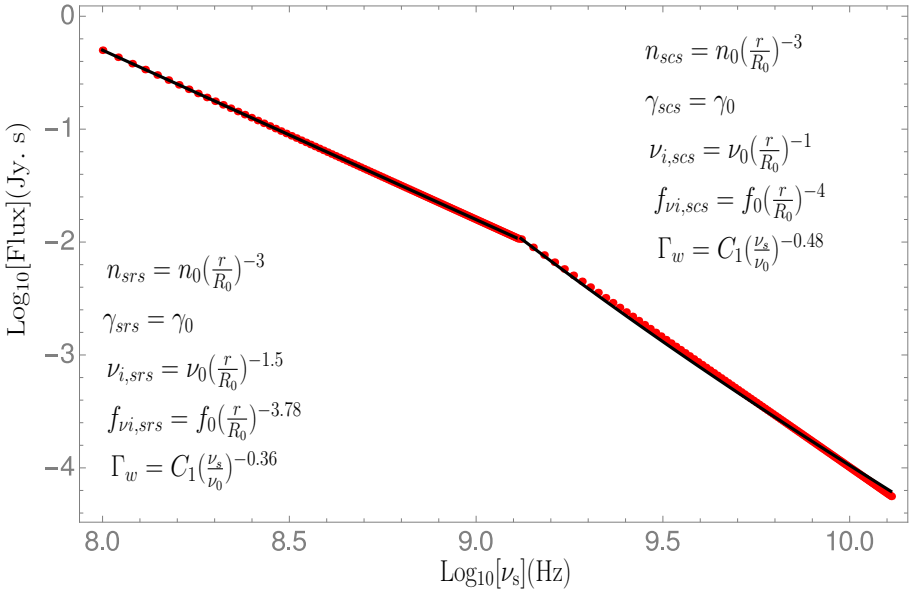

FIGURE 4.4: The power spectra of pulsar PSRB 2111+46. Background red dots represent the data extracted from the published table as given by Malofeev (1993), whereas black continuous curve is generated from the theory. The fitted values of plasma parameters are mentioned on the plot. Subscript "srs" corresponds to the fitted indices in SRS regime, whereas subscript "scs" corresponds to the same in SCS regime. y-axis shows the logarithm of flux density, in Jy.s unit and x-axis represent the logarithm of emitted or scattered EM wave frequency. The break frequency do appear at $\nu_s = 1.3 \times 10^9$ Hz. SRS operates in the regime $\log_{10}(\nu_s) \leq 9.1$ and SCS in the $\log_{10}(\nu_s) \geq 9.1$. The fitted indices values for SRS region are $\alpha_1 = 3$, $\alpha_2 = 1.5$, $\alpha_3 = 3.78$, and $m = -0.72$. For SCS region the fitted values are $\alpha_2 = 1$, $\alpha_3 = 4$ and $m = -0.96$ but α_1 is same as SRS region. The other parameters involved here are plasma density $n_0 \approx 7700$ cm^{-3}, distance $R_e = 4$ kpc, $\gamma_0 = 560$, spread of Lorentz factor $\delta\gamma \approx 15$, input flux of pump wave $f_0 = 5 \times 10^{-8}$ Jy, input initial frequency of pump wave 600 MHz, and plasma temperature $T_e = 2 \times 10^6$ K.

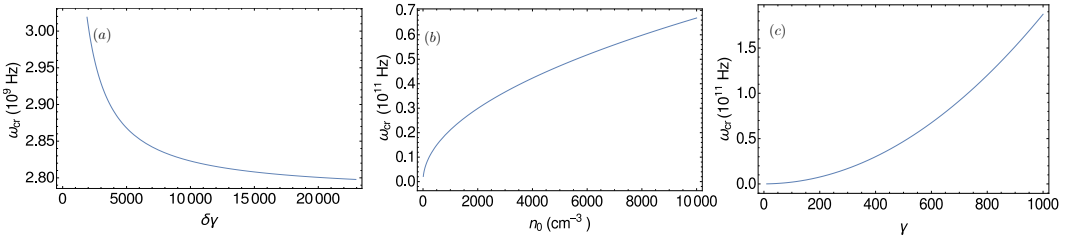

FIGURE 4.5: In panel (a), vertical axis represents critical frequency ω_{cr} and horizontal axis denotes Lorentz spread $\delta\gamma$ associated with electron beam. Constant chosen here are $\gamma_0 = 560$ and $n_0 \approx 7700$ cm^{-3}. In panel (b) critical frequency ω_{cr} is plotted with particle density for fixed value $\gamma_0 = 560$ and spread of $\delta\gamma = 15$ and in panel (c) ω_{cr} vs Lorentz factor is plotted for fixed $n_0 \approx 7700$ cm^{-3} and $\delta\gamma = 15$.

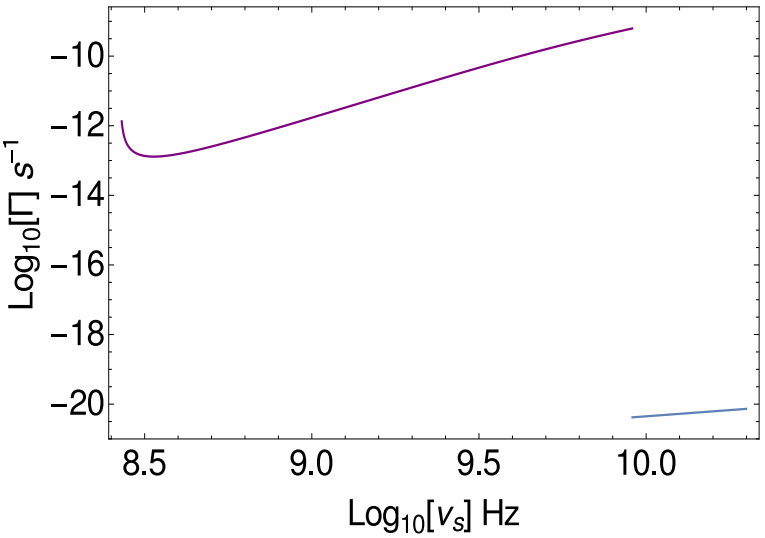

FIGURE 4.6: The growth rate is plotted with respect to the scattered Stokes mode frequency. Fitted indices used here, corresponds to PSRB 0329+54 and mentioned in the subsequent Figure 4.7. Purple color represent the growth rate due to SRS process in lab frame and blue color is due to SCS process. Other parameters used here are $\theta'_e = 0^o$, $\psi'_s = 1^o$, $\phi'_s = 180^o$, $\gamma_0 = 560$ and plasma density $n_0 \approx 76990$ cm^{-3}.

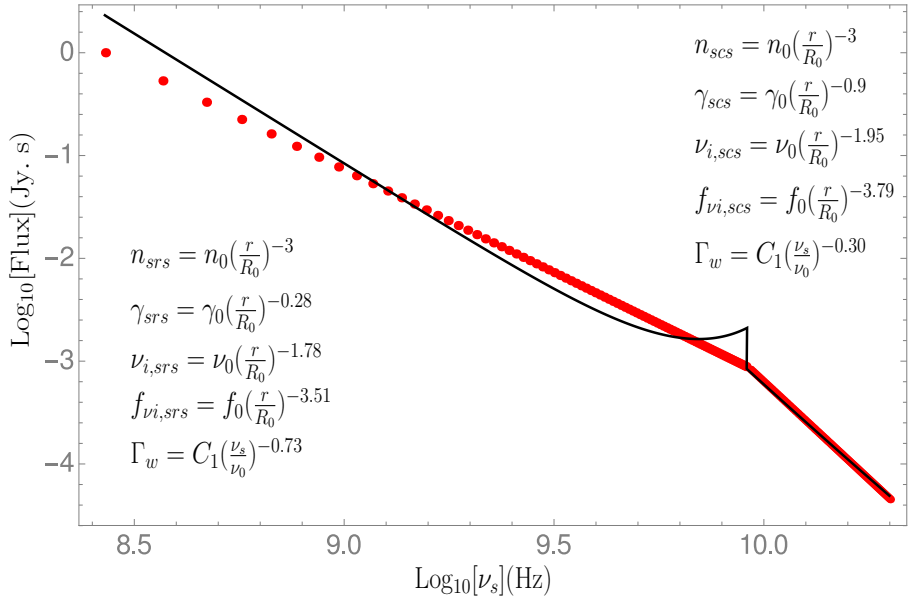

FIGURE 4.7: The spectrum of PSRB 0329+54, where the black colored curve represent the full spectrum as predicted theoretically, and red dots represent the data of flux from observations. It shows at $\log_{10}(\nu_s) \leq 9.98$ demarcates SRS regime and $\log_{10}(\nu_s) \geq 9.98$ shows SCS regime. To generate spectrum I have chosen plasma density $n_0 = 76990$ cm^{-3}, initial frequency of pump wave $\nu_0 = 5$ GHz, initial pump flux $f_0 = 0.0005$ Jyansky, $\gamma_0 = 560$, $\delta\gamma \approx 48.5$, spin period of pulsar ≈ 0.72 s, and distance of pulsar 1 kpc.

frequency.

If the particles are tied up on magnetic field lines, the density index corresponds to the exact dipolar field line should be 3 in principle. Suppose there is any deviation associated with the density index from the exact dipolar nature. In that case, one has to attribute the existence of multi-polar field lines near the pulsar surface. Now I move forward to explain the index associated with the Lorentz factor. First, I define relativistic force $\vec{F}_{rel}$, which is the rate of change of momentum $\vec{P}_r$ of particle. So $\vec{F}_{rel} = d\vec{P}_r/dt$, where relativistic momentum is $\vec{P}_r = \gamma m_0 \vec{v}_b$. Here m_0 is the rest mass of the particle and $\vec{v}_b$ the velocity of the particle. Therefore by differentiating relativistic momentum with respect time, I can get the relativistic force as $\vec{F}_{rel} = \gamma^3 m_0[(\vec{a}/\gamma^2) + \vec{v}(\vec{v}\cdot\vec{a})/c^2]$, where $\vec{a}$ and $\vec{v}$ are the acceleration and velocity vectors, respectively. For the case of pulsars, the expression of relativistic force reduces to $\vec{F}_{rel} = m_0\gamma\vec{a}$ as $\vec{v} \perp \vec{a}$. But for linear acceleration, i.e., $\vec{v} \parallel \vec{a}$, the relativistic force reduces to $\vec{F}_{rel} = m_0\gamma^3\vec{a}$. By considering force-free condition, one can write the equation of motion as $m_0\gamma dv_b/dt = 0$. The plasma of primary particles is off-resonant to the kind of pump wave I am considering here, as primary plasma particles possess very high energy. Couple of kilometers above the polar cap region, the component of the residual electric field would be shielded by the field of secondary electron-positron plasma. So the motion of secondary charged particles becomes mostly force-free. Here all symbols demonstrate their usual meaning in basic physics. So one can carry out the integration $m_0 \int \gamma(v_b)\frac{dv_b}{dt} = 0$, which simplifies to $m_0c^2/\gamma = \text{constant}$. Therefore I have taken, γ as a constant in the calculation.

Next, I try to calculate the spatial dependency of frequency and flux of pump wave from fundamental physics. Point to note that one cannot discriminate too much if one calculates then from curvature radiation formulae. Now, if I consider backwardly moving curvature photons as a source of pump wave, then the frequency variation of input pump wave should follow the formula $\omega = (3/2)\gamma^3(c/\rho)$

(Ruderman & Sutherland 1975). The previous analysis shows that for force-free configuration γ = constant and $\rho \propto r$. So plugging in the variation of γ and ρ in the expression of ω, I get, $\omega \propto r^{-1}$. Result of the model also shows the spatial variation of the pump wave as $\nu_i \propto r^{-1.5}$ in low frequency region and $\nu_i \propto r^{-1}$ in high frequency region (See Figure 4.4).

I have estimated the index associated with the spatial variation of the flux of pump wave from the expression of power emitted by curvature radiation. It is evident that the opposite lobe, with respect to plasma velocity, due to curvature radiation is nontrivial and original as well. The power in the opposite radiation lobe of curvature radiation, which propagates toward the neutron star, will be significantly high for the collective plasma system, whose number density of charged particles is enormously high. Hence, I can assume that some fraction of the energy due to curvature radiation can come back to the neutron star's surface as feedback through backward radiation lobes and serve as the source of pump wave. Now the rate of energy loss through curvature radiation by an electron or positron is given by equation (25a) of Ruderman & Sutherland (1975): $P = (2/3)(q^2/c^3)\gamma^4(c^2/\rho)^2$, where γ is the Lorentz factor and ρ the radius of curvature of field lines.

The flux can be defined as $f_{pump} = k \times L/(4\pi r^2)$, where L is the luminosity of the emitting source, whose unit is erg/s, k is some fractional, and r the distance between emitting source and observer. Since the luminosity and power have the same units, I can write $f_{\rm pump} \approx k \times P/(4\pi r^2)$. Now for force-free configuration γ is constant and $\rho \propto r$. So the spatial variation of luminosity comes to the order of $L \propto r^{-2}$ and therefore flux becomes proportional to $f_{\rm pump} \propto r^{-4}$. On the other hand, I can see flux variation as obtained in Figure 4.4 is 3.78 in the SRS region and 4 in SCS region. Also I have predicted the spectrum of slightly fast-rotating pulsar PSRB 0329+54 in Figure 4.7, which shows an almost similar type of indices like PSRB 2111+46 and can be explained by the same physics as described above. As the energy distribution over frequency as emitted by PSRB 0329+54 is slightly

different from PSRB 2111+46, it requires somewhat different indices to fit the spectra. Indeed, the plasma electrodynamics and underlying scattering processes in the pulsar magnetosphere decide the power spectra of radio pulsars. Also, the growth rate associated with PSRB 0329+43 in both SRS and SCS regimes, as shown in Figure 4.6, shows increasing trends concerning scattered frequency is having the same type of explanation like as Figure 4.3. Also, for the case of PSRB 0329+54, I have shown the growth rate behavior only over the frequency range in which pulsar emits actively in the radio band. The logic behind choosing the index associated with spatial variation of input pump frequency can be attributed to the radius to frequency mapping. That is, higher frequency comes from a lower altitude, and lower frequency originates from a higher altitude. But if there is no instability, spatial variation of input pump flux should increase with distance from the neutron star's surface in principle. As more you go radially outward from the surface of the neutron star, the more you come close to the source of the pump wave. In general, it is pretty challenging to predict the flux variation concerning space as it's a highly dynamic phenomenon. It depends on how strongly radiation and plasma get coupled to each other and satisfy the phase-matching condition. After that, it depends on how fastly or slowly the growth rate due to instability varies with scattered frequency. Now it is found that the growth rate of instability is sensitive to the chosen values of input pump frequency and input pump flux (see equations (4.36)-(4.37)). If the input pump frequency is chosen very close to plasma frequency, the scattered wave's growth rate of energy gets amplified with a very fast rate as it serves the perfect resonance condition. So it is very clear that the flux variation of input pump flux on space can be anything within a reasonable limit of dipolar magnetic field line configuration, and it can be determined from the combined action of energy, momentum conservation principle (equation (4.9)), the growth rate of the amplitude of the scattered wave (equation (4.6)) due to instability, the strength of pump wave (equation (4.37)), input pump frequency (equation (4.36)), damping mechanism of the medium, emission mechanism, etc. Moreover, the frequency variation of the radio beam width, as obtained in Figure

4.4 shows index at low-frequency regime -0.36 and in high-frequency regime -0.48. These deductions are very close to the literature values -1/3 and -1/2 at low and high-frequency radio counterparts, respectively (see equation (5) of Yang & Zhang (2018)). Moreover, the radio beam width obtained in the model shows an apparent narrowing in the high-frequency regime and is very much consistent with other literature.

4.5 Discussion

The main point is that the SRS and SCS processes are not applied to radio pulsars yet to generate a power spectrum. For the first time, it is being investigated by suitably chosen plasma parameters. SRS process is worthy enough to explain the single power law of pulsars, and if one adds SCS process as well, it can even explain the broken power-law. In the model, I have shown modeling a two-segmented broken power law. A simple power-law can be easily modeled by incorporating SRS, as growth rate due to SRS can be easily computed by using an analytical expression as shown in equation (4.29). Sieber (1973) has discussed four different models on spectral behaviors of radio pulsars: (1) Simple power-law, (2) Synchrotron-self-absorption, (3) Thermal absorption and (4) Two power-law model. But generating two-segmented broken power-law by theoretical approach is a futile task, as there is no exact asymptotic form for growth rate due to SCS. First, we need to fit and find the indices associated with the plasma parameters (see equations (4.35)-(4.37)) in the SRS regime. Then using the fitted indices corresponding to the SRS regime, we can compute the growth rate due to SCS, as it does not introduce significant error in the high-frequency regime. Subsequently, equation (4.34) is solved numerically to compute growth rate due to SCS by taking the zeroth-order term associated with Taylor series expansion of equation (4.34). It is evident that single power law is a rule and another type of power spectra like

a broken type of power law is an exception (Maron et al. 2000; Jankowski et al. 2018). I speculate that a pulsar with a single power-law might have a spectral break at a higher frequency. From Figure 4.5(a), it is evident that for a lesser value of $\delta\gamma$, critical frequency is almost infinity. Similarly, Figure 4.5(b) and Figure 4.5(c) shows increasing trends of break frequency with the increase of plasma number density and Lorentz factor. So from Figure 4.5(a) and Figure 4.5(b), I can infer that, for highly mono-energetic beam plasma interaction and highly denser pulsar magnetosphere, the break frequency is expected to be high. It is highly probable that the break frequency for such cases may literally occur in a very high-frequency regime, and it could be entirely outside the radio frequency range, and radio telescopes might not detect that radiation due to SCS. So in nature, we see most of the power spectra of radio pulsars exhibit predominantly by a single power law. Secondly, due to high Landau damping and high threshold conditions for triggering the SCS process, it is hard for the instability to survive with the significant growth rate. Therefore most of the power spectra of radio pulsars can be initiated by one scattering process, SRS. Hence they do exhibit single power law. The index α_1 as obtained associated with the plasma density spatial variation of PSRB 2111+46 and PSRB 0329+54 are 3 (see Figure 4.4) which correspond to dipolar magnetic field line configuration (Benford & Buschauer 1977).

It is interesting to discuss the correlation among the physically measurable parameters of pulsars such as spin period, rate of change of spin period, and magnetic field with the model-dependent parameters associated with power spectra. The spin period and derivative of the spin period of the pulsar are not directly involved in the theoretical model. It's merely the scattering processes associated with the parametric coupling of the out flowing plasma and background radiation in the pulsar magnetosphere for determining the power spectra. According to the model, parameters such as spin period and its derivative are not sensitive in determining pulsars' power spectra. But the spin period is involved in the expression of light cylinder radius, which can affect the emission altitude.

But in the model, I have expressed emission altitude in terms of emitted frequency to reduce the number of unknown parameters. Emission altitude is a parameter associated with the viewing geometry of pulsars. For millisecond pulsars, it is expected that the light cylinder radius to get squeezed by some factor. As a result, the open magnetic field region's volume expands means particle energy as carried out by field lines far away from the magnetic axis can emit in principle. As the radius of curvature of the field lines reduces as you move far away from the magnetic axis, those field lines can tune to the higher frequency of the radio counterpart. So in principle, millisecond pulsar can emit power more efficiently over a broader frequency range than normal pulsars. In the model, spatial dependency associated with plasma density, Lorentz factor, pump frequency, and pump flux and spread of Lorentz factor mainly determine the power spectra. Also, if one looks at the dispersion relation, i.e., equation (4.18), ω_p doesn't contain magnetic field term. So magnetic field of pulsar doesn't appear directly into the expression of emitted flux. The magnetic field's role is to generate an accelerating voltage across the polar cap and gives proper alignment to the plasma particles. But I speculate that radio emission geometry may have some influence on the shape of power spectra. In later, I have a plan to understand how the shape of power spectra depends on various radio emission geometry-related parameters in pulsars?

Here I try to make a brief comparison between the power spectrum of PSRB 2111+46 and PSRB 0329+54 (See Figure 4.4 and Figure 4.7). First of all, both are having a broken type of power-law by nature. PSRB 0329+54 is a slightly faster-rotating pulsar and shows spectral break at a higher frequency, which is very close to 10 GHz. For reproducing the power spectrum of PSRB 0329+54 within the reasonable limit of dipolar magnetic field line configuration, I have chosen plasma density 76990 cm^{-3}, initial flux 0.0005 Jy and initial frequency of pump wave 5 GHz. They are higher than the corresponding values chosen to recreate the spectrum of PSRB 2111+46 (see caption of Figure 4.4 and Figure 4.7). Reasons behind choosing higher plasma density and higher initial flux in the

case of PSRB 0329+54 are obvious, as it shows spectral break at higher frequency and emission over a broader range of frequency than the PSRB 2111+46. Besides, I have added extra spatial variation associated with the Lorentz factor for the case of PSRB 0329+54. From Figure 4.7, one can see that the index of spatial variation associated with the Lorentz factor is smaller in the SRS region, whereas the same quantity is slightly more in the SCS region. This can happen when the parallel component of the induced electric field above the polar cap region doesn't get shielded completely. Also, SCS is more prone to occur closes to the surface of the neutron star. As a result, plasma energy gets channelized through multipolar field lines. That might be why the index of the Lorentz factor in the SCS region is slightly higher (see Figure 4.7). The indices associated with the spatial variation of pump flux in both the Figure 4.4, Figure 4.7 show similar values. Moreover, the index associated with the pump wave frequency in the SRS region in both the Figure 4.4 and Figure 4.7 is similar to each other. Still, in the SCS region, the index values are slightly different. The reason could be the difference between initial pump frequency and break frequency in PSRB 0329+54 are quite a bit more. As a result, pump frequency needs to undergo sufficient frequency up-conversion to reprocess themselves through parametric coupling by satisfying resonance or phase-matching conditions and emits efficiently over a high-frequency range. Finally, the indices associated with frequency-dependent beam width, as obtained in Figure 4.7, show values -0.73 and -0.3 in SRS and SCS regions. These values are very close to the average value of frequency-dependent beam width -0.5 (Yang & Zhang 2018). But in principle, frequency-dependent beam width should become narrow, but Figure 4.7 does not show the same features. It can be because the extra spatial variation associated with the Lorentz factor is added for PSRB 0329+54. I speculate that, as PSRB 0329+54 emits over a broader frequency range even in the SCS regime, frequency-dependent beam width tries to expand slightly to make coverage over a broader frequency range in the high-frequency domain. Moreover, the chosen value of the initial pump frequency and initial flux value may not be a very good prediction. Hence those initial values are not exactly

appropriate to generate the power spectrum of PSRB 0329+54. Generation of the spectrum of PSRB 0329+54, within a reasonable limit of parameter space, is a complicated one than the PSRB 2111+46.

The geometric effects such as line-of-sight cut across the pulsar emission beam play an important role in pulsar spectral structure. Observations indicate that the core is emitted from a lower altitude and has a steeper spectrum than the conal emission that arises at higher altitudes. In this study, we have not included the geometric effects yet but we plan to take it up in our follow-up works. The derivation of dispersion relation of EM wave in magnetized plasma is given in Appendix E.

Pulsars that show single power-law may have break frequency at the higher frequency in the radio counterpart, and radio telescope cannot detect those fluxes as the signal strength of pulsars become progressively weak and falls below threshold value as frequency goes up. The single power-law may be the intrinsic emission property of most of the pulsars. The literature also suggests that pulsars show the log-parabolic type of spectra and gigahertz peaked spectrum (see Jankowski et al. (2018) and the references therein), which is quite difficult to explain according to our current theoretical understanding. The log parabolic type of profile suggests that the indices associated with power-law itself depend on frequency. The flux density and polarization properties of the Vela pulsar (PSR J0835–4510) at millimeter wavelengths, providing the first polarimetric study of any ordinary pulsar at frequencies above 32 GHz is given by Liu, et al. (2019). Also, the spectrum can be modified after generation in the presence of variable refractive index in the pulsar medium due to the propagation effect. But one must investigate in detail before claiming such type of power spectrum.

4.6 Conclusion

1. The growth rate of the SRS process is much more prominent than the SCS process. The growth rate due to the SRS process in the model shows a low-frequency turn-over, which might demarcate the position of onset of instability.

2. The critical frequency expression in the model has the potential to explain different morphology associated with power spectra of radio pulsars, such as single power law and broken power law.

3. The power spectra of two pulsars, PSRB 0329+54 and PSRB 2111+46, are successfully reproduced theoretically based on the model involving the plasma mechanisms, demonstrating the main result of the paper.

4. Since the critical frequency becomes higher for lower $\delta\gamma$, the power spectra are expected to break at higher frequencies for the mono-energetic beam interactions.

5. The critical frequency increases with Lorentz factor γ and plasma density n_0 as well. Hence, in the pulsars with higher plasma density and higher Lorentz factor associated with the secondary particles, the spectral break occur at higher frequencies.

Chapter 5

Influence of Stimulated Raman Scattering on the polarization state of pulsars

5.1 Introduction

The relativistically moving plasma in pulsars and AGNs is believed to be the source of radio emission (Blandford & Konigl 1979). In this chapter, I mainly limit my discussion to pulsars. The literature suggests wide diversity in the circular and linear polarization, and a significant portion of depolarized components exist in the radio emission of pulsars. Although the pulsars are found to be highly polarized objects among all the known radio sources in the universe, they show rapid temporal variability in intensity on the time scale ranging from millisecond to nano-second (Cordes 1983; Hankins & Eilek 2007). From radio observations it is evident that pulsars possess superstrong magnetic fields and their radio emission

mechanism is broadband. It is recognized that any changes in the direction of the magnetic field could alter the polarization state. It is evident from the literature that some pulsars show 100% polarization, and some others show very little polarization. Now the question is, why do they offer very high polarization sometimes and sometimes very little. This question is quite a puzzle, which tries to address one of the fundamental issues in pulsar astronomy. This chapter has tried to explain the polarization variability by incorporating some underlying plasma process such as Stimulated Raman Scattering (SRS).

While determining the polarization state of pulsars, one has to take care of the crucial factors such as (i) pulsars radio emission mechanism is broadband, and (ii) the influence of superstrong magnetic field. The orientation of magnetic field is expected to manifest itself through the polarization angle swing. The individual pulse trains associated with pulsar radio emission are very fluctuating in nature and exhibit a variable degree of circular and linear polarization ranging from 10% to 100% (Manchester et al. 1978). On the other hand, the integrated pulse profiles are very stable in nature. The degree of circular polarization in the integrated pulse profiles do vary from 10% to 30% from pulsar to pulsar. So, I suspect that some faster plasma process such as the Stimulated Raman Scattering (SRS) might be involved in altering the polarization state. Moreover, pulsar emission is known to be broadband, so different spectral components are expected to travel with different phase velocities, which can lead to phase shift by different amounts. After that, superimposition of them over the polarization limiting region could result in depolarization.

I have studied the change in electromagnetic waves' polarization state due to the SRS in an ambient plasma medium of a typical pulsar. In this process, an electromagnetic wave undergoes coherent scattering by plasma waves in a relativistic plasma moving in an outward direction from a neutron star. I have attempted to

explain some of the polarization properties of pulsars such as rapid temporal variations, sense reversal of circular polarization, rotation of the plane of polarization, i.e., polarization angle swing, etc., by considering the SRS. The superimposition of emissions from the polarization limiting region could result in depolarization.

Coherent radio emission from pulsar has drawn a tremendous attention of astrophysicists (e.g., Cordes 1979; Michel 1987; Asseo et al. 1990). Powerful collective emission is believed to occur when the relativistic plasma beam with density, one percent of the pair plasma density, scatter off coherently from the concentration of plasma waves (Benford 1992). von Hoensbroech et al. (1998) have demonstrated that the degree of linear polarization decreases with increasing frequency while the degree of circular polarization shows the opposite trend.

I have explored the influence of SRS on the polarization of EM waves propagating in the pulsar magnetosphere. We assume that the pulsar magnetosphere's physical conditions follow the classical standard model of Ruderman & Sutherland (1975). The beams and the pair plasma are in constrained relativistic motion along the bundle of open magnetic field lines. The SRS can be considered as a parametric decay of the initial transverse electromagnetic (pump) wave into another electromagnetic wave and longitudinal plasma wave. The physical mechanism and the interaction process of SRS is elaborated in many articles (e.g., Drake 1974; Kaw et al. 1976; Hasegawa & Mima 1978). There are two ways in which SRS can be crucial in the pulsar magnetosphere. Firstly, it may act as an effective damping mechanism for the EM wave generated by well-known radio emission mechanisms such as curvature radiation at the lower altitudes in the pulsar magnetosphere. At those altitudes, the resonant conditions for SRS (frequency and wavenumber matching conditions) might not be satisfied. This results in a short time scale variability which is generally observed in pulsar radio emission. Secondly, SRS may provide an effective saturation mechanism for the growth of EM waves, provided that the condition to excite radio waves and SRS are jointly fulfilled in the

emission region.

We neglect the non-linear stages of SRS and the development of Langmuir turbulence, which leads to wave-particle trapping or quasi-linear diffusion. If the pump is monochromatic, the growth rate of SRS becomes very high, as in conventional laboratory laser-plasma interaction. However, in the case of pulsars, the pump can be broadband. In the limit where the bandwidth $\Delta\omega$ of the pump wave is much larger than the growth rate of SRS, we can use random phase approximation to demonstrate the statistical behavior of the interacting waves.

I have given below the logic behind using dispersion relation to derive the SRS's scattered waves' growth rate. Sazonov & Tsytovich (1968) have given a general expression for the third-order non-linear currents excited in a magnetized plasma. Since the corresponding expressions are very complicated, it is tough to incorporate those equations and derive simplified expressions of scattered EM waves due to SRS. However, one can make some useful simplifications when considering SRS in the pulsar magnetosphere. In the presence of a super-strong magnetic field, we can expand the currents in terms of $1/\omega_B$, where ω_B is the cyclotron frequency. Secondly, suppose the pair plasma has identical distributions for the electrons and the positrons. In that case, some of the non-linear currents cancel out, as they are proportional to the third power of electric charge. But this current cancellation is exact for unmagnetized plasma. Thirdly all the interacting and excited waves propagate along the direction of the magnetic field, which eventually allow us to make some useful approximation to obtain the simplified dispersion relation for stimulated Raman scattering. The polarization of pulsar signals appears to depend upon time resolutions of observation (Gangadhara et al. 1999). One or more reversals of the sense of circular polarization have been observed in several pulsars' integrated profiles. However, in individual pulses, circular polarization changes sense many times across the pulse window. There has been a very preliminary investigation dedicated to explaining the depolarization and micro-variability by

using plasma mechanism (Benford 1992).

5.2 The polarization state of scattered radiation owing to Stimulated Raman Scattering

Consider a large amplitude elliptically polarized electromagnetic (EM) wave $(k_i\,, \omega_i)$ with an electric field

$$\vec{E_i} = \epsilon_i[\cos(\vec{k_i}.\vec{r} - \omega_i t)\hat{e}_x + \alpha_i \cos(\vec{k_i}.\vec{r} - \omega_i t + \delta_i)\hat{e}_y], \tag{5.1}$$

where δ_i is the initial phase difference. Let us assume an expression for plasma density in the presence of density perturbation as the sum of equilibrium density and some fluctuating quantity: $n = n_0 + \delta n_p$, where $\delta n_p = \delta n \cos(\vec{k}.\vec{r} - \omega t + \delta)$.

The coupling between the EM wave and the plasma density perturbations $\delta n_p(\vec{k}, \omega)$ is nonlinear because of the presence of pondermotive force which is proportional to ∇E_i^2. As a result of interaction between the incident EM radiation and plasma wave, density perturbation grows up and lead to currents at $(\vec{k_i} \pm \vec{k}, \omega_i \pm \omega)$. These currents in turn will generate mixed electromagnetic-electrostatic side band modes at $(\vec{k_i} \pm \vec{k}, \omega_i \pm \omega)$. Now the side band modes in turn interact with the incident wave field and producing pondermotive force, which then pushes the plasma and hence enhances the original density perturbations. So this non-linear force serve as a mediator of a positive feedback system and operates the instability. The electric field E_s of the EM wave scattered through an angle ϕ_s with respect to $\vec{k_i}$ can be written in the primed frame as

$$\vec{E_s'} = \epsilon_s[\cos(\vec{k_s}.\vec{r} - \omega_s t)\hat{e}_x' + \alpha_s \cos(\vec{k_s}.\vec{r} - \omega_s t + \delta_s)\hat{e}_y']. \tag{5.2}$$

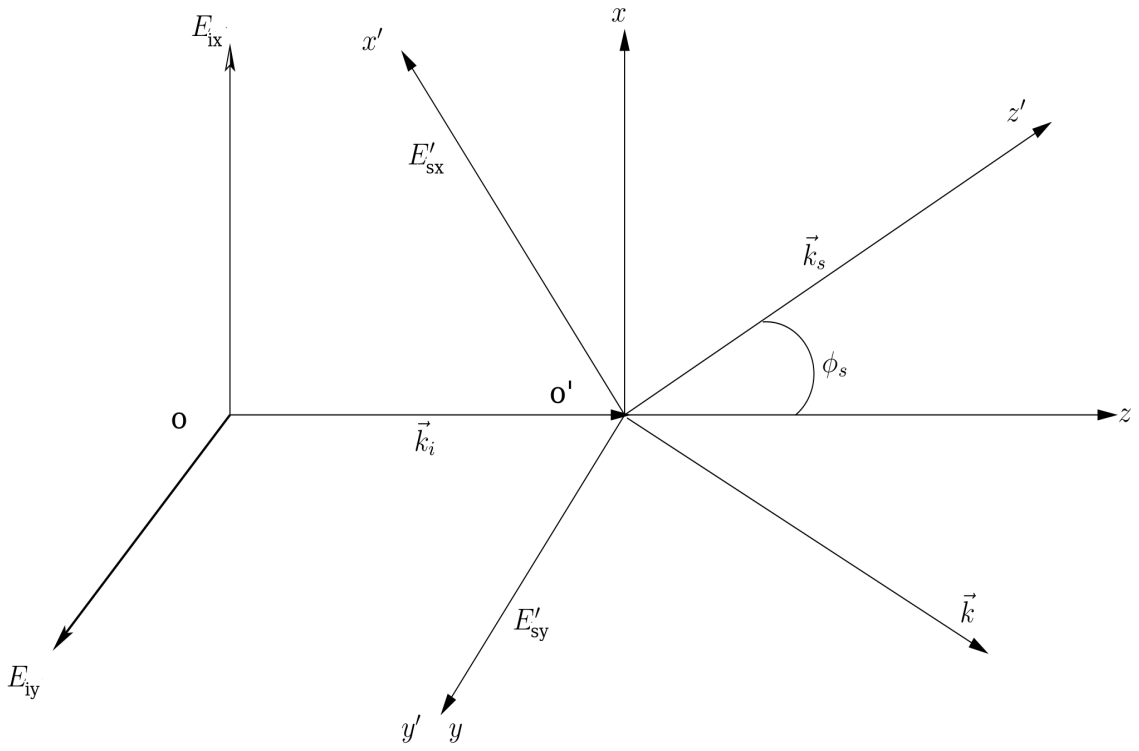

FIGURE 5.1: Geometry describing the SRS process. The incident electric field components are (E_{ix}, E_{iy}). The wave vector $\vec{k}_i$ of the incident radiation is pointed along z-axis. The components of the scattered EM wave electric field are (E'_{sx}, E'_{sy}). The wave vector of scattered radiation $\vec{k}_s$ subtends an angle ϕ_s with respect to the incident wave vector $\vec{k}_i$. The "$\prime$" symbol here denotes the scattered frame, which is rotated with respect to the frame attached with incident radiation.

The figure 5.1 shows that the directions of $\vec{k}_i$ and $\vec{k}_s$ in the orthogonal co-ordinate systems $(\hat{e}_x, \hat{e}_y, \hat{e}_z)$ and $(\hat{e}'_x, \hat{e}'_y, \hat{e}'_z)$. The co-ordinate system ($\hat{e}'_x$, $\hat{e}'_y$, $\hat{e}'_z$) is rotated through an angle ϕ_s about y-axis. Here, $\vec{k}_i \parallel \hat{e}_z$, $\vec{k}_s \parallel \hat{e}'_z$, and $\hat{e}'_y \parallel \hat{e}_y$. Hence the unit vectors are related by

$$\hat{e}'_x = \cos(\phi_s)\hat{e}_x - \sin(\phi_s)\hat{e}_z, \quad \hat{e}'_y = \hat{e}_y, \quad \hat{e}'_z = \sin(\phi_s)\hat{e}_x + \cos(\phi_s)\hat{e}_z. \tag{5.3}$$

The electric field due to scattering in the frame $(\hat{e}_x, \hat{e}_y, \hat{e}_z)$ can be written as:

$$\vec{E}_s = \epsilon_s[\cos(\vec{k}_s.\vec{r} - \omega_s t)(\cos(\phi_s)\hat{e}_x - \sin(\phi_s)\hat{e}_z) + \alpha_s \cos(\vec{k}_s.\vec{r} - \omega_s t + \delta_s)\hat{e}_y]. \tag{5.4}$$

The wave equation for the scattered EM wave is given by

$$(\nabla^2 - \frac{1}{c^2}\frac{\partial^2}{\partial t^2})\vec{E_s} = \frac{4\pi}{c^2}\frac{\partial \vec{J}}{\partial t}, \tag{5.5}$$

where c is the velocity of the light and $\vec{J}$ is the current density vector. The components of current density are $J_x = -e(n_0 + \delta n_p)u_x$, $J_y = -e(n_0 + \delta n_p)u_y$, $J_z = -e(n_0 + \delta n_p)u_z$, where u_x, u_y, and u_z are the components of oscillation velocity $\vec{u}$ of plasma particles in the presence of combined radiation field $\vec{E_i}$ and $\vec{E_s}$. Segregating the components of equation (5.5), we get

$$D_s E_{sx} = -\frac{2\pi e^2}{m_0}\epsilon_i \delta n[\frac{\omega_-}{\omega_i}\cos(\vec{k}_-.\vec{r} - \omega_- t - \delta) + \frac{\omega_+}{\omega_i}\cos(\vec{k}_+.\vec{r} - \omega_+ t + \delta)], \tag{5.6}$$

$$D_s E_{sy} = -\frac{2\pi e^2}{m_0}\alpha_i\epsilon_i \delta n[\frac{\omega_-}{\omega_i}\cos(\vec{k_-}.\vec{r} - \omega_- t + \delta_i - \delta) + \frac{\omega_+}{\omega_i}\cos(\vec{k_+}.\vec{r} - \omega_+ t + \delta_i + \delta)], \tag{5.7}$$

$$D_s E_{sz} = 0. \tag{5.8}$$

where $E_{sx} = \epsilon_s \cos(\phi_s)\cos(\vec{k}_s.\vec{r} - \omega_s t)$, $E_{sy} = \alpha_s\epsilon_s \cos(\vec{k}_s.\vec{r} - \omega_s t + \delta_s)$, $E_{sz} = -\epsilon_s \sin(\phi_s)\cos(\vec{k}_s.\vec{r} - \omega_s t)$, and $D_s = k_s^2c^2 - \omega_s^2 + \omega_p^2$. For $\phi_s = 0$ and π, the RHS of Eq. (5.8) goes to zero. Here $\omega_p = \sqrt{4\pi n_0 e^2/m_0}$ is the plasma frequency. The scattered radiation consists of two modes (i) Stokes mode and (ii) Anti-Stokes mode, respectively. When Stokes mode and Anti-Stoke mode are excited then their dispersion relations are: $D_\pm \approx k_\pm^2c^2 - \omega_\pm^2 + \omega_p^2 \approx 0$, where $\pm$ corresponds to the Anti-Stokes and Stokes modes, respectively. Apart from that following phase matching conditions also have to be satisfied to excite Anti-Stokes and Stokes modes resonantly. In quantum mechanical description the phase matching conditions are basically the consequences of energy and momentum conservation principles. So the phase matching conditions are follows:

$$\omega_i - \omega = \omega_-, \quad \vec{k}_i - \vec{k} = \vec{k}_-, \quad \omega_i + \omega = \omega_+, \quad \vec{k}_i + \vec{k} = \vec{k}_+. \tag{5.9}$$

Multiplying equation (5.6) on both sides by $\cos(\vec{k_i}.\vec{r}-\omega_i t)$ and ignoring the terms containing $(2\vec{k_i}, 2\omega_i)$ as being off resonant, we get

$$D_{\pm}\epsilon_{\pm}\cos(\phi_{\pm})\cos(\vec{k}.\vec{r}-\omega t) = -\frac{4\pi e^2}{m_0}\epsilon_i\delta n\cos(\vec{k}.\vec{r}-\omega t+\delta). \tag{5.10}$$

Similarly, if we multiply equation (5.7) by $\cos(\vec{k_i}.\vec{r}-\omega_i t+\delta_i)$, we obtain

$$D_{\pm}\alpha_{\pm}\epsilon_{\pm}\cos[\vec{k}.\vec{r}-\omega t\pm(\delta_{\pm}-\delta_i)] = -\frac{4\pi e^2}{m_0}\alpha_i\epsilon_i\delta n\cos(\vec{k}.\vec{r}-\omega t+\delta). \tag{5.11}$$

Similar to equations (5.9), the following conditions between phases do exist:

$$\delta_{\pm} = \delta_i \pm \delta. \tag{5.12}$$

Dividing equation (5.11) by (5.10), we have

$$\begin{aligned}\alpha_{\pm} &= \alpha_i\cos(\phi_{\pm}), \quad \text{for } \delta = 0;\\ &= -\alpha_i\cos(\phi_{\pm}), \quad \text{for } \delta = \pi.\end{aligned} \tag{5.13}$$

Now the electric fields $E_{\pm}$ of the EM waves scattered through the angles $\phi_{\pm}$ with respect to $\vec{k_i}$ can be written as follows:

$$\vec{E_{\pm}} = \epsilon_{\pm}[\cos(\vec{k_{\pm}}.\vec{r}-\omega_{\pm}t)\hat{e}'_x + \alpha_i\cos(\phi_{\pm})\cos(\vec{k}_{\pm}.\vec{r}-\omega_{\pm}t+\delta_i)\hat{e}'_y].$$

If we now multiply equation (5.10) by ϵ_i and equation (5.11) by $\alpha_i\epsilon_i$, thereafter substracting we find

$$(\alpha_i\alpha_{\pm}-\cos(\phi_{\pm})\epsilon_i\epsilon_{\pm}) = -\frac{4\pi e^2}{m_0}\epsilon_i^2(1+\alpha_i^2)\delta n\frac{1}{D_{\pm}}, \tag{5.14}$$

where $\delta = \pi$ has been used. Now our aim is to evaluate the plasma density perturbation δn. With the inclusion of the pondermotive force as a driving force, the Vlasov equation for the low frequency response of plasma particles can be

written as

$$\frac{\partial f}{\partial t} + \vec{v}.\nabla f + \frac{1}{m_0}(e\nabla\phi - \nabla\psi).\frac{\partial f}{\partial \vec{v}} = 0, \tag{5.15}$$

where $\phi(r,t)$ is the scalar potential associated with the electrostatic waves, $f(r,v,t)$ is the particle distribution function, and $\psi(r,t)$ is the potential function associated with pondermotive force. Linearizing equation (5.15) with $f(\vec{r},\vec{v},t) = f_0(\vec{v}) + \delta f_p(\vec{r},\vec{v},t)$, we get

$$\frac{\partial(\delta f_p)}{\partial t} + \vec{v}.\nabla(\delta f_p) + \frac{1}{m_0}(e\nabla\phi - \nabla\psi).\frac{\partial f_0}{\partial \vec{v}} = 0, \tag{5.16}$$

where $\delta f_p = \delta f \cos(\vec{k}.\vec{r} - \omega t + \delta)$. The pondermotive force of radiation field is given by $F_w = -\nabla\psi$. It depends quadratically on the amplitude and leads to a slow variation associated with the longitudinal field, corresponding physically to radiation pressure, which leads to slow longitudinal motion and modifies the density. The potential function corresponding to pondermotive force is given by

$$\psi = \frac{e^2}{2m_0} < (Re|\frac{\vec{E}_i}{i\omega_i} + \frac{\vec{E}_-}{i\omega_-} + \frac{\vec{E}_+}{i\omega_+}|)^2 >_\omega$$

$$= \frac{e^2}{2m_0\omega_i^2}[\epsilon_i\epsilon_- \cos(\phi_-)\cos(\vec{k}.\vec{r} - \omega t) + \epsilon_i\alpha_i\alpha_-\epsilon_- \cos(\vec{k}.\vec{r} - \omega t + \delta_i - \delta_-) +$$

$$\epsilon_i\alpha_i\alpha_+\epsilon + \cos(\vec{k}.\vec{r} - \omega t + \delta_+ - \delta_i) + \epsilon_i\epsilon_+ \cos(\phi_+)\cos(\vec{k}.\vec{r} - \omega t)] \tag{5.17}$$

The angle bracket $<>_\omega$ represents the ω frequency component of an average over the fast timescale ($\omega_i \gg \omega$). To determine ϕ self consistently we use the Poisson equation, which gives

$$\phi = -\frac{4\pi e}{k^2}\delta n_p. \tag{5.18}$$

Now substituting the expressions for δf_p, δn_p, ϕ, and ψ into equation (5.16), we get

$$\delta f + \frac{4\pi e^2}{m_0 k^2}[(\delta n + \frac{k^2}{8\pi m_0 \omega_i^2}[\mu_s \epsilon_i(\epsilon_+ \cos(\phi_+) + \epsilon_- \cos(\phi_-)) + \alpha_i \epsilon_i(\alpha_+ \epsilon_+ + \alpha_- \epsilon_-)]]\times$$

$$\frac{\vec{k}.\partial f_0/\partial \vec{v}}{\omega - \vec{k}.\vec{v}} = 0, \tag{5.19}$$

where $\mu_s = \sin(\vec{k}.\vec{r} - \omega t)/\sin(\vec{k}.\vec{r} - \omega t + \delta)$. For $\delta = \pi$ we obtain from equation (5.19),

$$\delta f = -\frac{4\pi e^2}{m_0 k^2}\Big(\delta n + \frac{k^2}{8\pi m_0 \omega_i^2} A\Big)\frac{\vec{k}.(\partial f_0/\partial \vec{v})}{\omega - \vec{k}.\vec{v}}, \tag{5.20}$$

where $A = \alpha_i \alpha_- - \cos(\phi_-)\epsilon_i \epsilon_- + \alpha_i \alpha_+ - \cos(\phi_+)\epsilon_i \epsilon_+$. The density perturbation δn is given by,

$$\delta n = \int_{-\infty}^{\infty} n_0 \delta f d\vec{v} = -\Big(\delta n + \frac{k^2}{8\pi m_0 \omega_i^2} A\Big)\chi, \tag{5.21}$$

where

$$\chi = \frac{\omega_p^2}{k^2}\int_{-\infty}^{\infty} \frac{\vec{k}.(\partial f_0/\partial \vec{v})}{\omega - \vec{k}.\vec{v}} d\vec{v}, \tag{5.22}$$

is the electron susceptibility function (Kaw et al. 1976; Fried & Conte 1961). So from equation (5.21) we have

$$\Big(1 + \frac{1}{\chi}\Big)\delta n = -\frac{k^2}{8\pi m_0 \omega_i^2} A. \tag{5.23}$$

Substituting equation (5.23) into equation (5.14), we obtain

$$\left(1 + \frac{1}{\chi}\right) = \frac{v_0^2 k^2}{2}\left(\frac{1}{D_-} + \frac{1}{D_+}\right), \tag{5.24}$$

where $v_0 = e\epsilon_i\sqrt{1 + \alpha_i^2}/(m_0 \omega_i)$ is the quiver velocity of plasma particles in the field of the incident EM wave. Equation (5.24) is the dispersion relation for SRS of the EM wave in a plasma medium. The SRS instability resonantly excites only when the frequency and wave-number matching conditions are satisfied (see equation (5.9)). The simplest SRS process is the one involving only one high frequency side

band, i.e., the Stokes component (k_-, ω_-). Therefore we neglect the anti-Stokes modes as being non resonant. Thus for this simple case $D_- \approx 0$ and $D_+ \neq 0$. This approximation is justified as long as $\omega \ll (c^2\vec{k}_i.\vec{k}/\omega_i)$; this condition breaks down for very small k (i.e., for long wavelength electrostatic perturbations) or if $\vec{k}$ is nearly perpendicular to $\vec{k}_i$. For back-scattering ($\phi_- = \pi$) if frequency and wave matching condition are fulfilled then $\vec{k} \approx 2\vec{k}_i$ and for forward scattering $\phi_- = 0$ it is approximately ω_p/c. For back scattering $D_- \approx 2\omega_i(\omega - c^2\vec{k}_i.\vec{k}/\omega_i + c^2k^2/(2\omega_i)) \approx 0$ for $\omega_i \gg \omega$. The dispersion relation solely for Stokes mode, and the back-scattered radiation is therefore satisfy

$$1 + \frac{1}{\chi} = \frac{1}{4}\frac{v_0^2k^2}{\omega_i(\omega - \Delta)}\frac{1 - \alpha_i^2R}{(1 + \alpha_i^2)(1 - R)}, \tag{5.25}$$

where

$$\Delta = \vec{k}.\vec{v}_g - \frac{k^2c^2}{2\omega_i}, \tag{5.26}$$

with $\vec{v}_g = \vec{k}_ic^2/\omega_i$. For $\omega^2 \approx \omega_p^2 + (3/2)k^2v_T^2$ and $\omega_-^2 \approx \omega_p^2 + c^2(\vec{k}_i - \vec{k})^2$, equation (5.25) can be written as follows:

$$(\omega - \omega_p + i\Gamma_p)(\omega - \omega_p + i\Gamma_-) = -\frac{v_0^2k^2\omega_p}{8\omega_i}, \tag{5.27}$$

where

$$\Gamma_p = \frac{\sqrt{\pi}}{\sqrt{2}}\frac{\omega_p}{(k\lambda_D)^3}\exp[-\frac{1}{2(k\lambda_D)^2} - \frac{3}{2}] + \nu_p, \tag{5.28}$$

is the damping rate of the electron plasma wave, $\nu_p = 3.632n\,ln\Lambda/T_p^{3/2}$ is the electron-positron collision frequency, and the coulomb logarithm $ln\Lambda \approx 10$. Here $\Gamma_- = \omega_p^2\nu_p/(2\omega_-^2)$ is the collisional damping rate of the scattered EM wave. Setting $\omega = \omega_e + i\Gamma$ and solving equation (5.27) for the growth rate Γ, we find

$$\Gamma = -\frac{1}{2}(\Gamma_e + \Gamma_-) \pm \frac{1}{2}\sqrt{(\Gamma_e - \Gamma_-)^2 + \frac{v_0^2k^2\omega_p(1 - R\alpha_i^2)}{2\omega_i(1 + \alpha_i^2)(1 - R)}}. \tag{5.29}$$

Setting $\Gamma = 0$, we obtain the threshold condition for the excitation of Raman scattering for $R = \alpha_i \approx 0$;

$$(v_0/c)_{thr} = \sqrt{\frac{2\Gamma_e\Gamma_-}{\omega_i\omega_p}}. \tag{5.30}$$

5.3 Numerical solution of general dispersion equation due to SRS and application to pulsars

For a strongly damped plasma wave with $k\lambda_D \approx 0.4$, it is not possible to expand $\chi(\omega, k)$ into an asymptotic series. At $k\lambda_D \approx 0.4$, the transition from SRS (Stimulated Raman Scattering) and SCS (Stimulated Compton Scattering) takes place (see chapter 4 as well as Gangadhara and Krishan 1992). Therefore we numerically solve equation (5.25) for the complex roots $\omega = \omega_e + i\Gamma$, by including all damping effects. I have chosen the following plasma and physical parameters of pulsars to compute Stokes parameters of the scattered wave and t time scale of variation as a function of the input pump wave frequency. The time scale t is a crucial parameter as it brings out a clear picture of the scattered wave growth rate, which depends upon various plasma parameters.

The time scale t is vital to reveal the shorter time scale fluctuations associated with the intensity. So the parameters used to compute the t are $\alpha_i = 0.5$ (ratio of the coefficients of the incident electric field along two fundamental axes), $R = 0.5$ (ratio of density perturbations along two fundamental axis), $r = 100\ R_{NS}$ (distance of the emitting region from the neutron star surface), where $R_{NS} \sim 10$ km (radius of neutron star), $n_e = 10^8/\text{cm}^3$ (density of plasma in pulsar magnetosphere), typical luminosity of source $L = 10^{30}$ erg sec^{-1}. We computed t as a function of frequency of the incident pump wave for different plasma temperature $T_e = 10^4,\ 10^5$, and 10^6 K. Plasma wave experiences a small collisional damping

but significant Landau damping at high temperatures. There is a fast rise in t in the lower frequency regimes. The curves due to different plasma temperatures do merge at the lower frequency regime, but in a higher frequency regimes they deviate from each other. It is noticeable from figure 5.2 that the t corresponding to different plasma temperatures show bumps at different time scales, which may be regarded as a rapid fluctuation phenomenon due to the plasma process SRS. The curve of t corresponding to higher temperature shows a bump at a faster time scale in the lower frequency regime.

We know from the observation of PSR 1133+16 by Cordes (1983) that its flux $I_i = 10^{-20}$ erg cm^{-2} sec^{-1} Hz^{-1} at the radio frequency $\nu_i = 600$ MHz. To find the relation between the incident flux I_i and the scattered flux I_s, we use the principle of conservation of wave-energy, i.e., the Manley-Rowe relation, is given by:

$$\frac{I_i}{\omega_i} = \frac{I_s}{\omega_s}. \tag{5.31}$$

It gives

$$I_s = (1 - \omega/\omega_i) I_i. \tag{5.32}$$

For $\omega \approx \omega_p$ and $\omega_i = 2.5\omega_p$, we get $I_s = 0.6 I_i$. In table (5.1), table (5.2) and table (5.3) the Stokes parameters for the incident and the forward, backward scattered electromagnetic waves in PSR 1133+16 are listed. They show that: (1) a linearly polarized incident electromagnetic wave ($\delta_i = \pi, \alpha_i = 0.5$) scatters into another linearly polarized electromagnetic wave with it's plane of polarization rotated through an angle $\Delta\chi$; (2) a elliptically polarized incident wave with counterclockwise sense ($\delta_i = 3\pi/4, \alpha_i = 1$) scatters into (i) a linearly polarized wave when $R = \delta n_2/\delta n_1 = 0$, (ii) elliptically polarzed wave with clockwise sense with major axis rotated through an angle by $\Delta\chi$ when $R = 0.4,\ 0.8$, and 1.2. (3) a circularly polarized incident wave with counterclockwise sense ($\delta_i = \pi/2, \alpha_i = 1$) scatters into (i) linearly polarized wave with $R = 0$, (ii) an elliptically polarized wave with clockwise sense when $R = 0.4$, 0.8 and (iii) circularly polarized wave

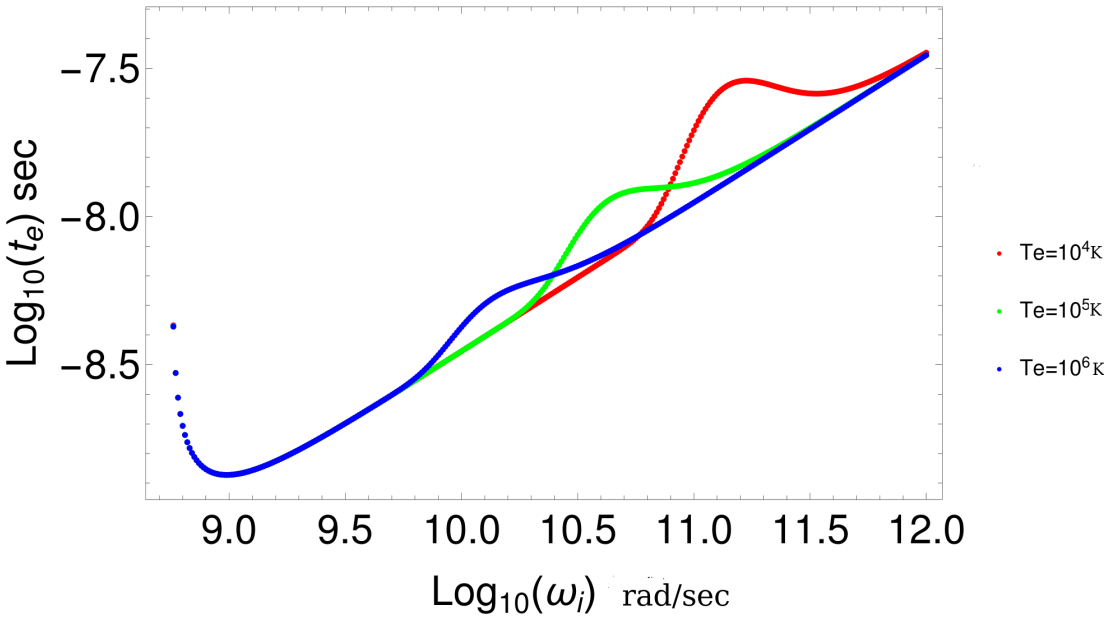

FIGURE 5.2: Plotted e-folding time t as a function of pump wave frequency ω_i in logarithmic scale for different plasma temperatures.

with clockwise sense when $R = 1$. Similar to forward scattering, backward scattering also reproduces the same type of polarization features after being scattered in the plasma medium. From table 5.2, it is showing that sense reversal for backward scattering does not occur.

In figure 5.3, we have plotted the change in polarization angle with respect to the phase of plasma wave for different input phases associated with the electric field of pump wave. The change in polarization angle shows a sinusoidal variation with respect to δ_e.

5.4 Stokes parameters due to SRS

The polarization state of the incident radiation changes due to SRS in an ambient plasma medium, with $\delta_e = \pi$. The Stokes parameters for the incident and scattered

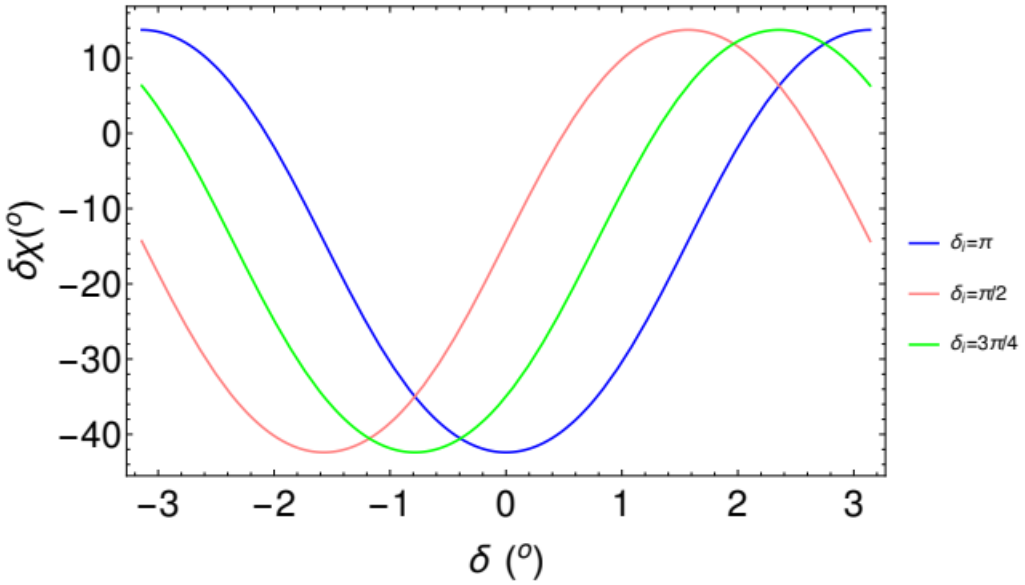

FIGURE 5.3: The change in polarization angle of the incident electric field is plotted as function of phase associated with the y-component. Parameters chosen to plot the above profiles are $\alpha_i = 0.5$, $R = 0.5$ and $\chi_i = 0.25$ rad.

EM waves (Rybicki & Lightman 1985) are:

$$I_j = \frac{c}{8\pi}(1+\alpha_j^2)\epsilon_j^2 \tag{5.33}$$

$$Q_j = \frac{1-\alpha_j^2}{1+\alpha_j^2} I_j, \tag{5.34}$$

$$U_j = \frac{2\alpha_j}{1+\alpha_j^2} I_j \cos(\delta_j), \tag{5.35}$$

$$V_j = -\frac{2\alpha_j}{1+\alpha_j^2} I_j \sin(\delta_j). \tag{5.36}$$

The sense of rotation of the electric field is given by

$$\sin(2\beta_j) = V_j/I_j = -\frac{2\alpha_j}{1+\alpha_j^2}\sin(\delta_j) \tag{5.37}$$

The magnitudes of the principle axes of the ellipse are

$$a_j = I_j|\cos(\beta_j)| \quad \text{and} \quad b_j = I_j|\sin(\beta_j)|.$$

Parameter	$IW_{\delta_i=\pi,\alpha_i=.5}$	$SW_{\delta_-=0,R=0}$	$SW_{\delta_-=0,R=0.4}$	$SW_{\delta_-=0,R=0.8}$	$SW_{\delta_-=0,R=1.2}$
I	1.0 E-20	6.0 E-21	6.0 E-21	6.0 E-21	6.0 E-21
Q	6 E-21	6.0 E-21	5.5 E-21	4.3 E-21	2.8 E-21
U	-8 E-21	0	-2.3 E-21	-4.1 E-21	-5.2 E-21
V	0	0	0	0	0
χ (rad)	-0.4636	0	-0.19	-0.38	-0.54
a	1.0 E-20	6.0 E-21	6.0 E-21	6.0 E-21	6.0 E-21
b	0	0	0	0	0
S_{Rot}	Nil	Nil	Nil	Nil	Nil
Nature	Linear	Linear	Linear	Linear	Linear

TABLE 5.1: I, Q, U, V are the Stokes parameters, IW stands for incident wave, SW stands for scattered wave, S_{rot} stands for sense of rotation, R is the ratio related to density perturbation along two orthogonal basis vectors, α_i is the coefficient associated with elliptically polarized wave, and δ_- corresponds to the phase of scattered wave.

The orientation of the major axis of the ellipse relative to $\hat{e}_x$ axis is given by

$$\tan(2\chi_i) = U_j/Q_j = \frac{2\alpha_j}{1-\alpha_j^2}\cos(\delta_j). \tag{5.38}$$

Here $j = i$ for the incident and - for the scattered EM waves. We use $\delta = \pi$, $\delta_- = \delta_i - \delta$ and $\alpha = \alpha_i R$ to compute the Stokes parameters of the scattered wave.

5.5 Discussion and Conclusion

Here I discuss a couple of exciting things related to the plasma interaction process due to SRS. Figure 5.3 shows that the polarization angle is seen to fluctuate between $-40^\circ \leq \delta\chi \leq 14^\circ$ for different phases associated with input pump wave, which indicates that the SRS is a relatively faster process. It isn't straightforward

Parameter	$IW_{\delta_i=3\pi/4,\alpha_i=1}$	$SW_{\delta_-=-\frac{\pi}{4},R=0}$	$SW_{R=0.4}$	$SW_{R=0.8}$	$SW_{R=1.2}$
I	1.0 E-20	6.0 E-21	6.0 E-21	6.0 E-21	6.0 E-21
Q	0	6.0 E-21	4.3 E-21	1.3 E-21	-1.0 E-21
U	-7.0 E-21	0	-2.9 E-21	-4.1 E-21	-4.1 E-21
V	-7.0 E-21	0	-2.9 E-21	-4.1 E-21	-4.1 E-21
χ (rad)	-0.70	0	-0.29	-0.63	0.60
a	9.0 E-21	6.0 E-21	5.8 E-21	5.5 E-21	5.5 E-21
b	3.8 E-21	0	1.5 E-21	2.2 E-21	2.2 E-21
S_{Rot}	CCW	CCW	CCW	CCW	CCW
Nature	Elliptical	Linear	Elliptical	Elliptical	Elliptical

TABLE 5.2: The computed value of Stokes parameters corresponding to the incident and back-scattered EM wave. I, Q, U and V are the Stokes parameters, IW stands for incident wave, SW stands for scattered wave, S_{rot} stands for sense of rotation, R is the ratio related to density perturbation along two orthogonal basis vectors, α_i is the co-efficient associated with elliptically polarized wave and δ_- corresponds to the phase of the scattered wave.

to compare the two processes: Faraday rotation and SRS, as they are different phenomena. If a pair plasma is involved with equal electron and positron densities, there is no Faraday rotation in the pulsar magnetosphere (Cordes 1986). So making exact fine-tuning or comparing between these two processes is a difficult task. It is evident from our study that SRS is a faster and more prominent process in pulsar. Therefore, using SRS as a potential tool to explain abrupt phenomena, such as rapid temporal fluctuation of intensity and sudden type of radio burst, is well justified.

Now if Γ is the growth rate due to monochromatic pump at ω_i, then the actual growth rate Γ' due to broad pump with a spectral width $\Delta\omega_i \geq \Gamma$ is given by (Kaw et al. 1976):

$$\Gamma' = \frac{1}{\Delta\omega_i}\Gamma^2. \tag{5.39}$$

Since pulsar radio emission is a broadband mechanism, the growth rate definitely

Parameter	$IW_{\delta_i=\pi/2,\alpha_i=1}$	$SW_{\delta_-=-\frac{\pi}{2},R=0}$	$SW_{R=0.4}$	$SW_{R=0.8}$	$SW_{R=1.2}$
I	1.0 E-20	6.0 E-21	6.0 E-21	6.0 E-21	6.0 E-21
Q	0	6.0 E-21	4.3 E-21	1.3 E-21	0
U	0	0	0	0	0
V	-1.0 E-20	0	-4.1 E-21	-5.8 E-21	-6.0 E-21
χ (rad)	Nil	0	-.29 E-17	-1.3 E-16	Nil
a	7.0 E-21	6.0 E-21	5.5 E-21	4.6 E-21	4.2 E-21
b	7.0 E-21	0	2.2 E-21	3.7 E-21	4.2 E-21
S_{Rot}	CCW	Nil	CCW	CCW	CCW
Nature	Circular	Linear	Elliptical	Elliptical	Circular

TABLE 5.3: We have shown Stokes parameters of the incident and back-scattered EM wave. I, Q, U and V are the Stokes parameters, IW stands for incident wave, SW stands for scattered wave, S_{rot} stands for sense of rotation, R is the ratio related to density perturbation along two orthogoanl basis vectors, α_i is the co-efficient associated with elliptically polarized wave and δ_- corresponds to the phase of the scattered wave.

reduced, but this reduction may be compensated by the existing coherent radio emission as proposed in the literature (i) emission by bunches from relativistic pair plasma beams (Kaw et al. 1976; Buschauer & Benford 1976; Benford & Buschauer 1977), (ii) curvature radiation (Gil & Snakowski 1990a,b), and (iii) amplified linear acceleration mechanism in radio pulsars (Melrose 1978).

Due to SRS, there is a shift in the scattered mode frequency, which depends upon the phase-matching condition. The two modes, namely Stokes mode and anti-Stokes mode, can be excited predominantly in the ambient plasma medium. However, if the frequency of the input incident wave is much closer to the plasma frequency, then the scattered waves' frequency differs very little from that of the incident wave.

The value of R can not be determined without invoking non-linear calculations. However, one can guess that the value of R may be closer to the value of α_i. Similar to the frequency and wavenumber matching conditions, we found conditions between the phases δ_i, $\delta_\pm$, and δ_e, in the process of three-wave interaction. R is a very crucial parameter in this model through which a circularly polarized wave can change into a linearly polarized, a circularly polarized, or an elliptically polarized wave or vice versa. The plane of polarization gets rotated through an angle $\chi_s - \chi_i$.

Direct measurement of the growth rate of instability is not possible by an observational approach. However, the e-folding time represents a characteristics time during which a significant change in the degree of polarization, sense, and rotation of the plane of polarization takes place. Therefore the observed variability time scale could be a few times the e-folding time scale.

Chapter 6

Summary and Conclusion

In this Chapter, I have basically summarized all the contributing chapters with future implications. Chapter 1 contains all the preliminary basics of radio pulsars such as polarization properties, electrodynamics of pulsar magnetosphere, emission mechanism etc. In the 2nd Chapter, I have given the details of incoherent curvature radiation model and shown the shape of the polar cap, simulated pulse profiles, emission regions, etc. for different geometrical parameters. This model is very important as it gives a detailed description of the radio emission geometry of pulsars (Gangadhara 2004). It is called a tangent model (Yuen & Melrose 2014).

As the incoherent curvature radiation model cannot explain the high brightness temperature of pulsars, it is essential to develop a coherent radiation model. In the 3rd chapter, I have given a detailed geometrical view of a 3-dimensional bunch embedded on dipolar magnetic field lines. In this chapter, I have generated simulated pulse profiles based on a coherent curvature radiation model for pulsars and shown that theoretically estimated brightness temperature is roughly agreeing with the observed brightness temperature.

In the 4th Chapter, I have reproduced the power spectra of two pulsars: PSRB 0329+54 and PSRB 2111+36. In this chapter, I have shown that the two-segmented broken power laws can be explained by introducing two plasma processes such as Stimulated Raman Scattering and Stimulated Compton Scattering. It is also shown that for highly mono-energetic beam plasma interaction with background pump wave, the two-segmented broken power law of the scattered radio wave reduces to a simple power law. It is shown that the different indices associated with the spatial variation of various plasma parameters presented in the model (for details, see chapter 4) can reproduce the power law of different pulsars.

In Chapter 5, I have shown that the Stimulated Raman scattering can play a very important role in explaining the polarization variation associated with pulsar radio emission. Just to summarize the results of this chapter I would say that the ratio of different density perturbations along two fundamental axes (for details see chapter 5) can change the incident polarization pattern from elliptically polarized wave to linear, circular wave, and vice versa.

Pulsars are exciting compact objects, which offer extreme physical conditions to test the physical laws. My future plans are as follows:

1. To test my models on (i) the coherent radio emission from pulsars and (ii) pulsar power spectra modeling, I plan to make observations using GMRT (Giant Meter Radio Telescope) or any other suitable radio telescopes.
2. I aim to revise my models to include the aberration-retardation (A/R) effects.
3. I want to study Orthogonal Polarization Modes (OPM) both in terms of theory and observations.

In addition to pulsars, my other future plans are to study Fast Radio Bursts (FRB). FRBs are exciting sources associated with galaxies. I expect, studying the

flux variability and the timing with sufficient observational inputs would allow us to understand those phenomena that would carry the signatures of the involved plasma processes. Also, there should be clear discrimination between persistent and transient sources associated with FRB.

Appendix A

Table of symbols appearing in Chapter 3

c	:	Velocity of light
q	:	Charge of single particle
R_{NS}	:	Radius of neutron star
$\hat{n}_{cf}$	:	Line of sight vector in XYZ-frame
$\underline{\hat{\mathrm{n}}}$	:	Line of sight vector in xyz-frame
$\vec{E}_{cf}$	:	Electric field due to radiation in XYZ frame (Lab frame)
$\vec{E}_{NS}$	:	Electric field due to radiation in xyz frame
		(Lab frame, origin is centered with neutron star)
$\vec{J}'$	:	Current density in co-moving frame associated with Langmuir waves
$\vec{J}$	:	Current density in XYZ frame associated with Langmuir waves
R	:	Distance between emission region in pulsar magnetosphere and observer
γ	:	Lorentz factor of secondary pair plasma particles
γ_p	:	Lorentz factor of primary plasma particles

B_0	:	Surface magnetic field of neutron star
ω_0'	:	Angular frequency of perturbed Langmuir wave in co-moving frame
k_0'	:	Wave number of perturbed Langmuir wave in co-moving frame
ω_0	:	Angular frequency of perturbed Langmuir wave XYZ-frame
k_0	:	Wave number associated with perturbed Langmuir wave in XYZ-frame
ω	:	Angular frequency of the electromagnetic radiation emitted
$\vec{k}$	:	Wave number of the electromagnetic radiation emitted
$\vec{r}_b$	:	Position vector of an arbitrary point inside the bunch in XYZ-frame
ϕ_c	:	Dynamical angular span of charge column (See Figure 3.1) in XYZ-frame
σ_0	:	Charge density in lab frame
n′	:	Charge number density in co-moving frame
J_0	:	Magnitude of current density in lab frame
N	:	Number of co-operating particle in bunch
ξ	:	Beaming factor
ξ_0	:	Radial width of the bunch (See Figure 3.1)
η_0	:	Vertical height of the bunch, measured with respect to symmetry axis in XYZ frame (See Figure 3.1)
S_0	:	Length of the bunch
α_m	:	Angular width of the charge column
α	:	Inclination angle of magnetic axis with respect to the rotation axis
σ	:	Minimum impact angle of line of sight with magnetic axis
Γ	:	Half-beam opening angle of pulsar
θ	:	Magnetic co-latitude
ϕ	:	Magnetic azimuth
$\Theta = \theta'$	:	Co-latitude in rotation axis centered frame
Φ	:	Azimuth angle in rotation axis centered frame

ρ_0 : Radius of curvature of magnetic field line passing through the center of momentum of bunch

ζ : Angle between line of sight and rotation axis

r_e : Dipolar field line constant of magnetic field line

μ : Angle between the line of sight and the plane of magnetic field line

ϕ' : Rotation phase or pulse longitude

$\vec{b_t}$: Tangent of magnetic field line

$\vec{k_t}$: Curvature of magnetic field line

$\hat{\epsilon}$: Bi-normal to magnetic field line

$\hat{\epsilon}_{\parallel}$: Projected spin axis vector on the plane of sky

$\hat{\epsilon}_{\perp}$: A vector perpendicular to line of sight and projected spin axis

Appendix B

Radio emission height from geometrical point of view

By assuming dipolar magnetic field, the expression for radius of curvature was derived by Gangadhara (2004):

$$\rho = r_e \sin\theta \frac{(5+3\cos(2\theta))^{3/2}}{3\sqrt{2}(3+\cos(2\theta))}, \tag{B.1}$$

where θ is the polar angle, r_e the dipolar field line constant, which is defined as the distance between center of neutron star and the intersection point of magnetic field line at equatorial plane, i.e., at $\theta = \pi/2$. Now for relativistic plasma emission θ is very small. The angle θ is the angle between magnetic axis and position vector $\vec{r}$, which is related with the angular width of pulsar radio beam in polar direction. At lower altitudes the values of $\theta \ll 1$, so, if we make approximations that $\sin\theta \approx \theta$, $\cos 2\theta \approx 1$, and $r_{em} = r_e \sin^2\theta \approx r_e\theta^2$ (termed as emission radii of the emitting source on magnetic field line, measured from center of neutron star), then equation (B.1) becomes:

$$\rho \approx \frac{4}{3}\frac{r_{\rm em}}{\theta}. \tag{B.2}$$

Pulsar radio emission is believed to be coherent curvature radiation due to the secondary pair plasma or soliton like charge clump streaming along the tangent of dipolar magnetic field line. The characteristics frequency of curvature radiation at which radio emission peaks, is given by Ruderman & Sutherland (1975):

$$\nu_s \approx \frac{3}{4}\frac{c\gamma^3}{\rho}. \tag{B.3}$$

Now if I plug in the expression of ρ from equation (B.3) into equation (B.2), it immediately gives,

$$r_{\rm em} = \frac{9\gamma^3 c}{16\nu_s}\theta. \tag{B.4}$$

The half be opening angle Γ_w of radio beam is connected with polar angle θ via the following equation (Gangadhara 2004):

$$\cos(2\theta) = \frac{1}{3}(\cos\Gamma_w\sqrt{8+\cos^2\Gamma_w} - \sin^2\Gamma_w). \tag{B.5}$$

As radio beam of pulsar is produced by relativistic particles, the observed beam width is expected to be about $1/\gamma$. Although the above mentioned width is not very robust, but rather it is having frequency dependency. Theoretical study by Yang & Zhang (2018) shows that the width of the beaming angle at a lower frequency is more compared to a higher frequency. For $\Gamma_w \ll 1$, equation (B.5) reduces to $\theta \sim (2/3)\Gamma_w$. So by plugging in the value of θ into equation (B.4) we obtain

$$r_{\rm em} \approx \frac{3\gamma^3 c}{8\nu_s}\Gamma_w. \tag{B.6}$$

If Γ_w is having a dependency with frequency like $\Gamma_w = C_1(\nu_s/\nu_0)^{m/2}$, then the expression of $\rm r_{em}$ can be written as follows:

$$r_{\rm em} \approx \frac{3\gamma^3 c}{8\nu_s}C_1(\nu_s/\nu_0)^{m/2}, \tag{B.7}$$

where C_1 is a normalization constant. ν_s is the emitted frequency and ν_0 is the

corresponding frequency at which the luminosity become maximum. $m/2$ is the index.

Appendix C

Derivation of the transformation of wave amplitude

If a wave with slowly varying amplitude $\mathrm{A}'(z', t')$ grows in time and space at a temporal growth rate Γ', in the beam frame, then I can write:

$$A' = A(z', t'), \tag{C.1}$$

So by applying partial differentiation I can write,

$$\frac{dA'}{dt'} = \frac{\partial A'}{\partial t'} + \frac{\partial A'}{\partial z'}\frac{\partial z'}{\partial t'}. \tag{C.2}$$

Now assuming an exponential dependence of growth rate Γ' with $A' = A'_0 \exp[\Gamma' t']$ and group velocity in the beam frame as $v'_g = dz'/dt'$, the above equation can be reduced to

$$\frac{\partial A'}{\partial t'} + v'_g \frac{\partial A'}{\partial z'} = \Gamma' A'. \tag{C.3}$$

Now equation (C.3) can be written as

$$\frac{\partial A'}{\partial t} + v'_g \frac{\partial A'}{\partial z}\frac{\partial t'}{\partial t}\frac{\partial z}{\partial z'} = \frac{\partial t'}{\partial t}\Gamma' A'. \tag{C.4}$$

Using the Lorentz transformation I can write as $z' = \gamma(z - v_b t)$, where v_b is the beam velocity. Then by differentiating we have

$$\delta z' = \gamma \delta z (1 - \frac{v_b}{v_z}), \tag{C.5}$$

where $v_z = dz/dt$ is the beam velocity in lab frame, and $\gamma = (1 - v_b^2/c^2)^{-1/2}$. Now by substituting $v_z = (v_b + v'_z)/(1 + (v_b v'_z)/c^2)$, one can show from equation (C.5) after some manipulation that

$$\frac{\delta z'}{\delta z} = \gamma \frac{v_b + v'_z}{v'_z}. \tag{C.6}$$

Here v'_z is described as the velocity plasma particles in the beam frame due to tiny fluctuation. Similarly, by differentiating the equation related to Lorentz transformation $t' = \gamma(t - (z\ v_b)/c^2)$ with respect to t, and substituting $v_z = (v_b + v'_z)/(1 + (v_b v'_z)/c^2)$, and doing little bit of algebra, we can show that

$$\frac{\delta t'}{\delta t} = \frac{1}{\gamma(1 + (v_b v'_z)/c^2)}. \tag{C.7}$$

Next, by substituting equations (C.6) and (C.7) into equation (C.4), I get,

$$\frac{\delta A'}{\delta t} + \frac{v_b + v'_g}{1 + (v_b v'_g)/c^2}\frac{\delta A'}{\delta z'} = \frac{\Gamma' A'}{\gamma(1 + (v_b v'_g)/c^2)}. \tag{C.8}$$

Note that v_z and v'_z are nothing but the group velocity v_g and v'_g in the lab frame and the beam frame, respectively. Similar to equation (C.3), the wave with amplitude A and with temporal growth rate Γ, will satisfy the following equation in lab frame:

$$\frac{\partial A}{\partial t} + v_g \frac{\partial A}{\partial z} = \Gamma A. \tag{C.9}$$

The amplitudes of wave in lab frame and prime frame are linearly proportional to each other, so one can always write by comparing equation (C.8) and equation (C.9) that:

$$v_g = \frac{v_b + v'_g}{1 + (v_b v'_g)/c^2}, \tag{C.10}$$

and

$$\Gamma = \frac{\Gamma'}{\gamma(1 + (v_b v'_g)/c^2)}. \tag{C.11}$$

For $v_b = v'_g \approx c$, one can write the expression of growth rate amplitude of wave in lab frame approximately as $\Gamma = \Gamma'/(2\gamma)$.

Appendix D

Derivation of pondermotive force

When an electromagnetic wave of very high intensity interacts with plasma, several non-linear processes arise and because of that radiation pressure is coupled to the plasma particles in somewhat subtle way and is called pondermotive force. Many non-linear phenomenon in physics can be explained in a very simple manner by using the concept of pondermotive force, such as self focussing, parametric instability. To derive this I will follow the way as shown by Chen (1984), for single particle method. The equation of motion of an electron in the oscillating electric and magnetic field of a wave is

$$m_e \frac{d\vec{v}}{dt} = -e(\vec{E}(\vec{r}) + (\vec{v}/c) \times \vec{B}(\vec{r})). \tag{D.1}$$

The source of non-linearity is basically arising from two term (i) $\vec{v} \times \vec{B}(\vec{r})$, which is of the second order. (ii) While evaluating $\vec{E}(\vec{r})$, the actual position is taken rather than at the initial position. I can expand the position and velocity of the particle as follows:

$$\vec{r} = \vec{r}_0 + \vec{r}_1 + \vec{r}_2 + ... \tag{D.2}$$

$$\vec{v} = \vec{v}_0 + \vec{v}_1 + \vec{v}_2 + ... \tag{D.3}$$

Let $\vec{E}(\vec{r}) = \vec{E}_s(\vec{r})\cos(\omega t)$ be the electric field associated with electromagnetic wave. Now using the first order term in equation (D.1), I evaluate $\vec{E}(\vec{r})$ at the initial position $\vec{r}_0$

$$m_e \frac{d\vec{v}_1}{dt} = -e\vec{E}(\vec{r}_0). \tag{D.4}$$

Integrating equation (D.4) I get

$$\vec{v}_1 = -\frac{e}{m_e\omega}\vec{E}_s(\vec{r}_0)\sin\omega t. \tag{D.5}$$

Integrating again equation (D.5) I get

$$\vec{r}_1 = \frac{e}{m_e\omega^2}\vec{E}_s(\vec{r}_0)\cos\omega t. \tag{D.6}$$

Now expanding $\vec{E}(\vec{r})$ about r_0 I get,

$$\vec{E}(\vec{r}) = \vec{E}_s(\vec{r}_0) + ((\vec{r}_1.\vec{\nabla})\vec{E}_s(\vec{r}_0))_{r=r_0} + ... \tag{D.7}$$

From the second order term of equation (D.1) I get,

$$m_e \frac{d\vec{v}_2}{dt} = -e((\delta\vec{r}_1.\vec{\nabla})\vec{E}_s(\vec{r}_0) + \frac{\vec{v}_1}{c} \times \vec{B}_s(\vec{r}_0)). \tag{D.8}$$

Using Maxwell equation

$$\vec{\nabla} \times \vec{E}_s = -\frac{1}{c}\frac{d\vec{B}_s}{dt}, \tag{D.9}$$

I find

$$\vec{B}_s(\vec{r}_0) = -\frac{c}{\omega}\vec{\nabla} \times \vec{E}_s(\vec{r}_0)\sin(\omega t). \tag{D.10}$$

Inserting equations (D.5), (D.6), (D.10) into equation (D.8), and averaging over time $t = 2\pi/\omega$, I get

$$< m_e \frac{d\vec{v}_2}{dt} >= \vec{f}_{NL}$$

$$= -\frac{e^2}{4m_e\omega^2}((\vec{E}_s(\vec{r}_0).\vec{\nabla})\vec{E}_s(\vec{r}_0) + \vec{E}_s(\vec{r}_0) \times (\vec{\nabla} \times \vec{E}_s(\vec{r}_0)). \tag{D.11}$$

Here I have used $< \cos^2(\omega t) >=< \sin^2(\omega t) >= \frac{1}{2}$. Now using vector identity I get from equation (D.11),

$$\vec{f}_{NL} = -\frac{\omega_{pe}^2}{16\pi n_0 \omega^2}\vec{\nabla}E_s^2. \tag{D.12}$$

So the force per cm^3 is given by

$$\vec{F}_{NL} = n_0\vec{f}_{NL} = -\frac{\omega_{pe}^2}{8\pi\omega^2}\vec{\nabla} < E_s^2(\vec{r}_0) >, \tag{D.13}$$

where $\vec{\nabla}E_s^2 = 2 \times \vec{\nabla} < E_s^2(\vec{r}_0) >$.

Appendix E

Dispersion relation of EM wave in magnetized plasma

Consider the electromagnetic radiation propagating in the direction parallel to magnetic field lines. If the magnetic field B is having direction parallel to z-axis, I can write the propagation vector as $\vec{k}_R = k\hat{z}$, $\vec{E}_R = E_x\hat{x} + E_y\hat{y}$. Now I assume that the electromagnetic radiation propagates in the plasma medium with characteristics electric and magnetic fields: $\vec{E}_R$ and $\vec{B}_R$. Then the relevant Maxwell equations can be written as:

$$\vec{\nabla} \times \vec{E}_R = -\frac{\partial \vec{B}_R}{\partial t}, \tag{E.1}$$

$$\vec{\nabla} \times \vec{B}_R = \frac{\vec{j}_c}{\epsilon_0 c^2} + \frac{1}{c^2}\frac{\partial \vec{E}_R}{\partial t}. \tag{E.2}$$

Here $\vec{j_c}$ is the current density arises because of the electron motion, ϵ_0 the electric permittivity. Now by taking curl on the both the sides equation (E.1), we have

$$\vec{\nabla} \times (\vec{\nabla} \times \vec{E}_R) = \vec{\nabla}(\vec{\nabla} \cdot \vec{E}_R) - \nabla^2 \vec{E}_R = -\vec{\nabla} \times \dot{\vec{B}}_R. \tag{E.3}$$

Here dot represent the time derivative. Now eliminating $\vec{\nabla} \times \dot{\vec{B}}_R$ and assuming $\exp[i(\vec{k}.\vec{r} - \omega t)]$ dependence, equation (E.3) reduces to

$$-\vec{k}(\vec{k}_R \cdot \vec{E}_R) + k^2 \vec{E}_R = \frac{i\omega}{\epsilon_0 c^2} \vec{j}_c + \frac{\omega^2}{c^2} \vec{E}_R, \tag{E.4}$$

here ω is the angular frequency of the emitted radiation, $\vec{k}$ is the propagation vector, r the spatial variable, and t the time variable. For pure transverse wave $\vec{k}.\vec{E}_R = 0$, so equation (E.4) reduces to

$$(\omega^2 - c^2 k^2)\vec{E}_R = -\frac{i\omega \vec{j_c}}{\epsilon_0}. \tag{E.5}$$

The current density expression is given by

$$\vec{j_c} = -n_0 q \vec{v}. \tag{E.6}$$

Here n_0 is the equilibrium plasma density, q is the net charge in pair plasma in short time scales of the order of $T \sim 2\pi/\omega_i$, $\vec{v}$ is the velocity of electrons. So the equation of motion of plasma particles in the combined electric and magnetic field becomes:

$$m\frac{\partial \vec{v}}{\partial t} = q(\vec{E}_R + \vec{v} \times \vec{B}). \tag{E.7}$$

Here m is the mass of electron, $\vec{B}$ is the external magnetic field of pulsar. By separating the velocity components in equation (E.7) we get

$$v_x = \frac{iq}{m\omega} \frac{E_x - i(\omega_c E_y)/\omega}{1 - \omega_c^2/\omega^2}, \tag{E.8}$$

$$v_y = \frac{iq}{m\omega} \frac{E_y + i(\omega_c E_x)/\omega}{1 - \omega_c^2/\omega^2}, \tag{E.9}$$

where in above equations $\omega_c = (qB)/m$ is designated as the cyclotron frequency. Now keep segregating the current density components and plugging into equation (E.5) and again resolving the electric field components I get the following equations:

$$(\omega^2 - c^2k^2)E_x = \frac{\omega_p^2}{1-\omega_c^2/\omega^2}(E_x - i\frac{\omega_c}{\omega}E_y), \tag{E.10}$$

$$(\omega^2 - c^2k^2)E_y = \frac{\omega_p^2}{1-\omega_c^2/\omega^2}(E_y + i\frac{\omega_c}{\omega}E_x), \tag{E.11}$$

where ω_c and ω_p are designated as the cyclotron and plasma frequency. Now the above two equations can be written in the following forms:

$$(\omega^2 - c^2k^2 - \alpha_p)E_x + i\frac{\omega_c\alpha_p}{\omega}E_y = 0, \tag{E.12}$$

$$-i\frac{\omega_c\alpha_p}{\omega}E_x + (\omega^2 - c^2k^2 - \alpha_p)E_y = 0, \tag{E.13}$$

where in the above equations α_p is defined as $\alpha_p = \omega_p^2/(1-\omega_c^2/\omega^2)$. Now dividing equation (E.12) by equation (E.13), I get,

$$(\omega^2 - c^2k^2 - \alpha_p)^2 = (\frac{\omega_c\alpha_p}{\omega})^2. \tag{E.14}$$

By solving above equation (E.14), I can write:

$$\frac{c^2k^2}{\omega^2} = 1 - \frac{\frac{\omega_p^2}{\omega^2}}{1 \mp \frac{\omega_c}{\omega}}. \tag{E.15}$$

Now the refractive indices of the two types of waves: R-wave and L-wave in the case of $\omega_c \gg \omega$ can be written as:

$$n_R^2 = 1 + \frac{\omega_p^2}{\omega\omega_c}, \tag{E.16}$$

$$n_L^2 = 1 - \frac{\omega_p^2}{\omega\omega_c}. \tag{E.17}$$

Now I discuss two cases: (i) In the limit $\omega\omega_c \gg \omega_p^2$, the refractive index of left circularly polarized wave and right circularly polarized wave reduces to $n_R =$

$n_L \approx 1$. Which means that, in the case of $\omega\omega_c \gg \omega_p^2$, emitted radio waves in pulsars will propagate like EM wave in vacuum, without much interfering with plasma and associated magnetic field. (ii) Also in the limit $\omega_c/\omega \ll 1$, dispersion relation will reduce to un-magnetized one (see equation (E.15)). It is possible that case (i) is more viable in pulsar magnetosphere than the case (ii). There is a strong possibility that these two types of waves, i.e., left circularly polarized and right circularly polarized waves, can be produced in the presence of magnetized plasma in pulsar.

Bibliography

Arons J., 1983, in Burns M. L., Harding A. K., Ramaty R., eds, American Institute of Physics Conference Series Vol. 101, Positron-Electron Pairs in Astrophysics. pp 163–193, doi:10.1063/1.34087

Arons J., Barnard J. J., 1986, *Astrophys. J.*, 302, 120

Arons J., Scharlemann E. T., 1979, *Astrophys. J.*, 231, 854

Asseo E., 1993, in Guyenne H. T. D., Hunt J. J., eds, Plasma Physics and Controlled Nuclear Fusion (ITC-4). pp 305–308

Asseo E., Porzio A., 2006, *Mon. Not. Roy. Astron. Soc.*, 369, 1469

Asseo E., Pelletier G., Sol H., 1990, *Mon. Not. Roy. Astron. Soc.*, 247, 529

Backer D. C., 1970, *Nature*, 228, 42

Backer D. C., Rankin J. M., 1980, *Astrophys. J. Suppl.*, 42, 143

Baring M. G., Harding A. K., 1998, *Astrophys. J. Lett.*, 507, L55

Bartel N., Sieber W., 1978, *Astron. Astrophys.*, 70, 307

Bell M. E., et al., 2016, *Mon. Not. Roy. Astron. Soc.*, 461, 908

Benford G., 1992, *Astrophys. J. Lett.*, 391, L59

Benford G., Buschauer R., 1977, *Mon. Not. Roy. Astron. Soc.*, 179, 189

Beskin V. S., Gurevich A. V., Istomin I. N., 1988, *Astrophys. Space Sci.*, 146, 205

Bhattacharya D., 1992, in Hankins T. H., Rankin J. M., Gil J. A., eds, IAU Colloq. 128: Magnetospheric Structure and Emission Mechanics of Radio Pulsars. p. 27

Bhattacharya D., van den Heuvel E. P. J., 1991, *Physics Reports*, 203, 1

Biggs J. D., 1992, *Astrophys. J.*, 394, 574

Bilous A. V., et al., 2016, *Astron. Astrophys.*, 591, A134

Blaskiewicz M., Cordes J. M., Wasserman I., 1991, *Astrophys. J.*, 370, 643

Boriakoff V., Ferguson D. C., Slater G., 1981, in Sieber W., Wielebinski R., eds, IAU Symposium Vol. 95, Pulsars: 13 Years of Research on Neutron Stars. pp 199–204

Brueck M. T., 1978, *Astron. Astrophys.*, 68, 181

Buschauer R., Benford G., 1976, *Mon. Not. Roy. Astron. Soc.*, 177, 109

Buschauer R., Benford G., 1980, *Mon. Not. Roy. Astron. Soc.*, 190, 945

Cairns I. H., Johnston S., Das P., 2001, *Astrophys. J. Lett.*, 563, L65

Chen F., 1984, *Sky and Telescope*, 67, 527

Cheng A., Ruderman M., Sutherland P., 1976, *Astrophys. J.*, 203, 209

Cheng A. F., Ruderman M. A., 1979, *Astrophys. J.*, 229, 348

Cheng K. S., Ho C., Ruderman M., 1986, *Astrophys. J.*, 300, 500

Cordes J. M., 1976, *Astrophys. J.*, 210, 780

Cordes J. M., 1978, *Astrophys. J.*, 222, 1006

Cordes J. M., Rankin J. M., Backer D. C., 1978, *Astrophys. J.*, 223, 961

Cordes J. M., 1979, *Space Sci. Rev.*, 24, 567

Cordes J. M., 1983, in Burns M. L., Harding A. K., Ramaty R., eds, American Institute of Physics Conference Series Vol. 101, Positron-Electron Pairs in Astrophysics. pp 98–112, doi:10.1063/1.34136

Cordes J. M., 1986, *Astrophys. J.*, 311, 183

Cordes J. M., Kramer M., Lazio T. J. W., Stappers B. W., Backer D. C., Johnston S., 2004, *New Astronomy Reviews*, 48, 1413

Kramer, M., Wielebinski, R., Jessner, A., Gil, J. A., & Seiradakis, J. H. 1994, A&AS, 107, 515

Kramer, M. et al. 2007, *Mon. Not. Roy. Astron. Soc.*, 377, 107

Kramer, M. et al. 1999, *Astrophys. J.*, 526, 957

Cordes J. M., Wasserman I., 2016, *Mon. Not. Roy. Astron. Soc.*, 457, 232

Cox J. L. J., 1979, *Astrophys. J.*, 229, 734

Craft H. D., Comella J. M., Drake F. D., 1968, *Nature*, 218, 1122

Crawford J., Kazanas D., 2001, in APS April Meeting Abstracts. p. B13.014

Daugherty J. K., Harding A. K., 1983, *Astrophys. J.*, 273, 761

Deutsch A. J., 1955, Annales d'Astrophysique, 18, 1

Drake J. F., 1974, Proceedings of the Royal Society of London Series A, 340, 457

Drake J. F., Kaw P. K., Lee Y. C., Schmid G., Liu C. S., Rosenbluth M. N., 1974, Physics of Fluids, 17, 778

Dyks J., Harding A. K., 2004, *Astrophys. J.*, 614, 869

Eilek J. A., Hankins T. H., 2016, Journal of Plasma Physics, 82, 32

Foster R. S., Fairhead L., Backer D. C., 1991, *Astrophys. J.*, 378, 687

Fried B. D., Conte S. D., 1961, The Plasma Dispersion Function

Fussell D., Luo Q., Melrose D. B., 2003, *Mon. Not. Roy. Astron. Soc.*, 343, 1248

Gangadhara R. T., 1997, *Astron. Astrophys.*, 327, 155

Gangadhara R. T., 2004, *Astrophys. J.*, 609, 335

Gangadhara R. T., 2005, *Astrophys. J.*, 628, 923

Gangadhara R. T., 2010, *Astrophys. J.*, 710, 29

Gangadhara R. T., Gupta Y., 2001, *Astrophys. J.*, 555, 31

Gangadhara R. T., Krishan V., 1992, *Mon. Not. Roy. Astron. Soc.*, 256, 111

Gangadhara R. T., Xilouris K. M., von Hoensbroech A., Kramer M., Jessner A., Wielebinski R., 1999, *Astron. Astrophys.*, 342, 474

Gedalin M., Gruman E., Melrose D. B., 2002, *Mon. Not. Roy. Astron. Soc.*, 337, 422

Gil J., 1983, *Astron. Astrophys.*, 123, 7

Gil J., 1986, *Astrophys. J.*, 309, 609

Gil J. A., 1987, *Astrophys. J.*, 314, 629

Gil J. A., 1993, in van Riper K. A., Epstein R. I., Ho C., eds, Isolated Pulsars. p. 190

Gil J., Mitra D., 2001, *Astrophys. J.*, 550, 383

Gil J., Rudnicki W., 1985, *Astron. Astrophys.*, 147, 184

Gil J. A., Snakowski J. K., 1990a, *Astron. Astrophys.*, 234, 237

Gil J. A., Snakowski J. K., 1990b, *Astron. Astrophys.*, 234, 269

Gil J., Kijak J., Zycki P., 1993, *Astron. Astrophys.*, 272, 207

Gil J., Lyubarsky Y., Melikidze G. I., 2004, *Astrophys. J.*, 600, 872

Ginzburg V. L., Zhelezniakov V. V., 1975, *Ann. Rev. Astron. Astrophys.*, 13, 511

Goldreich P., Julian W. H., 1969, *Astrophys. J.*, 157, 869

Gould D. M., Lyne A. G., 1998, *Mon. Not. Roy. Astron. Soc.*, 301, 235

Gunn J. E., Ostriker J. P., 1970, *Astrophys. J.*, 160, 979

Gupta Y., Gangadhara R. T., 2003, *Astrophys. J.*, 584, 418

Gurevich A., Beskin V., Istomin Y., 1993, Physics of the Pulsar Magnetosphere

Han J. L., 1997, *Astron. Astrophys.*, 318, 485

Han J. L., Manchester R. N., Xu R. X., Qiao G. J., 1998, *Mon. Not. Roy. Astron. Soc.*, 300, 373

Hankins T. H., 1971, *Astrophys. J.*, 169, 487

Hankins T. H., Eilek J. A., 2007, *Astrophys. J.*, 670, 693

Harrison P. A., Lyne A. G., 1993, *Mon. Not. Roy. Astron. Soc.*, 265, 778

Hartman J. W., Bhattacharya D., Wijers R., Verbunt F., 1997, *Astron. Astrophys.*, 322, 477

Hasegawa A., Mima K., 1978, *J. Geophys. Res.*, 83, 1117

Helfand D. J., Tademaru E., 1977, *Astrophys. J.*, 216, 842

Hewish A., Bell S. J., Pilkington J. D. H., Scott P. F., Collins R. A., 1968, *Nature*, 217, 709

Igoshev A. P., Popov S. B., 2015, Astronomische Nachrichten, 336, 831

Izvekova V. A., Kuzmin A. D., Malofeev V. M., Shitov I. P., 1981, *Astrophys. Space Sci.*, 78, 45

Jackson J. D., 1975, Classical electrodynamics

Jankowski F., van Straten W., Keane E. F., Bailes M., Barr E. D., Johnston S., Kerr M., 2017, Monthly Notices of the Royal Astronomical Society, 473, 4436

Jankowski F., van Straten W., Keane E. F., Bailes M., Barr E. D., Johnston S., Kerr M., 2018, *Mon. Not. Roy. Astron. Soc.*, 473, 4436

Jones P. B., 1980, Technical report, Pair formation and electric field boundary conditions at neutron star magnetic poles

Karpman V. I., Norman C. A., Ter Haar D., Tsytovich V. N., 1975, *Physica Scripta*, 11, 271

Kaspi V. M., Helfand D. J., 2002, Constraining the Birth Events of Neutron Stars. p. 3

Kaw P. K., Kruer W. L., Liu C. S., Nishikawa K., 1976, Advances in plasma physics. Vol._6.

Kazbegi A. Z., Machabeli G. Z., Melikidze G. I., 1991a, Australian Journal of Physics, 44, 573

Kazbegi A. Z., Machabeli G. Z., Melikidze G. I., 1991b, *Mon. Not. Roy. Astron. Soc.*, 253, 377

Kijak J., Gil J., 1997, *Mon. Not. Roy. Astron. Soc.*, 288, 631

Kijak J., Kramer M., Wielebinski R., Jessner A., 1998, *Astron. Astrophys. Suppl.*, 127, 153

Komesaroff M. M., 1970, *Nature*, 225, 612

Konar S., 2017, Journal of Astrophysics and Astronomy, 38, 47

Kramer M., 1998, in Shibazaki N., ed., Neutron Stars and Pulsars: Thirty Years after the Discovery. p. 229

Kramer M., Jessner A., Doroshenko O., Wielebinski R., 1997, *Astrophys. J.*, 488, 364

Kramer M., Xilouris K. M., Lorimer D. R., Doroshenko O., Jessner A., Wielebinski R., Wolszczan A., Camilo F., 1998, *Astrophys. J.*, 501, 270

Kramer M., Lange C., Lorimer D. R., Backer D. C., Xilouris K. M., Jessner A., Wielebinski R., 1999, *Astrophys. J.*, 526, 957

Kumar D., Gangadhara R. T., 2012a, *Astrophys. J.*, 746, 157

Kumar D., Gangadhara R. T., 2012b, *Astrophys. J.*, 754, 55

Kumar D., Gangadhara R. T., 2013, *Astrophys. J.*, 769, 104

Liu, K., et al. 2019, *Astrophys. J. Lett.*, 885, L10

Liu C. S., Kaw P. K., 1976, Advances in Plasma Physics, 6, 83

Lorimer D. R., Yates J. A., Lyne A. G., Gould D. M., 1995, *Mon. Not. Roy. Astron. Soc.*, 273, 411

Lorimer D. R., Bailes M., Harrison P. A., 1997, *Mon. Not. Roy. Astron. Soc.*, 289, 592

Luo Q., Melrose D. B., 1992, *Mon. Not. Roy. Astron. Soc.*, 258, 616

Lyne A. G., 1982, in Rees M. J., Stoneham R. J., eds, NATO Advanced Science Institutes (ASI) Series C Vol. 90, NATO Advanced Science Institutes (ASI) Series C. p. 405

Lyne A. G., Lorimer D. R., 1994, *Nature*, 369, 127

Lyne A. G., Manchester R. N., 1988, *Mon. Not. Roy. Astron. Soc.*, 234, 477

Lyne A. G., Anderson B., Salter M. J., 1982, *Mon. Not. Roy. Astron. Soc.*, 201, 503

Lyne A. G., Manchester R. N., Taylor J. H., 1985, *Mon. Not. Roy. Astron. Soc.*, 213, 613

Lyubarskii Y. E., Petrova S. A., 2000, *Astron. Astrophys.*, 355, 406

Malofeev V. M., 1993, Astronomy Letters, 19, 138

Malofeev V. M., Malov I. F., 1980, *Soviet Astron.*, 24, 54

Malofeev V. M., Gil J. A., Jessner A., Malov I. F., Seiradakis J. H., Sieber W., Wielebinski R., 1994, *Astron. Astrophys.*, 285, 201

Malofeev V. M., Shishov V. I., Sieber W., Jessner A., Kramer M., Wielebinski R., 1996, *Astron. Astrophys.*, 308, 180

Manchester R. N., 1971, *Astrophys. J. Suppl.*, 23, 283

Manchester R. N., Taylor J. H., Huguenin G. R., 1975, *Astrophys. J.*, 196, 83

Manchester R. N., Lyne A. G., Taylor J. H., Durdin J. M., Large M. I., Little A. G., 1978, *Mon. Not. Roy. Astron. Soc.*, 185, 409

Manchester R. N., Hobbs G. B., Teoh A., Hobbs M., 2005, VizieR Online Data Catalog, p. VII/245

Maron O., Kijak J., Kramer M., Wielebinski R., 2000, *Astron. Astrophys. Suppl.*, 147, 195

Melrose D. B., 1978, *Astrophys. J.*, 225, 557

Melrose D. B., 1981, in Sieber W., Wielebinski R., eds, IAU Symposium Vol. 95, Pulsars: 13 Years of Research on Neutron Stars. pp 133–139

Melrose D. B., 1989, *Solar Phys.*, 120, 369

Melrose D. B., 1992, Philosophical Transactions of the Royal Society of London Series A, 341, 105

Melrose D. B., 1996, *Publication. Astron. Soc. Australia*, 13, 140

Melrose D. B., Luo Q., 2004, *Mon. Not. Roy. Astron. Soc.*, 352, 915

Melrose D. B., Arons J., Cordes J. M., Ferguson D. C., Kahn F. D., Rickett B. J., 1981, in Sieber W., Wielebinski R., eds, IAU Symposium Vol. 95, Pulsars: 13 Years of Research on Neutron Stars. p. 155

Meltzer D. W., Thorne K. S., 1966, *Astrophys. J.*, 145, 514

Menou K., Esin A. A., Narayan R., Garcia M. R., Lasota J.-P., McClintock J. E., 1999, *Astrophys. J.*, 520, 276

Michel F. C., 1978, *Astrophys. J.*, 220, 1101

Michel F. C., 1987, *Astrophys. J.*, 322, 822

Mitra D., Gil J., Melikidze G. I., 2009, *Astrophys. J. Lett.*, 696, L141

Morris D., et al., 1997, *Astron. Astrophys.*, 322, L17

Mukherjee S., Kembhavi A., 1997, *Astrophys. J.*, 489, 928

Narayan R., Ostriker J. P., 1990, *Astrophys. J.*, 352, 222

Narayan R., Vivekanand M., 1983, *Astrophys. J.*, 274, 771

Oppenheimer J. R., Volkoff G. M., 1939, Physical Review, 55, 374

Ostriker J. P., Gunn J. E., 1969, *Astrophys. J.*, 157, 1395

Pacini F., 1970, *Nature*, 226, 622

Pataraia A., Melikidze G., 1980, *Astrophys. Space Sci.*, 68, 49

Petrova S. A., Lyubarskii Y. E., 2000, *Astron. Astrophys.*, 355, 1168

Radhakrishnan V., Cooke D. J., 1969, *Astrophysical Letters*, 3, 225

Radhakrishnan V., Rankin J. M., 1990, *Astrophys. J.*, 352, 258

Rankin J. M., 1983, *Astrophys. J.*, 274, 333

Rankin J. M., 1990, *Astrophys. J.*, 352, 247

Rankin J. M., 1993a, *Astrophys. J. Suppl.*, 85, 145

Rankin J. M., 1993b, *Astrophys. J.*, 405, 285

Rankin J. M., Comella J. M., Craft H. D. J., Richards D. W., Campbell D. B., Counselman C. C. I., 1970, *Astrophys. J.*, 162, 707

Rickett B. J., 1975, *Astrophys. J.*, 197, 185

Ritchings R. T., 1976, *Mon. Not. Roy. Astron. Soc.*, 176, 249

Robinson B. J., Cooper B. F. C., Gardiner F. F., Wielebinski R., Landecker T. L., 1968, *Nature*, 218, 1143

Romani R. W., 1996a, High Energy Pulsars: Pulses and Populations. p. 331

Romani R. W., 1996b, *Astrophys. J.*, 470, 469

Rowe E. T., 1995, *Astron. Astrophys.*, 296, 275

Roy T., Gangadhara R. T., 2019, *Astrophys. J.*, 878, 148

Ruderman M. A., Sutherland P. G., 1975, *Astrophys. J.*, 196, 51

Rybicki G. B., Lightman A. P., 1979, Radiative processes in astrophysics, A Wiley-Interscience Publication, New York: Wiley

Rybicki G. B., Lightman A. P., 1985, Radiative processes in astrophysics.

Sang Y., Chanmugam G., 1987, *Astrophys. J. Lett.*, 323, L61

Sang Y., Chanmugam G., 1990, *Astrophys. J.*, 363, 597

Sazonov V. N., Tsytovich V. N., 1968, Izvestiia Vysshaia Uchebn. Zaved., Radiofizika, 11, 1287

Sieber W., 1973, *Astron. Astrophys.*, 28, 237

Sieber W., Wielebinski R., Stepney S., 1982, Journal of the British Astronomical Association, 92, 102

Seiradakis J. H., Wielebinski R., 2004, *Astron. Astrophys. Rev.*, 12, 239

Seiradakis J. H., Gil J. A., Graham D. A., Jessner A., Kramer M., Malofeev V. M., Sieber W., Wielebinski R., 1995, *Astron. Astrophys. Suppl.*, 111, 205

Shapiro S. L., Teukolsky S. A., 1983, Journal of the British Astronomical Association, 93, 276

Sieber W., 1973, *Astron. Astrophys.*, 28, 237

Slee O. B., Alurkar S. K., Bobra A. D., 1986, Australian Journal of Physics, 39, 103

Staelin D. H., Reifenstein Edward C. I., 1968, Science, 162, 1481

Stinebring D. R., Condon J. J., 1990, *Astrophys. J.*, 352, 207

Stollman G. M., 1987, *Astron. Astrophys.*, 178, 143

Stovall K., et al., 2015, *Astrophys. J.*, 808, 156

Sturrock P. A., 1971, *Astrophys. J.*, 164, 529

Torne, P., et al. 2017, *Mon. Not. Roy. Astron. Soc.*, 465, 242

Toscano M., Bailes M., Manchester R. N., Sand hu J. S., 1998, *Astrophys. J.*, 506, 863

Vivekanand M., Ables J. G., McConnell D., 1998, *Astrophys. J.*, 501, 823

Wang P. F., Wang C., Han J. L., 2012, *Mon. Not. Roy. Astron. Soc.*, 423, 2464

Weisberg J. M., Taylor J. H., Fowler L. A., 1981, Scientific American, 245, 74

Xilouris K. M., Kramer M., 1996, in Johnston S., Walker M. A., Bailes M., eds, Astronomical Society of the Pacific Conference Series Vol. 105, IAU Colloq. 160: Pulsars: Problems and Progress. p. 245

Xu J.-L., Wang J.-J., 2010, Research in Astronomy and Astrophysics, 10, 151

Xue M., et al., 2017, *Publication. Astron. Soc. Australia*, 34, e070

Yang Y.-P., Zhang B., 2018, *Astrophys. J.*, 868, 31

You X.-P., Han J.-L., 2006, Chinese Journal of Astronomy and Astrophysics Supplement, 6, 56

Yuen R., Melrose D. B., 2014, *Publication. Astron. Soc. Australia*, 31, e039

Zhou X., Tong H., Zhu C., Wang N., 2017, *Mon. Not. Roy. Astron. Soc.*, 472, 2403

van Ommen T. D., D'Alessandro F., Hamilton P. A., McCulloch P. M., 1997, *Mon. Not. Roy. Astron. Soc.*, 287, 307

von Hoensbroech A., Lesch H., Kunzl T., 1998, *Astron. Astrophys.*, 336, 209